# THE COMPOSITION OF ULTRA HIGH ENERGY COSMIC RAYS THROUGH HYBRID ANALYSIS AT TELESCOPE ARRAY

by

Elliott L. Barcikowski

A dissertation submitted to the faculty of
The University of Utah
in partial fulfillment of the requirements for the degree of

Doctor of Philosophy

in

Physics

Department of Physics and Astronomy

The University of Utah

December 2011

## The University of Utah Graduate School

# STATEMENT OF DISSERTATION APPROVAL

The dissertation of **Elliott L. Barcikowski**

has been approved by the following supervisory committee members:

**Pierre Sokolsky** , Chair **9/29/2011** Date Approved

**John Belz** , Member **9/29/2011** Date Approved

**Stephan LeBohec** , Member **9/29/2011** Date Approved

**Jordan Gerton** , Member **9/29/2011** Date Approved

**Peter Alfeld** , Member **9/29/2011** Date Approved

and by **David Kieda** , Chair of

the Department of **Physics and Astronomy**

and by Charles A. Wight, Dean of The Graduate School.

# ABSTRACT

The chemical composition of cosmic rays is critically important to understanding cosmic ray sources as well as a cosmic ray's propagation through the Galaxy and Universe. Theories explaining the features seen in the cosmic ray spectrum depend strongly on the chemical composition of cosmic rays. Composition has implications for anisotropy studies as atomic nuclei with large atomic number are more susceptible to deflection by Galactic and extragalactic magnetic fields.

This work presents a composition analysis using data from the Telescope Array (TA) experiment and uses the point of shower maximum, $X_{max}$, as the marker of a cosmic ray's chemical composition. TA is the largest cosmic ray detector in the Northern Hemisphere and makes use of both ground array as well as nitrogen fluorescence methods for detecting cosmic rays. This analysis combines both ground array and fluorescence data in a hybrid analysis to obtain resolutions of 0.5° in reconstructed pointing directions and 20 $\mathrm{g/cm^2}$ in reconstructed $X_{max}$.

Above $10^{18.5}$ eV, measured $X_{max}$ distributions using hybrid TA data are compatible with proton MC and exclude iron. However, above $10^{19.3}$ eV, the statistical power is limited and the data is compatible either proton or iron MCs. The shapes of the $X_{max}$ distributions independent of their means are compared, showing again that the data is compatible with protons and incompatible with iron. However, the statistical power for this measurement is limited above $10^{18.8}$ eV.

# CONTENTS

**CHAPTERS**

# LIST OF FIGURES

# LIST OF TABLES

# ACKNOWLEDGMENTS

I would like to thank Dr. Pierre Sokolsky and Dr. John Belz for the opportunity to be part of the Telescope Array experiment. With their support as well as that of other members of Telescope Array, I have progressed dramatically as a student and a researcher. Additionally, his work draws upon the work of many members of Telescope Array. A few that deserve mention are Ben Stokes and Dmitri Ivanov for their surface detector simulation and Sean Stratton and Lauren Scott for their fluorescence detector simulation. These two simulations provide the foundation of a hybrid detector simulation and are used directly in this analysis.

Telescope Array is supported by several full-time staff members that help with issues both technical and administrative in nature. Without their support neither this work nor any other would be possible. These people include Gary McDonough, Frank Misak, Jeremy Smith, and Stan Thomas.

The Telescope Array experiment is supported by the Japan Society for the Promotion of Science through Grants-in-Aid for Scientific Research on Specially Promoted Research (21000002) "Extreme Phenomena in the Universe Explored by Highest Energy Cosmic Rays", basic research awards 18204020(A), 18403004(B) and 20340057(B); by the U.S. National Science Foundation awards PHY-0307098, PHY-0601915, PHY-0703893, PHY-0758342, and PHY-0848320 (Utah) and PHY-0649681 (Rutgers); by the National Research Foundation of Korea (2006-0050031, 2007-0056005, 2007-0093860, 2010-0011378, 2010-0028071, R32-10130); by the Russian Academy of Sciences, RFBR grants 10-02-01406a and 11-02-01528a (INR), IISN project No. 4.4509.10 and Belgian Science Policy under IUAP VI/11 (ULB). The foundations of Dr. Ezekiel R. and Edna Wattis Dumke, Willard L. Eccles and the George S. and Dolores Dore Eccles all helped with generous donations. The State of Utah supported the project through its Economic Development Board, and the University of Utah through the Office of the Vice President for Research. The experimental site became available through the cooperation of the Utah School and Institutional Trust Lands

Administration (SITLA), U.S. Bureau of Land Management and the U.S. Air Force. We also wish to thank the people and the officials of Millard County, Utah, for their steadfast and warm support. We gratefully acknowledge the contributions from the technical staffs of our home institutions and the University of Utah Center for High Performance Computing.

# CHAPTER 1

# INTRODUCTION TO COSMIC RAY PHYSICS

Cosmic rays are high energy particles traveling through the universe, some of which reach the Solar System and enter the Earth's atmosphere. These particles are relativistic ionized atomic nuclei and have a large range of energies. The analysis presented here studies the composition of cosmic rays above $10^{18.5}$ eV as measured by the Telescope Array Experiment (TA) in hybrid mode.

Victor Hess discovered cosmic rays in 1912 in a series of high altitude balloon flights. In that period, physicists knew of an anomalous radiation that would discharge electroscopes, early instruments used to measure electric charge. The source of this radiation was unknown, and scientists speculated whether the source of the radiation was terrestrial or extra terrestrial in origin. Taking electroscopes on manned balloon flights in excess of 5 km in altitude, Hess found that the rate of these discharges increased with altitude, showing that the radiation was coming from space[33]. The actual name "cosmic ray" was coined ten years later by Robert Andrews Millikan in 1925.

Cosmic ray studies are generally divided into three categories which are discussed in the sections below. Section 1.1 discusses the flux and energies of cosmic rays, known as the cosmic ray spectrum. Section 1.2 discusses the study of the chemical composition of cosmic rays. Lastly, Section 1.3 discusses the search for anisotropy in cosmic ray arrival directions.

## 1.1 Cosmic Ray Spectrum

Cosmic rays are measured with a large range of energies, from as low as $10^9$ eV to as high as $10^{20}$ eV in a steady power law in energy with a spectral index of close to $-3$ across the entire range of energies. Figure 1.1 shows the all particle spectrum as measured by a variety of cosmic ray experiments. Figure 1.2 shows the cosmic ray spectrum above $10^{17}$ eV.

The steady $E^{-3}$ power law gives rise to large differences in the flux of cosmic rays. At low energies, cosmic rays are very numerous. Indeed, secondary muons from low energy cosmic rays are a regular background for ground array cosmic ray detectors. On the other hand, above $10^{19.5}$ eV, cosmic rays are rare, having a flux of approximately 1 $\mathrm{km}^{-1}\mathrm{year}^{-1}$.

The orders of magnitude differences in cosmic ray flux require dramatically different methods of cosmic ray detection. At energies below $10^{15}$ eV, the flux is large enough that direct detection methods are possible. Such an experiment would involve attaching a particle detector to a high altitude balloon or satellite. Much above this $10^{15}$ eV, the low flux of cosmic rays requires the use of the cosmic ray's interaction in the atmosphere or the extensive air shower(EAS).

The physics of the EAS are discussed in detail in Chapter 2, but a brief introduction is provided here. When a cosmic ray enters the atmosphere, it interacts with oxygen and nitrogen nuclei and creates a cascade of secondary particles. This air shower will reach approximately one particle per GeV at its maximum.

The charged secondary particles in the air shower excite nitrogen gas in the atmosphere, which then emit ultra-violet (UV) photons via fluorescence. Nitrogen fluorescence can be measured using telescopes sensitive in the UV. Additionally, secondary particles may be detected directly with particle counters on the ground.

This phenomena was discovered by Pierre Victor Auger in 1938, by measuring coincident hits on particle counters placed a few meters apart. Auger made estimates of cosmic ray energies of greater than $10^{11}$ eV[8].

Telescope Array (TA) incorporates both nitrogen fluorescence and ground array techniques to get an accurate reconstruction of the arrival direction, core location, and the energy of the primary cosmic ray. The discussion of the TA detector and its detection methods is found in Chapter 3.

Close inspection of Figure 1.1 reveals subtle features in the cosmic ray spectrum. There are two steepenings, known colloquially as the "knee" and the "second knee" at $10^{15}$ and $10^{17}$ eV respectively. There is also a softening above $10^{18.5}$ eV known as the "ankle" and a sharp cutoff after $10^{19.5}$ eV. Each of these features has important implications for the sources of cosmic rays, their composition, and their propagation both inside and outside the Galaxy. Theories of sources and propagation model of cosmic rays are discussed in detail in Section 1.4.

In Figures 1.1 and 1.2, it is difficult to discern the features found in the cosmic ray spectrum. Thus, it is common to scale the spectrum by some power of the reconstructed cosmic ray energy. Figures 1.3 and 1.4 show the cosmic ray spectrum where the flux is scaled by the $E^3$, effectively removing the general trend of $E^{-3}$. Now, the previously mentioned features are unmistakable. For example, below $10^{15}$ eV, the knee, the spectrum has a spectral index of closer to 2.8. Also, the $E^3$ scaling makes clear the systematic energy scale differences between experiments.

## 1.2 Composition

Understanding the composition of cosmic rays has important ramifications on any theoretical models either of cosmic ray sources of cosmic ray propagation in the universe. Indeed, any theory explaining the features in the cosmic ray spectrum will be tied to the composition at the energy of the feature.

Figure 1.5 shows the chemical abundances relative to silicon for cosmic rays and solar system matter[40]. This figure shows an overabundance in the cosmic ray measurement of critical elements, namely elements with masses lighter than the CNO group (carbon, nitrogen, oxygen) and iron. This is caused by spallation as cosmic rays interact with cosmic microwave background (CMB) photons or other particles as they travel through the galaxy. As the majority of interstellar matter is produced as Fe or CNO elements. Galactic rays lose nucleons through spallation, lowering their atomic number.

As mentioned earlier, TA does not measure cosmic rays directly and must use observables in the EAS process to determine the composition of cosmic rays. One such observable is the point the air shower has the maximum number of particles, or $X_{max}$. The derivation of dependence of $X_{max}$ to the atomic mass is left until Chapter 2, but it will be shown that

$$X_{max} \propto \log_{10}\left(\frac{E_0}{A}\right) \tag{1.1}$$

where $A$ is the atomic mass of the cosmic ray and $E_0$ is the energy of the primary cosmic ray.

The study presented in this work makes use of $X_{max}$ as the indicator of composition. Additionally, because $X_{max}$ is subject to statistical fluctuations, the chemical composition of cosmic rays can not be determined on a shower by shower basis. Instead, composition is inferred from the measured distributions of $X_{max}$.

## 1.3 Anisotropy

Cosmic ray physicists attempt to identify the sources of cosmic rays directly searching for anisotropy in the cosmic ray arrival directions. Studies of these kind are called anisotropy searches. This may involve auto-correlations in the data, comparing the reconstructed positions of cosmic rays to that of known astronomical objects, or using models of galactic propagation to predict an excess of cosmic ray arrival directions. Cosmic ray arrival directions are expected to have a randomized component due to their finite charge and the galactic and extra-galactic magnetic fields through which cosmic rays propagate.

A statistically significant measurement of anisotropy could show direct evidence of where and possibly how cosmic rays are produced. Correlating cosmic rays to specific types of astronomical objects would give an insight to the mechanisms behind the most energetic particles in the universe.

## 1.4 Sources and Propagation

### 1.4.1 Sources

The precise mechanisms responsible for accelerating particles to energies greater than $10^{17}$ eV, or into the UHECR regime, are not well understood. This section will discuss a few possible models of UHECR sources. In general, these models come in two categories: top-down and bottom-up.

Top-down models require a massive exotic particle decay or topological defect, which appears to have a large mass[11]. When the decay occurs a large number of photons, neutrinos, and leptons are produced as well as a few protons and neutrons[15]. Because of the large initial rest mass, the protons and neutrons will be produced with large energies and could appear as UHECRs if they propagate to the Solar System.

Bottom-up models involve a particle being produced with relatively low energies in a violent astrophysical environment. These particles are then accelerated to high energies through strong electric and magnetic fields or shock fronts.

One example of a bottom up acceleration model is statistical acceleration, which involves a cosmic ray passing back and forth across a plasma shock front. After each pass, the a particle has a finite probability of being carried by the shock again and accelerated farther. When this happens, the cosmic ray's energy increases by an amount proportional its current energy[19]. Hillas presented a calculation of the maximum energy a cosmic ray could receive from such successive stochastic shocks[25].

$$E_{max} \simeq \left(10^{18}\,\mathrm{eV} Z\beta\right)\left(\frac{R}{\mathrm{kpc}}\right)\left(\frac{B}{\mu\,\mathrm{G}}\right) \tag{1.2}$$

where $R$ represents the length scale of an astrophysical object, $Z$ is the particles charge, $B$ the objects magnetic field, and $\beta$ is the acceleration efficiency.

Using Equation 1.2, Hillas showed the magnetic field strength of various astrophysical objects versus their size[25]. A reproduction of this finding is found in Figure 1.6. This plot provides some reference for astrophysical objects that could be responsible for the highest energy cosmic rays.

### 1.4.2 Propagation

Particles that are seen on the Earth as cosmic rays depend as much on their interactions as they travel to the Solar System on their sources. Propagation models have direct relevance to spectrum, composition, and anisotropy studies.

#### 1.4.2.1 Propagation in the Galaxy

The propagation of cosmic rays in the galaxy is often modeled as a "leaky-box." This means that particles created inside the galaxy are bound it by its magnetic fields. However, if a cosmic ray reaches a certain energy threshold, it may escape. The distance scale that a charged particle may move inside a magnetic field is on order of its Larmor radius[16],

$$r_L = \frac{E}{qcB} = (1.08\,\mathrm{kpc})\,\frac{E/\,\mathrm{PeV}}{Z\,(B/\mu\,\mathrm{G})} \tag{1.3}$$

This shows that higher energy cosmic rays are less bound to the galaxy as are cosmic rays with a smaller atomic number (i.e. protons). A rough estimate can show that a proton with energy on order of $10^{16}$ eV has a Larmor radius of about the size of the galaxy, 8 kpc. This is close to where the knee is located in the cosmic ray spectrum though about an order of magnitude high.

The KASCADE experiment, claimed to be able to measure the composition of cosmic rays on a event by event basis, allowing them to measure a different spectrum for each cosmic ray species. Their analysis seems to show lighter particles dropping out of their measured spectrum in the the knee region, corroborating the leaky box theory. Figure 1.7 shows the measured KASCADE spectra for cosmic rays with various atomic masses[26].

An alternative explanation for the KASCADE data is that the Knee represents an acceleration limit for cosmic rays that are galactic in origin. Cosmic rays with an atomic number $Z$ would be expected to have an acceleration limit

$$E^{Z}_{max} = ZE^{p}_{max} \tag{1.4}$$

where $E^{p}_{max}$ is the acceleration limit of proton cosmic rays[16].

Both of the above explanations of the KASKADE data lends one to expect a similar mechanism to cause cosmic rays with larger atomic number to leave the spectrum at a higher energy. This is a natural explanation for the $2^{nd}$ knee feature in all particle cosmic ray spectrum, around $10^{17}$ eV. Unfortunately, the second knee energy region is poorly probed and there is little composition data, so there is still no data showing that cosmic rays in the $2^{nd}$ knee are heavier in composition. As such, it is impossible to confirm theories explaining galactic cosmic rays and the KASCADE data. New experiments like the HEAT extension to the Pierre Auger Observatory (PAO) and the TALE extension to TA may shed new light on this region of the cosmic ray spectrum[34, 48].

#### 1.4.2.2 GZK Mechanism

The all-particle spectrum shown in Figure 1.4 reveals a sharp cutoff in the mid $10^{19}$ eV decade. This cutoff is effectively the end of the cosmic ray spectrum and has been observed by both the HiRes and PAO experiments[3, 5]. Such a feature had been predicted in 1966 and named the GZK effect after its discoverers, Greisen, Zatsepin, and Kuz'min[52], [20]. These two publications were done independently and published at approximately the same time. As such, the name of this effect reflects all three authors.

As an UHECR travels through the universe to the Solar System, it passes through the Cosmic Microwave Background (CMB), discovered in 1965[39]. CMB photons are low energy, having an energy spectrum consistent with a 2.74 K black body distribution. However, in the frame of an UHE proton, a CMB photon is seen with a large Lorentz boosted energy. If the cosmic ray proton's energy is high enough, the center of mass energy may reach the threshold for pion production. Pion production from a $p\gamma$ interaction may be described as

$$p + \gamma \rightarrow \Delta^{+}_{1232} \rightarrow \begin{cases} \pi^0 + p \\ \pi^+ + \mu^- + \bar{\nu_\mu} + n \\ \pi^- + \mu^+ + \nu_\mu + n \end{cases} \tag{1.5}$$

where the $\Delta^{+}_{1232}$ resonance decays to either charged or neutral pions and a nucleon.

Figure 1.8 shows the cross section for the $p\gamma$ interaction. This cross section peaks at $\sqrt{s}$ equal to 1232 MeV, which corresponds to the production of the the $\Delta^{+}_{1232}$ resonance. Given a CMB photon with a mean energy of $6.4 \times 10^{-4}$ eV, this center of mass energy is achieved with a $2.5 \times 10^{20}$ eV proton [21].

Including other energy loss mechanisms, such as a cosmic ray source having a large redshift with respect to the Earth lowers the energy where such a cutoff would be observed to $5.8 \times 10^{19}$[10, 12]. The HiRes measurements of the cosmic ray spectrum are compatible with this theoretical expectation of the GZK cut off[2].

Understanding the composition of UHECRs becomes critical to further validate the GZK mechanism's responsibility for the cut off in the UHECR spectrum. If the flux in cosmic rays is not dominated by protons in this region, then the GZK effect would only become relevant at much higher energies and could not be responsible for the cut off measured by current experiments. Indeed, the HiRes experiment's measurement of composition using fluorescence detectors in stereo mode is compatible with protons greater than $10^{18}$ eV[4].

The GZK effect also has important implications for anisotropy studies as photo-pion production would put a limit on the distance that any cosmic ray proton with energy above $2.4 \times 10^{20}$ eV could travel. At the center of mass energy of 1232 MeV, corresponding to the peak of the $p\gamma$ cross section, the inelasticity, $\kappa$ is equal to 0.22[43, 20]. The energy loss distance scale

$$\lambda_{attn} = \frac{1}{\kappa n_\gamma \sigma} \tag{1.6}$$

may be estimated. Using $n_\gamma = 412$ cm$^{-3}$ as the density of CMB photons and an average cross section of $\sigma = 0.12$ mb, $\lambda_{attn} = 9.2 \times 10^{24}$ cm or 3 Mpc[21]. Full simulations of UHECR propagation put a GZK horizon at $\approx 100$ Mpc for protons[22, 37].

#### 1.4.2.3 The Ankle Region

In addition to the cut off in the mid $10^{19}$ eV decade, Figure 1.3 shows a softening of the cosmic ray spectrum in the second half of the $10^{18.5}$ eV. This feature has been named the “ankle”. The HiRes experiment found the center of this feature to at $10^{18.6}$ eV in energy[3].

The Ankle may be described with the GZK mechanism combined with lower energy proton primaries producing electron-positron pairs as they interact with CMB photons[10]. GZK attenuated protons produce a “pile up” just below the GZK threshold and the pair production attenuate causes a steepening.

The pair production interaction may be described as

$$p + \gamma \rightarrow p + e^{+} + e^{-} \tag{1.7}$$

As the electron mass is only 511 keV, this interaction will occur at a much lower energy than the GZK effect. Also, this interaction will attenuate the energy of the proton slightly. As photo-pion production removes energy from primaries above $10^{19.5}$ eV, a pileup occurs just below the photo-pion threshold energy, resulting in a softening on the right side of the ankle. The pair production causes a slight steepening around $10^{18.4}$ eV. Together these two effects result in the the ankle feature. Simulations of production and the propagation of UHECR protons including both pair-production and pion production look very much like the measured UHECR spectrum by the HiRes experiment[13]. The resulting contributions to the cosmic ray spectrum from these simulations are found in Figure 1.9.

Berezinsky's modeling of proton cosmic ray propagation provides a simple theoretical explanation for the spectral features in the flux of UHECRs. However, these results are only valid if the spectrum is dominated by protons in this region. If a heavier composition is measured, the cutoff at $10^{19.5}$ eV could be caused by an acceleration limit of the cosmic ray sources, analogous to the what has been described by the KASCADE experimentation the Knee region[6]. The Ankle, alternatively, could be described by a transition to extra-galactic cosmic rays, especially if a composition change is seen in this region. The results of a composition study such as presented in this work are essential to explain and understand the flux of cosmic rays.

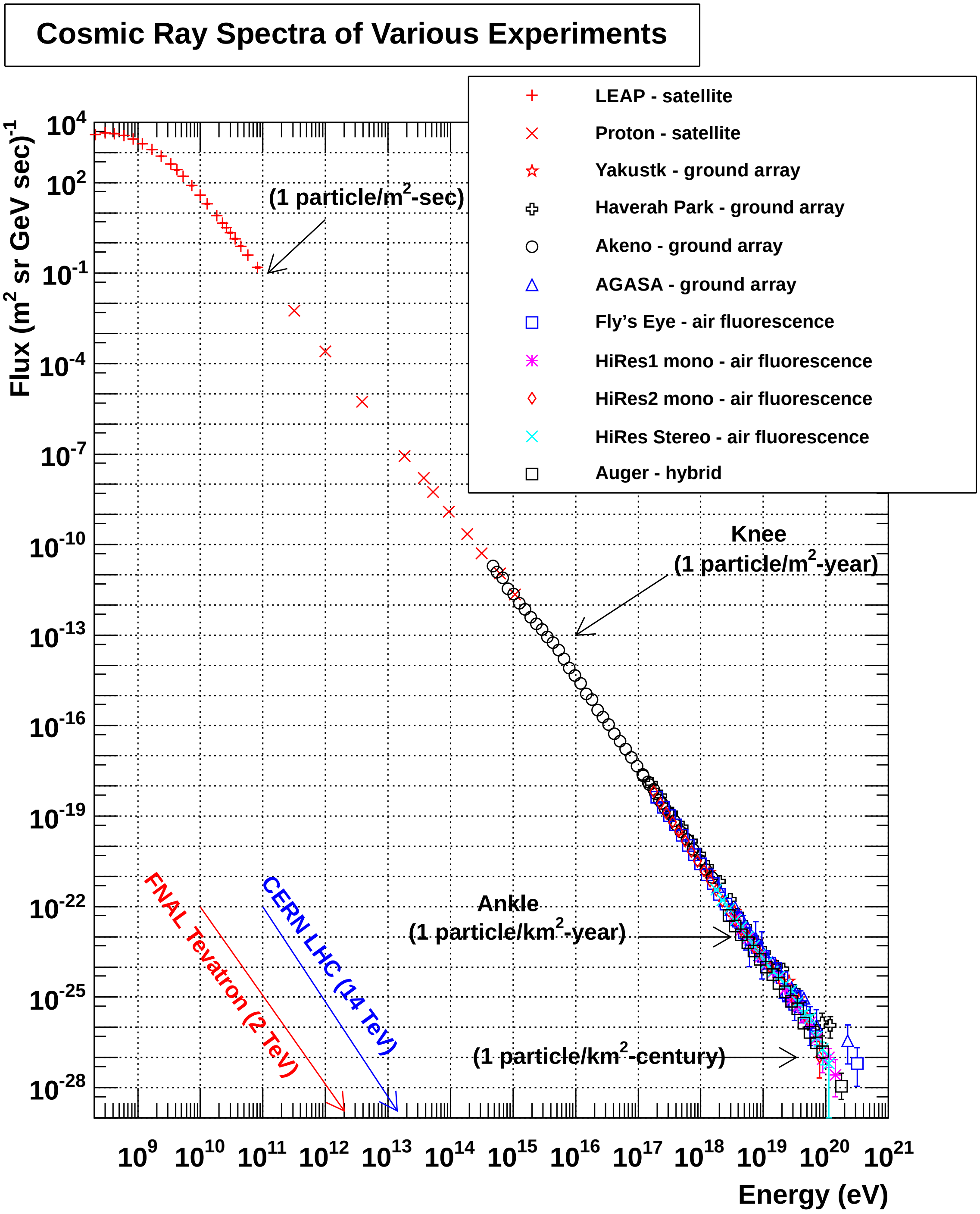

**Figure 1.1**: The all particle cosmic ray spectrum as measured by various experiements.

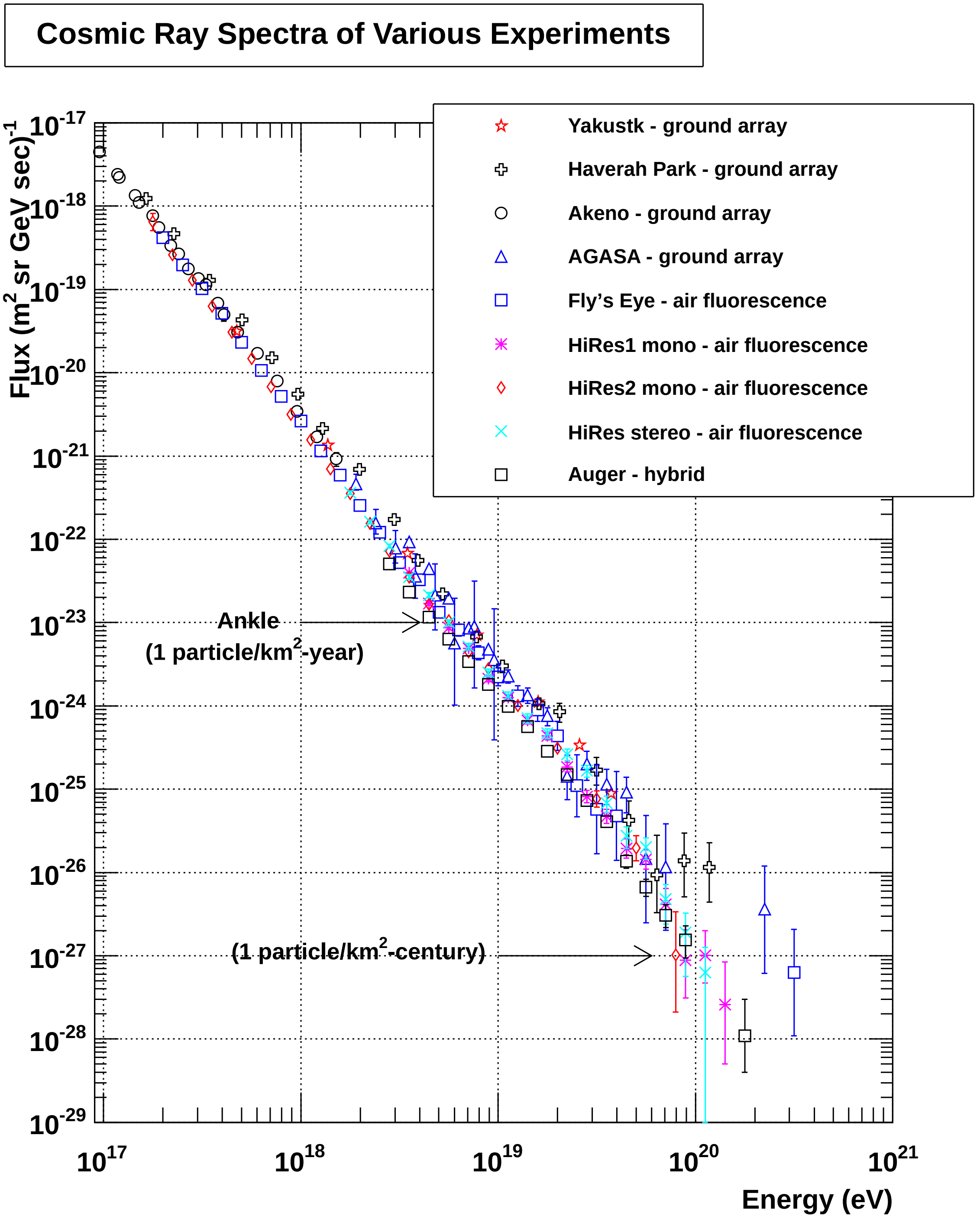

**Figure 1.2**: The all particle cosmic ray spectrum with reconstructed energy greater than $10^{17}$ eV, as measured by various experiements.

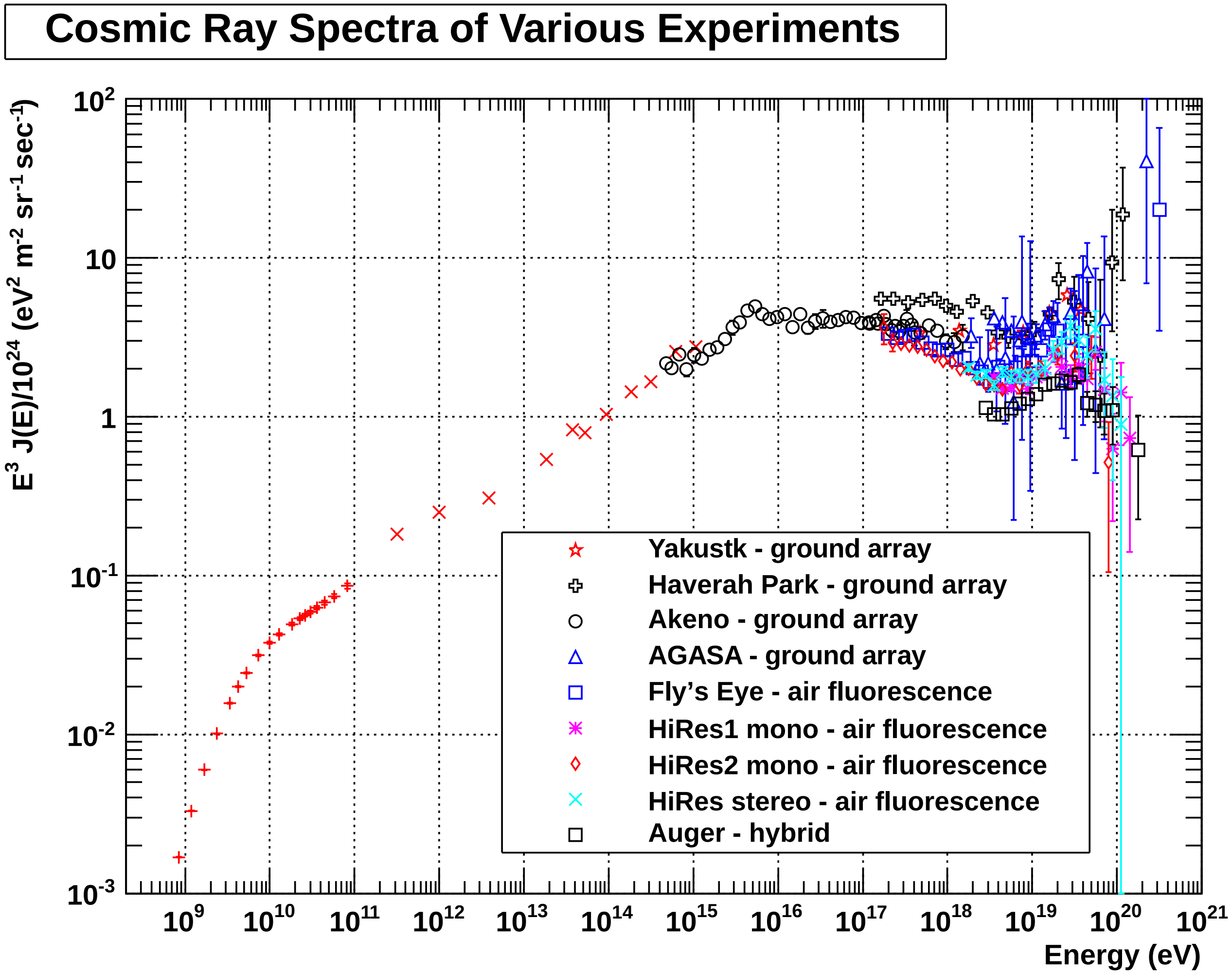

**Figure 1.3**: The all particle cosmic ray spectrum, scaled by $E^3$, as measured by various experiments.

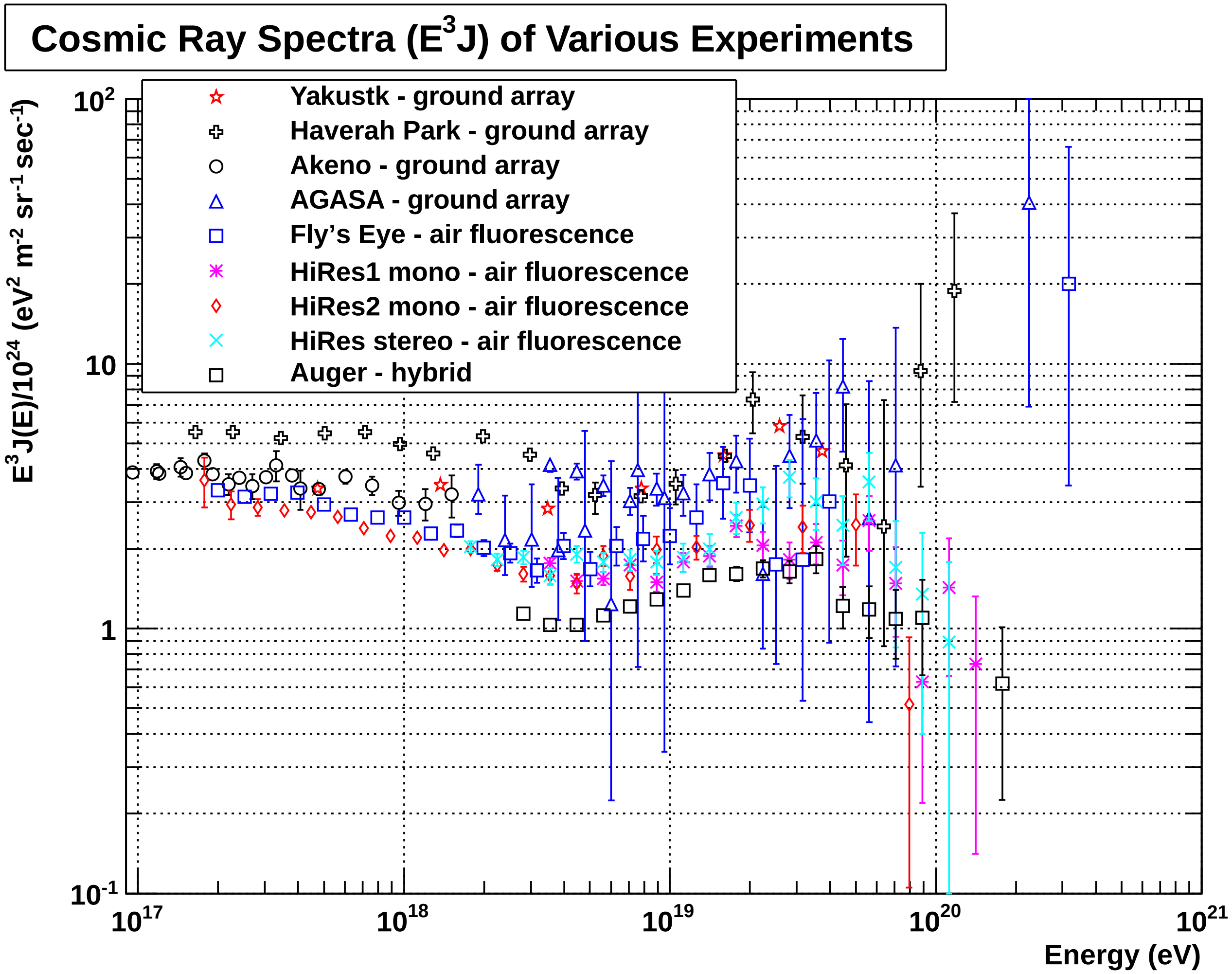

**Figure 1.4**: The all particle cosmic ray spectrum with reconstructed energy greater than $10^{17}$ eV, scaled by $E^3$, as measured by various experiments.

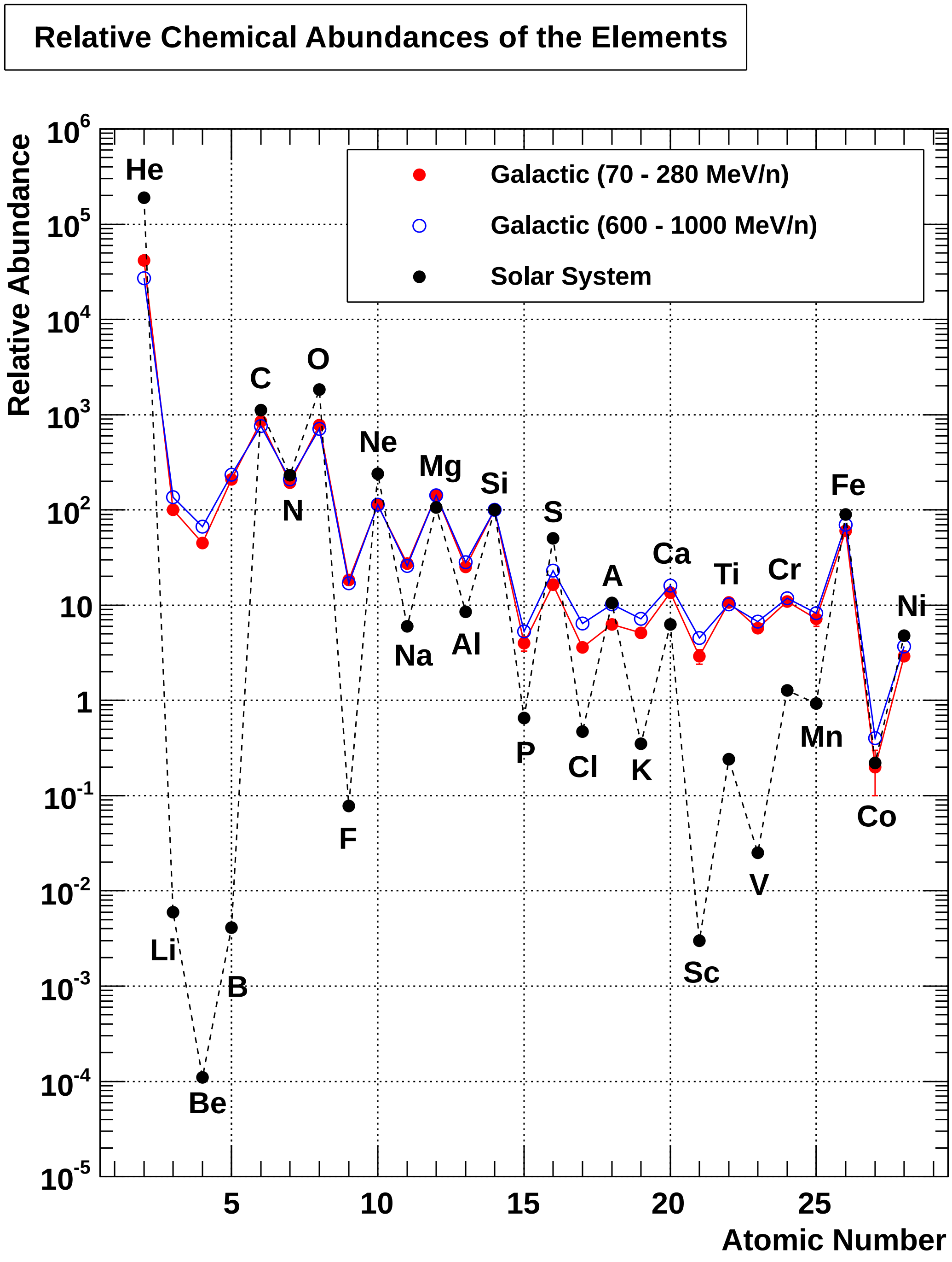

**Figure 1.5**: The relative abundance of elements in directly detected cosmic rays overlaid with the relative abundances of solar system matter[40].

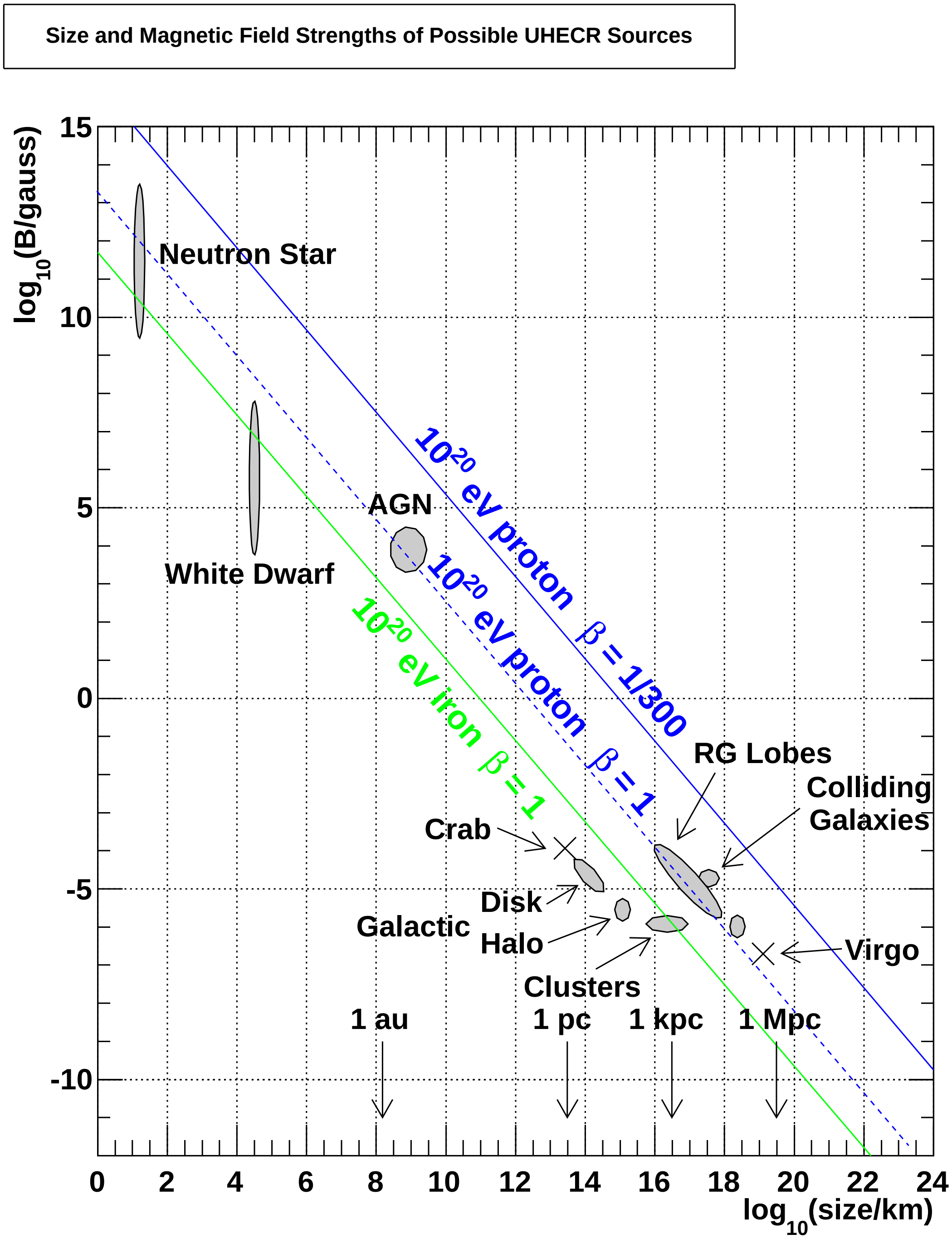

**Figure 1.6**: Hillas plot showing magnetic field strength versus size for several astrophysical objects[25]. The lines show the requirements for magnetic field strength and an objects size for $E_{max}$ of $10^{20}$ eV as described by Equation 1.2. The blue lines are using protons (atomic number of 1), with the solid and dashed corresponding to $\beta$ being set to 1/300 and 1 respectively. The green line is for iron (atomic number of 56) with $\beta = 1$.

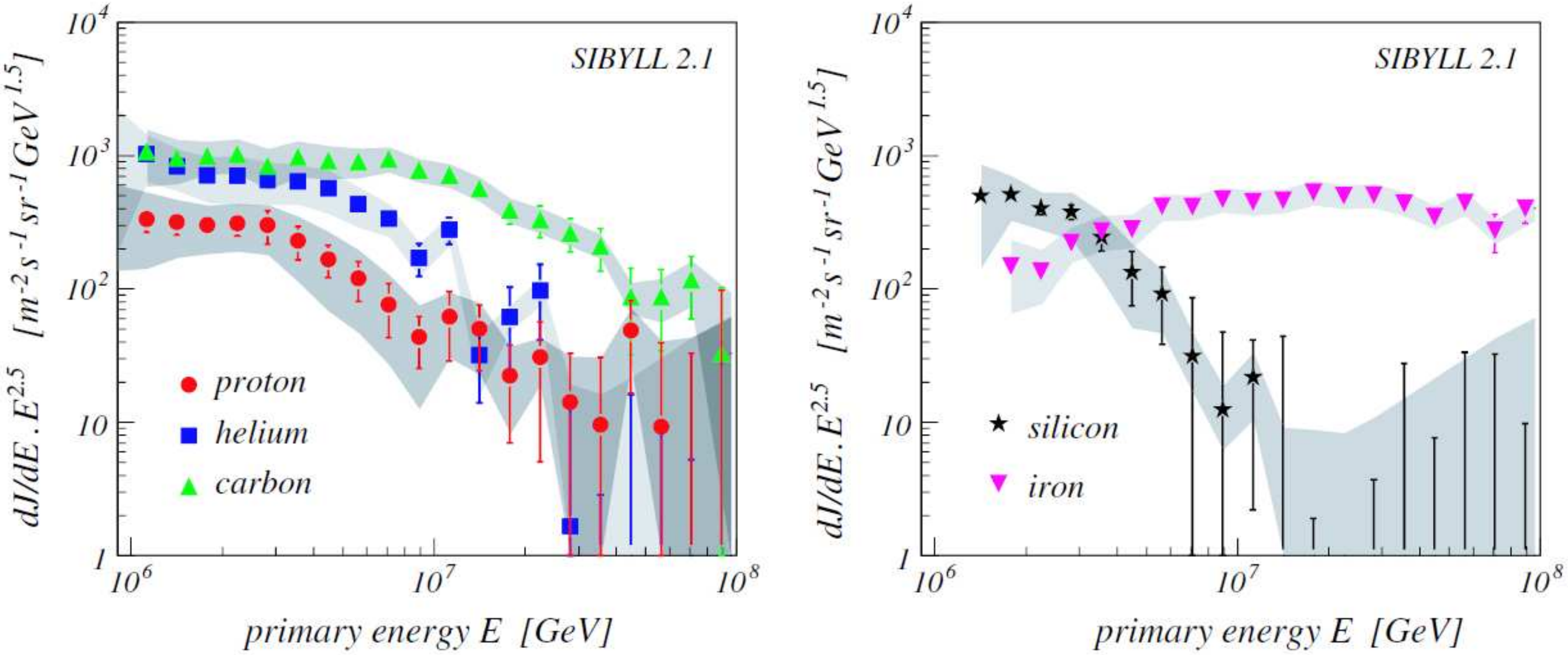

**Figure 1.7**: Cosmic ray spectra differentiated by particle species as seen by the KASCADE experiment using the Sibyll2.1 hadronic model[7]. Reprinted with permission.

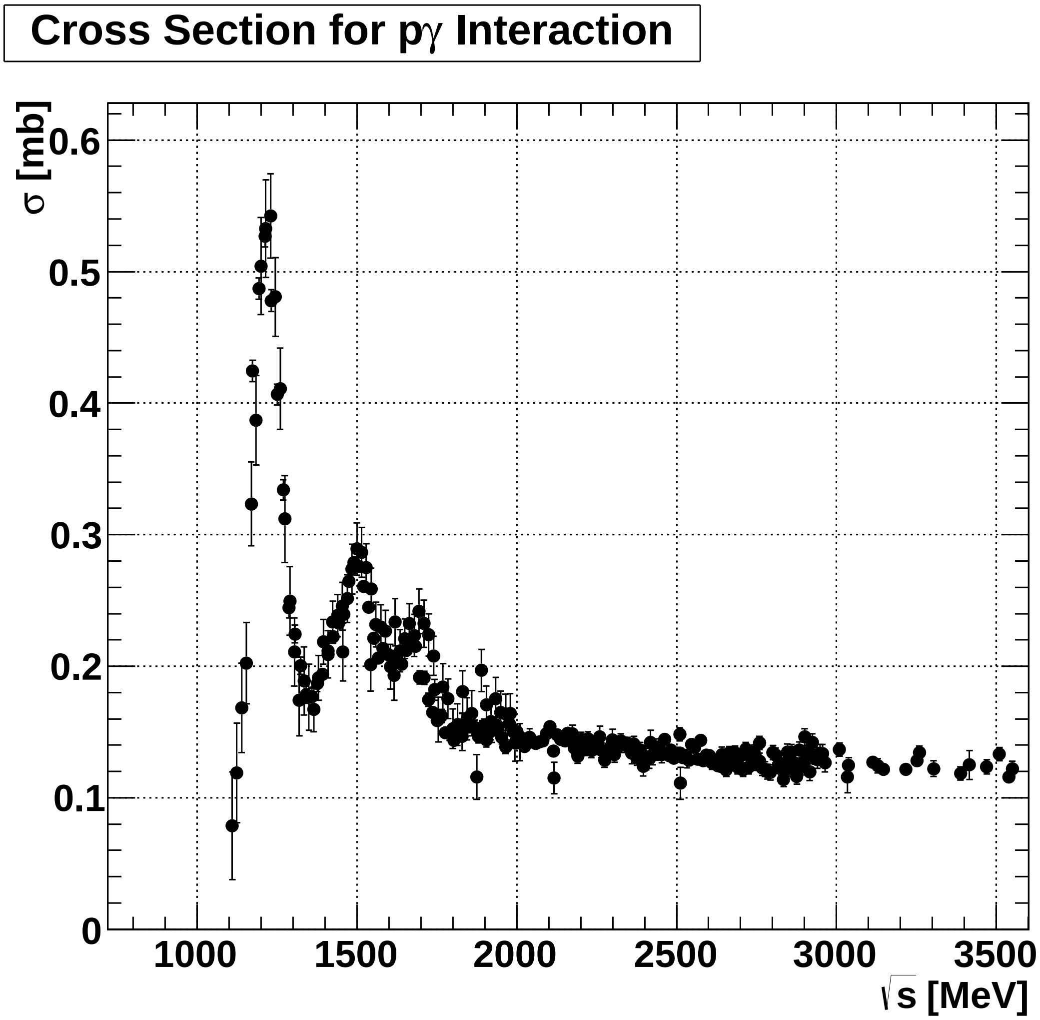

**Figure 1.8**: p$\gamma$ cross-section[17]. The strong peak corresponds to production of the $\Delta^+_{1232}$ resonance.

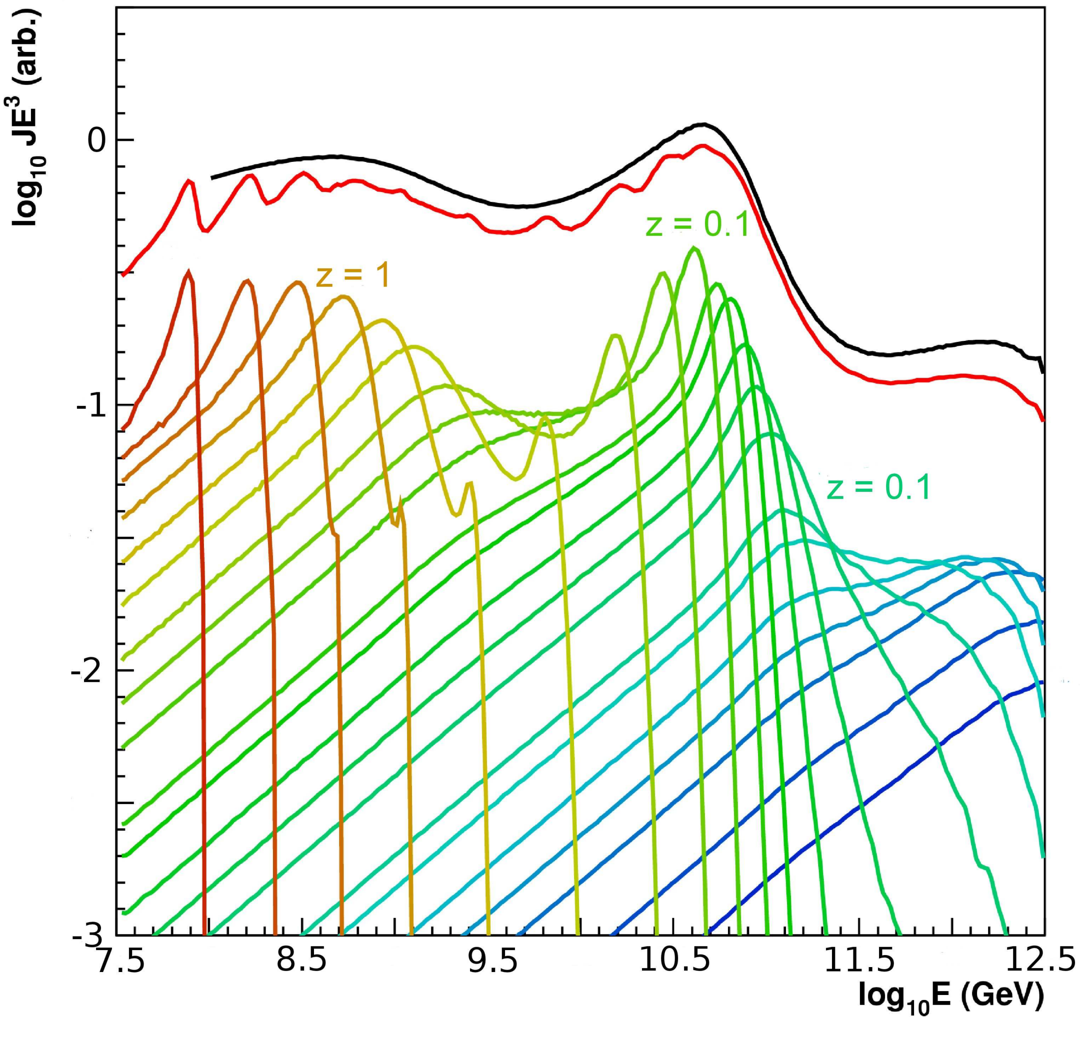

**Figure 1.9**: Reproduction of Berezinsky's simulations of UHECR proton propagation from shells of various redshift, $z$, resulting in the GZK cutoff and ankle features[10, 14]. The red curve is the resulting summation of the shown z shells. The black curve is the result when approaching a continuous distribution of shells.

# CHAPTER 2

# THE EXTENSIVE AIR SHOWER

In Section 1.1, it was mentioned that TA does not detect cosmic rays directly but instead detects the result of a cosmic ray's interaction the atmosphere. This process is know as the extensive air shower (EAS) and is discussed in detail here.

When a primary cosmic ray particle enters the atmosphere, it interacts with $N_2$ or $O_2$ molecules, producing secondary particles. In the early part of the EAS, the number of secondary particles grows as a power law, consisting mostly of electrons and muons, though hadrons are found in the core of the EAS. This cascade of particles eventually reaches a maximum of approximately $10^9$ particles per GeV of energy in the primary[41]. The particles in the EAS develop in three channels: a hadronic core, an electromagnetic cascade, and a muon component. Figure 2.1 shows a cartoon of these basic processes.

In the first few generations of secondary particles the hadronic component is dominant, though in general, hadrons will exist in the core of an EAS until it reaches the ground. This part of the EAS involves strong force interactions, and produces mostly pions and kaons, though some protons and neutrons also be generated. The kaons, protons, and neutrons will feed back into the hadronic component.

Neutral pions decay to photons as

$$\pi^0 \rightarrow 2\gamma \tag{2.1}$$

These high energy photons began an electro-magnetic cascade. The process of an electro-magnetic cascade is found in Section 2.1.

Charged pions decay into muons with a branching ratio of 99.987% as

$$\pi^{\{+,-\}} \rightarrow \mu^{\{+,-\}} + \nu_\mu \tag{2.2}$$

Muons produced here become the muonic component of the EAS, and in general do not interact until they reach the ground. Muon's in the EAS do not produce fluorescence photons and thus are not observed by the fluorescence detectors. However, they will result in signal in the surface detectors.

## 2.1 The Electro-Magnetic Cascade

The electro-magnetic cascade is a process where electrons, positrons, and high energy photons interact with ionized gas in the core of the EAS, repeatedly multiplying in number. Production of new particles occurs through photons in the shower pair producing, and electrons and positrons producing photons by bremsstrahlung interaction with ionized gas. As the number of particles increases, the mean energy per particle must decrease. Eventually the energy lost through ionization becomes dominate. This energy is called the critical energy $E_c$ of the medium. At this point, the number of particles in the cascade stops growing, and shower maximum has been reached. Shower maximum provides two important parameters: $X_{max}$, the point where shower maximum was reached, and $N_{max}$, the maximum number of particles in the shower.

As was mentioned in Section 1.2, $X_{max}$ is a quantity sensitive to the chemical composition of a primary cosmic ray. $N_{max}$ depends linearly with the energy of a primary cosmic ray. Both parameters are important in reconstructing the primary particle's energy.

The EM cascade is responsible for the fluorescence photons produced in the EAS, and thus is what is observable by the fluorescence method. This allows FDs to measure $X_{max}$ and $N_{max}$. Additionally, as particles in the EM cascade pass through the ground, they may be detected by ground arrays.

A simple model proposed by Heilter in 1944 [24] is useful in describing the general behavior of an EM cascade and how the quantities $X_{max}$ and $N_{max}$ relate to the primary cosmic ray. The Heilter model makes two assumptions. First, that at any point in the shower, the energy is divided evenly among the particles in the shower. Second, that the radiation length for pair production is is equal to the mean free path for an electron or positron interacting via bremsstrahlung. This is labeled $\lambda$. Figure 2.2 shows the general outline of this process and the following will walk through the process found there.

Let us first consider a $\gamma$ particle with energy $E_0$. After it has traveled a distance

$\lambda$ it pair-produces, producing an electron and a positron each with an energy $E_0/2$. Both the electron and positron themselves travel a distance $\lambda$ and produce a $\gamma$ by bremsstrahlung off an ion, giving the $\gamma$ half their kinetic energy. After two foldings, the original $\gamma$ has created four particles (two $\gamma$s, an electron and a positron), each with an energy $E_0/4$. In the Heilter model, it should be clear that after $i$ steps we have,

$$N_i = 2^i, \tag{2.3}$$

and each particle has an energy,

$$E_i = E_0/2^i. \tag{2.4}$$

Putting this in terms of the distance instead of foldings gives us,

$$N(x) = 2^{x/\lambda}, \tag{2.5}$$

and,

$$E(x) = E_0/2^{x/\lambda}. \tag{2.6}$$

This process continues with the number of particles growing as a power law in the distance traveled, until the energy per particle reaches the critical energy, $E_c$. At this point $x = X_{max}$. In this simple model,

$$N_{max} = E_0/E_c. \tag{2.7}$$

Solving for $X_{max}$, we see that,

$$X_{max} = \lambda \frac{\ln(E_0/E_c)}{\ln(2)}. \tag{2.8}$$

The dependence of $X_{max}$ on the energy of the primary is called the elongation rate, and reveals the the logarithmic dependence on energy that was asserted in Equation 1.1.

As was mentioned in Chapter 2, the $\gamma$ particles that begin the EM cascade come from the hadronic core of the shower when a proton produces neutral pions that decay into two $\gamma$s. For the case of a heavy nuclei, the cosmic ray would interact through its conduit nucleons, each producing its own subshower. Thus, a cosmic ray primary with an atomic mass $A$, would produce $A$ subshowers. The Heilter model above would begin with a starting energy of $E_0/A$. Finally, the dependence on $X_{max}$ is found that was stated in Equation 1.1. Including $E_c$ and $\lambda$ gives

$$X_{max} \propto \lambda \log_{10}\left(\frac{E_0}{E_c A}\right) \tag{2.9}$$

where log based 10 has been using in lieu of the natural log using in Equation 2.8.

In addition to proton and iron $X_{max}$ distributions being separated by different means, the shape of the distributions also depends on the chemical composition of the primary cosmic rays. As described above, when a heavy nucleus of atomic mass, $A$, interacts in the atmosphere, it initiates $A$ subshowers. These subshowers result in an averaging effect on in a single air shower. The result is that EM cascades resulting from heavier nuclei have fewer fluctuations and thus result in a narrower distribution of $X_{max}$. This effect is apparent in Figure 2.3.

In addition to the EM cascade, the point of first interaction plays an important role in an air shower's development to $X_{max}$. The point of first interaction has an exponential distribution with a decay rate that is inversely proportional the nuclei's cross section. As iron nuclei have a much larger cross section than protons, iron cosmic rays reach first interaction much earlier than proton primaries on average. The resulting $X_{max}$ distributions from proton cosmic rays have a high side tail that is not seen in corresponding iron distributions. The presence of this high side tail in proton $X_{max}$ and lack of it in iron is apparent in Figure 2.3.

Figure 2.4 presents a toy MC to illustrate the full structure of the $X_{max}$ distribution. In this figure, the lower plot is the resulting $X_{max}$ distribution of two random processes with distributions found in the upper and middle plots.

Though the Heilter model gives the correct dependence on the observables $X_{max}$ and $N_{max}$, a more robust treatment is needed. The general form used for fitting the development of charged particles in an EAS is known as the Gaisser-Hillas equation,

$$N(x) = N_{max}\left(\frac{x - X_0}{X_{max} - X_0}\right)^{\frac{X_{max}-X_0}{\lambda}} \exp\left(\frac{X_{max} - x}{\lambda}\right) \tag{2.10}$$

This formula describes the longitudinal development of an EAS with four parameters: $N_{max}$, $X_{max}$, $X_0$, and $\lambda$. This parametrization was developed using complex simulations of the EAS process [18].

The variable, $x$, used above to describe the distance that an air shower has traveled through the atmosphere is generally referred to as "slant depth" and is the density of the atmosphere integrated along the path of the shower.

$$x = \int \rho(x')dx'. \tag{2.11}$$

So, the dimension of $x$ in cgs would be,

$$[x] = \mathrm{g/cm^3\,cm} = \mathrm{g/cm^2} \tag{2.12}$$

This is the appropriate variable to describe air shower development as the probability of particle interactions depends on the amount of material that the air shower has traversed and not directly on the distance traveled. Using slant depth accounts for the fact that a shower with a high zenith angle has traveled through more material than a vertical one, resulting in observing the shower at a later time in its development. When describing a showers development, the use of slant depth allows us to compare showers irrespective of their zenith angle.

The $1/\log(A)$ dependence on composition is generally smaller than the natural statistical fluctuations of $X_{max}$ in a cosmic rays shower development. It is, thus, not possible to use $X_{max}$ to determine the chemical species of primaries individually. Instead, the composition must be inferred from the distributions of $X_{max}$. Figure 2.3 shows $X_{max}$ distribution of simulated air showers at $10^{18.3}$ eV for proton and iron primaries.

Figure 2.5 shows the $< X_{max} >$ vs. $\log_{10}(E/\,\mathrm{eV})$ for proton and iron nuclei in simulations using the CORSIKA code. This figure shows that that simulation driven results have an intrinsic model dependence. This is discussed more in the final sections of this work.

## 2.2 Lateral Distribution

Electrons in an EAS have a lateral spread that is parametrized by the Nishimura-Kamata-Greisen, or NKG, function[30]

$$\rho(r) = \frac{N}{r^2} f\left(s, \frac{r}{r_m}\right) \tag{2.13}$$

where

$$f\left(s, \frac{r}{r_m}\right) = \left(\frac{r}{r_m}\right)^{s-2} \left(1 + \frac{r}{r_m}\right)^{s-4.5} \left(\frac{\Gamma(4.5-s)}{2\pi\Gamma(s)\Gamma(4.5-2s)}\right) \tag{2.14}$$

Here $N$ is the number of particles at any point in the shower, $s$ is the shower age, and $r$ is the distance from the shower axis. The shower age is a unitless variable describing the shower development relative to $X_{max}$ and is found in Equation 4.4.

As opposed to FDs, ground arrays do not see the longitudinal development, but the lateral distribution parametrized by the NKG function. However, a strong SD simulation needs to correctly account for statistical fluctuations air shower development which can not be reproduced by an analytical function.

In addition, the NKG function is used in FD simulations to estimate the width of the region in the core of the shower where fluorescence and Cherenkov radiation are produced.

## 2.3 Air Fluorescence

The fluorescence method uses nitrogen fluorescence to measure the longitudinal development of an EAS as it moves through the atmosphere. This is the cosmic ray detection method used by the TA fluorescence detectors (FDs).

As the EAS develops, secondary charged particles excite nitrogen gas which then emit ultra violent (UV) fluorescence photons. The FDs measure the flux of photons that reach their mirrors, however it is a non-trivial process to connect this signal to the precise number of charged particles in the EAS. The next couple of paragraphs provides a brief introduction into this method. Specific details of the simulations used to model this process and the TA FDs is found in Section 4.4.

The fluorescence yield is a measurement that provides the number of fluorescence photons per energy deposited by an air shower as well as the distribution of these photons in wavelength. The fluorescence yield depends mostly on energy deposited, but has as a weak dependence on air pressure and temperature. The Kakimoto fluorescence yield from [29] has the form

$$Y = \frac{(dE/dx)}{(dE/dx)_{1.4\,\mathrm{MeV}}}\rho\left(\frac{A_1}{1+\rho B_1\sqrt{T}} + \frac{A_2}{1+\rho B_2\sqrt{T}}\right) \tag{2.15}$$

where $\rho$ is the atmospheric density and $T$ is the atmospheric temperature. The ratio

$$\frac{(dE/dx)}{(dE/dx)_{1.4\,\mathrm{MeV}}} = 1.668 \tag{2.16}$$

and provides a conversion of the fluorescence yield per meter and the fluorescence yield per MeV. The fit parameters in Equation 2.15 are described in Table 2.1. The

Kakimoto fluorescence yield is shown in Figure 2.7 using the pressure and temperature from the US standard atmosphere. As fluorescence photons are emitted isotropically the angular distribution of photons is simply

$$\frac{d^2N_\gamma^{fl}}{dld\Omega} = \frac{Y}{4\pi}\frac{dE}{dx} \tag{2.17}$$

The fluorescence yield is critical to understanding the energy deposited in the atmosphere while reconstruction air shower profiles. Figure 2.7 shows the number of fluorescence photons per energy deposited in the atmosphere as measured by Kakimoto *et al.*[29]. The dependence of Figure 2.7 on altitude is really a result of a weak dependencies on atmospheric pressure and density. Figure 2.6 shows the nitrogen fluorescence spectrum as measured by the FLASH experiment[1]. The work presented here uses the FLASH spectrum and the Kakimoto absolute fluorescence yields to model EAS profiles.

## 2.4 Cherenkov Radiation

Cherenkov radiation is produced when a relativistic charged particle passes through a medium at a speed faster than the phase velocity of light in the medium. Many particles in an EAS will be above this threshold, and their contribution to the flux of light seen by an FD must be accounted for in order to understand what fraction of the photon flux is caused by fluorescence. Cherenkov photons are not emitted isotropically as with fluorescence, but at an angle

$$\theta_c = \text{ acos}\left(\frac{1}{n\beta}\right) \tag{2.18}$$

with respect to the charged particle, where $n$ is the index of refraction of light and

$$\beta = v/c \tag{2.19}$$

The threshold for the production of Cherenkov radiation clearly is

$$\beta_{th} = 1/n \tag{2.20}$$

For the case of an electron in air, the energy threshold for the production of Cherenkov radiation is

$$E_{th} \approx \frac{m_e}{\sqrt{2(n_{air}-1)}} = 20MeV \tag{2.21}$$

**Table 2.1**: Kakimoto fluorescence yield parameters for Equation 2.15.

| | |
|---|---|
| $A_1$ | 89.0 $\mathrm{m^2kg^{-1}}$ |
| $B_1$ | 1.85 $\mathrm{m^2kg^{-1}K^{-1/2}}$ |
| $A_2$ | 55.0 $\mathrm{m^2kg^{-1}}$ |
| $B_2$ | 6.50 $\mathrm{m^2kg^{-1}K^{-1/2}}$ |

Figure 2.8 shows the photon flux from a reconstructed air shower event at TA, showing the contributions from fluorescence and Cherenkov radiation.

The number of Cherenkov photons produced by an EAS thus depends on the number of charged particles as well as the distributions of their energies. The Cherenkov photon yield for an electron traveling with energy $E$ may be written as [35]

$$y_\gamma^{ch} = \frac{2\pi\alpha}{\rho}\left(2\delta - \frac{m_e^2c^4}{E^2}\right)\int_{\lambda_1}^{\lambda_2}\frac{d\lambda}{\lambda^2} \tag{2.22}$$

where $\rho$ is the atmospheric density, $\alpha$ is the find structure constant, $m_e$ is the mass of the electron. The integral

$$\int_{\lambda_1}^{\lambda_2}\frac{d\lambda}{\lambda^2} \tag{2.23}$$

provides the wavelength dependence on the overall Cherenkov yield. Using Equation 2.22, the number of Cherenkov photons at a point in the shower is

$$N_\gamma^{ch}(X) = \int_{ln(E_{th})^{\inf}} y_\gamma^{ch}(E)f_e(X,E)d\ln E \tag{2.24}$$

where $f_e$ is the energy spectrum of electrons in the air shower.

The angular distribution of Cherenkov photons is also described in [35] as

$$\frac{d^2N_\gamma^{ch}}{dld\Omega} = \frac{dN_\gamma^{ch}}{dl}\frac{e^{-\theta/\theta_0}}{2\pi\sin(\theta)} \tag{2.25}$$

with $\theta_0 = 0.83E_{th}^{-0.67}$.

Cherenkov photons can reach a telescope either by atmospheric scattering or directly if the telescope is inside the Cherenkov cone. However, air shower events with a large proportion of direct Cherenkov photons can are very difficult to reconstruct and are often cut.

## 2.5 Atmospheric Scattering

Because the Cherenkov photons are produced mostly in the forward direction of the air shower, most of the Cherenkov photons that reach an FD do so through atmospheric scattering. Additionally, atmospheric attenuation occurs as photons propagating to an FD are scattered out of the field of view. Scattering may be categorized with two limiting conditions: Rayleigh scattering, when the size of the scatterer is much smaller than the wavelength of scattered light and Mie scattering when the size of the scatterer is close to or larger than the wavelength of scattered light.

### 2.5.1 Rayleigh Scattering

Rayleigh scattering occurs when photons scatter from of nitrogen and oxygen molecules in the atmosphere. On clear nights, Rayleigh scattering may account for all the scattered Cherenkov light and atmospheric attenuation in a cosmic ray event. The amplitude of scattered Rayleigh photons per length for a given number of photons $N$ is

$$\frac{dN}{dl} = -\rho \frac{N}{x_R} \left( \frac{400\,\mathrm{nm}}{\lambda} \right)^4 \tag{2.26}$$

where $x_R$ is the the mean free path at 400 nm and is equal to 2970 g/cm$^2$. The $\lambda^{-4}$ dependence causes UV photons to be preferentially scattered.

The angular distribution of the resulting scattered light has the form

$$\frac{d^2N}{dl d\Omega} = \frac{dN}{dl} \frac{3}{16\pi} (1 + \cos^2 \theta) \tag{2.27}$$

This is results in a probability of a photon traveling a depth $\Delta x$ without being scattered of

$$T_R = \exp \left( -\frac{\Delta x}{x_R} \left[ \frac{400}{\lambda} \right]^4 \right) \tag{2.28}$$

where, $\rho$ is the atmospheric density. The value $T$ is know as the atmospheric transmission.

As Rayleigh scattering occurs due to the molecular component of the atmosphere, it can be modeled using pressure and density information found in atmospheric radiosonde data taken daily at airports. Although seasonal variations are significant, the atmospheric density, $\rho$, changes little from night to night. TA uses daily radiosonde measurements from near by airports in Elko, Nevada and Salt Lake City, UT.

### 2.5.2 Mie Scattering

Mie scattering occurs in a dusty atmosphere, when the light scatters off of larger dust grains or other aerosols. Because Mie scattering is dependent on the amount of dust in the atmosphere it can vary significantly from night to night, and so it is measured on a nightly basis at TA using the Central Laser Facility (CLF) and LIght Detecting and Ranging (LIDAR) systems. Details of the CLF can be found in Section 3.3.1.

The amplitude Mie scattering depends on the atmospheric density as well as two parameters that must be measured, the scale height, $H_M$, and the horizontal attenuation, $L_M$. As of this writing, the analysis of atmospheric aerosols at TA is still on going. In the current analysis, $H_M$ and $T_M$ are set to as 25 km and 10 km respectively. The parameters defining Mie scattering used in this work are found in Table 2.2.

The amplitude of Mie scatter light is given by

$$\frac{dN}{dl} = -\frac{N}{L_M}\rho(h) \tag{2.29}$$

Mie scattered photons are strongly preferentially scattered in the forward direction. This is described in the equation below in the function $\phi(\theta)$.

$$\frac{d^2N}{dl d\Omega} = \frac{dN}{dl}\phi(\theta) \tag{2.30}$$

$\phi(\theta)$ is an empirical function in the viewing angle but is shown in Figure 2.9.

The transmission coefficient of Mie scattered light is given by

$$T_M = \exp\left(\frac{H_M}{\cos(\theta)L_M}\left(\exp^{-h_1/H_M} - \exp^{-h_2/H_M}\right)\right) \tag{2.31}$$

where $h_1$ and $h_2$ are the altitudes of the detector and the source respectively and $\theta$ is the viewing angle of the source.

**Table 2.2**: Mie scattering parameters used in this work.

| Mie Scattering Parameter | value |
|---|---|
| $H_M$ | 10.0 km |
| $L_M$ | 25.0 km |
| VAOD | 0.04 |

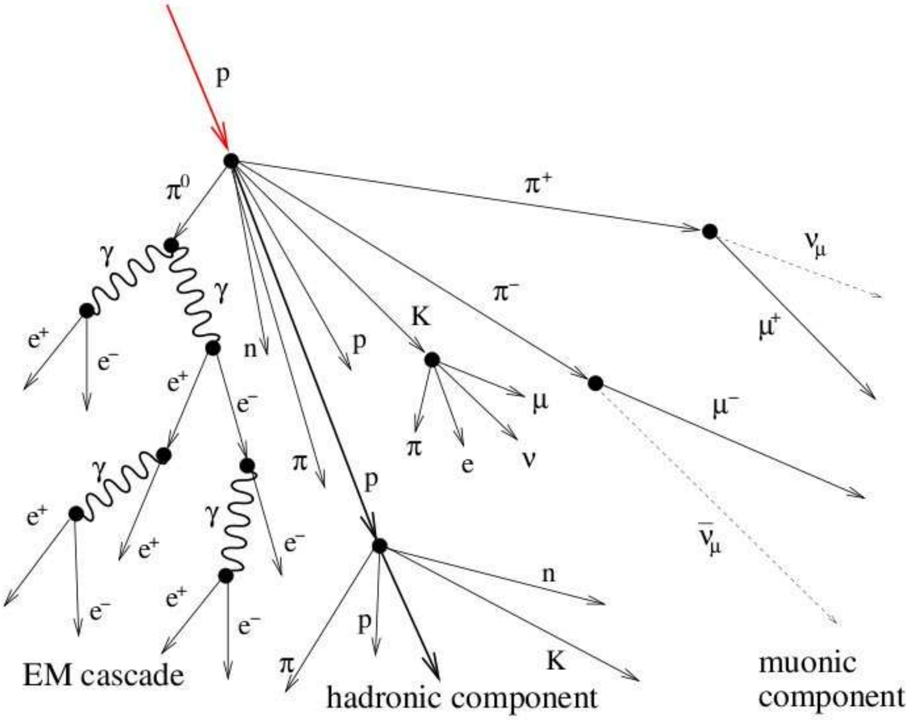

**Figure 2.1**: An outline of the basic processes in an cosmic ray induced extensive air shower. The hadronic component involves mostly strong force interactions, producing gammas and leptons which feed into the other two components. The EM cascade is discussed in Section 2.1 and is responsible for the fluorescence which is detected by the telescopes at TA. Muons rarely interact in the atmosphere, and in general travel directly to the ground. The signal in ground arrays may come from all three components, but it is mostly represented by the EM and muonic component.

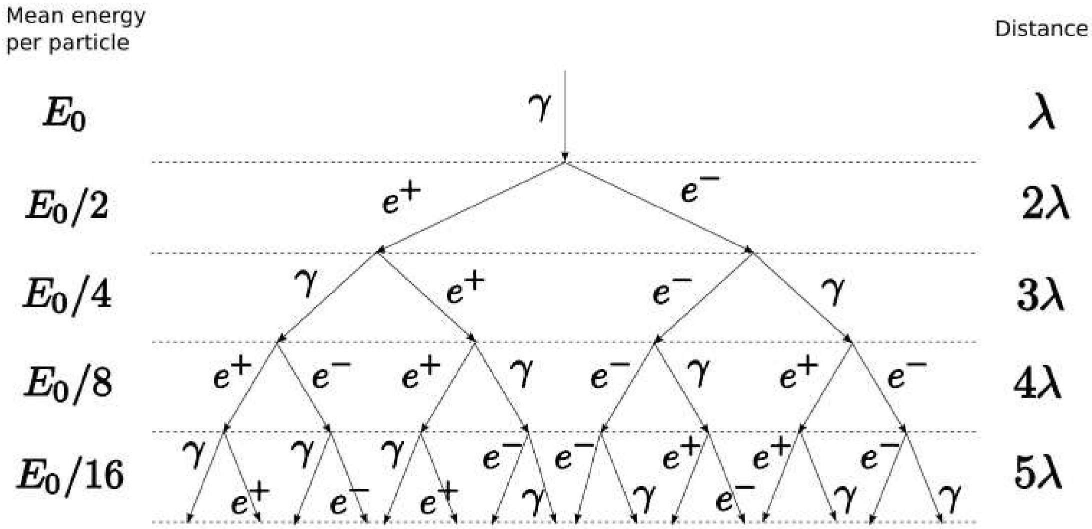

**Figure 2.2**: First four folding in a Heilter Model [24] of an electro-magnetic cascade initiated by a high energy $\gamma$. Two interaction perpetuate this cascade, the pair-production by a $\gamma$ particle and an electron or a positron producing bremsstrahlung radiation as it passes by an ion in the cascade.

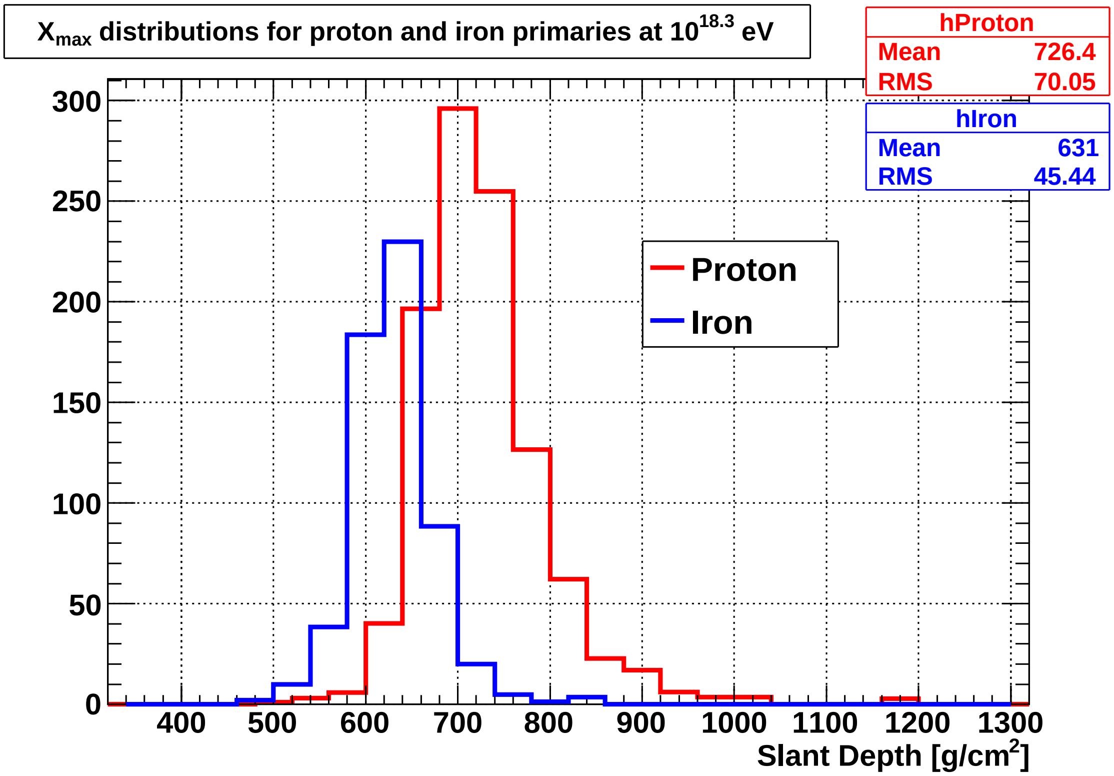

**Figure 2.3**: $X_{max}$ distributions for proton and iron primaries with energy $10^{18.3}$ eV simulated by the CORSIKA code with the QGSJetII hadronic model.

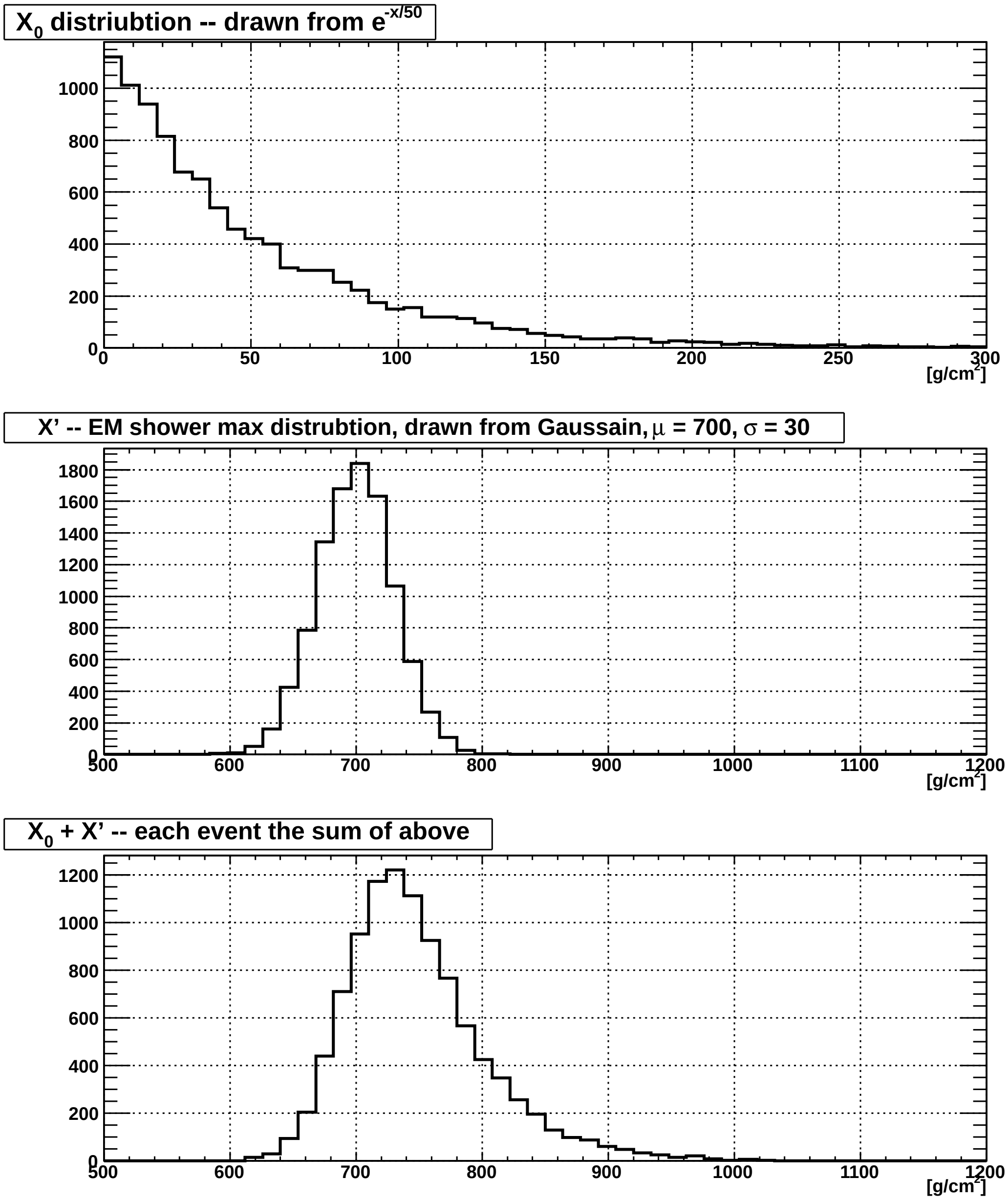

**Figure 2.4**: $X_{max}$ distributions (bottom) is the result of two random processes, the first interaction, $X_0$, (top) and the distance to reach $X_{max}$ from $X_0$, $X'$. The first interaction has a distribution corresponding to exponential decay. The $X'$ distribution is Gaussian.

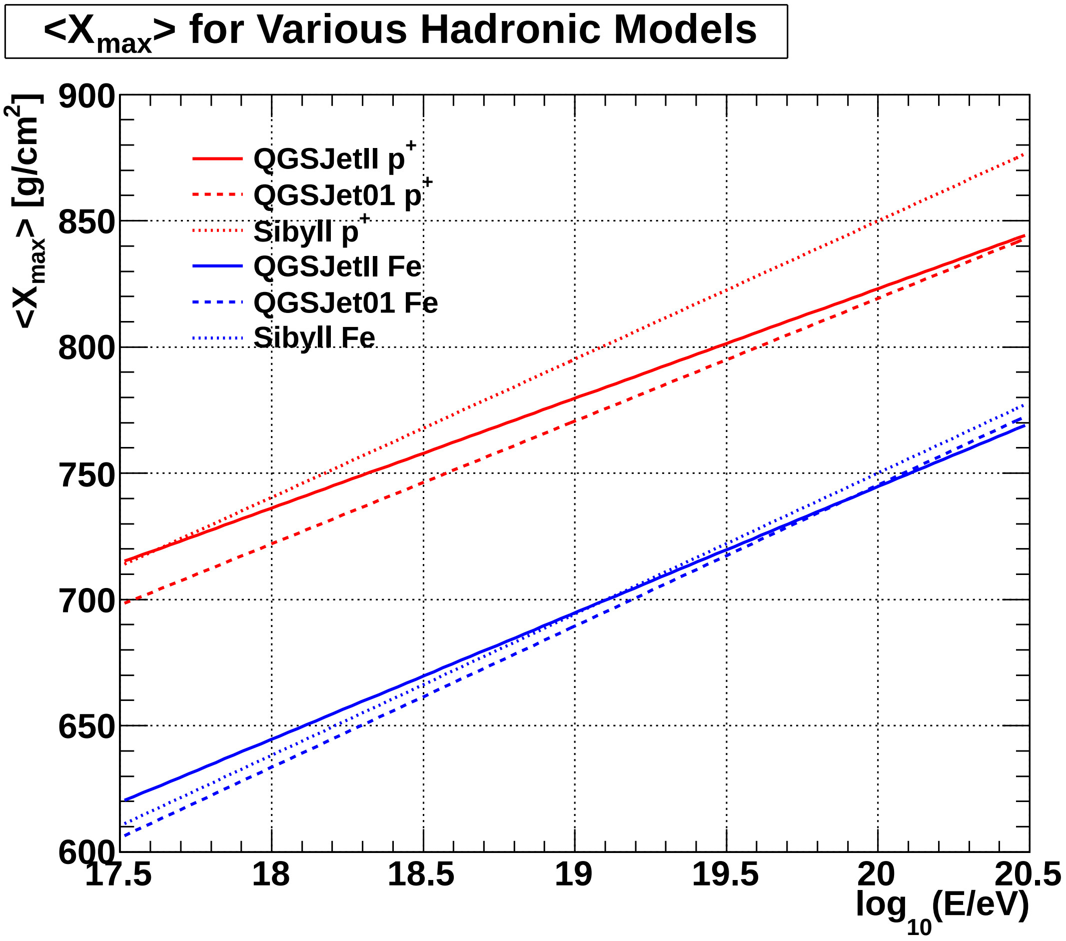

**Figure 2.5**: $< X_{max} >$ versus $\log_{10}(E/\,\mathrm{eV})$ for simulated proton and iron primaries with the CORSIKA code using various models for the hadronic physics.

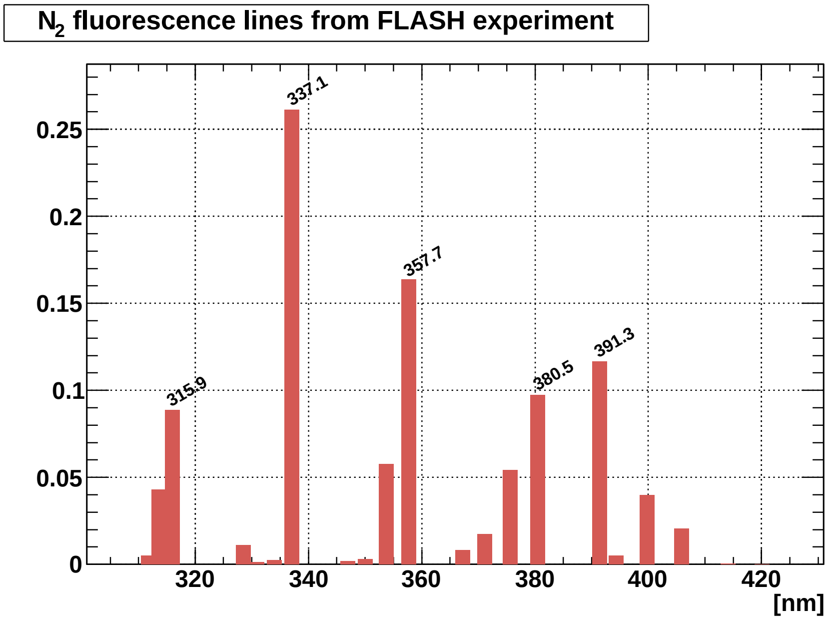

**Figure 2.6**: Fluorescence spectrum measured by the FLASH experiment[1] This scaling of the y-axis is determined by simply scaling the plots area to 1.

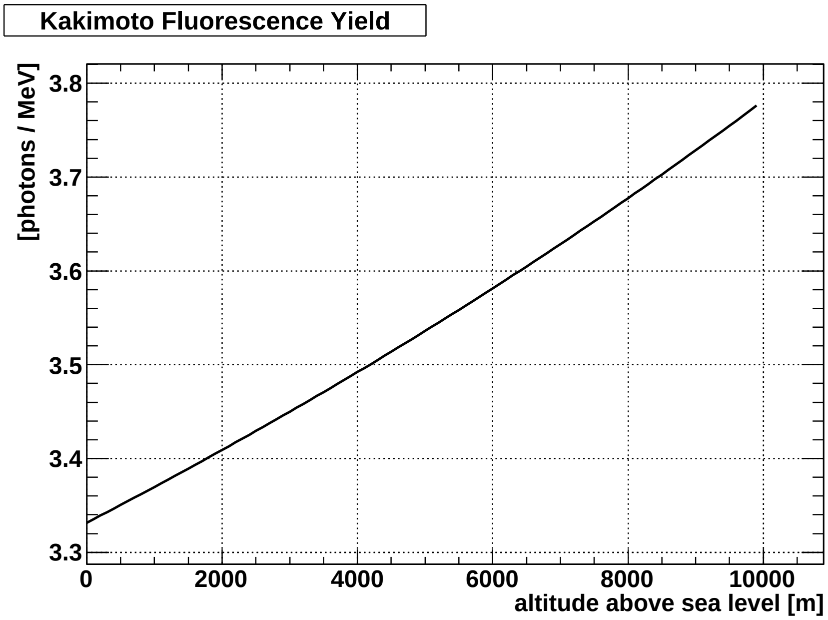

**Figure 2.7**: The Kamimoto fluorescence yield as described in Equation 2.15 using US standard atmosphere[29]. This measurement provides the number of fluorescence photon per energy deposited in the atmosphere by an air shower.

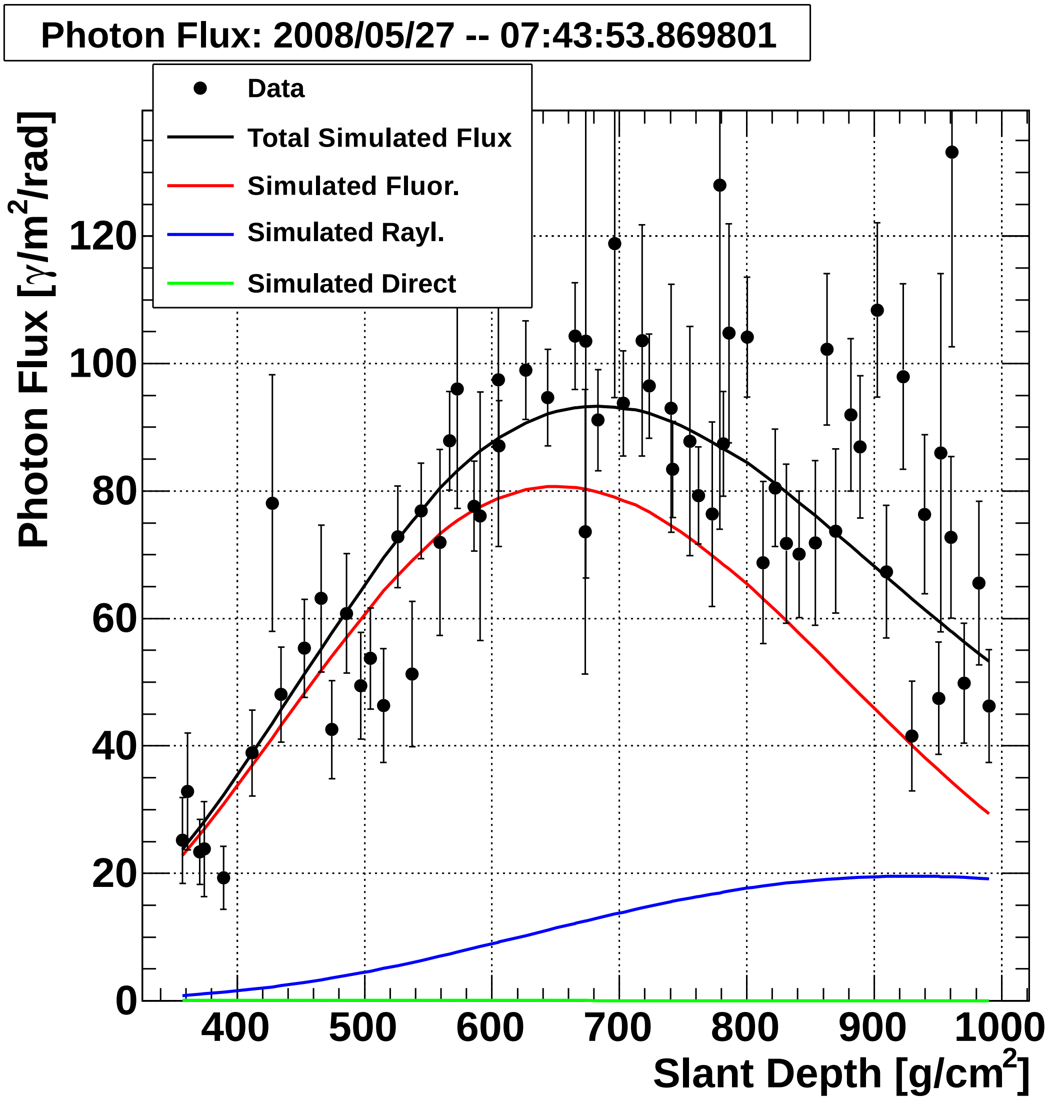

**Figure 2.8**: Photon flux at for a data event at a Black Rock Mesa telescope in the Telescope Array experiment. This event saw very little direct Cherenkov, which is strongly dependent on the geometry of the shower in relation to the telescope.

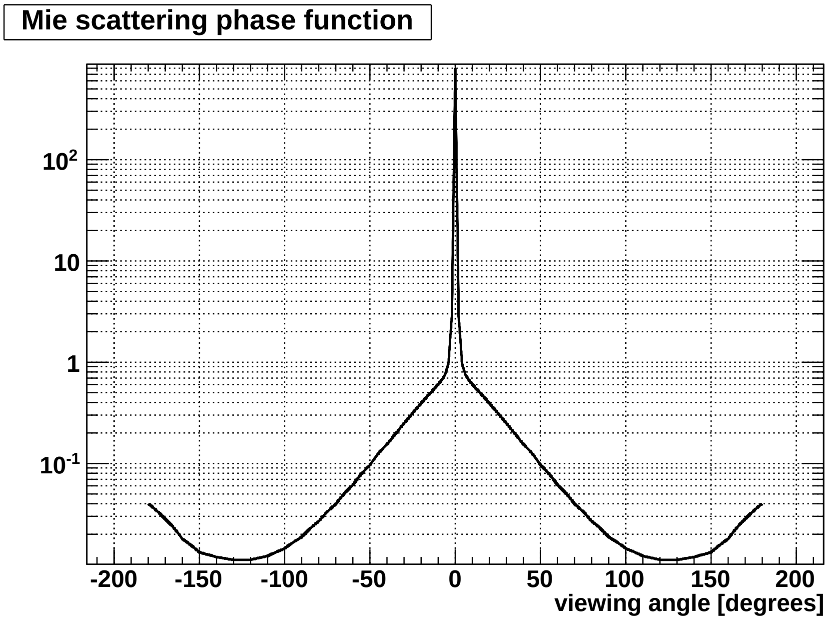

**Figure 2.9**: Angular distribution of Mie scattered light.

# CHAPTER 3

# THE TELESCOPE ARRAY DETECTOR

The Telescope Array experiment consists of three fluorescence detectors (FDs) and an array of 507 surface detectors (SDs). The experiment is located 15 km West of Delta, Utah and approximately two hours from The University of Utah in Salt Lake City.

The FD and SD each sample a cosmic ray air shower during different parts of its development, the FD measuring nitrogen fluorescence as an air shower propagates through the atmosphere, whereas the SD measures particles as they reach the ground. Figure 3.1 shows a map of the TA experiment.

## 3.1 Surface Detectors

The surface detectors consist of a 680 km$^2$ array of individual particle counters in a 1200 m square grid. The SDs are self powered with a 1 m$^2$ solar panel that can generate up to 125 W. A single deep cycle battery holds enough charge to power the detectors overnight and during cloudy periods. On the edges of the SD array are three communication towers that provide microwave links to individual SDs. This network facilitates triggering and provides data storage. Figure 3.2 shows a photograph of a SD deployed in the field.

The surface detectors consist of two layers of scintillating plastic each attached to a photomultiplier tube (PMT) by strands of fiber optic cables, with one PMT attached to each layer of scintillating plastic[38]. A diagram of the SD scintillators and PMT is found in Figure 3.3. When secondary particles pass through the SD scintillators, fluorescence photons are produced in the plastic. The photons are gathered by fiber optics and transmitted to the SD PMTs. The signal produced by the PMTs is then digitized using Flash Analog to Digital Conversion (FADC) in 20 ns bins and recorded[9].

### 3.1.1 SD Trigger

The SD array trigger consists of two parts: a trigger local to each SD counter, which causes an SD to store waveforms to a buffer, and a host level trigger, which allows the communication towers to receive the previously buffered waveforms.

The SD local trigger has two levels labeled 0 and 1 that are based on integrals of a running 8 FADC bin window, corresponding to 160 ns. The lower, level 0 trigger, occurs when this integral reaches 15 FADC counts, which causes the SD to store a 128 bin, or 2560 ns, waveform. The threshold for the level 1 trigger is achieved when the 8 bin window contains 45 FADC counts. This causes the SD to store a waveform and inform the tower that this trigger level has occurred. Figure 3.4 shows an example waveform and includes references to the level 0 and 1 trigger thresholds.

The level 2 trigger, which corresponds to an event level trigger, occurs in the communication tower electronics and occurs when the tower receives notifications of level 1 triggers from three or more adjacent SDs. The tower then collects waveforms from all SDs that buffered waveforms due to level 0 or 1 triggers. Figure 3.5 shows geometries of minimum level 1 conditions for a level 2 trigger to occur.

### 3.1.2 Surface Detector Calibration

The SDs are calibrated using the signal created by atmospheric muons produced by low energy cosmic rays that interact high in the atmosphere. Atmospheric muons hit the SD detectors at an average rate of 20 per second and deposit a predictable amount of energy in the SD scintillators corresponding to the minimum ionizing energy for muons. This allows for calibrations to be made relative to a single Minimum Ionizing Particle(MIP).

Over 10 minute intervals, every local SD trigger is summed over 24 bins and the result is stored in a histogram. The peak of the distribution of background signals corresponds to the detector response from a single muon, as single hits are the most frequent. This peak is then fit and the result provides the conversion of FADC counts to charged particles passing through the detector. A GEANT4 provides a way to calculate the actual energy deposited by a particle passing through the SD and allows for the muon based calibration to be applied to any particle species. This is calculation is important in the SD detector simulation discussed in Section 4.3. The lower panel of Figure 3.6 shows a sample of a so-called “1 MIP” histogram.

A complementary method is used to find the value of the SD waveform’s pedestal. In this case, every 8 bin window that does not have enough signal to cause a level 0 trigger is summed over its 8 bins and recorded in a “pedestal” histogram over a 10 minute period. This histogram will be sharply peaked at the pedestal value. An example of a pedestal histogram is shown in the upper panel of Figure 3.6.

## 3.2 Fluorescence Detectors

TA has three fluorescence detectors (FDs) that come in two types: two using a new FD design produced by the Institute for Cosmic Ray Research (ICRR) at the University of Tokyo, and one consisting of refurbished HiResI mirrors, PMTs, and electronics that were re-engineered at the University of Utah. The FD stations are named after geographical features on which they are built. The two built with the ICRR design are located in the South-West of the SD array, and are called Black Rock Mesa (BR) and Long Ridge (LR) respectively. The third FD station, consisting of refurbished HiResI equipment, is located in the Northern part of the array and named as Middle Drum (MD), as it sits at the base of the Middle Drum Mountain.

Each telescope consists of a large spherical mirror that focuses light onto a cluster box of 256 PMTs, in effect creating an image with coarse ($\approx 1^\circ$) angular resolution. However, because PMTs are used as pixels, these detectors are sensitive to very small amounts of light and have resolutions on the order of 100s of nanoseconds in time. As was discussed in Section 2.3, the nitrogen spectrum is in the UV, and as such the PMTs used in this experiment must be sensitive to wavelengths as low as 300 nm. The PMT signal in the cluster boxes is fed to electronics that perform the triggering, digitization, and data acquisition.

Each FD detector covers approximately 100° in the azimuthal direction and 30° in altitude. The FD detectors over-look the SD array so that a given cosmic ray event may trigger in stereo, with two or more FDs, or in hybrid mode, with an FD and an SD trigger. Figures 3.7 and 3.8 show photographs of the LR and MD telescope buildings respectively. The BR detector is identical to LR in design, so a separate photo is not provided.

### 3.2.1 Black Rock Mesa and Long Ridge Detectors

The BR and LR telescope facilities are built into two story buildings and each have 12 telescopes. Each telescope consists of a 3.3 m diameter mirror, resulting in a total detector field of view of 110° in the azimuthal angle and 30° in altitude, looking from 3° to 33° above the horizon. The LR detector is oriented so that its field of view point to the North-East, whereas the BR detector looks to the North-West, so that the center of the FDs fields of view overlaps in the center of the SD array. Figures 3.9 and 3.10 show a schematic of the fields of view of BR and LR with respect to the geographic East and North.

The output of the cluster of 256 PMT cluster box is fed to electronics that perform triggering and digitization. The PMT signal is digitized with Flash Analog to Digital Conversion (FADC) into 100 ns bins, similar to what was done with the SDs discussed in Section 3.1. BR and LR waveforms can be up to 51.2 $\mu$s in length. Figure 3.11 shows a camera display of a sample cosmic ray event including the digitized waveform form many of the triggered tubes.

### 3.2.2 Black Rock Mesa and Long Ridge Trigger

The BR and LR triggering system consists of three trigger levels. The “level 1” trigger is on the single PMT level, selecting PMTs that have a total signal 6 sigma above the night sky background. The night sky background is measured for each tube by maintaining a running average of nontriggering tube signals[47].

The “level 2” trigger is obtained by the Track Finder (TF) module that performs pattern recognition in the PMTs selected by the level 1 trigger. To facilitate this, a 5x5 PMT matrix is swept across the 256 tube cluster box searching for tube patterns of 3 adjacent PMTs. To handle events that trigger PMTs along the the edges of a camera, a smaller 4x4 PMT matrix scans along the vertical edges the camera. Figures 3.12 and 3.13 show level 2 trigger criteria for both the 5x5 and 4x4 PMT searches. When this trigger condition is met the TF module reports this to the Central Trigger Distributor (CTD) that determines triggered cosmic ray events [47].

The CTD coordinates triggers from individual cameras and provides a central “final trigger” to all the cameras in the detector. When the CTD receives a level 2 triggers from one or more TF modules in the camera, the “final trigger” is generated.

This causes all the cameras in the experiment to record waveforms and send them to the CTD where they are stored. In addition, to the triggering, the CTD interfaces with a GPS module and provides absolute timing to the event[47].

### 3.2.3 Black Rock Mesa and Long Ridge Calibration

The Black Rock and Long Ridge fluorescence detectors have a five step calibration system that maintains an absolute calibration of each detector's PMTs on an hourly basis[27]. This method consists of making an absolute PMT calibration of a subset of the FD PMTs in the lab before installation, then using a variety of relative calibration methods to ensure a any PMTs absolute gain can be measured against the PMT gains that were measured in the lab. The total PMT gain may be described by five factors

$$G = G_0 \times G_1 \times G_2 \times G_3 \times G_4 \tag{3.1}$$

where $G_0$ is the absolute FADC tube response per photo-electron and each factor $G_1$ through $G_4$ are dimensionless corrections for each PMTs variation from the $G_0$ factor. Variations may occur due to aging, temperature, or just variations between PMTs. Each of these factors is described in the paragraphs below.

The main value of the PMT gain, $G_0$, is found using the "Calibration using RAYleigh Scattering" (CRAYS) system[49, 50]. A diagram of the CRAYS experimental apparatus is found in Figure 3.14. A 337.1 nm laser with a measured intensity is fired into a circular vessel filled with pure nitrogen gas. A PMT used in either the BR or LR FD is then optically sealed to this vessel. The number of photons scattered onto the face of the PMT may be calculated and compared to the measured PMT response. This system uses a 300 $\mu$J per 4 ns pulse laser. As only 10 PMTs can be calibrated with the CRAYs system per day, this is only done for three PMTs per telescope[50].

In addition, each of the CRAYS calibrated PMTs is outfitted with an alpha emitter based light source called a YAP. The YAP consists of a 4 mm diameter, 1 mm thick piece of $YAlO_3$:Ce scintillator and a 50 Bq alpha source. One of these is epoxied to the center of the photo-cathode of each CRAYS PMT. The YAP is a very stable light source that typically produces 450 photo electrons at 370 nm for each 20 ns pulse[50]. The YAP allows for the measurement of the long-term drift of the PMTs due to aging. In Equation 3.1, analysis of YAP events provides factor $G_3$.

The calibration of the non-CRAYS calibrated PMTs is done using a Xe light source mounted at the center of each mirror, which flashes directly onto the cluster PMT box. This flasher typically produces on order of $2 \times 10^4$ photo electrons per PMT per 2 $\mu$s pulse[50]. This allows the absolute gains of all the PMTs to be measured using the CRAYs PMTs as a reference.

The first of the relative calibration factors, $G_1$ comes from a high voltage adjustment that is done several times a year. Using the Xe flasher, the PMT high voltage is adjusted so that the signal matches that from the CRAYs PMTs. Any residual deviations from the CRAYs gain is put into the $G_1$ factor.

The PMT gains need to be measured more often than several times a year to understand nightly and hourly variations. For this, hourly measurements of PMT gains are done with the Xe flasher. This allows for adjustments of the gains of PMTs relative to the three CRAYS calibration on an hourly basis and is the factor $G_2$ in Equation 3.1.

Lastly, the $G_4$ factor represents a temperature correction made to all the PMTs. A linear relationship of $-0.720 \pm 0.053\%/^\circ$ is used, as was measured in the lab[27, 36].

An additional calibration tool is an two-dimensional scanner that may be placed across the entire cluster box at the BR and LR detectors. This tool allows for the measurement of the variation in the efficiency of PMTs across each PMTs face. When combined with ray tracing, the uniformity map allows for the accounting of these variations. The average result for PMT uniformity is shown in Figure 3.15.

### 3.2.4 Middle Drum Detector

Like the BR and LR FDs, the Middle Drum (MD) detector looks over 120° in azimuth and 30° in altitude. However, being on the North side of the SD array, this detector looks mostly to the South. The aperture is divided into 14 mirrors in two rings, one looking from 3° to 17° and another from 17° to 32°. Figure 3.16 shows a schematic of the MD field of view.

In contrast to narrow, tall buildings housing the BR and LR telescopes, the MD building is built into a single story and has a much larger footprint. The MD mirror building is built in an arc shape that allows for calibrations against a single light source placed at the center of curvature of the building's arc.

The equipment at MD is refurbished from the HiResI FD which was located on 5 Mile Hill at Dugway Proving Grounds, Utah. However, the mirror configuration was completely re-engineered as the HiResI FD only had ring one mirrors. As with HiResI, the MD electronics have sample and hold electronics, which do not digitize a waveform. Instead, only two values are digitized for each triggered PMT, the trigger time and the integrated signal of the tube. Sample and hold electronics allow for a much reduced data stream, but add difficulties in understanding exactly what the digitized trigger time corresponds to.

The analysis in this work will only use data from the BR and LR detectors and so the more detailed specifics of the MD detector will not be presented here.

## 3.3 Additional Calibration Tools

### 3.3.1 Central Laser Facility

The Central Laser Facility (CLF), is a 355 nm nitrogen laser located in the center of the SD array 20 km from all three FD sites. In Figure 3.1, the CLF is the blue cross in the center of the SD array. The CLF is fired every half hour at 10 Hz producing 50 shots per firing and is observed by all three FDs. The CLF is an important tool in understanding the FDs' photometric scale, but also provides important information on atmospheric scattering.

By modeling the laser's attenuation and the light scattered to the FD, the number of photons in the CLF beam can be reconstructed as well as the actual laser energy. This reconstructed energy can then be compared to the laser energy found using a radiometer built into the housing of the CLF. This provides an "end-to-end" calibration of an FD detector and is another way of establishing an absolute calibration. In addition, the CLF allows for comparisons between different FDs.

The CLF is also an important tool for understanding the atmosphere at the TA site. Using a CLF shots on clear nights, where molecular scattering is dominant as a baseline, the number of aerosol scatters can be measured in a relative manner. This can provide a complimentary analysis to the aerosol measurement with the LIDAR system installed at BR.

The Analysis of CLF data is still on going at TA and the results are currently not finalized.

### 3.3.2 Roving Xenon Flasher

The Roving Xenon Flasher (RXF) is a stable, mobile flasher that was the main calibration tool at the HiRes experiment and was used at both HiResI and HiResII sites. The flasher is powered by 12 V batteries and is moved between telescopes allowing for a single light source to cross calibrate all the telescopes in the experiment. As with HiRes, the RXF is the main calibration tool at the MD detector, but it has been used at all three FDs to ensure the photometric scale is consistent. The RXF also provides an important connection to the HiRes calibrations and helps ensure that TA's results are comparable to HiRes.

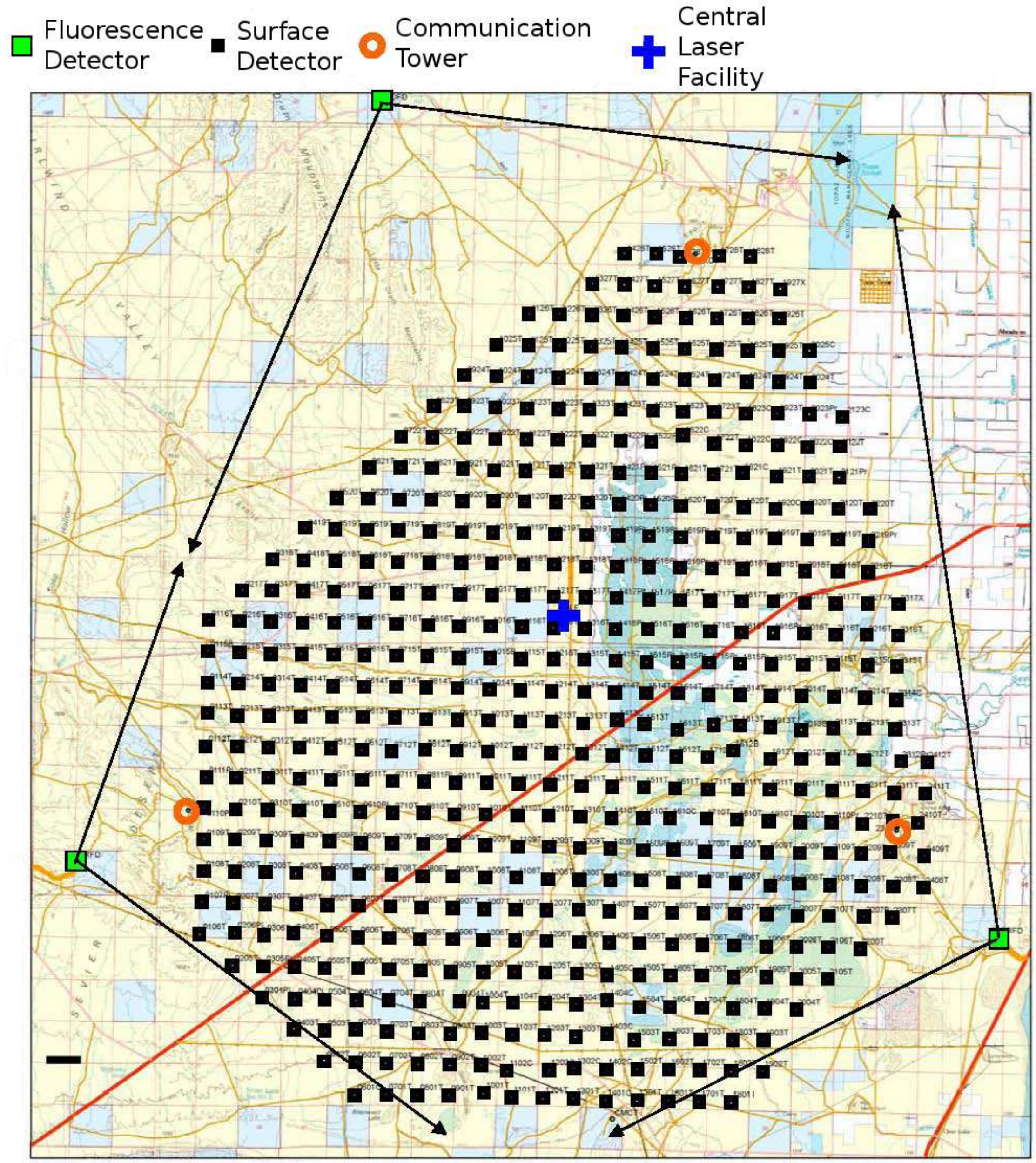

**Figure 3.1**: The Telescope Array experiment, showing fluorescence detectors, represented as green squares and surface detectors, represented as black squares. The blue cross in the center is the Central Laser Facility. The town of Delta, Utah is about 15 km from the Eastern edge of the SD array. The arrows show azimuthal extent of the field of view of each fluorescence detector. Reprinted with permission from [47].

**Figure 3.2**: Telescope Array surface detector in the field.

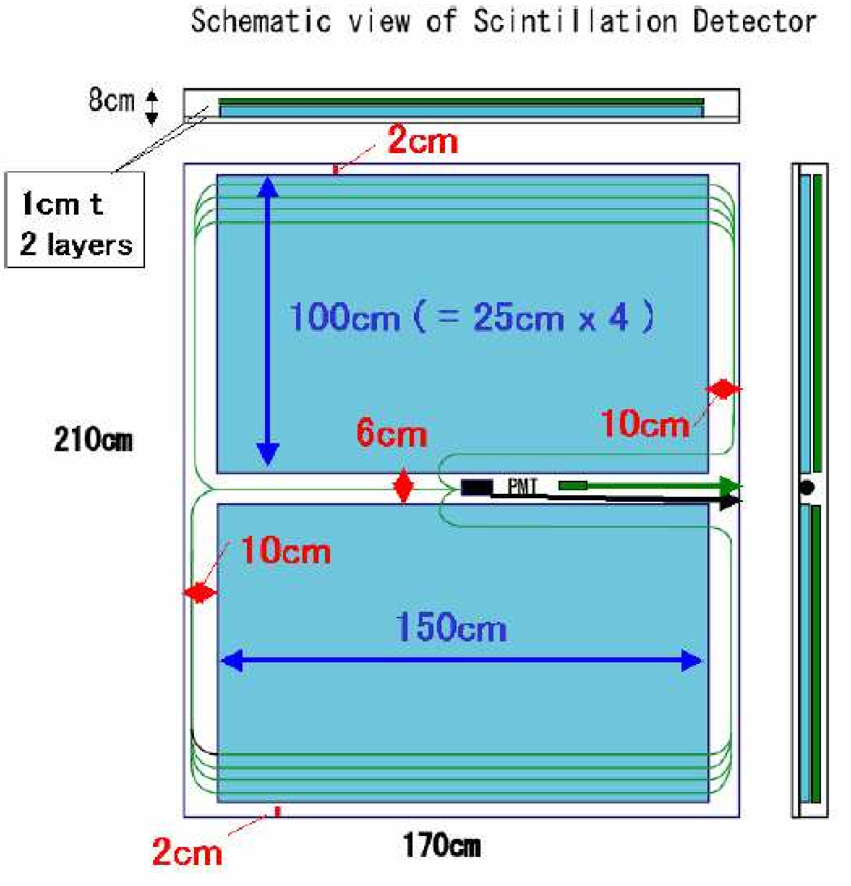

**Figure 3.3**: Configuration of surface detector scintillators[9]. SDs have 6 m$^2$ of 1 cm thick scintillating plastic in two layers. There is one PMT for each layer of scintillator, attached by fiber optic cable.

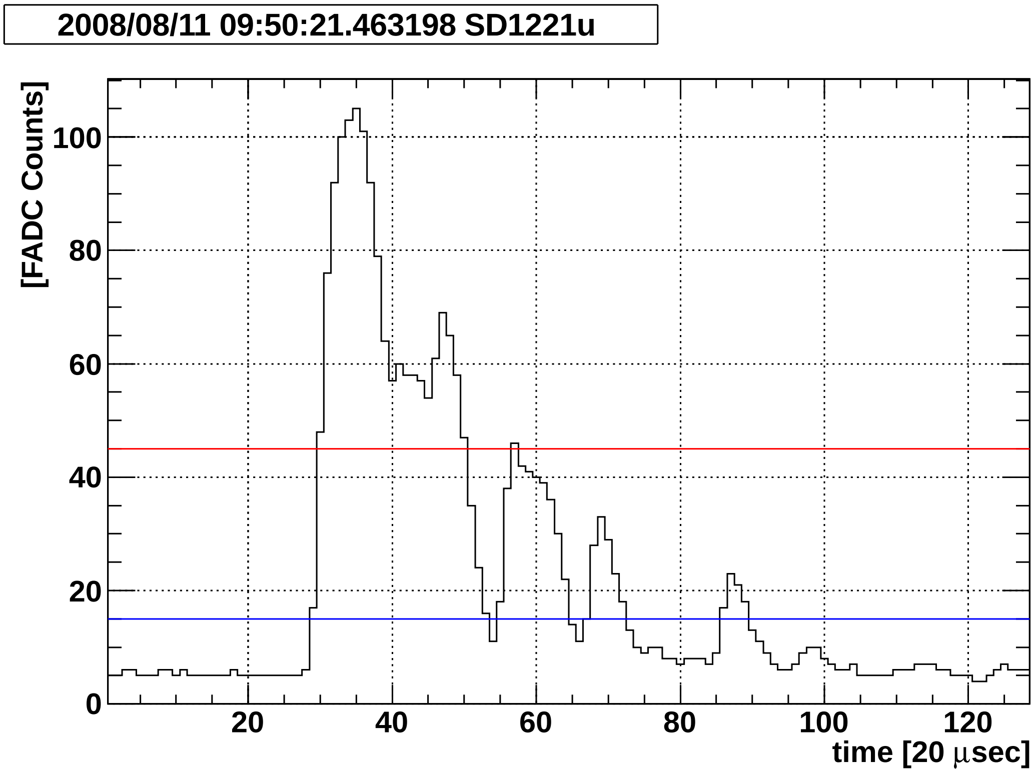

**Figure 3.4**: Sample of a digitized waveform for a SD event, showing for reference the number of FADC counts required for a level 0 (blue) and level 1 (red) trigger.

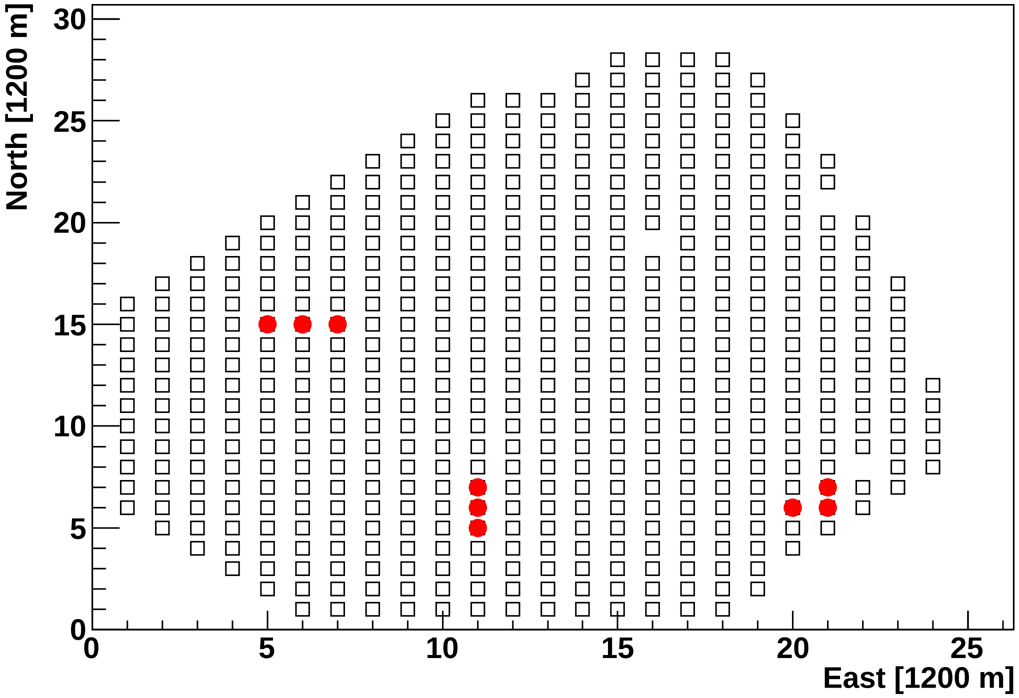

**Figure 3.5**: Examples of possible geometries for 3 SDs with level 1 triggers to create a level 2 (host level) trigger. In the event of level 2 trigger, the individual SD counters send buffered waveforms to their respective communication tower.

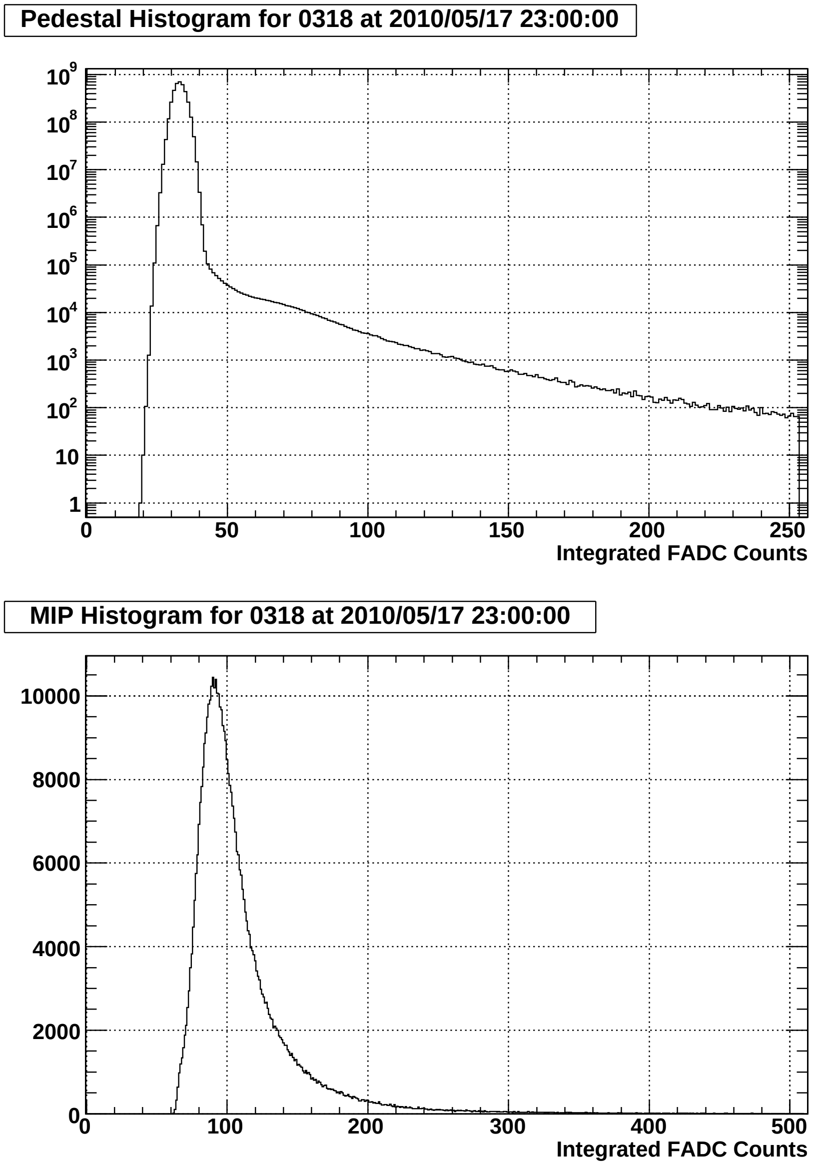

**Figure 3.6**: *top* Histogram of integrated FADC signal when no trigger condition occurs over a 10 minute period. The peak of this distribution gives a measurement of the pedestal for this 10 minute period. The actual pedestal is the peak of this histogram divided by 8. The high side tail of this histogram is caused by parts of event signals that did not reach a level 0 trigger. *bottom* Histogram of integrated FADC signal of all local triggers in a ten minute period. This is distribution is peaked at most frequent occurrence, a single atmospheric muon passing through the SD. The actual number of FADC corresponding to a single muon is the peak of this histogram divided by 24. The high side tail of this histogram is caused by double muon events or cosmic ray shower.

**Figure 3.7**: Aerial photograph of the Long Ridge telescope building.

**Figure 3.8**: Aerial photograph of the Middle Drum telescope building.

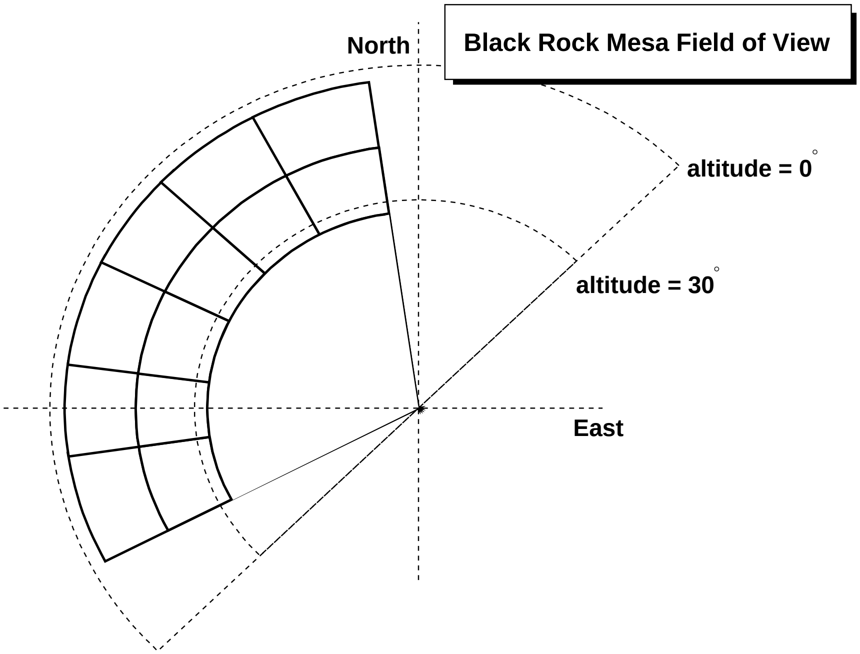

**Figure 3.9**: Black Rock Mesa fluorescence detector field of view

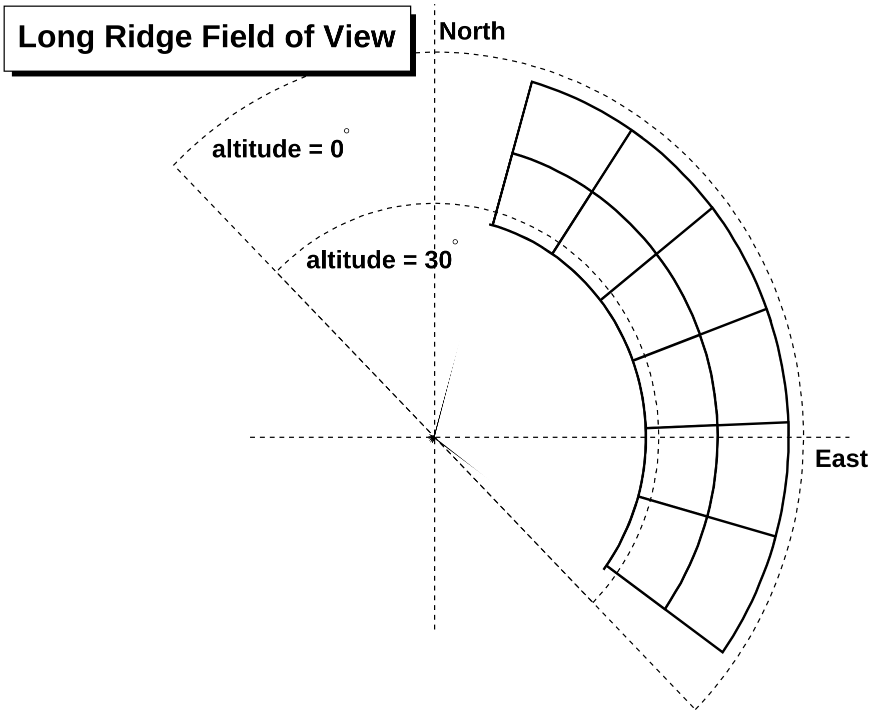

**Figure 3.10**: Long Ridge fluorescence detector field of view

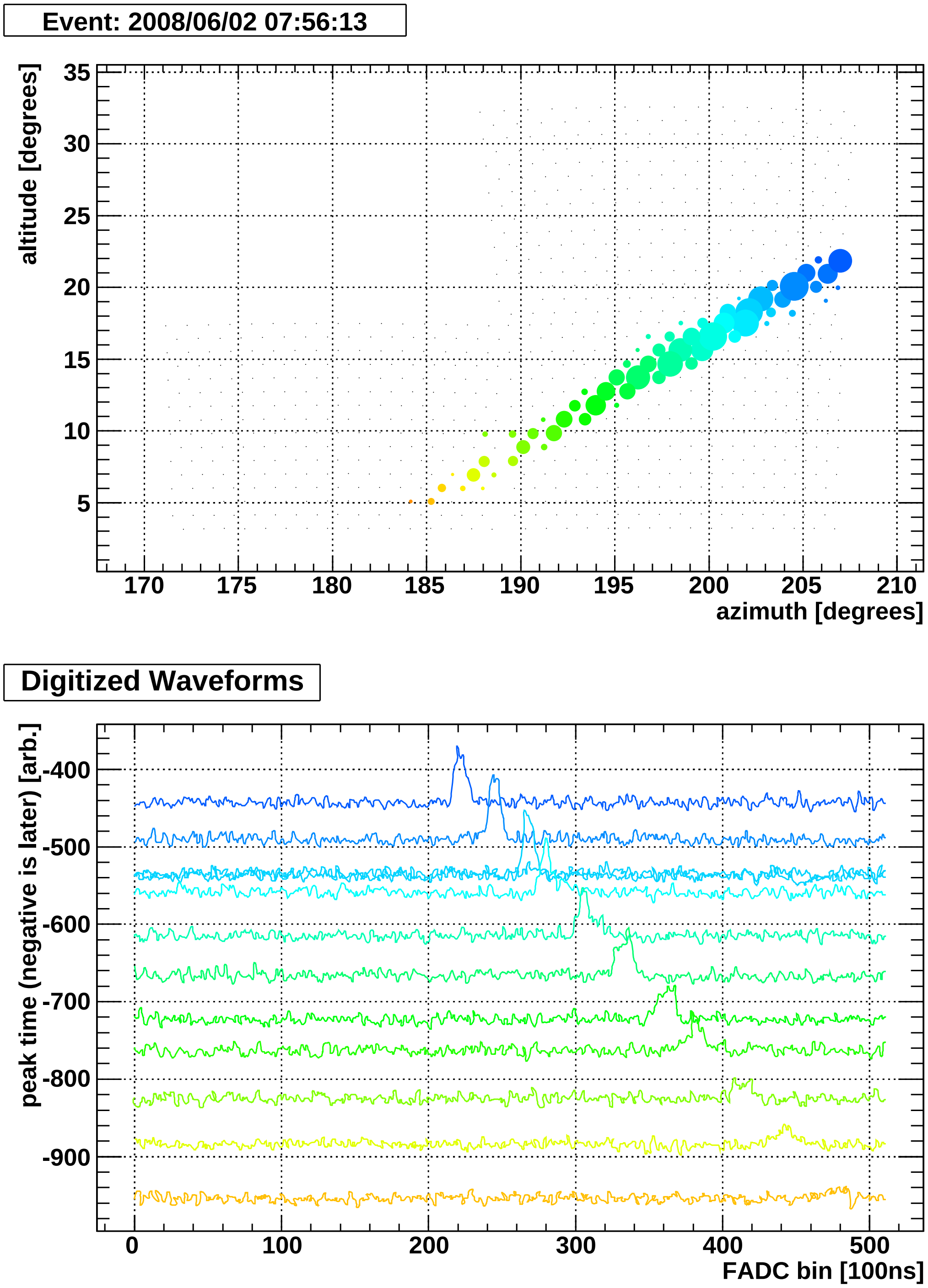

**Figure 3.11**: *top* Mirror display showing good tubes. The radius of the marker is proportional to the number of photo electrons in that tube and the color of the marker show the tube trigger time. *bottom* Collection of digitized waveforms from good tubes in this event. The waveforms have been shifted down in the y axis in proportion to the time of the peak and the color of the trace matches the corresponding tube color in the upper plot.

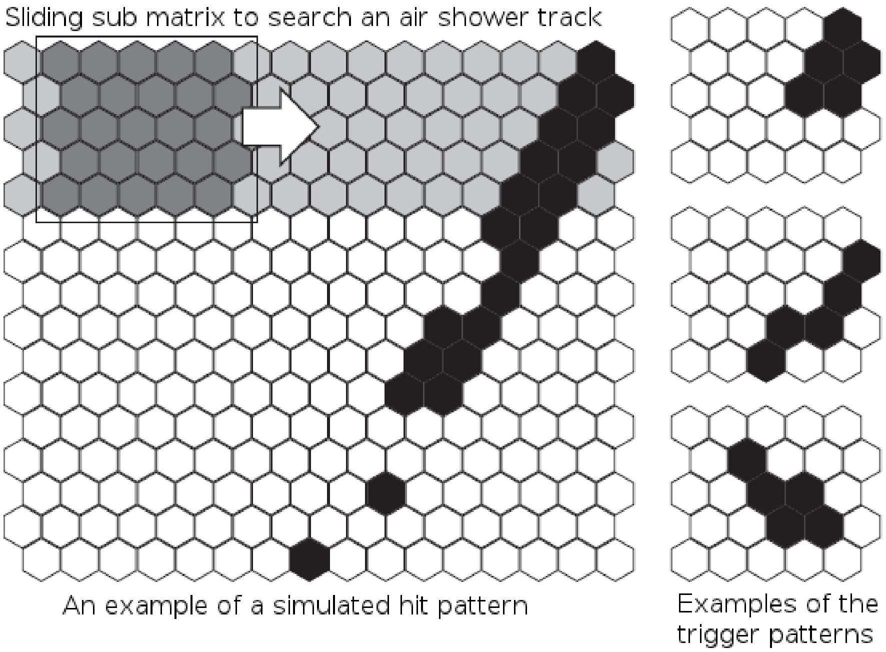

**Figure 3.12**: Trigger patterns for the 5x5 matrix trigger search at Black Rock and Long Ridge[47]. Reprinted with permission.

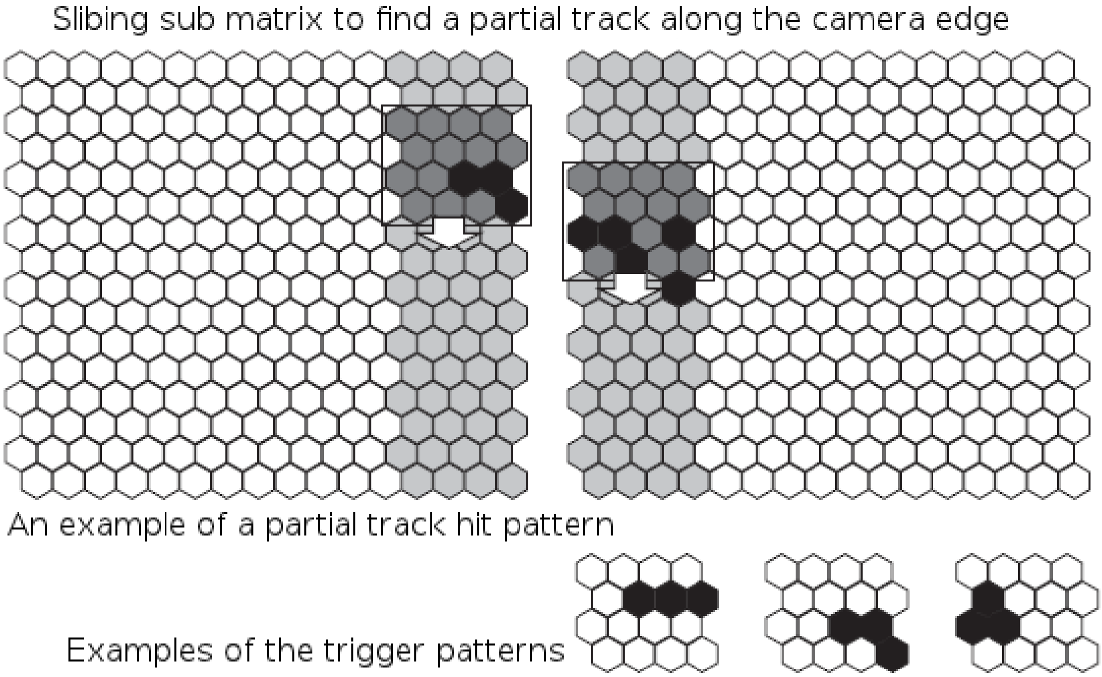

**Figure 3.13**: Trigger patterns for the 4x4 search matrix for the cluster box edges at Black Rock and Long Ridge[47]. Reprinted with permission.

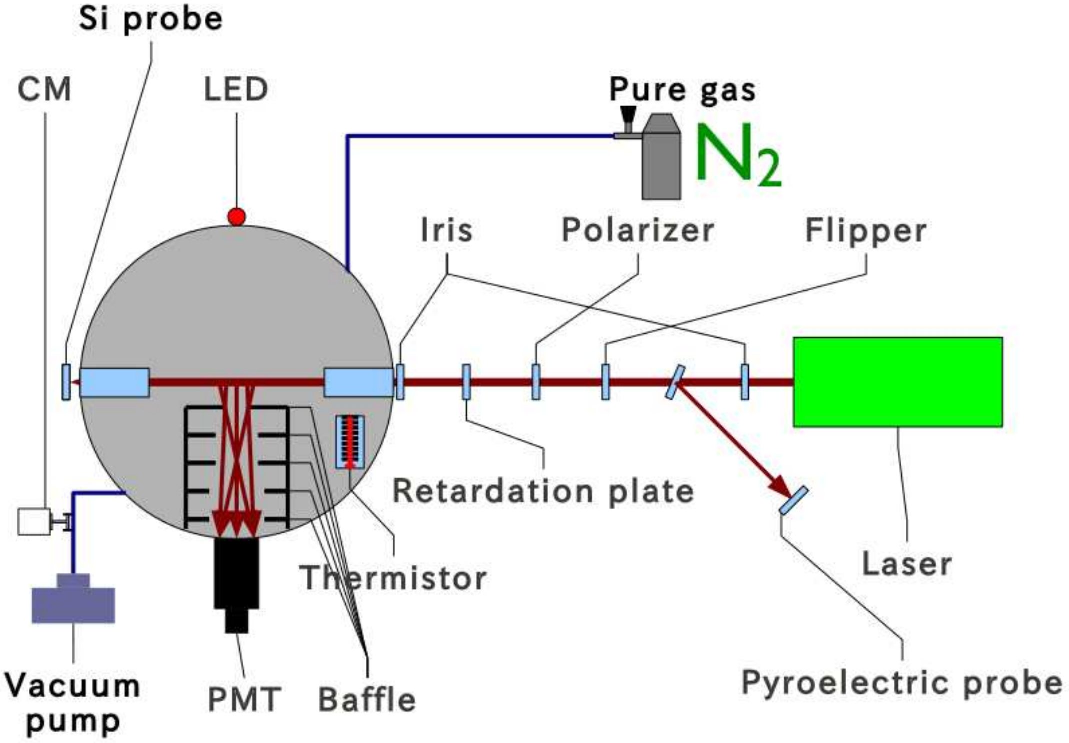

**Figure 3.14**: Experimental setup for Calibration using RAYleigh Scattering (CRAYS) system for absolute calibration of the PMTs used at the Black Rock Mesa and Long Ridge detectors.

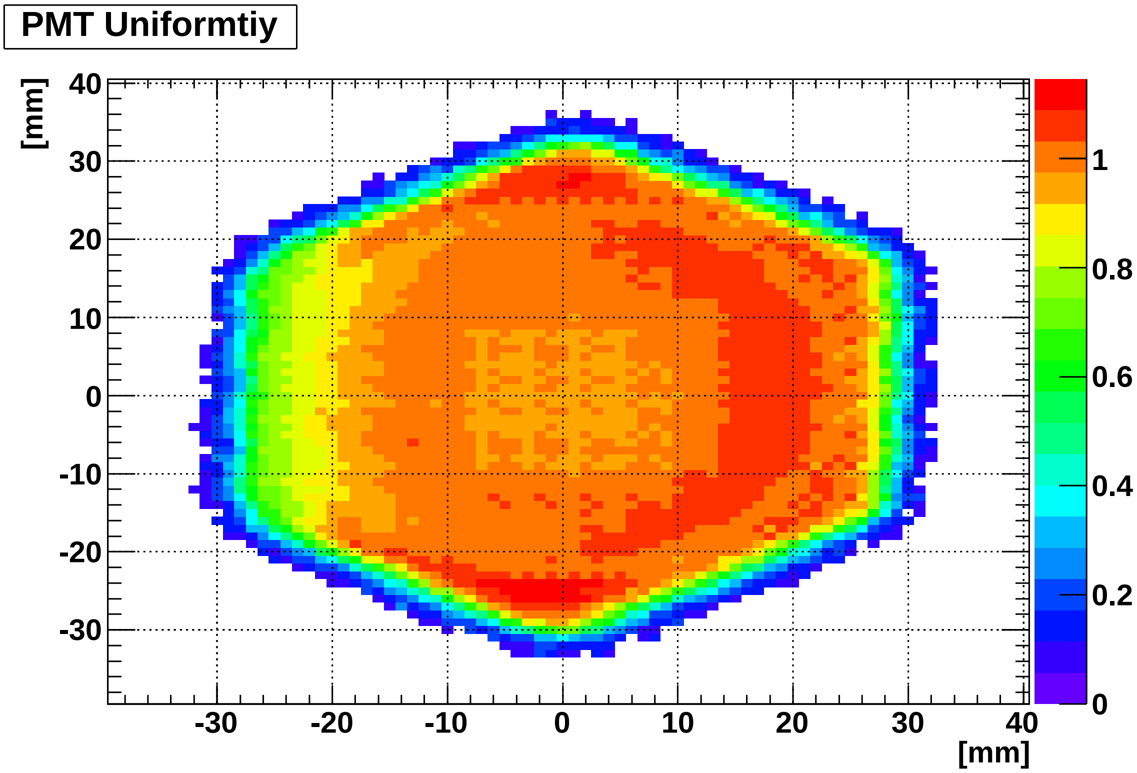

**Figure 3.15**: Average PMT uniformity using the X-Y scanner.

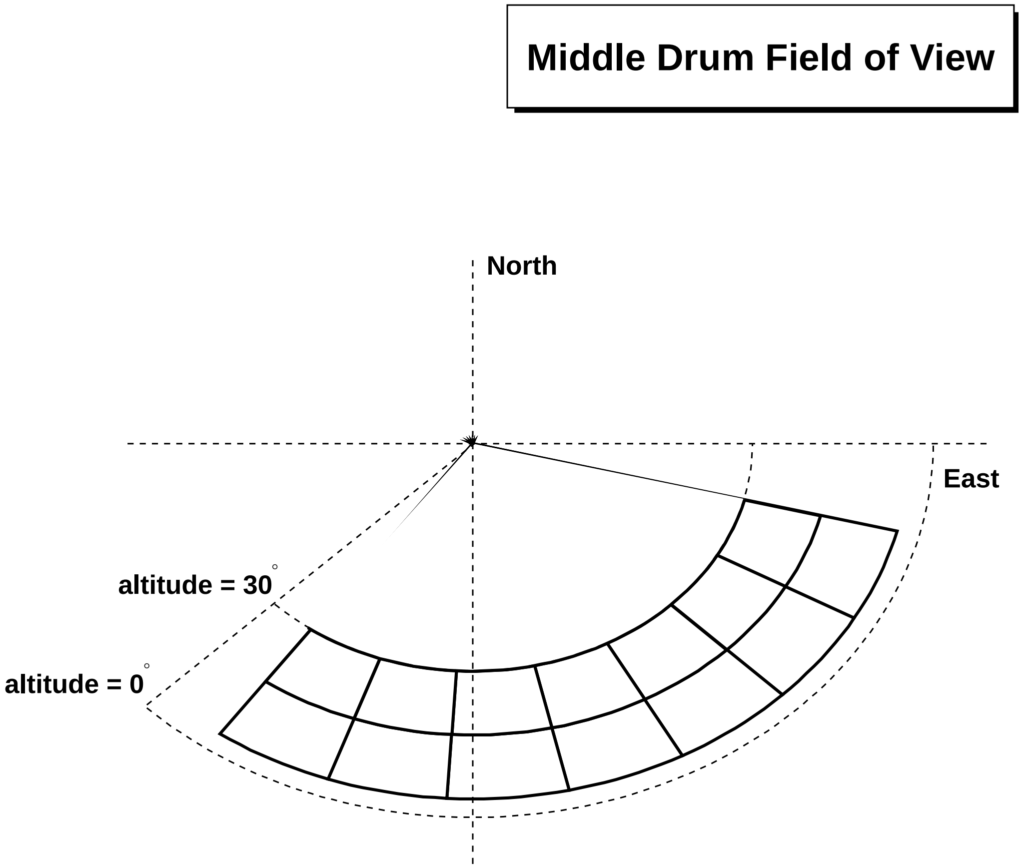

**Figure 3.16**: Middle Drum fluorescence detector field of view

# CHAPTER 4

# SIMULATION

Trusting event reconstruction and interpreting physics results with a complex detector can be difficult without using realistic simulations. In cosmic ray physics and, indeed, at the TA experiment, both a cosmic ray's interactions in the atmosphere and the actual detector response are simulated. The cosmic ray's interaction in the atmosphere in this work is modeled by a standard $3^{rd}$ party package called CORSIKA which is discussed in Section 4.1. Coupling CORSIKA with detector modeling allows for the full simulation of a cosmic ray event. Such a simulation allows for trigger efficiencies, detector acceptance and reconstruction biases to be understood. The goal of the detector simulation is to produce Monte Carlo (MC) data that is indistinguishable from data produced by the actual detector. The MC data is reconstructed with the same programs as the real data and must reproduce the same distributions found in the experimental data.

The adequacy of air shower and detector simulations used in this work is validated by comparing distributions of many observables produced by the experimental data and the MC, ensuring that both are representative of the same parent distributions. This process can be arduous and time consuming, but results strong, well tested simulations. The MC is a tool with which reconstruction resolutions may be understood, as well as, biases caused by either reconstruction or the detector acceptance. The full discussion of data-MC comparisons is found in Section 6.4.

As mentioned above, event simulations are divided into two independent parts, the simulation of a cosmic ray in the atmosphere and the simulation of the detector and triggering. Both of these are described below. As this work concerns a hybrid analysis, simulations of both the FD and SD are presented.

## 4.1 CORSIKA Air Shower Simulation

The air shower simulations used in this work are done with the CORSIKA (COsmic Ray SImulations for KAscade) package[23]. As the name implies, this code was first developed by and for the KASCADE experiment, and has become a piece of software in cosmic ray physics. CORSIKA is a large, complex piece of software that allows for the simulation of cosmic rays with any chemical composition and energy. A user is able to change many rules for how an EAS simulation develops, tracks particles, and monitors energy deposited in the atmosphere. As such, when using CORSIKA simulations for physics, it is important to clearly document the options that are used. This section attempts to discuss basic CORSIKA parameters and show the options used in this study. Table 4.1 gives a summary of the most important CORSIKA run parameters for the simulations used in this work.

An important parameter for any CORSIKA run is a limit on how low in energy CORSIKA will track secondary particles. This energy is called the "cutoff energy". As was shown in Section 2.1, as the number of particles in an air shower increases the energy per particle must decrease. When a particle falls below the cutoff energy, $E_{cut}$, CORSIKA stops tracking it and its energy is added to the tallies of energy deposited in the atmosphere. Independent cutoff energies may be specified for hadrons, muons, electrons, and photons. In the simulations used in this work, the cutoff energy for electrons, positrons, and $\gamma$s is 250 keV.

For cosmic rays above $10^{18}$ eV, the number of secondary particles becomes too

**Table 4.1**: CORSIKA simulation parameters for the generated proton and iron showers used in this work.

| Selected CORSIKA Parameters | |
|---|---|
| $E_{cut}$ ($e^{+/-}$, $\gamma$) | 250 keV |
| $E_{cut}$ ($\mu^{+/-}$) | 50 keV |
| $E_{cut}$ (hadrons) | 50 keV |
| THIN | $10^{-6}$ |
| UPWARDS | no |
| Interaction Model | QGSJetII |
| Observation Height | 1430 m |

numerous to realistically track, even with large cutoff energies. In fact, a single air shower produced by a $10^{18}$ eV cosmic ray can take days to simulate using standard CORSIKA. To speed up simulations, CORSIKA has developed a statistical thinning method, where a single particle may represent many particles with a weight to ensure that energy and momentum are conserved. The resulting single particle may represent the energies of hundreds of particles in the air shower[31]. The thinning option accepts a parameter $\epsilon_{th}$, the thinning level, and at any stage in the EAS development CORSIKA will combine particles with energy,

$$E_{particle} < \epsilon_{th} E_0 \tag{4.1}$$

where $E_0$ is the energy of the primary cosmic ray. The particle that will represent all the thinned particles is chosen randomly from all particles that meet the criteria in Equation 4.1 with a probability

$$p_i = E_i / \sum_{j=0}^{N} E_j \tag{4.2}$$

Then, each thinned particle contributes $1/p_i$ to the weight of the chosen particle in order to conserve energy.

Close to the core of an EAS, where the particle density is high, a moderate amount of thinning does not have a significant effect on the overall particle and energy deposition distributions. Since the production of fluorescence photons depends on the overall energy deposited, thinned showers work well in simulating air showers for FD simulations. Figure 4.1 shows the number of charged particles in CORSIKA simulations with $\epsilon_{th}$ set to $10^{-6}$ and $10^{-3}$. It it clear in this figure that the $10^{-6}$ thinning results in a smooth distribution of charged particles, whereas, the $10^{-3}$ simulation results in large unphysical fluctuations. The CORSIKA simulations used in this work use $10^{-6}$ thinning level.

Any level of thinning causes large fluctuations in the particle densities away from the shower core where the particle densities are low. Figure 4.2 compares the distributions of charged particles from two CORSIKA simulations, one using $10^{-6}$ thinning and the other using no thinning. As SDs measure the lateral distributions of charged particles, thinned showers cannot be used directly to simulate the SD array. However, a method has been developed by the TA collaboration to recover the information lost by thinning and successfully use thinned showers to simulate SD data. This process has been called “dethinning” and is discussed in Section 4.2.

CORSIKA longitudinal profiles are parametrized well with the Gaisser-Hillas (GH) equation described in Equation 2.10. As described in Section 4.1, every shower’s longitudinal profile in the shower library is parametrized by a fit to the GH equation. Then, when performing the detector simulation, a shower may be generated by its GH parameters and the GH function. This eases computational efforts and greatly reduces data storage. The distributions of GH parameters for the proton and iron shower libraries used in this work are shown in Figure 4.3. These showers are the core of the simulations used in this analysis.

## 4.2 Dethinned CORSIKA

The goal of dethinning is to restore the information lost in CORSIKA’s particle thinning by using a randomized process to spread out the weighted particles[46]. This or a similar process is required to use thinned showers for the purpose of SD simulations. The difficulty is to spread particles out in a physical way that results in lateral distributions that are consistent with those produced by unthinned CORSIKA. To validate dethinning, approximately 100 unthinned air showers with primary energies greater than $10^{18}$ eV were generated by running the CORSIKA code the with high performance many-processor computing clusters[44]. The dethining process was validated by ensuring that unthinned and dethinned showers result in matching lateral distributions[45].

To begin dethinning a CORSIKA shower, a weighted particle is chosen from the list of particles that reach the ground. Each particle is reported from CORSIKA with a three vector position, a three vector momentum, and a time. A vertex is chosen off the EAS axis that represents the stage in the air shower development where the thinned particle was created. Using this vertex, a two-dimensional Gaussian cone is constructed and the weights of the thinned CORSIKA particles are distributed randomly on the surface of the cone. Figure 4.4 shows an example of a supposed vertex and resulting Gaussian cone used to spread out weighted particles.

A comparison of the lateral distributions from dethinned and unthinned COR-

SIKA showers is shown in Figure 4.5. The lateral distributions produced by the dethinning procedure agree with the unthinned lateral distributions.

## 4.3 Surface Detector Simulation

To simulate the SD array, the dethinned CORSIKA showers are each given a random core location and azimuthal angle with respect to the SD array. Then the resulting particles from the dethinned CORSIKA shower are passed through simulated SD counters using each SDs measured coordinates[28].

As discussed in Section 3.1, the SDs measure the number of charged particles by the energy deposited in two layers of scintillating plastic. A GEANT4 (GEometry ANd Tracking) simulation is used to accurately model the energy deposited in an SDs for a particle with a given species, momentum, and incident geometry to the SD. This simulation requires a full model of the SD to be build using the GEANT4 interface.

To speed up the running of the SD simulations, the SD GEANT4 simulation has been sampled thousands of times and the results built into a look-up table which may be accessed though an incoming particles parameters. In a high performance computing setting, this table may then be read into memory and sampled directly as the particles are read out from the dethinning.

The energy deposited in the SD scintillators is then combined with the SD calibration information to calculated the number of FADC counts in a given time bin. Then, to account for the shaping of the FADC signal due to the SD electronics, a general waveform shape is applied for a single incident particle, that was derived using many SD waveforms from the data[28]. This waveform shape is found in Figure 4.6. The area of this waveform is scaled to the number of FADC counts found from the SD calibration. The full waveform is generated by applying this procedure to every particle resulting from dethinning that is incident a given SD.

With the creation of SD waveforms, the SD triggering mechanisms that were discussed in Section 3.1.1 are simulated. Finally, the waveforms are packaged in the same format as the data to create MC data that appear identical to the data coming out of the real SD array.

## 4.4 Fluorescence Detector Simulation

Simulating the FD detector response consists of three parts, generation of longitudinal EAS profiles, calculating the number of photons that reach the FD, and simulating the detector response and the detectors trigger. Each of these is discussed below.

The generation of the EAS longitudinal profile is done with using the Gaisser-Hillas (GH) equation, defined in Equation 2.10 and the CORSIKA longitudinal shower library described in Section 4.1. For a given CORSIKA shower, the four GH parameters, $N_{max}$, $X_{max}$, $\lambda$, and $X_0$ are selected and the number of charged particles are calculated at any depth in the shower. An example of this fit to a CORSIKA longitudinal distribution is found in Figure 4.7.

The number of fluorescence photons created as the EAS develops in the atmosphere depends on the energy deposited in the atmosphere and not directly on the number of charged particles, so a conversion between number of charged particles and energy deposited is needed. This calculation is done using the the average ratio of charged particles to energy deposited from the earlier CORSIKA runs[35]. This quantity is called $\alpha$ and is determined by

$$\alpha(s) = \frac{\left(\frac{dE_{dep}}{dX}\right)}{N_{ch}}(s) \tag{4.3}$$

where $\frac{dE_{dep}}{dX}$ is the average energy deposited in the atmosphere by the EAS and $N_{ch}$ is the number of charged particles in the shower. $\alpha$ is generally calculated as a function of the shower age, $s$. $s$ is defined in terms of the slant depth, $X$, as

$$s = \frac{3X}{X + 2X_{max}} \tag{4.4}$$

As such, $s$ is 0 when $X$ equals 0, 1 at shower maximum, and approaches 3 when $X \gg X_{max}$.

The mean $dE/dX$ is calculated for both the proton and iron CORSIKA simulations used in this work. Both are shown in Figure 4.8. It is clear that above $s$ equal to 0.4, the proton and iron $\alpha$ calculations agree. Below, $s$ equal to 0.4, no significant amount of particles exist and this disagreement is negligible. For this reason, the fit to mean $dE/dX$ for protons is used in both proton and iron FD simulations.

For purposes of generating a shower for FD simulations, mean $dE/dX$ is fit to the function

$$\alpha(s) = \frac{c_1}{(s+c_2)^{c_3}} + c_4 + c_5 s \tag{4.5}$$

Then the fit may be used to generate the energy deposited at given point in the air shower described by $s$. The fit to proton MC shown in Figure 4.8 is found in Table 4.2.

The number of fluorescence photons is then calculated using the energy deposited by the air shower and the fluorescence yield from Equation 2.15. The number of Cherenkov photons is calculated from Equation 2.22 and the number of charged particles in the shower. The Cherenkov light is produced preferentially along the shower axis, and as such, the number of Cherenkov photons will increase as the shower develops. Figure 4.9 shows the number of charged particles, energy deposited, and the fluorescence and Cherenkov photons produced in the FD simulation.

Using the number of particles produced along shower axis, the density of photons that reach an FD mirrors can be calculated from a given shower segment $dl$ and shower zenith angle, $\theta$.

$$N_\gamma = \sum_\lambda T_{atm}(\lambda)\left(\frac{d^2N_\gamma^{fl}}{d\Omega}(\lambda,\theta) + \frac{d^2N_\gamma^{cv}}{d\Omega}(\lambda,\theta) + \frac{d^2N_\gamma^{ray}}{d\Omega}(\lambda,\theta) + \frac{d^2N_\gamma^{mie}}{d\Omega}(\lambda,\theta)\right) dl d\Omega \tag{4.6}$$

where $d\Omega$ is

$$d\Omega = \frac{A_0\cos(\phi)}{r^2} \tag{4.7}$$

where $r$ is the distance to the shower segment, $A_0$ is the mirror area, and $\phi$ is the viewing angle between the FD and the shower axis[42]. $N_\gamma^{fl}$ is the number of

**Table 4.2**: Fit parameters for $< dE/dX >$ for CORSIKA simulated QGSJetII protons. This fit is shown in Figure 4.8 using Equation 4.5.

| $< dE/dX >$ Fit Parameters | |
|---|---|
| $c_1$ | 1.32250e-03 |
| $c_2$ | 2.42454e-01 |
| $c_3$ | 9.85513 |
| $c_4$ | 2.37289 |
| $c_5$ | 1.01926e-01 |

fluorescence photons and $N_\gamma^{cv}$ is the number of direct Cherenkov photons. $N_\gamma^{ray}$ and $N_\gamma^{mie}$ are the number of Rayleigh and Mie scattered Cherenkov photons. $T_{atm}(\lambda)$ is the amount of light attenuated by Rayleigh and Mie scattering as the photons travel from the shower axis to the FD. Figure 4.10 shows an example of the integral described in Equation 4.6 for a single simulated EAS.

After the number of photons that reach the mirrors is calculated, the reflected photons are ray traced to determine which PMTs at the FD trigger and to account for any obstructions that could block photons. Obstructions could consist of the PMT camera box, the mount holding the camera box, or any other support structures inside the FD station. The ray-tracing process determines how many of the photons in Figure 4.10 actually result in PE in the PMTs. The result of ray tracing from a single point for the Black Rock detector is shown in Figure 4.11. The ray traced are combined with the PMT uniformity map found in Figure 3.15 to account variations in the acceptances across the PMT face as well as cracks between adjacent PMTs.

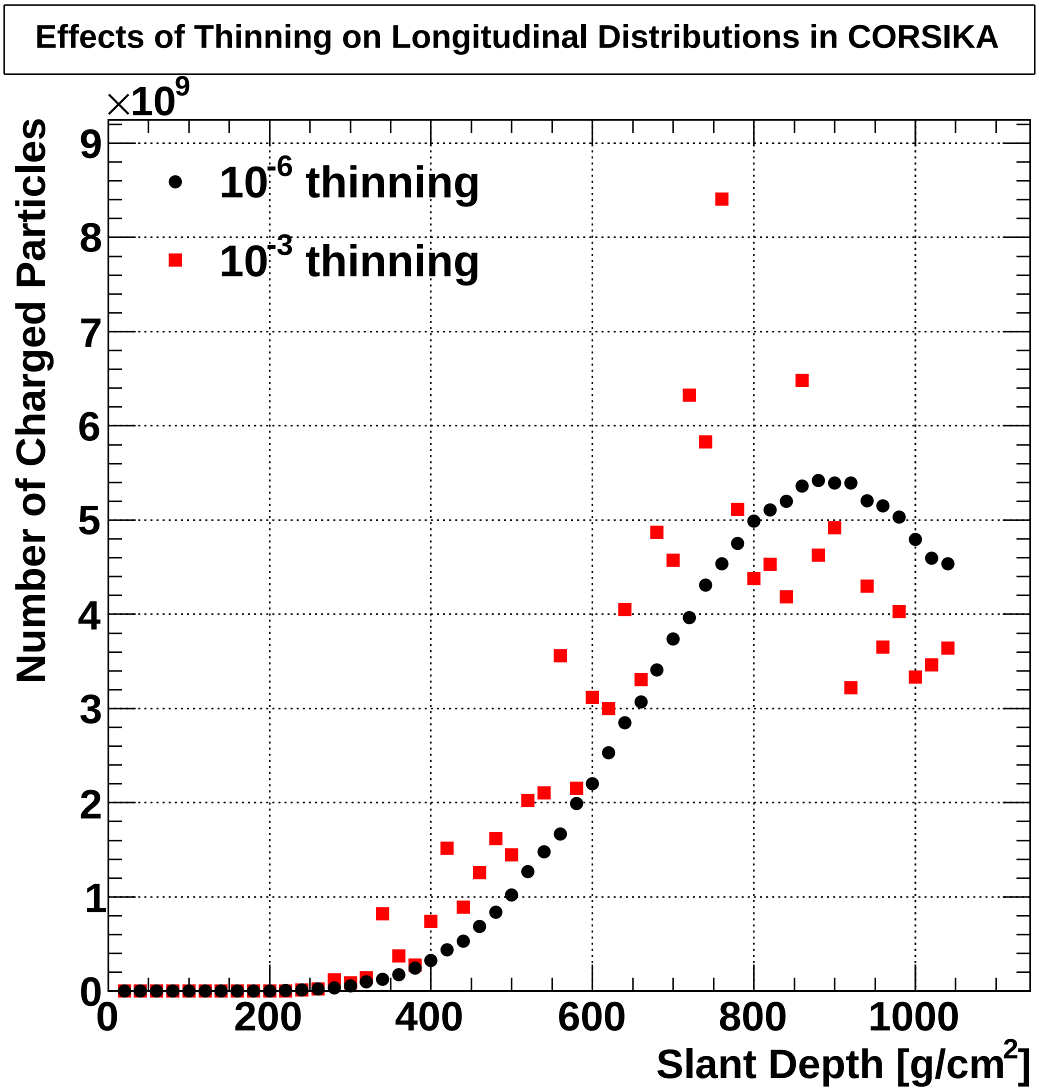

**Figure 4.1**: The effect of shower thinning on the longitudinal distributions of the number of charged particles in CORSIKA for a vertical $10^{19}$ eV cosmic ray air shower. The red squares were generated with an extreme, $10^{-3}$, level of thinning, the black circles with a low level of thinning, $10^{-6}$.

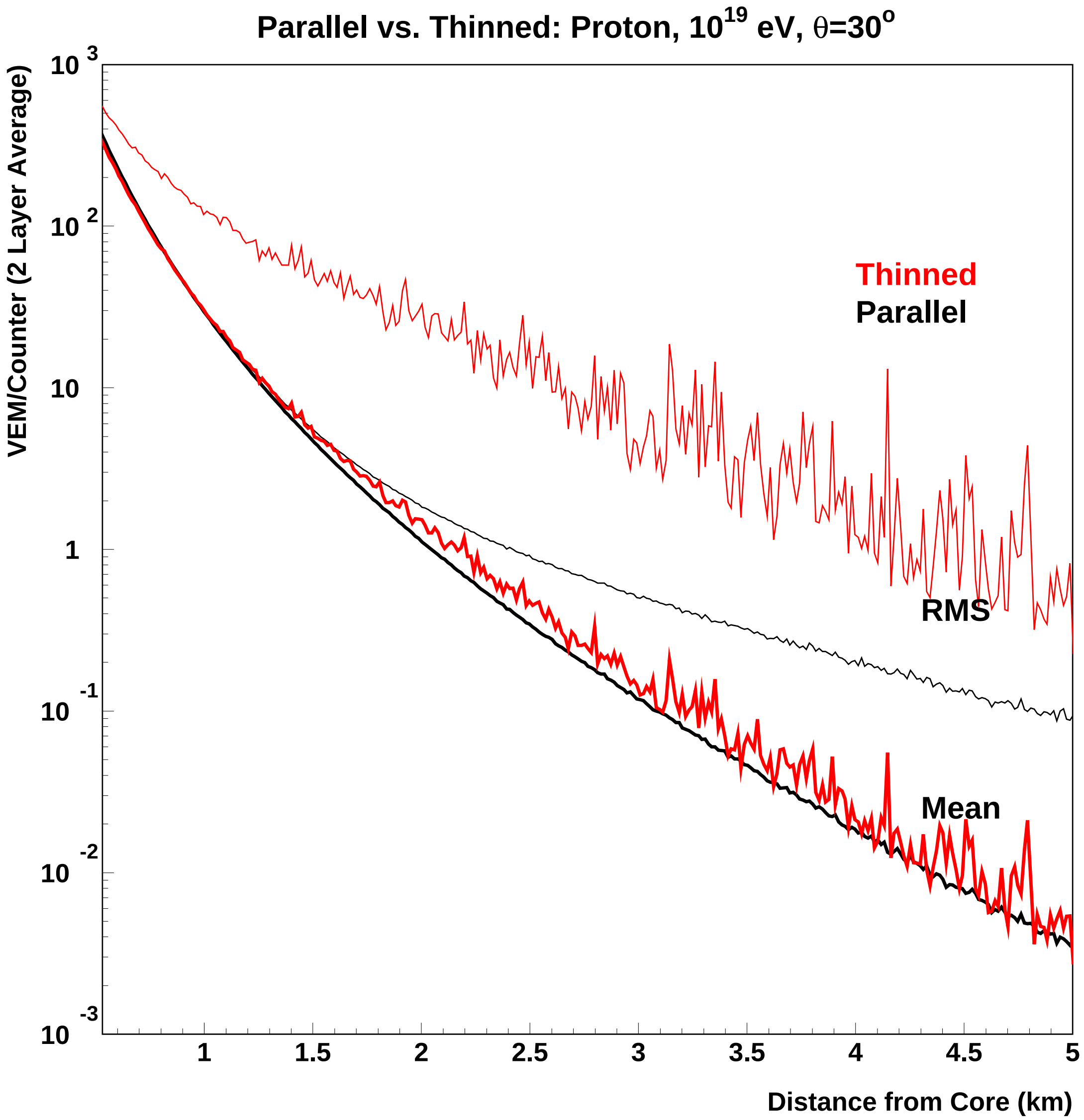

**Figure 4.2**: The lateral distributions of thinned CORSIKA showers (red) and unthinned showers (black) with the same starting parameters[46]. The axis is the energy deposited in SD counters in the unit of VEM (Vertical Equivalent Muon), though is a measurement of shower density because SD counters have a fixed area. It is clear in this figure that the particle densities more than a kilometer from the shower axis have large fluctuations that could not be used in a successful SD simulation. Reprinted with permission.

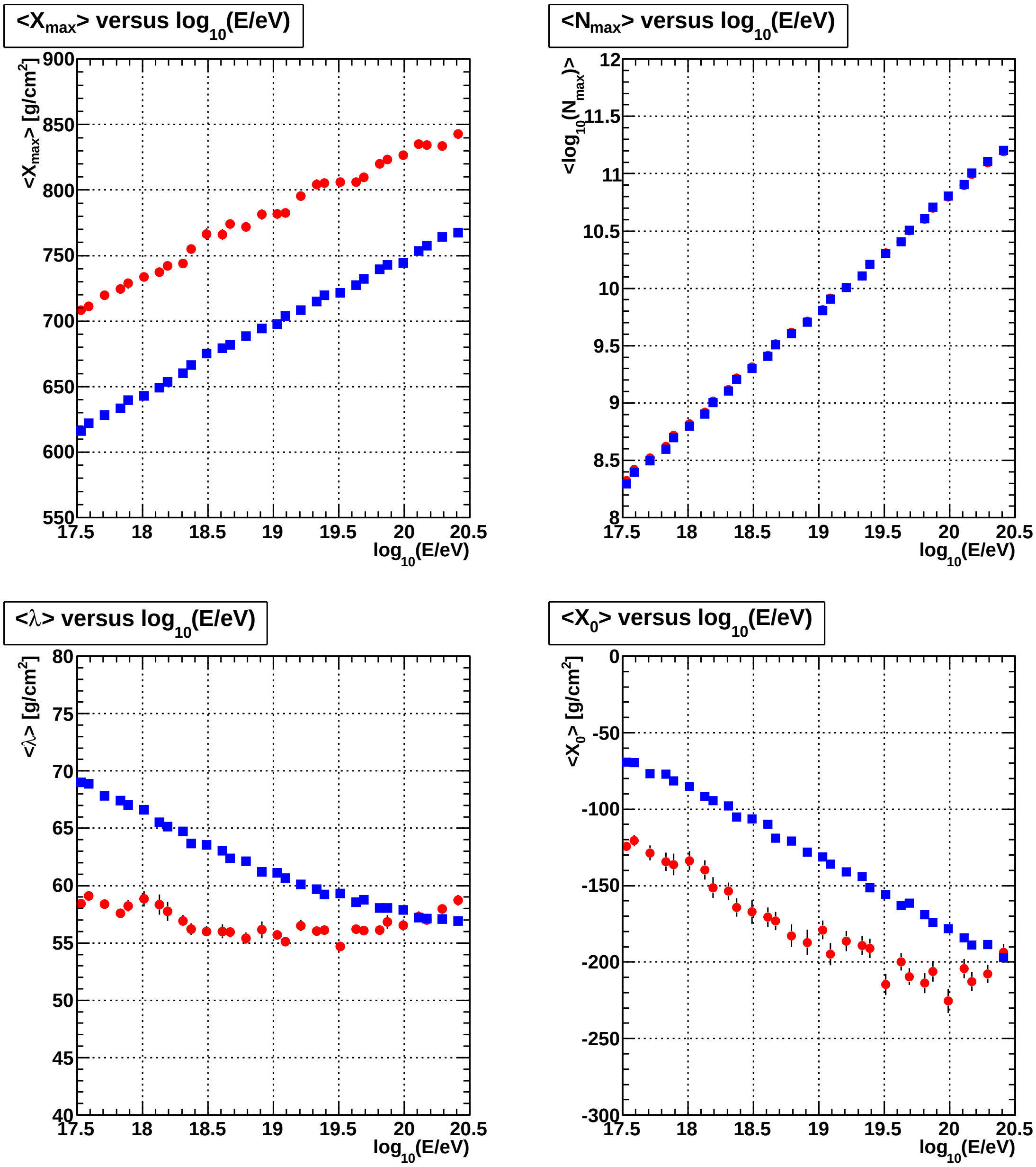

**Figure 4.3**: Mean Gaisser Hillas parameters from CORSIKA simulations.

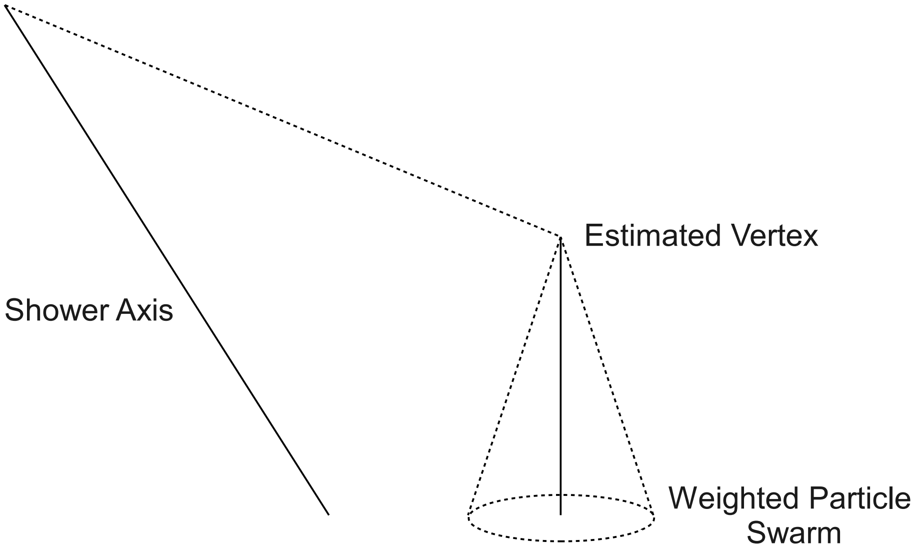

**Figure 4.4**: The basic geometries for distributing weighted particles from thinned CORSIKA showers in the dethinning process. Adapted from [45].

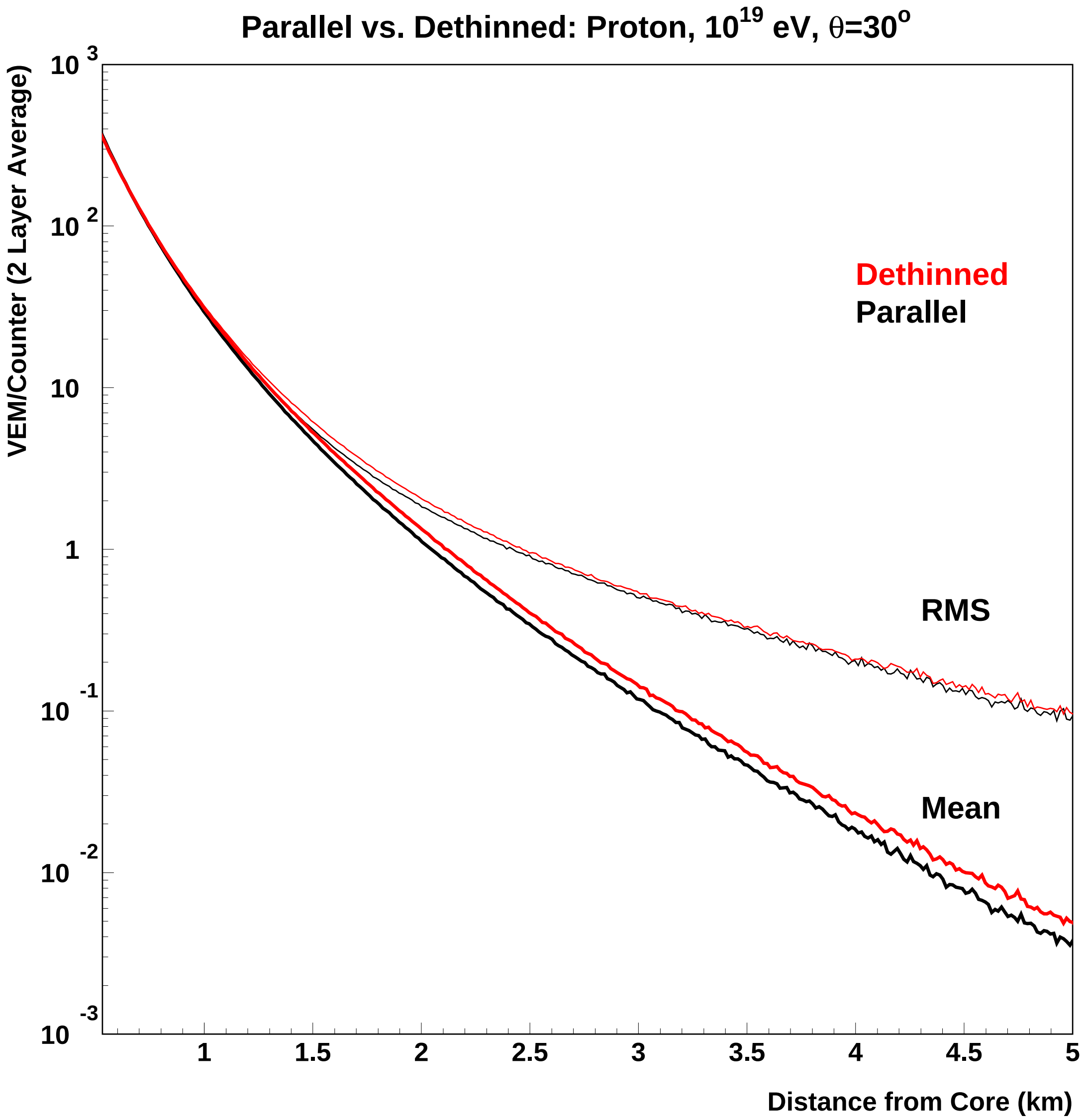

**Figure 4.5**: Lateral distributions of dethinned and unthinned CORSIKA showers using the same initial parameters[46]. Dethinned showers successfully create distributions of particles that match unthinned CORSIKA showers. Reprinted with permission.

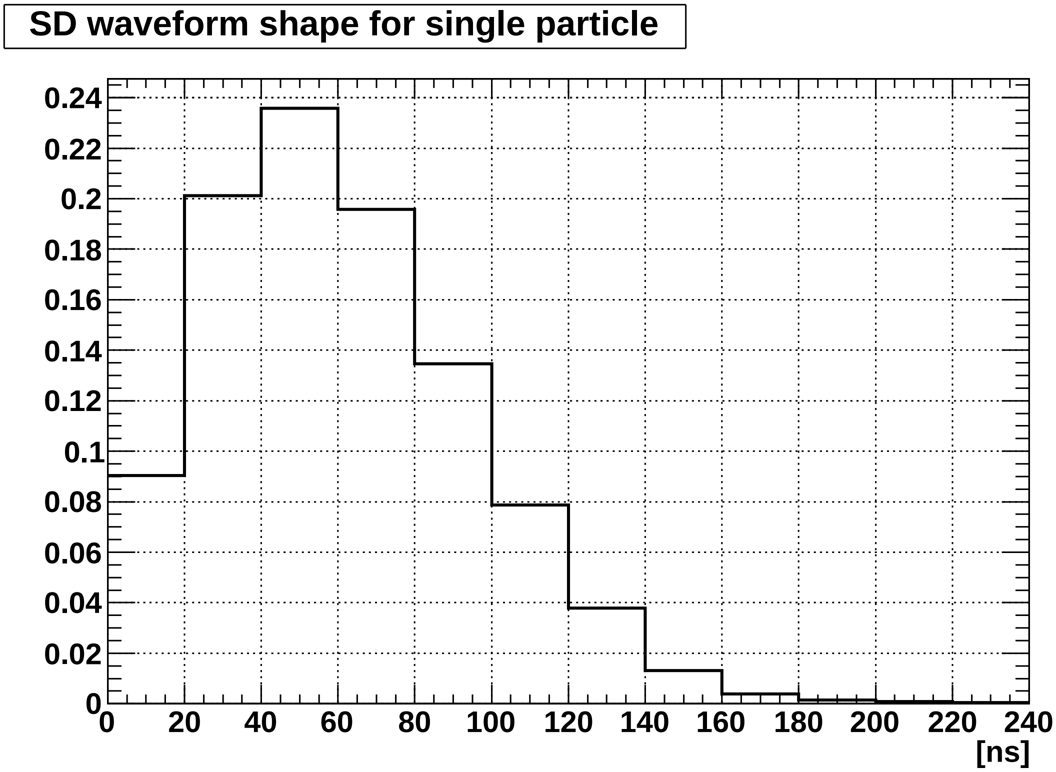

**Figure 4.6**: Basic shape of the SD waveform shown per incident FADC count. Note that the histogram above has 20 ns bins as this is the bin size of the SD FADC waveforms.

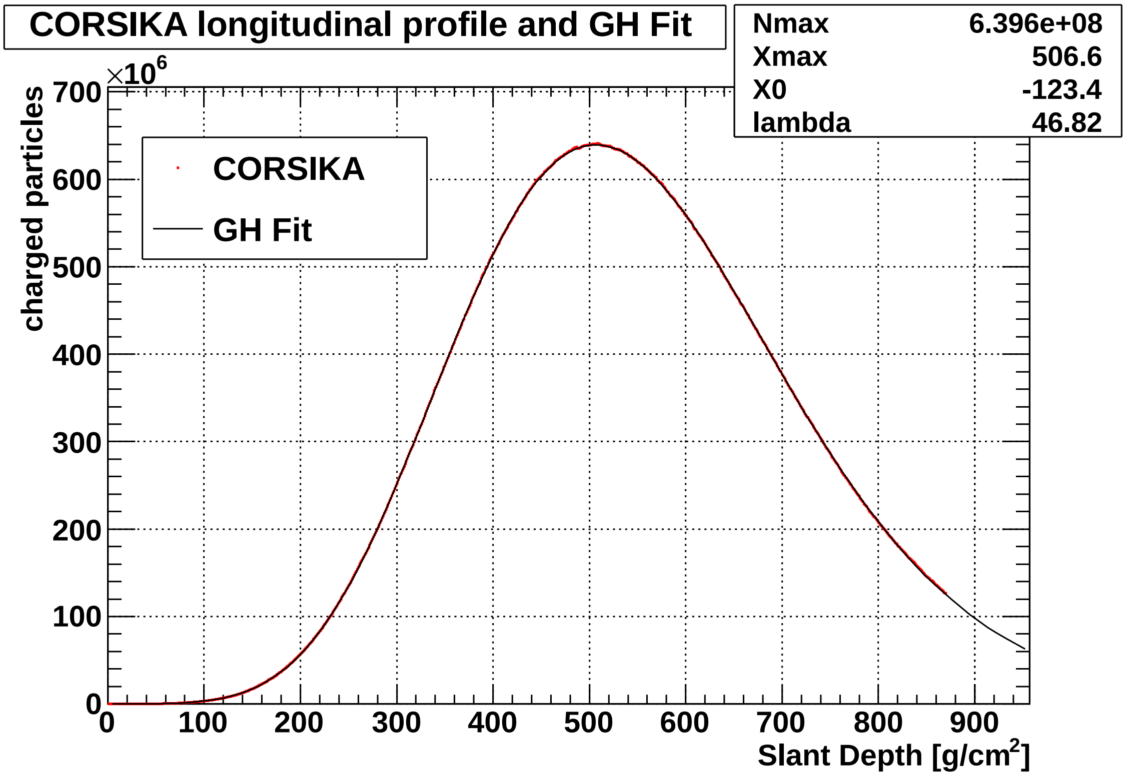

**Figure 4.7**: An example fit of CORSIKA longitudinal distributions fit by Equation 2.10.

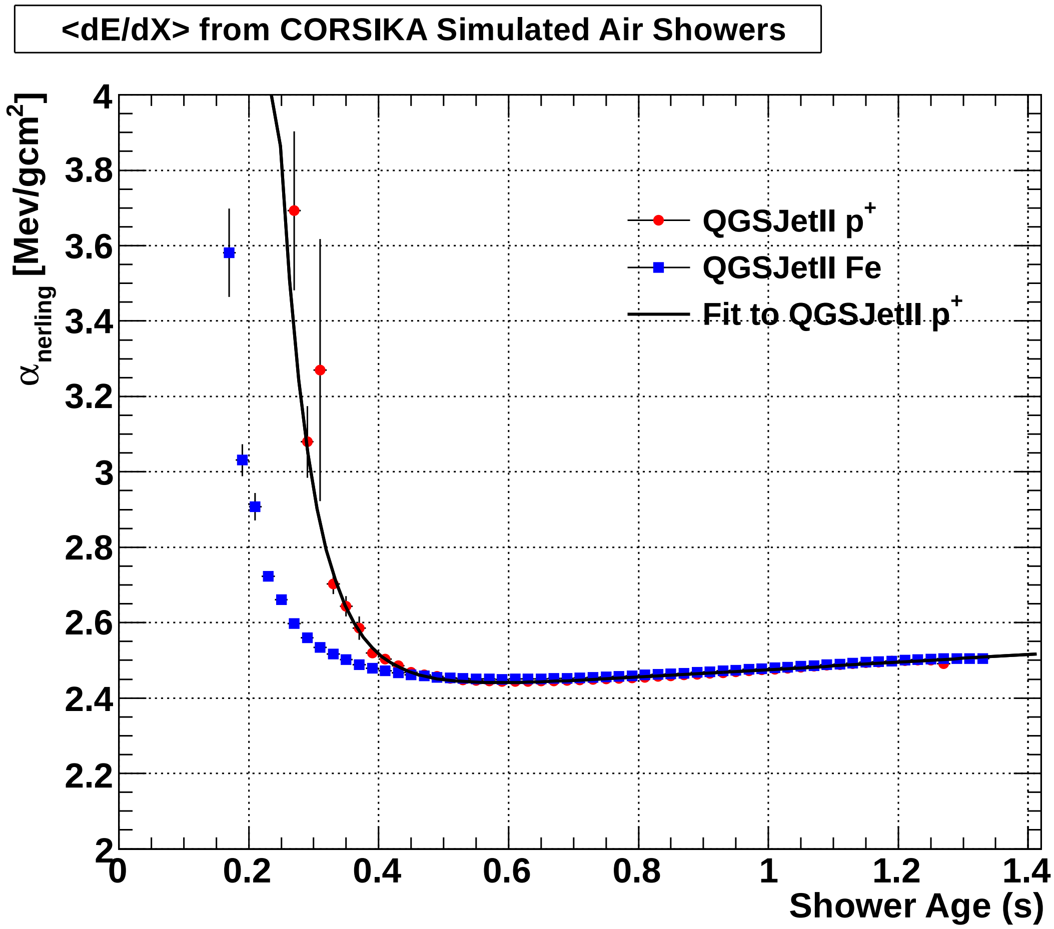

**Figure 4.8**: The energy deposited in CORSIKA air showers per charged particle, $\alpha$ [35]. It is clear that above $s$ equal to 0.4, iron and proton simulations agree for a given set of CORSIKA parameters. The fit was only performed for the proton simulation.

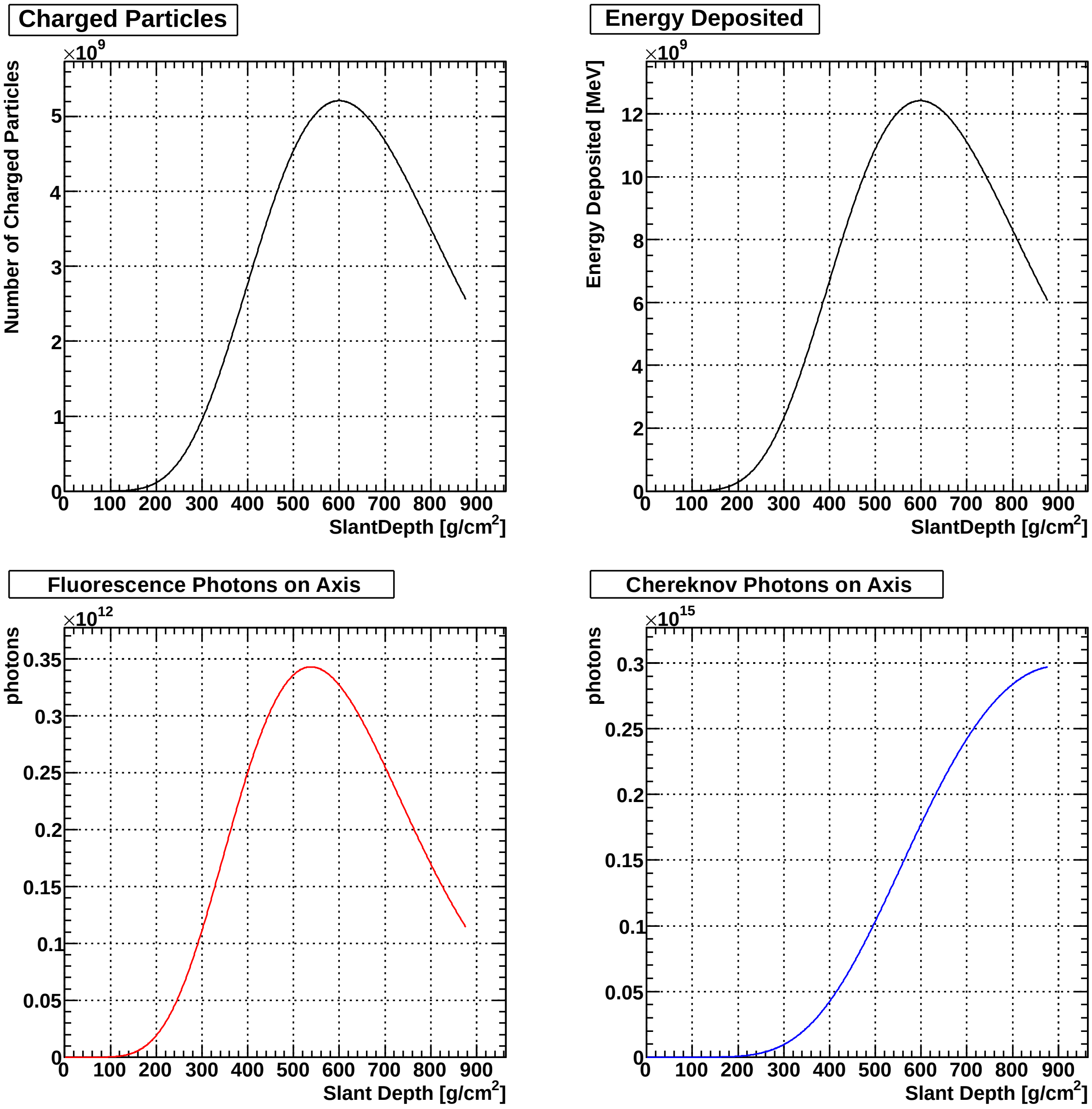

**Figure 4.9**: *Clockwise from upper right:* The number of charged particles, energy deposited, the number of fluorescence photons, and the number of Cherenkov photons generated by the shower generator in the FD simulation for a vertical $10^{19}$ eV cosmic ray with an $X_{max}$ of 600 $g/cm^2$

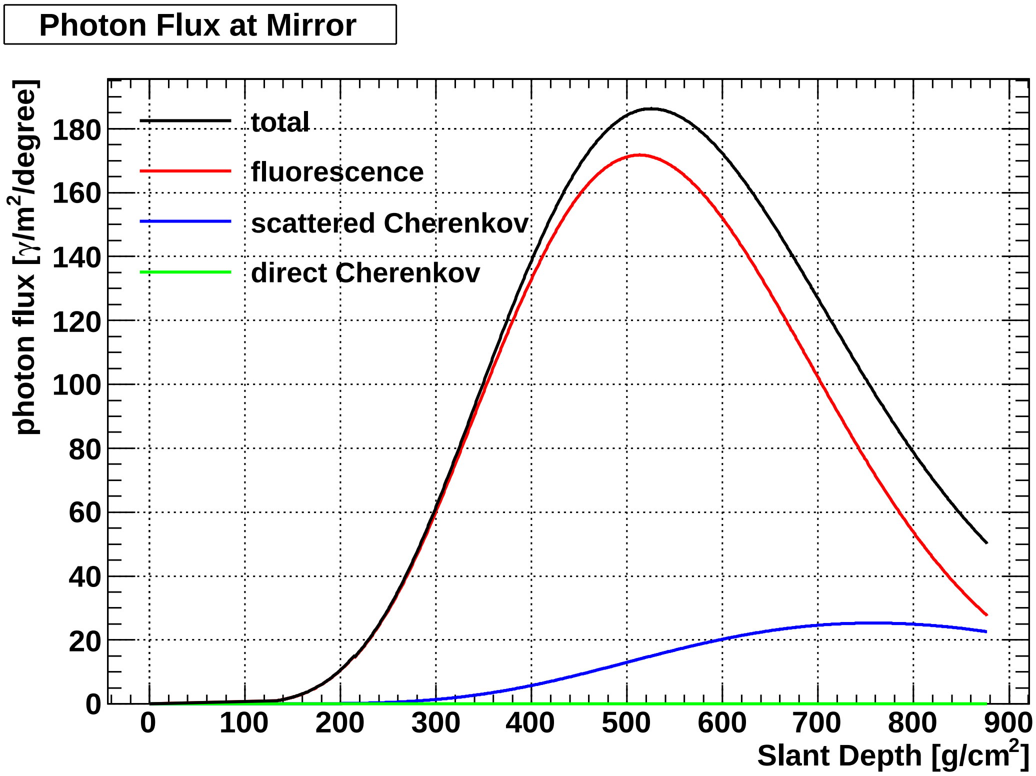

**Figure 4.10**: Photon flux at mirror generated by FD simulation calculated with equation 4.6.

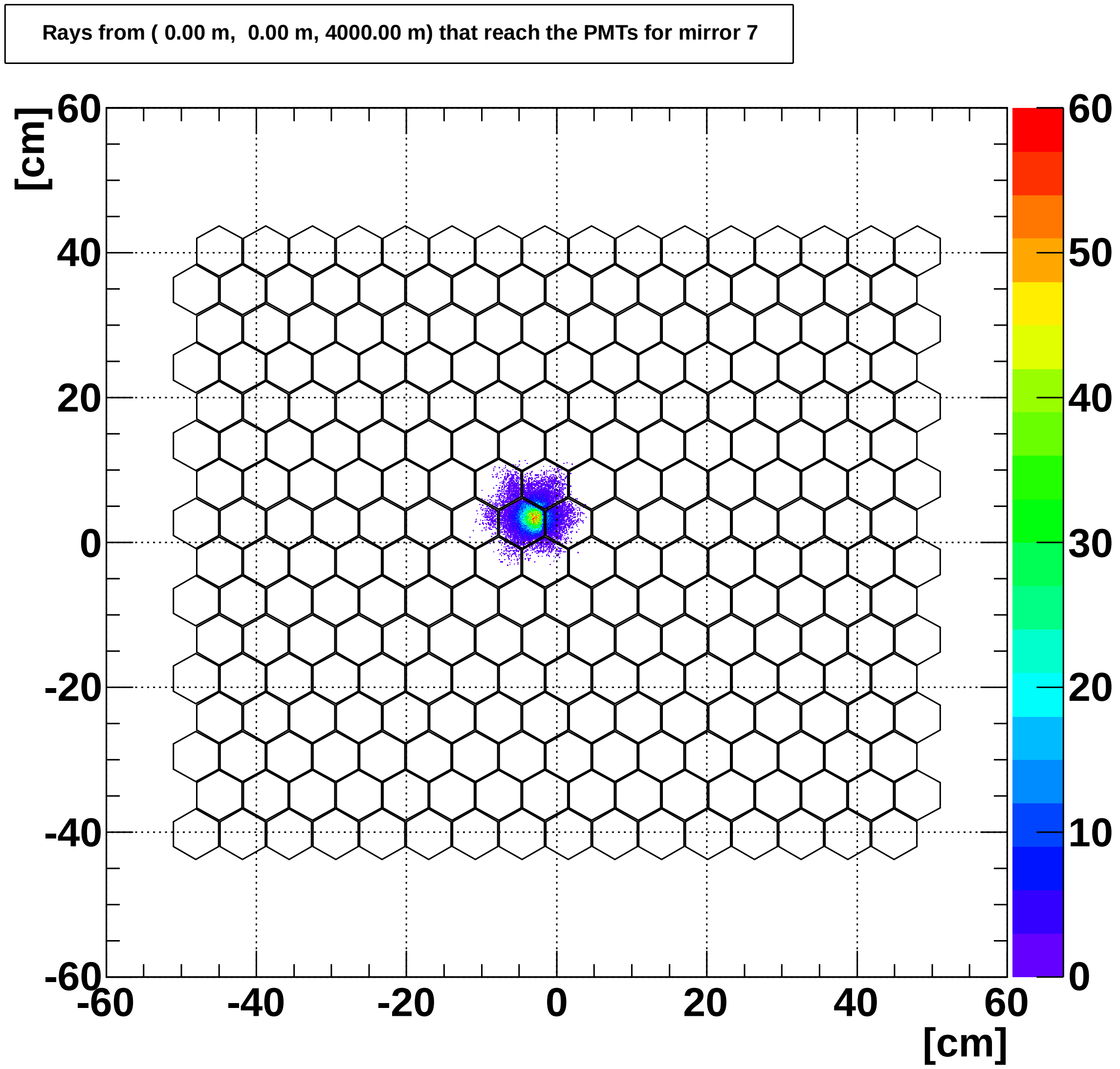

**Figure 4.11**: Photons that successfully reach the PMT cluster from a single point 4 km above the CLF. Photons from this point are directly in the center of the field of view of Black Rock Mesa's mirror 7.

# CHAPTER 5

# EVENT RECONSTRUCTION

This chapter explains in detail the hybrid event reconstruction that is used in this analysis. As this analysis makes use of both SD and FD data, the hybrid event reconstruction is built upon previously developed FD mono and SD event reconstructions. As such, these reconstructions are also discussed.

## 5.1 Mono Geometry Reconstruction

Reconstructing a cosmic ray event with a single FD detector is considered "mono" reconstruction. This is analogous to trying to understand a three-dimensional world from a two-dimensional image. The two dimensions in the plane of the image are well defined; however, there is little information about the depth of the image. In reconstruction presented here, the pointing directions of the triggered PMTs define a plane in which the EAS must have traveled, but PMT timing must be used to discern the depth of the shower axis.

Mono geometry reconstruction is generally done in two steps. First the plane created by the shower track and the FD station is found by the geometry of the triggered PMTs. Then, the PMTs timing is used to determine the "depth" of the cosmic ray track.

### 5.1.1 Tube Selection

Before any reconstruction methods may begin, tubes that are truly part of the event must be identified and kept, while noise tubes must be discarded. The PMT selection described here is that used at the BR and LR detectors.

The first stage of tube selection is to quantify the "brightness" or the number of photo electrons (PE) of all the triggered PMTs with respect to the average night sky background, for which a running average is kept by the BR and LR firmware. PMTs with a signal $8\sigma$ above the average night sky background are immediately kept and PMTs with signals less than $4\sigma$ are immediately discarded.

Next, a quantitative measurement of the topological connectivity is made for the remaining PMTs. The $i^{th}$ PMTs connectivity is quantified as

$$k_i = \sum_{j=0}^{N} \begin{cases} \frac{S_j}{2} e^{-\theta_{ij}/w} & i \neq j \\ S_j & i = j \end{cases} \tag{5.1}$$

where $S_j$ is the signal of the $j^{th}$ PMT, $\theta_{ij}$ is the angle between the $i^{th}$ and $j^{th}$ PMT, and $w$ is an overall scale that is set to 1.36° in this analysis. The tube with the maximum $k_i$ is added to our list of kept PMTs.

Finally, the tubes with signal greater than $4\sigma$ are scanned and are kept if they have an opening angle of less than 1.8° and a trigger time of less than 5 $\mu$s of any tube in the original list. Figure 5.1 shows the before and after effects of this tube selection method.

### 5.1.2 Shower Detector Plane

The first stage in mono geometry reconstruction is to use the pointing directions of triggered PMTs to determine the plane created by the FD and the EAS axis. This basic geometry is shown in shown in Figure 5.2.

A general description of a plane are the points in three space, $\vec{r}$, that satisfy the equation

$$\vec{n} \cdot (\vec{r} - \vec{r_0}) = 0 \tag{5.2}$$

In the case of FD reconstruction, the vector $\vec{n}$ corresponds to the vector normal to the SDP and the vector $\vec{r_0}$ corresponds to the position of the FD. The vector $\vec{n}$ may be found by finding the vector most normal to all the PMT pointing directions that are part of the event. Writing this as a $\chi^2$ function

$$\chi^2 = \sum_{i=0}^{N} \vec{n} \cdot \vec{t_i} w_i \tag{5.3}$$

where $t_i$ is the three-dimensional pointing direction of the $i^{th}$ PMT and $w_i$ is a weighting proportional to the number of PE seen in the $i^{th}$ PMT. With the requirement that

$$|\vec{n}| = 1 \tag{5.4}$$

the minimum of Equation 5.3 will correspond to the solution for the SDP for a given event. The bottom half of Figure 5.1, shows a mirror display and the projection of the reconstructed SDP along the field of view of the Black Rock Mesa FD.

### 5.1.3 Mono Timing Fit

The SDP only constrains the shower geometry to two-dimensional space. In the case of mono reconstruction, PMT timing must be used to reconstruct information about the position of the EAS in that space.

Figure 5.3 illustrates the basic geometry of the EAS in the SDP. In this two-dimensional picture, the shower geometry is completely determined by three parameters: $R_p$, the distance of closest approach to the FD, $\psi$, the angle created by the EAS track in the SDP as it intersects with the ground, and $t_0$, the time that the EAS passes through the point of closest approach.

Also shown in Figure 5.3, is the viewing angle of the FD at a given point on the shower track, denoted $\chi_i$. In practice, the viewing point will be given by the geometry of a single PMT and so $\chi$ becomes a discrete variable. An additional point of interest is that the angle $\psi$ is less than $\pi/2$ when the EAS is traveling away from the FD and greater than $\pi/2$ when the EAS is traveling towards the FD.

Given that an EAS travels through the atmosphere near the speed of light, $c$, the time an EAS travels from the distance of closest approach to the angle $\chi_i$ is

$$\frac{R_p}{c}\frac{1}{\tan(\pi - \psi - \chi_i)} \tag{5.5}$$

Note that this term is negative when $\psi - \chi_i$ is less than $\pi$. The time for the light to travel from the point where the FD observes the EAS to the FD detector itself is

$$\frac{R_p}{c}\frac{1}{\sin(\pi - \psi - \chi_i)} \tag{5.6}$$

Bringing these two terms together and applying a trigonometric identity, the PMT trigger time is

$$t_i = t_0 + \frac{R_p}{c}\tan\left(\frac{\pi - \psi - \chi_i}{2}\right) \tag{5.7}$$

A $\chi^2$ may be built by including all of the PMTs that pass the selection criteria

$$\chi^2 = \sum_{i=0}^{N}\frac{1}{\sigma_i}\left(t_i - t_0 + \frac{R_p}{c}\tan\left(\frac{\pi - \psi - \chi_i}{2}\right)\right) \tag{5.8}$$

Here, $t_i$, is the time that the $i^{th}$ PMT triggered and the $\sigma_i$ is the uncertainty in that measurement. In the analysis that is presented here, $\sigma$ is calculated as the RMS of the PMT signal. An example of the time versus angle fit is found in Figure 5.4.

## 5.2 SD Geometry Reconstruction

The SD reconstruction is also an important part of understanding hybrid geometry reconstruction. It provides the selection criteria for good SDs as well the treatment of SD waveforms.

### 5.2.1 Treatment of SD Waveforms

Like the FADC digitized waveforms in the FD, the SD waveforms need to be processed to provide two key pieces of information, the time of the triggered SD and the total signal that was seen in the SD.

To obtain a consistent and reliable timing measurement the leading edge is chosen to represent the timing of a given SD[28]. To find this point, the first and second derivatives are calculated in each bin and the first bin that reveals an inflection point is chosen to represent the trigger time of the SD. Figure 5.5 shows an example of a SD waveform and the calculated trigger time.

The signal seen in a given SD is calculated from the integrated number of FADC counts above pedestal. The “1 MIP” calibration discussed in Section 3.1.2 provides the conversion from FADC counts to number of charged particles passing through an individual SD. Figure 5.6 shows the signal calculated from a sample waveform.

### 5.2.2 Moments of SD Signal

With the number of charged particles passing through each SD determined, the first analysis stage is to calculate the moments of SD counters weighted by their charge. The first moment, or the the center of the number of charged particles that have passed through the SD counters, gives the first estimate of the EAS core location and is generally quite close to the final reconstructed values[28]. The first moment is calculated as

$$\vec{R}_{cm} = \frac{1}{S}\sum_{i=0}^{N} s_i \vec{r_i} \tag{5.9}$$

where $\vec{R}_{cm}$ is the center of charge, $s_i$ is the signal in the $i^{th}$ counter, and $\vec{r}_i$ is the position of the $i^{th}$ counter. $S$ is the total signal in the event,

$$S = \sum_{i=0}^{N} s_i \tag{5.10}$$

The second order moments are also calculated and allow us to solve for the principal axis' of the SD event. The principal axis give the earliest indication of the direction of the that the EAS was traveling along. Figure 5.7 shows an SD display showing the center of charge and principal axis.

### 5.2.3 SD Timing Fit

To model the timing of the SD counters, recall that the particles in an EAS exists in a thin "pancake" traveling near the speed of light. Close to the shower axis, this pancake is planar. However, away from the shower axis, particles are delayed with respect to the theoretical planar shower front. Additionally, the fluctuations of particle arrival times increases away from the shower axis. Figure 5.8 shows an EAS including shower front curvature, $t_d$, and shower width, $t_s$. In this study, $t_d$ and $t_s$ are parametrized as

$$t_d = (0.8\,\mathrm{ns})\,a\left(1+\frac{r}{30m}\right)^{1.5}\left(\frac{\rho}{\mathrm{VEM/m^2}}\right)^{-0.5} \tag{5.11}$$

and

$$t_s = (0.6\,\mathrm{ns})\,a\left(1+\frac{r}{30m}\right)^{1.5}\left(\frac{\rho}{\mathrm{VEM/m^2}}\right)\rho^{-0.3} \tag{5.12}$$

In Equations 5.11 and 5.12, $r$ is the distance from the shower axis and $\rho$ is the density of particles in the shower. In practice, $rho$ is measured by the number of particles found to be passing through a given surface detector and is measured in Verticle Equivalent Muons(VEM).

These were first derived by Linsley but were also used by the AGASA[51, 32]. Here $r$ is the distance perpendicular to the shower axis, and $\rho$ is the density of particles in the shower. In this work, the unit-less parameter $a$, is varied slightly from Linsley to better represent TA data[28]. The parameter $a$ used here has some dependence on the zenith angle, $\theta$.

$$a(\theta) = \begin{cases} A_1 + A_2\theta & \theta < 25.0^\circ \\ B_1(\theta + B_2)(\theta^2 + B_3\theta + B_4) & 25.0^\circ \leq \theta < 35.0^\circ \\ e^{C_1 + C_2\theta} & \theta > 35.0^\circ \end{cases} \tag{5.13}$$

The parameters used above are found in Table 5.1.

Examining Figure 5.8 and allowing the time an EAS reaches the ground to be $t_c$, the time that shower front plane reaches an SD counter would be

$$t_p = t_c - \frac{1}{c}\sqrt{d^2 - r^2} \tag{5.14}$$

where $r$ is the distance of closest approach between the SD and the EAS and $d$ is the distance between the shower core and the SD.

A $\chi^2$ function may be developed for fitting the shower parameters, $x_c$, $y_c$, $\theta$, $\phi$, and $t_c$. For the $i^{th}$ SD, the modeled trigger time is

$$f(x_c, y_c, \theta, \phi, t_c; \vec{r_i}) = t_p + t_d \tag{5.15}$$

where $\vec{r_i}$ is the 3 vector position of the $i^{th}$ SD counter.

$$\chi^2 = \sum_{i=0}^{N} \frac{(t_i - f(x_c, y_c, \theta, \phi, t_c; \vec{r_i}))}{t_s^2} \tag{5.16}$$

The uncertainty of the trigger time of an SD will be dominated by the width of the the EAS from Equation 5.12, so $\sigma$ is set to $t_s$ for each SD.

**Table 5.1**: Parameters for shower curvature functions used in $a(\theta)$ in Equations 5.12 and 5.11. The parameters in this table assume that $\theta$ is measured in degrees.

| | |
|---|---|
| $A_1$ | 3.3836 |
| $A_2$ | -0.01848 |
| $B_1$ | $6.511 \times 10^{-5}$ |
| $B_2$ | 0.2615 |
| $B_3$ | -134.7902 |
| $B_4$ | 4558.524 |
| $C_1$ | $-3.2 \times 10^{-2}$ |
| $C_2$ | 2.0 |

## 5.3 Hybrid Geometry Reconstruction

A hybrid reconstruction combines data from both FD and SD detectors, strongly constraining the EAS geometry. The hybrid reconstruction presented here uses four basic pieces of data to constrain the reconstructed EAS geometry. They are the pointing directions of triggered FD tubes, the trigger times of the FD tubes, the trigger times of the SD tubes, and the geometric center of charge of the SD counters. Each of these pieces of data has been discussed in the above sections as well as its use in FD mono or SD reconstructions. Each of these pieces of data provides a $\chi^2$ term. This results in a four component $\chi^2$ function that uses all the available information from both the FD and SD detectors.

$$\chi^2 = \chi^2_{SDP} + \chi^2_{COC} + \chi^2_{SD} + \chi^2_{FD} \tag{5.17}$$

This function is minimized with respect to the shower parameters $x_c$, $y_c$, $\theta$, $\phi$, and $t_c$, with $x_c$ and $y_c$ being the shower core location, $\theta$ and $\phi$ being the shower zenith and azimuthal angles, and $t_c$ being the time that the shower reaches the ground.

The term $\chi^2_{SDP}$ is the same $\chi^2$ function that was discussed in Section 5.1.2 and is shown in Equation 5.3.

The term $\chi^2_{COC}$ is a single data point, but helps to ensures that the fitter does not stray from the shower core. This may be written as

$$\chi^2_{COC} = \left( \frac{(x_c - R_{cmx})^2 + (y_c - R_{cmy})^2}{\sigma^2_{coc}} \right) \tag{5.18}$$

using the solution for center of charge found in Equation 5.9.

The FD timing is represented by the term $\chi^2_{FD}$ and is same as the timing $\chi^2$ function used in FD mono reconstruction. This is discussed in detail in Section 5.1.3 and found in Equation 5.8.

Lastly, the SD timing information is included, which is represented in Equation 5.17 as the $\chi^2_{SD}$ component. The SD timing is calculated from the point of view of the FD detector, which allows for the SD timing to be modeled with the same function as the FD timing, using Equation 5.5. Figure 5.9 shows the basic geometries involved in viewing the SD data from the point of view of the FD. First, the time that the planar shower front passes through the SD is calculated using Equation 5.14. Then, the time required for light from the shower axis to reach the FD station is included. In Figure 5.9, this is the distance between the point $t_i$ and the FD station. This term is analogous to the Equation 5.6 in mono FD reconstruction. Lastly, the shower curvature, $t_d$ is included from Equation 5.11 is included.

Now $\chi^2_{SD}$ may be written in the same form as the timing fit from FD mono analysis 5.5.

$$\chi^2_{SD} = \sum_{i=0}^{N} \frac{(t_i - f(t_0, R_p, \psi; \chi_i))^2}{t_s^2} \tag{5.19}$$

where $f(t_0, R_p, \psi; \chi_i)$ is the fit equation in Equation 5.5. $t_s$ is theoretical width of the distribution of particle arrival times given in Equation 5.12.

Figure 5.10 shows the SD and FD time measurements with the expected times resulting from the hybrid reconstruction. Figure 5.11 shows trigger SD counters and the reconstructed core and SDP.

## 5.4 Profile Reconstruction

Reconstructing the longitudinal profile using the FD data provides the energy of the primary cosmic ray and $N_{max}$ and $X_{max}$ of the resulting EAS. In Section 2.3, it was shown that the nitrogen fluorescence produced by the EAS is proportional to the number of charged particles in the shower at any point in the EAS development. However, the modeling the number of photons that reach the FD mirrors and thus the PMT response requires knowledge of the EAS geometry. The FD simulation discussed in Section 4.4 provides a basis for an inverse Monte Carlo reconstruction, finding the GH function that best reproduces the observed event. In the reconstruction described here, only $X_{max}$ and $N_{max}$ are varied, the parameters $\lambda$ and $X_0$ are fixed to 70 g/cm$^2$ and -60 g/cm$^2$ respectively.

For a given event, a geometry reconstruction is chosen depending on the goal of the analysis. This may be mono, discussed in Section 5.1, hybrid, discussed in Section 5.3, or a stereo reconstruction. As this work presents a hybrid analysis, the hybrid geometry reconstruction presented in Section 5.3 will be used. However, the profile reconstruction discussed here does not directly depend on any method of reconstructing the air shower geometry.

Using the FD simulation described in Section 4.4, an air shower is generated using the chosen reconstructed geometry. To begin the fitting process, an $X_{max}$ of 750 g/cm$^2$ and $N_{max}$ of $8 \times 10^8$ is chosen. This initial air shower allows for the calculation of the percentage of light that reflects from a mirror results in photo-electrons (PE) produced at the PMTs. This quantity, called the "tube acceptance", accounts for any optical obstructions or irregularities that may be part of the FD itself. The tube acceptance, $A_i$, may be written as

$$A_i = n_i/N_i \tag{5.20}$$

where $n_i$ is the number of photons that successfully create photo electrons in the $i^{th}$ PMT and $N_i$ is the number of trials. The number of thrown photons, $N_i$, will vary depending on the photon flux at the point in the shower where the $i_{th}$ PMT is looking.

The acceptance depends slightly on $X_{max}$ and $N_{max}$ due to the lateral spread of shower which is described by the NKG function in Equation 2.13. Because of this the acceptance calculation may be performed more than once in the fitting process. In this way, the calculation of the acceptance is an iterative process which converges as $X_{max}$ and $N_{max}$ are fit.

The actual data quantity that is fit is the number of photo electrons in each tube. This is calculated simply by

$$n_{pei} = \sum_{t_0}^{t_f} \frac{S_i - B_i}{G_i} \tag{5.21}$$

where $S_i$ is the raw FADC output, $B_i$ is the pedestal, and $G_i$ is the PMT gain. $t_0$ and $t_f$ are the limits of the signal in the FADC waveform. As a minimization routine searches $N_{max}$ and $X_{max}$ space, the photon flux is calculated in the same way as was seen in Figure 4.6. The $\chi^2$ function used for minimization is

$$\chi^2(N_{max}, X_{max}) = \sum_{i}^{N} \frac{(n_i - A_i \Phi_i(N_{max}, X_{max}))^2}{\sigma_i^2} \tag{5.22}$$

where $f(N_{max}, N_{max}; i)$ is the simulated number of PE in the the $i^{th}$ PMT and $\sigma_i$ is the Poissonian uncertainty in $n_{pei}$. $\sigma_i$ includes the Poissonian uncertainty in the number of PE, the night sky background, as well as the binomial uncertainty in the tube acceptance. $\sigma_i^2$ is found as

$$\sigma_i^2 = \sqrt{n_i} + \Phi_i \left( \frac{A_i(1 - A_i)}{N_i} \right) + < N_{nsbg} > \tag{5.23}$$

where $N_i$ is the number of thrown photons for the $i_{th}$ tube and $< N_{nsbg} >$ is the average PE due to night sky background.

Figures 5.12 and 5.13 show the reconstructed photon on flux and longitudinal profile for a hybrid event recorded on January $27^{th}$, 2010, at 09:49:50.015198. The photon acceptance for this event is found in Figure 5.14.

The total energy deposited in the atmosphere is found by the combination of the number of charged particles and the average energy deposited per charged particle that was obtained in CORSIKA, summarized as the function $\alpha(s)$ discussed in Section 4.4. This calculation is done by performing the convolution of the reconstructed GH function and Equation 4.3.

$$E_{dep} = \int\limits_{0}^{2000\,\mathrm{g/cm^2}} f_{gh}(X)\alpha(s)dX \tag{5.24}$$

where $f_{gh}(X)$ is the GH function from Equation 2.10 and $\alpha(s)$ is Equation 4.3. Recall, that $X$ and $s$ are different parameters of the development of the EAS in the atmosphere, so the coordinate transformation in Equation 4.4 will have to be applied to one of these functions. The upper limit in the integral in Equation 5.24 is somewhat arbitrary, but should reflect a slant depth that is larger than is possible to observe with the TA detector.

## 5.5 Missing Energy Correction

When a cosmic ray interacts in the atmosphere, some particles are produced that do not result in photons produced by scintillation. These particles are thus undetectable using the fluorescence method. These generally consist of neutrinos that pass through the entire atmosphere before interacting or muons which deposit their energy underground[41]. This “missing energy” means that the reconstructed energy resulting from a longitudinal shower profile and Equation 5.24 will be systematically lower than the true primary energy[32].

CORSIKA simulations are used to understand the missing energy. For an individual shower, the calorimetric energy is calculated in the same way as was described for profile reconstruction, using Equation 5.24. This requires fitting a GH function to the CORSIKA shower as well as the earlier calculation for mean $dE/dX$, shown in Equation 4.3. Then, the total calorimetric energy is compared to the original primary energy. Figure 5.15 shows the average ratio of calorimetric energy to primary energy for proton and Fe induced air showers.

Figure 5.15 shows that the missing energy is a function of primary energy and depends strongly on the primary nuclei. Air shower events that are reconstructed using the fluorescence must have a correction for this missing energy applied. However, the missing energy for protons is 4% smaller than for iron.

The difference in missing energy between proton and iron air showers presents a difficulty in event reconstruction. Only one reconstruction may be used for both data and MC. Here, the proton missing energy is used to correct the data as well as both proton and iron MC. Because of this choice, it is expected that the iron MC will reconstruct 4% lower in energy than a corresponding proton induced air shower. The results of this difference are discussed in Section 6.5.

Air shower simulations using the CORSIKA software package and discussed in Section 4.1 allow for the calculation of the missing energy effect. As discussed earlier, the longitudinal distributions of charged particles from the simulated air showers are fit the the Gaisser Hillas function. The integral described in Equation 5.24 is performed and compared to the primary cosmic ray energy. The missing energy correction used in reconstruction is the average ratio of these energies using over many CORSIKA simulations.

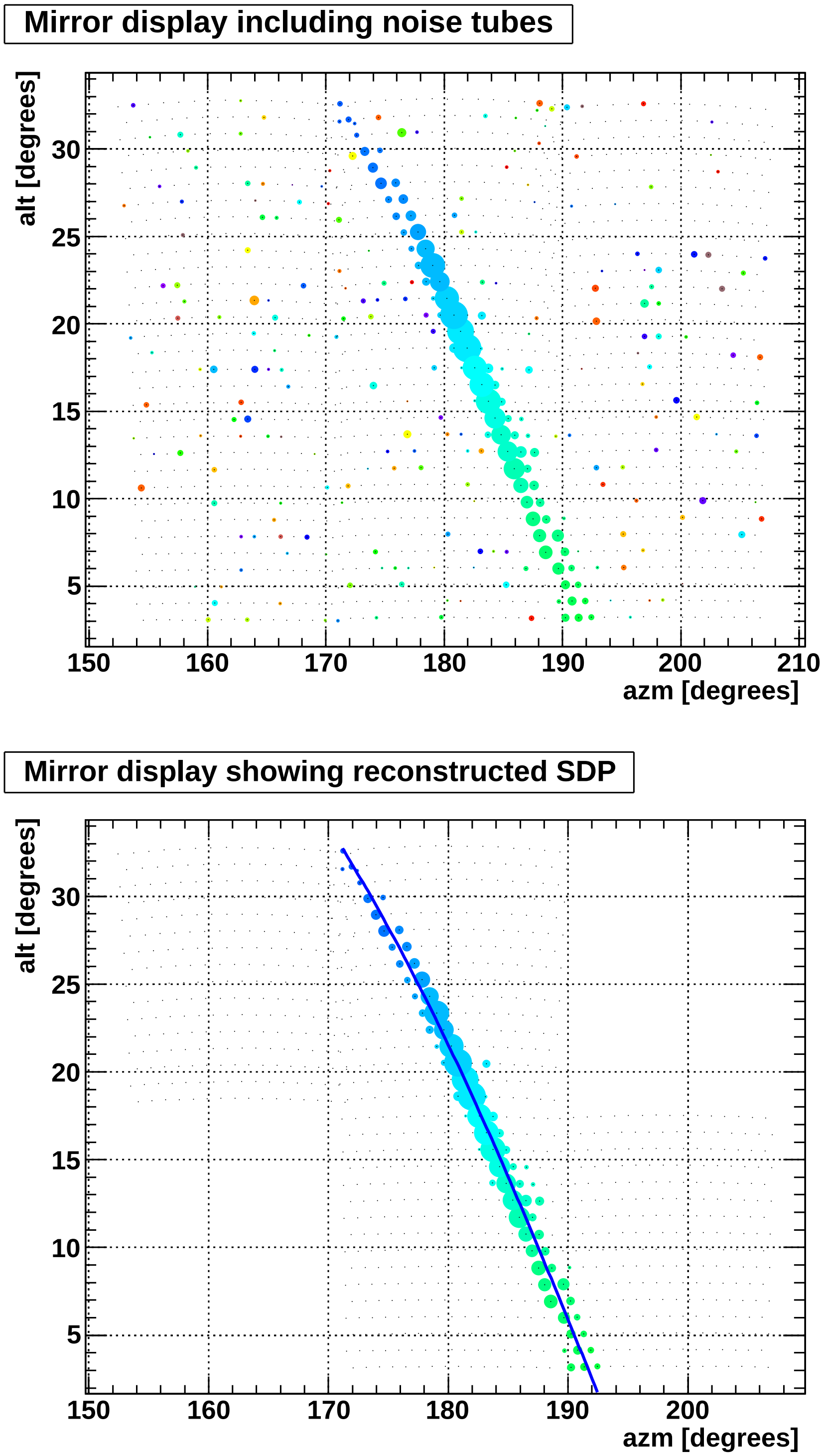

**Figure 5.1**: *top* Mirror display before the tube selection described in Section 5.1.1 is applied. *bottom* Mirror display with tube selection applied and reconstructed shower SDP projected over the triggered PMTs

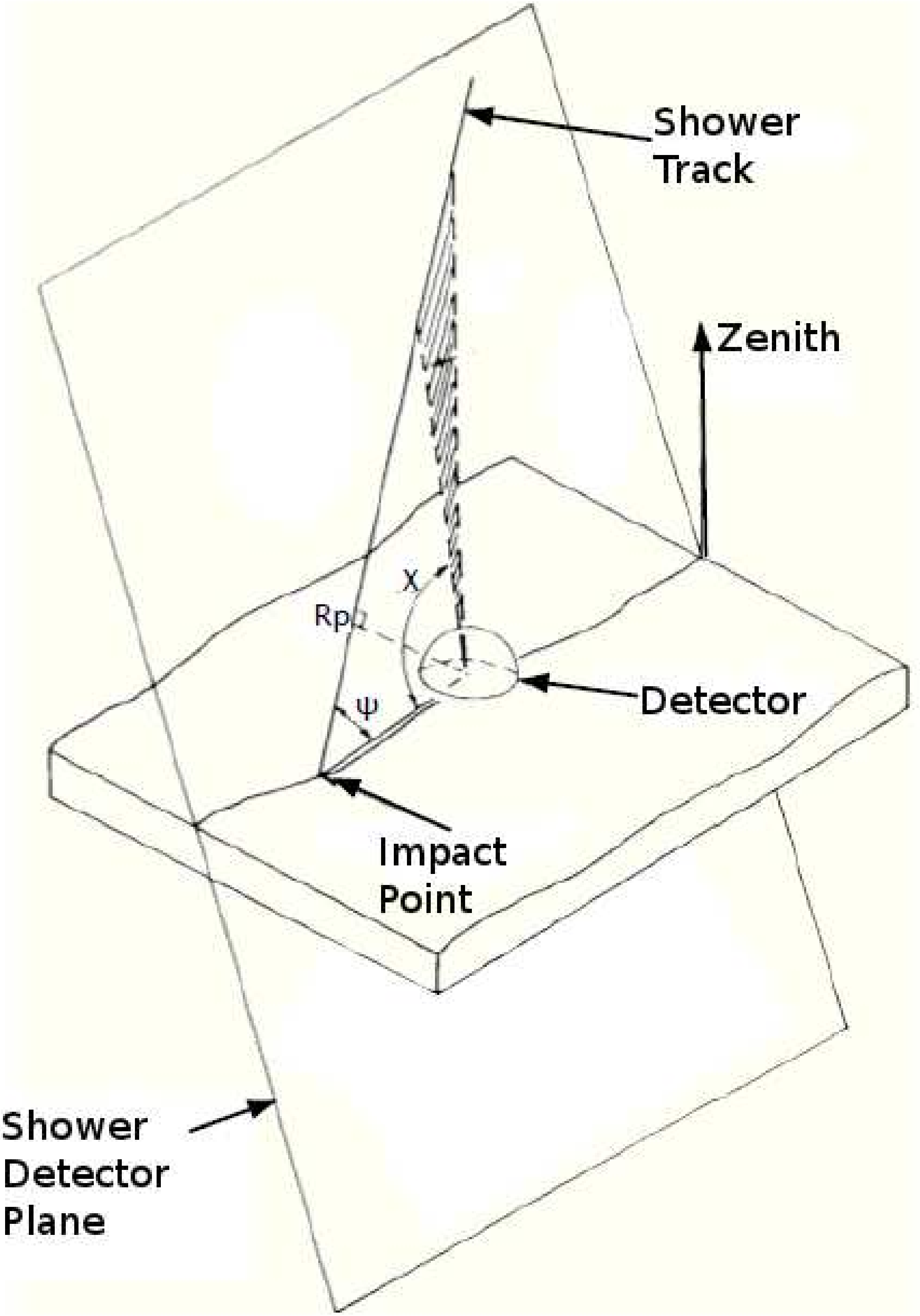

**Figure 5.2**: Geometries of Shower Detector Plane (SDP). Adapted from [41].

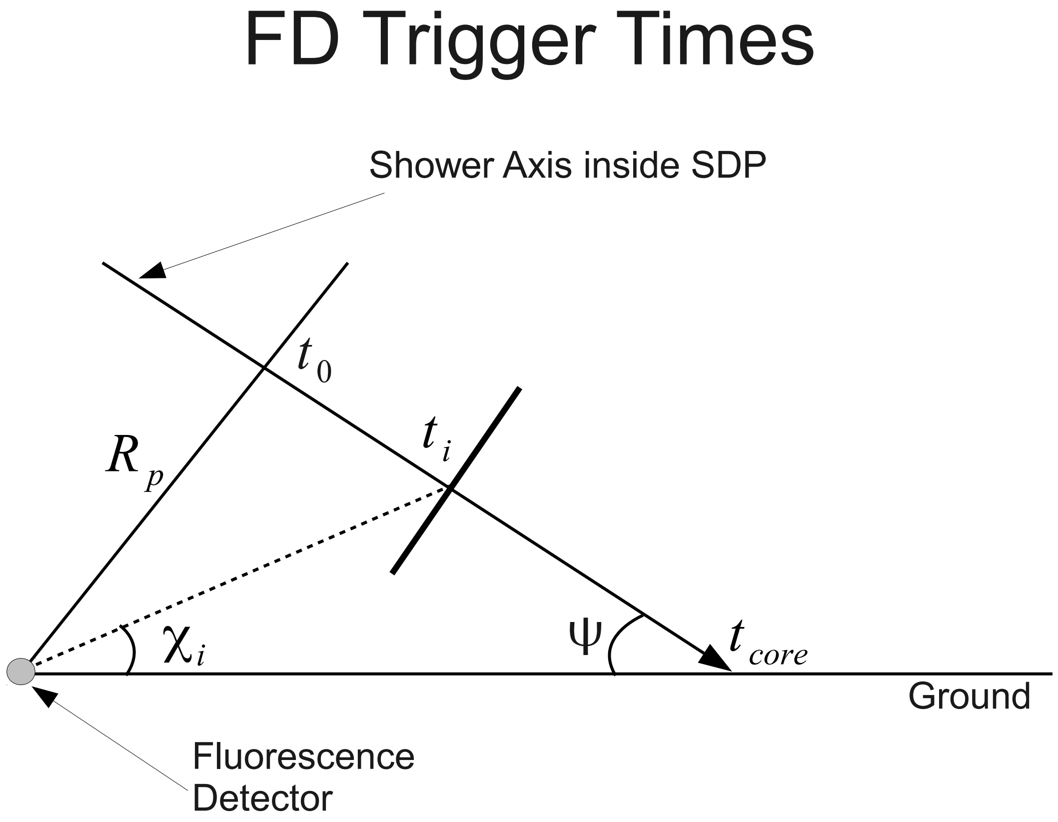

**Figure 5.3**: Diagram of the EAS geometry inside the shower detector plane, showing the three fit parameters $R_p$, $\psi$, and $t_0$.

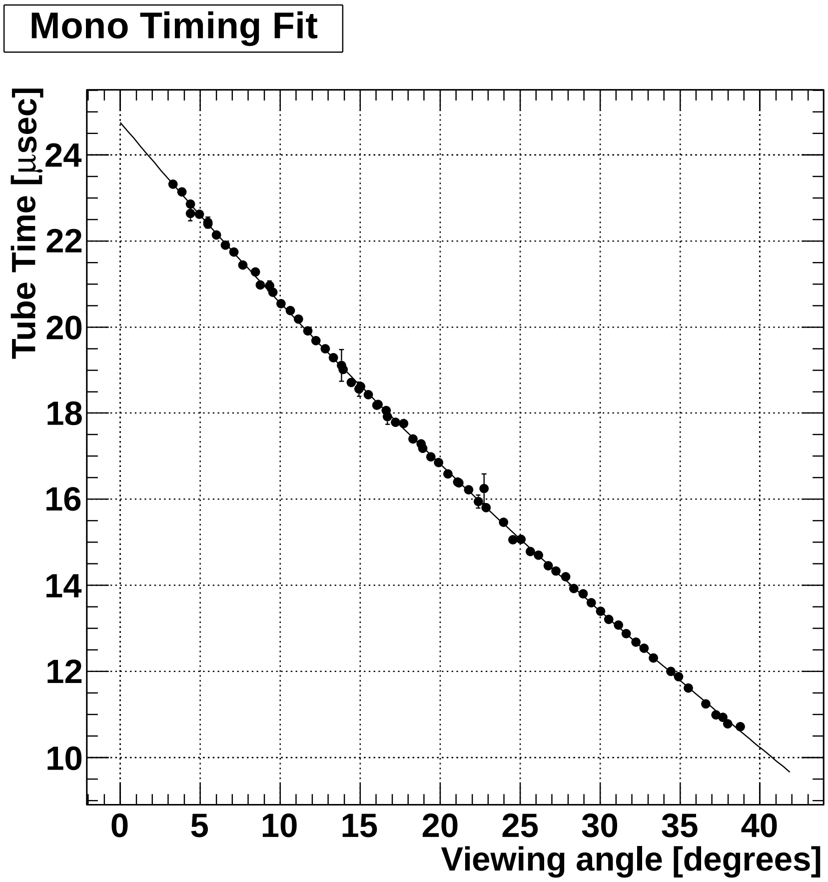

**Figure 5.4**: FD Mono time versus angle fit. The y-axis shows the time after the start of the event that an FD PMT triggered. The x-axis shows the viewing of a FD PMT as defined in Figure 5.3. The line is best fit using the $\chi^2$ function in Equation 5.8.

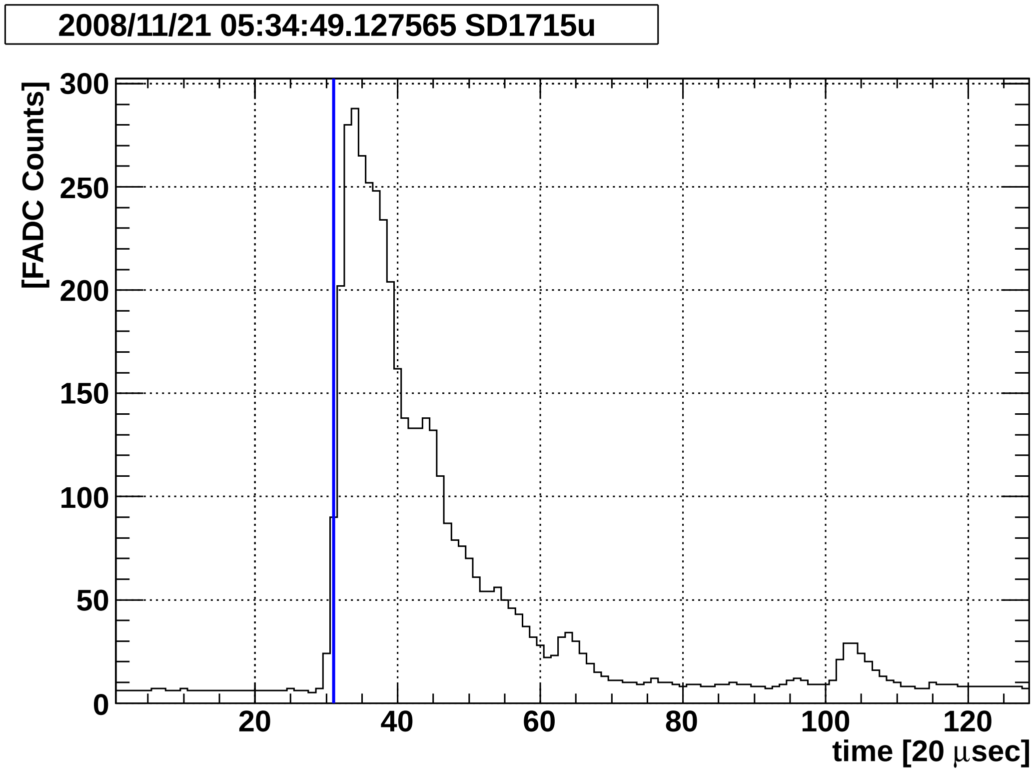

**Figure 5.5**: Surface detector waveform showing the bin used for SD timing in surface detector and hybrid analysis.

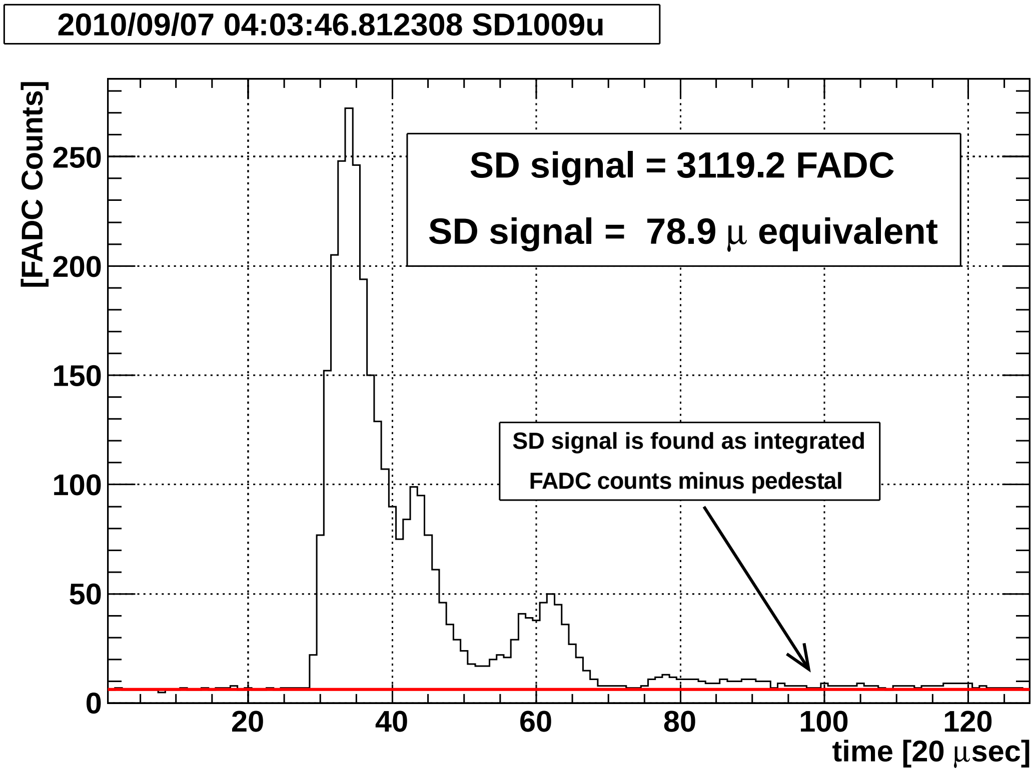

**Figure 5.6**: The signal for a SD waveform is found as the integrated number FADC counts minus the pedestal. The integrated FADC counts is converted to number of charged particles by the "1 MIP" calibration quantity detailed in Section 3.1.2.

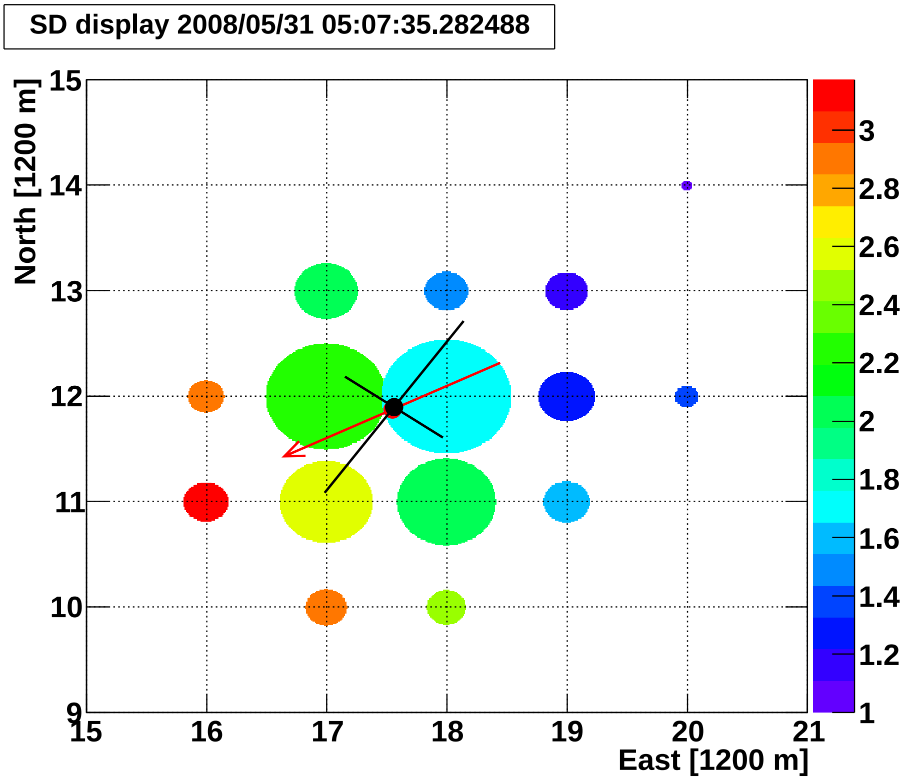

**Figure 5.7**: SD event display showing the trigger time and the number of charged particles triggered in an SD event. The log of number of charged particles is proportional to the size of the circle centered around each triggered SD, and the SD trigger time is shown by the circles color. The trigger times are shown in units of 1200 $m/c$ and are with respect to the earliest triggered counter. The center of charge is shown as the black circle and the principle axises of the distribution of charge are shown by the black lines. The red arrow shows the direction of the final reconstructed event.

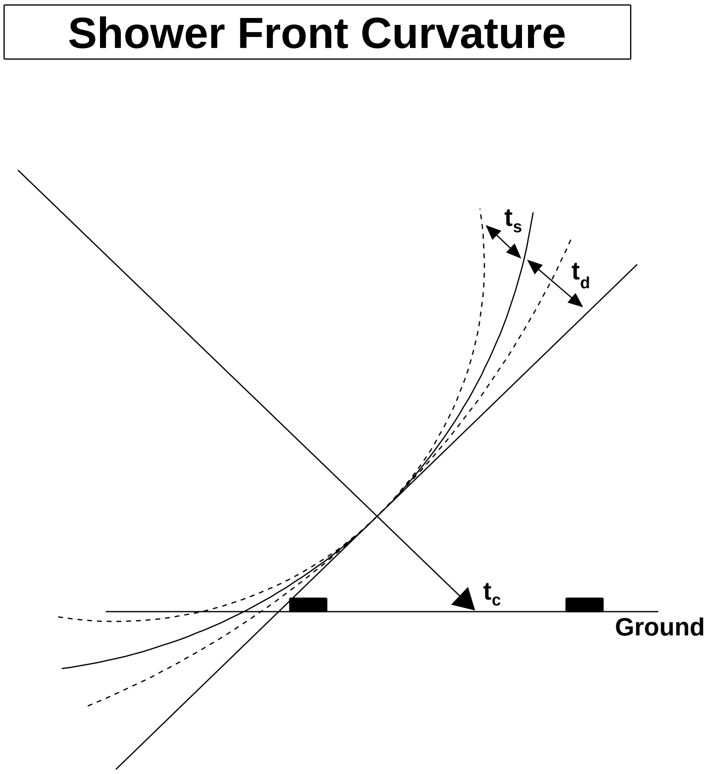

**Figure 5.8**: Diagram showing the timing distribution of particles away from the EAS axis. Close to the axis, particles may considered to exist on the shower front plane. Away from the EAS axis, however, the delay of particles, $t_d$, and the width of the distribution of arrival times, $t_s$, must be considered.

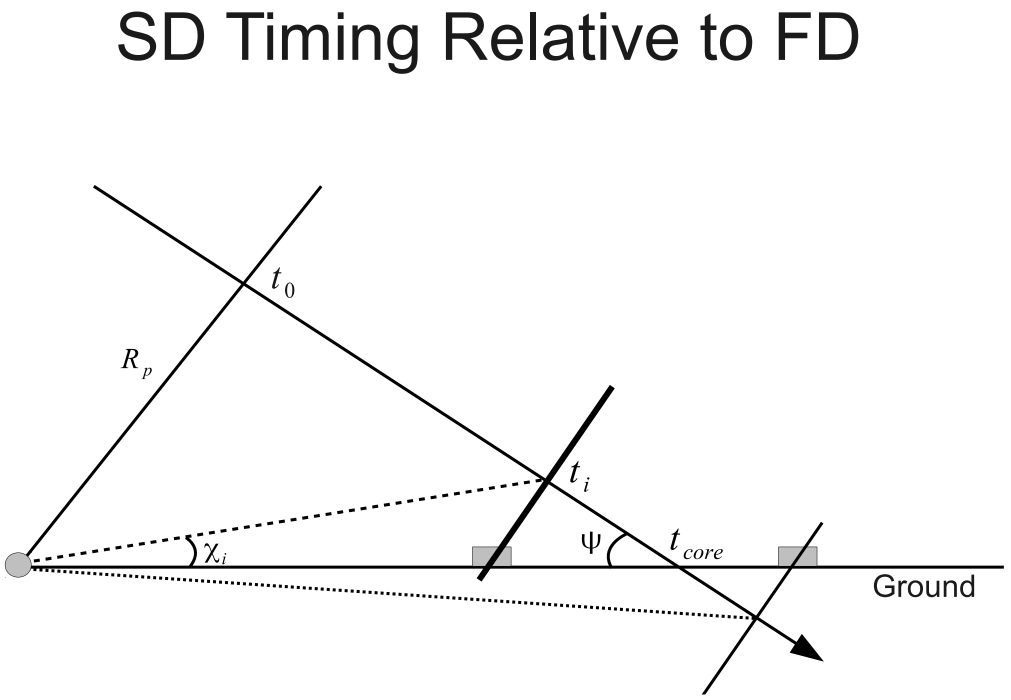

**Figure 5.9**: Diagram showing geometries involved in finding theoretical FD trigger times from SD data. The time that an SD triggered corresponds to $t_i$ shown on the shower axis. The viewing angle relative to the FD is the angle $\chi_i$. Of course, shower curvature seen in Figure 5.8 and Equation 5.11 must also be included, but is not included in this figure for clarity.

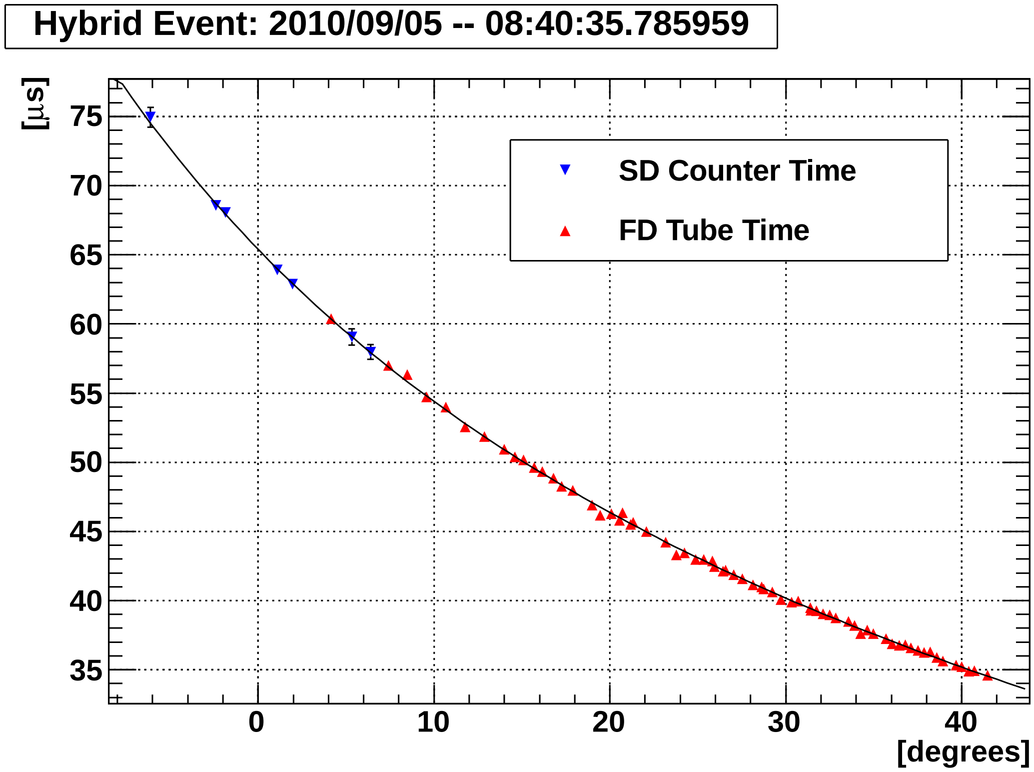

**Figure 5.10**: Hybrid time versus angle fit. This figure shows the result of putting the SD counter trigger times after they've been put in terms of the FD tube times, as seen in Figure 5.9. Just as in the FD mono time versus angle plot in Figure 5.4, the red triangles represent FD PMT trigger times. The blue triangles represent the timing individual SD counters.

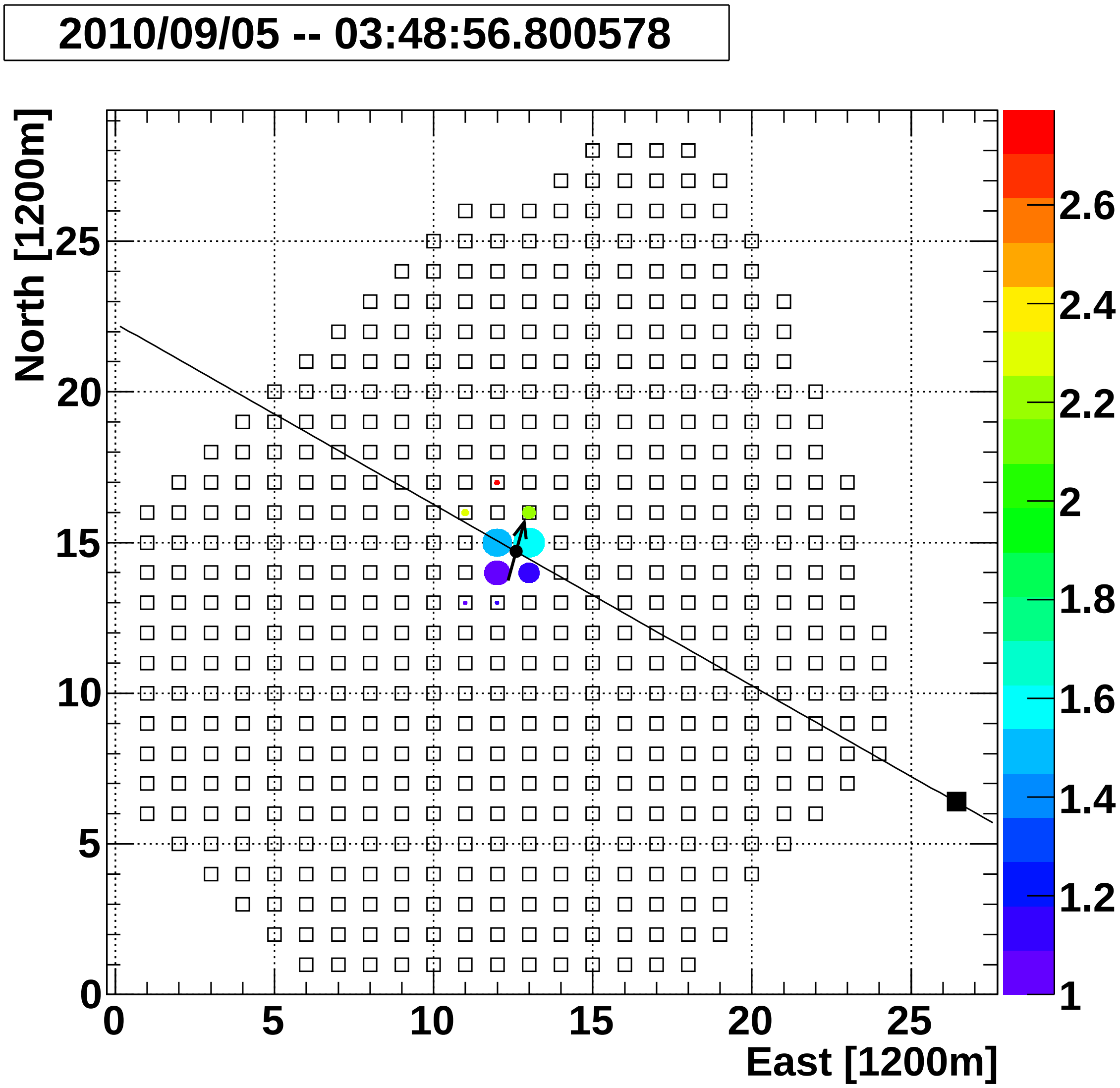

**Figure 5.11**: Event display showing triggered surface detectors in a hybrid event. The colored circles represent triggered SD. The size of the circle is proportional to the log of the number of charged particles that passed through the detector and the color is representative of the SD trigger time in units of (1200 m/$c$. The empty squares show all the counters in the SD array. The black line is the hybrid reconstruction shower detector plane project along the ground. The black square in the lower right marks the location of the Black Rock Mesa FD.

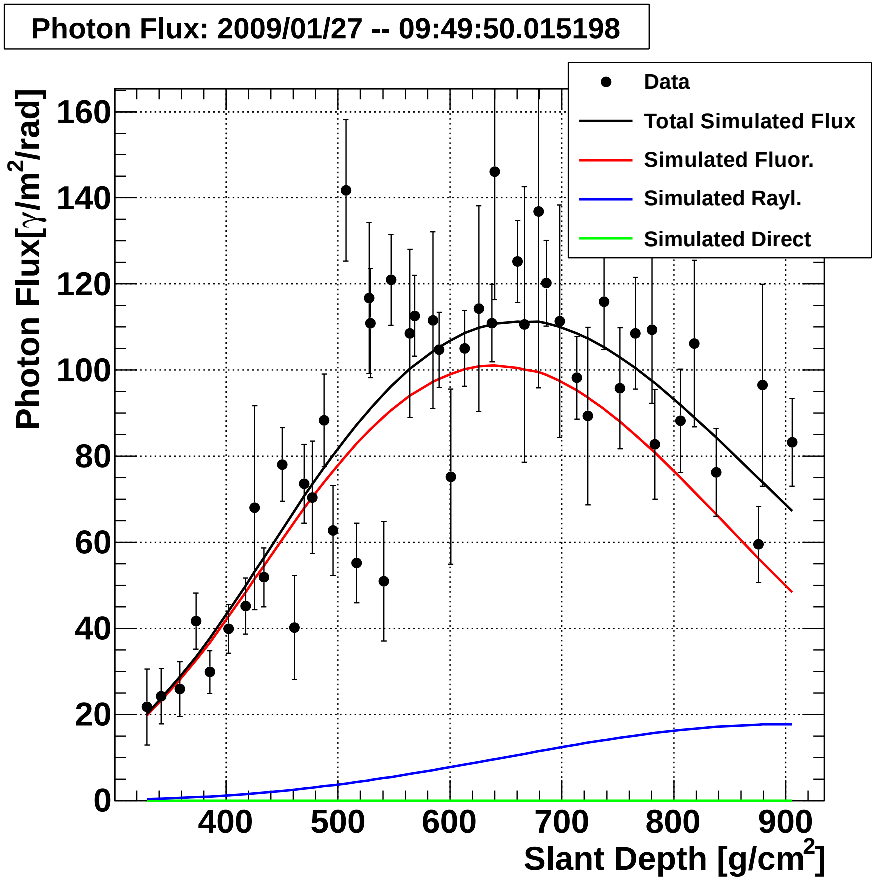

**Figure 5.12**: Photon flux fit for event 2010/01/27 – 09:49:49.015198.

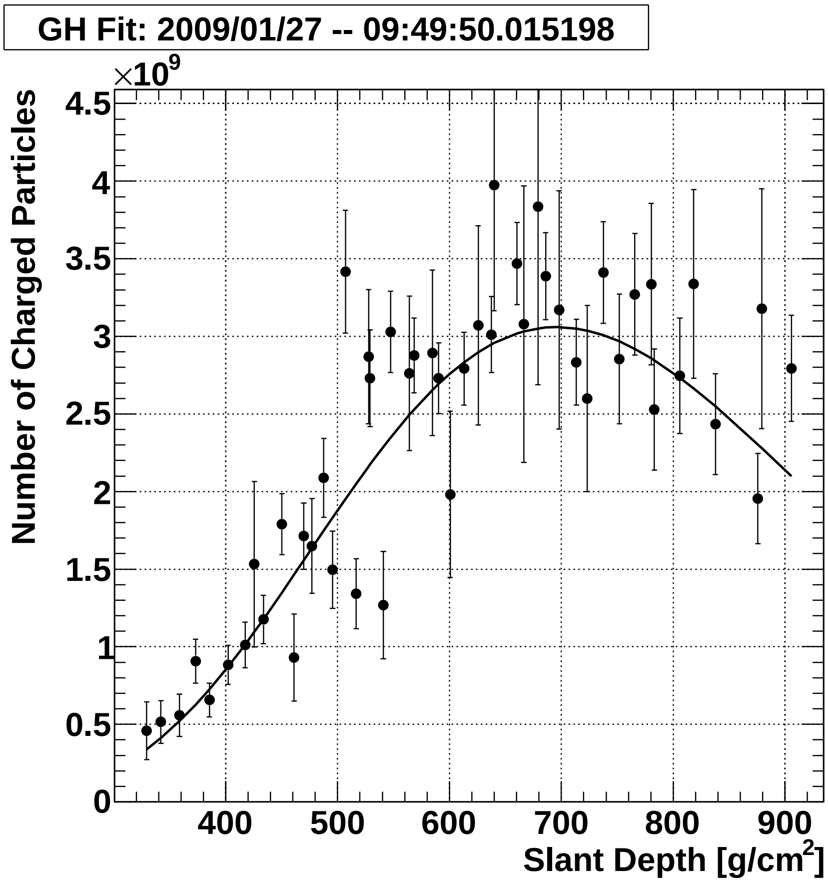

**Figure 5.13**: Solution to the Gaisser-Hillas Function from Equation 2.10 for event 2010/01/27 – 09:49:50.015198.

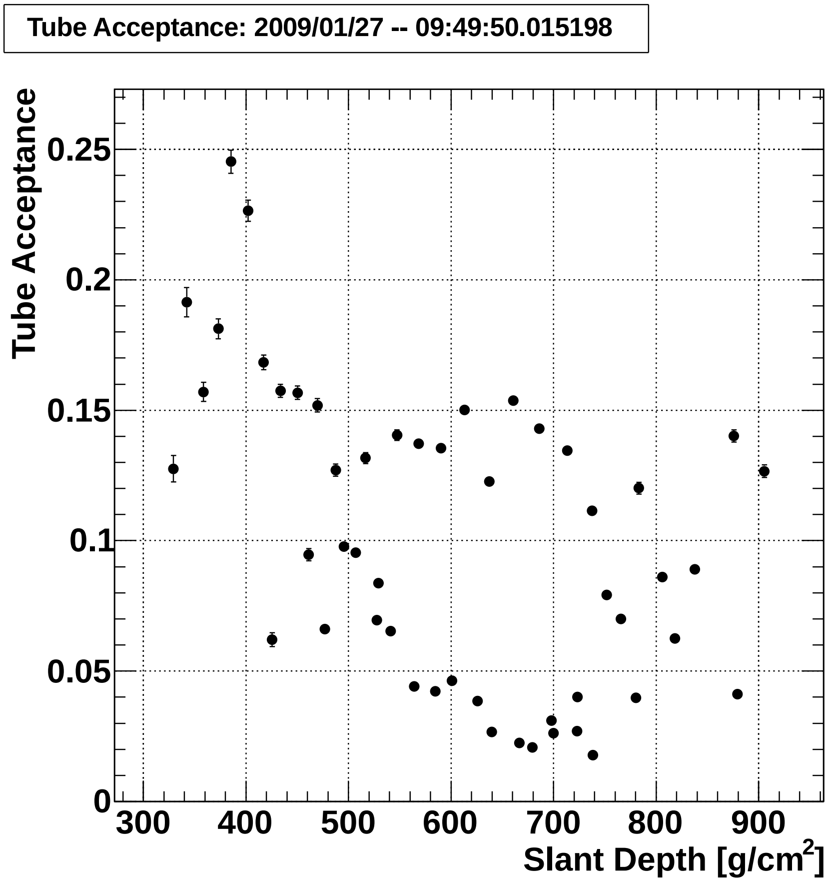

**Figure 5.14**: Tube acceptance calculated in reconstructing data event from 2010/01/27 – 09:49:50.015198. Acceptance is the percentage of light that crosses a mirror that actually results in photo-electrons in the PMTs. The x-axis shows the slant depth that a given PMT is viewing for this shower.

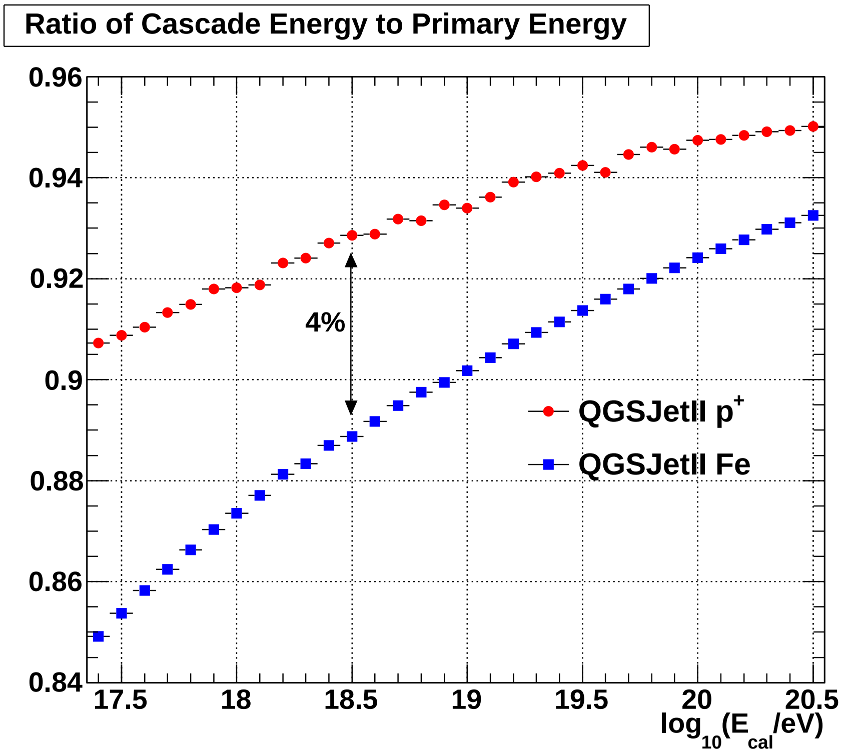

**Figure 5.15**: Ratio of calorimetric energy to primary energy in CORSIKA simulations using in this analysis.

# CHAPTER 6

# RESULTS

In the chapter, the results of a composition analysis using the observable $X_{max}$ are presented. First, validity of the Monte Carlo is confirmed using data-Monte Carlo comparisons. Then, the resolution of the reconstruction methods are shown. Lastly, the resulting $X_{max}$ distributions are shown and compared to proton and iron Monte Carlo.

## 6.1 Data Set and Quality Cuts

The data set used in this work is from May $27^{th}$, 2008 to September $9^{th}$ 2010. These dates correspond to the first FD-SD coincident events before the implementation of a hybrid trigger, where the SD array may be directly triggered by an FD station. This updated trigger requires a modification of the SD detector simulation and is beyond the scope of this work. Before quality cuts the hybrid data set used in this work contains 3085 Black Rock Mesa events and 2720 Long Ridge events, found directly through time matching. Of these, 477 are hybrid stereo events.

The quality cuts used in this analysis are the following:

1. The reconstructed energy must be greater than $10^{18.5}$ eV. The energy cut is especially important and arises due to an energy scale difference between the SD and FD detectors. This cut is discussed in detail in Section 6.3.

2. The reconstructed zenith angle, $\theta$, must be less than 55 degrees. This cut is required because the SD MC is only thrown to 60 degrees. The SD detector simulation is potentially not trustworthy for highly elongated showers[28].

3. Sky must be clear based on Middle Drum weather codes, or WEAT codes. Although this analysis uses data from the BR and LR detectors, the analysis of the weather monitoring data from those sites is still ongoing. However, during

MD operations, hourly measurements are made by MD operators making hourly weather observations and storing the observation as a 7 digit code. In this analysis, these weather codes are used to determine clear sky data for the BR and LR detectors. It is required that the sky is clear to the South and East for BR events and clear to the South and West for LR events. For events at either station, the overhead cloud coverage must be less than 1/4 of the sky.

4. The $\chi^2$ per degree of freedom for the geometry reconstruction must be less than 5.
5. The $\chi^2$ per degree of freedom for the profile reconstruction must be less than 5.
6. The reconstructed $X_{max}$ must be larger than the lowest observed depth and smaller than the highest observed depth. The reconstructed $X_{max}$ must be seen by the detector to successful reconstruct this parameter.
7. The angle inside the SDP, $\psi$, must be less than 130 degrees and the FD must observe the event for longer than 7 $\mu$s. This cut removes events where the FD signal is dominated by Cherenkov radiation. Cherenkov dominated events are difficult to model and are rarely well reconstructed.
8. The reconstructed core position must be inside the bounds of the SD array. Events reconstructed outside the SD array are often misreconstructed.

These cuts yield 443 hybrid events, including 71 hybrid stereo events. Table 6.1 shows the effects of each cut for BR and LR events.

## 6.2 MC Set

As described in Chapter 4, both the cosmic ray interaction in the atmosphere and as well as the SD and FD detectors are simulated. The MC events are thrown with realistic parameters that will result in distributions that are identical to the distributions from the actual experimental data.

It is important to thrown MC events with distributions larger than the boundaries of where the experiment is sensitive. This allows for the calculation of the acceptance

**Table 6.1**: Results of quality cuts on hybrid data. The number given for each cuts is the number of events cut using only the stated quality cut.

| Cut | BR events cut | LR events cut |
|---|---|---|
| None | 3085 | 2720 |
| $E > 10^{18.5}$ eV | 1644 | 1440 |
| WEAT cut | 516 | 428 |
| $\theta < 55°$ | 425 | 361 |
| $\chi^2_{prfl}/DOF < 5$ | 345 | 321 |
| $\psi < 130°$ and time extent $< 7$ $\mu$s | 317 | 298 |
| $X_{high} > X_{max} > X_{low}$ | 292 | 265 |
| $\vec{r}_{core}$ is inside array | 274 | 248 |
| $\chi^2_{geom}/DOF < 5$ | 271 | 243 |

due to experimental boundaries and results in distributions that resemble the experimental data. Figure 6.1 shows the two-dimensional core positions of thrown MC showers. Figures 6.2 and 6.3 show thrown SDP angles, $\psi$, and the distances of closest approach, $R_p$ respectively relative to the Black Rock Mesa FD station.

Throwing a $E^{-3}$ spectrum over a few decades in energy and maintaining good statistics is difficult. Additionally, good MC statistics at all energies is especially important for an $X_{max}$ analysis where distributions in the data are compared directly to the MC distributions. To handle this, events are thrown with an $E^{-2}$ spectrum, and MC events are then weighted by $E^{-1}$ to correctly represent an $E^{-3}$ distribution. Figure 6.4 shows both the thrown spectrum and the result of the of the $E^{-1}$ weighting. As there is a low energy cut at $10^{18.5}$ eV, events are only thrown as low as $10^{18.0}$ eV.

## 6.3 SD-FD Energy Scale Differences

There is an important difference in the energy scales of reconstructed FD and SD events in Telescope Array data. The SD energy reconstruction relies directly on number of particles that result in CORSIKA simulations. In contrast reconstructed FD energies are derived from energy deposited on the shower axis combined with the fluorescence yield. Only the missing energy correction component of the FD reconstruction is truly model based. In this way the FD energy scale has a calorimetric basis. To ensure that the SD energy scale reflects this calorimetric energy scale, SD energies are rescaled to the FD energy scale.

Figure 6.5 shows the percent difference in reconstructed SD energies, before rescaling, and hybrid energies for hybrid events that pass both SD and hybrid quality cuts. It is clear that SD energies are systematically reconstructed 27% higher than the FD energies. CORSIKA simulated air showers result in simulations that are Representative of the TA SD data, however, the reconstructed energies are high by 27% compared to the FD[28].

This is problematic because the hybrid MC must correctly simulate the hybrid efficiency, which depends on both the SD and FD trigger efficiencies independently. If the energy scales, are not correctly represented in the MC, the combination of the trigger efficiencies will be wrong.

There are three ways of addressing this this problem:

1. Adjust the SD energy scale MC by introducing more particles in the lateral distribution.
2. Adjust the FD energy scale in the MC by reducing the number of particles in the longitudinal profile so that the energy scale difference between the FD and SD are the same in the MC and the data.
3. Use a region of the data where the SD trigger aperture does not depend on the primary energy, and thus the mismatch of energy scales does not effect the overall hybrid trigger aperture.

In the analysis presented here, the third option is used. This choice allows for the direct use of CORSIKA showers with no need to make adjustments either the longitudinal or lateral CORSIKA distributions. However, this means that data cannot be used below the efficiency plateau of the SD array. Figure 6.6 shows the SD trigger aperture. Above $10^{18.5}$ eV the trigger aperture is flat and the difference in energy scale has a very small effect the overall hybrid aperture. This is the justification for the cut in energy at $10^{18.5}$ eV in hybrid energy.

## 6.4 Data - Monte Carlo Comparison Plots

As discussed in Chapter 4, it is essential to validate the Monte Carlo(MC) by ensuring that distributions of observed quantities are identical in the MC and data.

In this section, distributions of many observables found in the data and produced by the MC are compared. The MC, in general, reproduces the distributions found in the data very well. A comparison of data and MC is shown for all distributions on which a cut is made, as described in Section 6.1, to ensure that our quality cuts effect the data and MC in the same way. These comparison plots are found in Figures 6.7 through 6.22.

In each comparison plot found in the following pages, the distribution found in the data is shown with full black points and the MC distribution is shown with a solid line. Below each set of compared distributions is a plot showing the ratio of each bin and a linear fit to that ratio. The ratio plots aid in revealing trends in the compared distributions and are sensitive to disagreements in the MC that may not be obvious to the eye.

Additionally, a comparison plot is shown for both proton and iron MC for each observable. For each comparison, the proton MC is found on the *left* and is shown with a solid *red* histogram. The corresponding comparison to iron MC is found on the *right* has a solid *blue* histogram.

A few comparison plots require comment.

## 6.5 Resolution Studies

A detector MC and event simulation that has been validated through data/MC comparisons may be used to understand the resolution of the event reconstruction. This is done by comparing reconstructed parameters to thrown parameters for MC events. For each reconstructed parameter, $X$, a histogram is made of either the difference between the reconstructed value and the thrown value or the percent difference.

If the simple difference is used, the quantity

$$X_{REC} - X_{MC} \tag{6.1}$$

is histogrammed, where $X_{REC}$ is the reconstructed value for the parameter $X$ and $X_{MC}$ is its thrown value.

For parameters whose reconstructed values span two or more orders of magnitude, such as energy, it is more appropriate to use percentage difference. In following analysis,

$$\ln\left(\frac{X_{REC}}{X_{MC}}\right) \tag{6.2}$$

is used to calculate the percent difference instead of the traditional formula for percent difference. To first order these are equivalent using a Taylor series expansion,

$$\ln\left(\frac{X_1}{X_2}\right) = \ln\left(1 + \frac{X_1 - X_2}{X_2}\right) \approx \frac{X_1 - X_2}{X_2} \tag{6.3}$$

Using the natural logarithm of the ratio has the benefit of being completely anti-symmetric in an exchange of $X_1$ and $X_2$.

In the following figures, the width of these distributions is called the *resolution* and represents an average reconstruction precision. The mean of these distributions is called the *reconstruction bias* and is the average amount that a parameter is systematically misreconstructed. This analysis always uses the RMS to measure the resolution and the distribution's directly calculated mean to measure the reconstruction bias. For each reconstructed parameter, comparisons are shown for both proton and iron MC. The figures for proton MC will always be shown on the *right* in *red* and the figures for iron MC will always be shown on the *left* in *blue*.

The hybrid geometry reconstruction has resolutions of 0.5° for angular quantities such as $\phi$, $\theta$, and $\psi$, 90 m for the distance of closest approach, $R_p$, and 60 m for distances East and North of the CLF, $X_c$ and $Y_c$. The reconstruction bias in these geometrical quantities is essentially zero for every parameter. The full distributions are found in Figures 6.23 to 6.28. These results do not depend on the primary species.

The profile reconstruction described in Section 5.4 has a resolution of 7% in energy for both proton and iron MC. However, the reconstruction bias for proton and iron MC differ by about 6%. The proton MC reconstruction bias is +8%, and for iron MC, the reconstruction bias is +2%. 4% of this difference is due to the difference in missing energy in proton and iron showers. In the profile reconstruction, the missing energy correction calculated using simulated proton showers is applied to the data and simulated proton and iron showers. This is needed to fulfill the requirement that the same reconstruction is applied to both data and MC. However, Figure 5.15

shows that the missing energy for proton and iron MC differ by about 4%. These distributions are found in Figures 6.29 and 6.30.

The profile reconstruction used in this work results in a resolution in $X_{max}$ of 20 g/cm$^2$ and 15 g/cm$^2$ for protons and iron respectively. The reconstruction bias in $X_{max}$ is -2 g/cm$^2$ for proton MC and -4 g/cm$^2$ for iron MC. These results are found in Figure 6.31.

Figures 6.32 and 6.33 shows the reconstruction bias and resolution in $X_{max}$ as a function of reconstructed energy. The upper plots show that the reconstruction bias does not depend significantly on the energy of the primary cosmic ray. The lower panels show resolutions of 20 g/cm$^2$ and 15 g/cm$^2$ for protons and iron MC respectively. This resolution steadily improves as the reconstructed energy increases.

A summary of these results is found in Table 6.2.

An extension of the resolution studies is to use the detector MC to measure biases introduced by the hybrid detector. The detector may bias the data in a variety of ways including the limited field of view of the FD stations, the $1/r^2$ reduction in photon flux from the air shower track, as well as more subtle effects caused by the triggering logic or analog to digital converters. Understanding and reproducing these effects is one of the critical benefits of the detector simulations. The bias in a given quantity may be measured by comparing the thrown MC distribution to the resulting distribution

**Table 6.2**: Results from proton and iron resolution studies. This table shows the mean and RMS of the histograms found in Figures 6.23 through 6.31.

| Parameter | Resolution | | Bias | |
|---|---|---|---|---|
| | proton | iron | proton | iron |
| $\theta$ | 0.54° | 0.52° | 0.02° | −0.012° |
| $\phi$ | 0.53° | 0.52° | −0.01° | −0.1° |
| $\psi$ | 0.54° | 0.53° | −0.05° | −0.11° |
| $R_p$ | 90 m | 90 m | 28 m | 15 m |
| $X_c$ | 67 m | 67 m | 4 m | 3 m |
| $Y_c$ | 63 m | 64 m | 13 m | 5 m |
| $E_{cal}$ | 7.3% | 6.1% | +8.7% | +6.5% |
| $E$ | 7.2% | 6.0% | +8.6% | +2.3% |
| $X_{max}$ | 19.7 g/cm$^2$ | 15.3 g/cm$^2$ | -2.3 g/cm$^2$ | -3.9 g/cm$^2$ |

after detector triggering, reconstruction, and quality cuts. Such a calculation of bias in $X_{max}$ is shown for proton and iron showers in Figures 6.34 and 6.35. These figures show a slight difference in proton and iron MC due to iron showers generally reaching shower maximum at lower depth or higher in the atmosphere. At high energies, proton showers will often reach the ground before reaching shower maximum. These deeper showers are subsequently cut by the $X_{max}$ bracketing cut. As simulated iron MC reach $X_{max}$ earlier, iron showers rarely reach $X_{max}$ past the lower field of view of the FD detectors.

## 6.6 $X_{max}$ Analysis

In this section, the distributions of reconstructed $X_{max}$ found in the data are examined closely and compared to the $X_{max}$ distributions produced by CORSIKA for proton and iron induced showers, including the hybrid detector simulation. Up to this point, the MC simulations have been used as a tool to ensure the TA detector in hybrid mode is well understood as well as to calculate resolutions and the acceptance biases. Here, the MC simulations play an important role in interpreting the chemical composition of cosmic rays observed by the TA detector.

In Chapter 2, it was shown that $X_{max}$ can not be used to determine the chemical composition of a cosmic ray on an event by event basis because $X_{max}$ distributions for proton and iron MC overlap. However, $X_{max}$ distributions resulting from proton and iron MC have significant differences. Proton showers tend to develop deeper in the atmosphere than iron simulations. Additionally, proton showers have larger fluctuations in $X_{max}$ resulting in wider $X_{max}$ distributions. Figure 6.36 presents a scatter plot of the $X_{max}$ and energy of every event passing the quality cuts described in Section 6.1.

Although both the mean and width of $X_{max}$ distributions are indicative of the chemical composition of cosmic rays, the most complete information is found in the full distributions. Before more quantitative comparisons are shown between the data and the proton and iron MC, $X_{max}$ distributions are presented in bins of 0.1 in $\log(E/\,\mathrm{eV})$. These distributions are shown in Figures 6.37 through 6.39. These figures are clearly compatible with proton MC and exclude iron. As the flux of cosmic rays is proportional to $E^{-3}$, the statistics near $10^{18.5}$ eV are good, but deteriorate energy increases. Above $10^{19.3}$ eV, due to poor statistics, the data is compatible with both proton and iron MC.

To quantify the compatibility of the data with protons or iron simulations, a Kolmogorov-Smirnov (KS) statistical test is performed on the distributions found in Figures 6.37 through 6.39. Figure 6.40 shows the p-values for these KS tests. Figure 6.40 shows compatibility with protons at all energies and completely excludes the iron MC below $10^{19.3}$ eV. Above $10^{19.3}$ eV, the data is compatible with either protons or iron.

Figure 6.41 shows the mean $X_{max}$ versus $\log_{10}(E/\,\mathrm{eV})$ for proton and iron MC air showers. As expected, this shows that proton and iron MC each produce a steady elongation rate when the detector simulation is included. The fit $< X_{max} >$ has a slope of 35 g/cm$^2$ and 48 g/cm$^2$ for protons and iron respectively. The difference here is reflective of the difference in the acceptance in $X_{max}$ shown in Figures 6.34 and 6.35. Though the overall distributions overlap, the mean $X_{max}$ for proton and iron simulations are sufficiently separated to be resolve the two species in the data. The linear fits found in Figure 6.41 for the proton and iron simulations are used in Figure 6.42 to compare to the $< X_{max} >$ in the data.

The mean $X_{max}$ found in the data is then plotted against the fit elongation rates in Figure 6.41. Overall, the mean $X_{max}$ in the data is 10 g/cm$^2$ shallower than that seen in the simulated QGSJetII proton MC. This is expected as it is seen in the overall $X_{max}$ data-MC comparison plot found in Figure 6.22. On the other hand, the data is significantly deeper than simulated iron showers, showing compatibility with proton MC but not iron.

As discussed earlier, cosmic ray simulations show that the $X_{max}$ distributions resulting from proton and iron induced air showers have very different shapes. In order to compare the shape of $X_{max}$ distributions found in the data and simulated air showers independently of the mean of the distributions, the means are subtracted from the $X_{max}$ distributions in Figures 6.37 through 6.39. Figures 6.45 through 6.46 show these mean subtracted $X_{max}$ distributions.

In these figures, it is clear that even with the means removed, the $X_{max}$ distributions in the data looks more like the proton MC than the iron MC. The data is consistently wider than the iron MC, and additionally, have a long high side tail that is not present in the iron MC. The presence of this high side tail is due to the proton air cross section and was discussed in Chapter 2. Looking at these figures by eye, however, it is clear that the statistical power to resolve the two distributions falls away after $10^{18.8}$ eV.

As was done with the distributions from Figures 6.37 through 6.39, KS statistical tests were done with the mean subtracted $X_{max}$ distributions. Figure 6.47 shows the resulting p-values from the KS tests to proton and iron MC. According to these statistical tests, protons are compatible with the data at all energies. Iron MC is excluded at low energies, but above $10^{18.8}$ eV the shape of the $X_{max}$ distributions in the data is compatible with both proton and iron MC.

A simpler way to compare the shapes of two distributions is use a measurement of their widths. This method is beneficial as it is much simpler than the earlier mentioned KS tests, though it may not be as sensitive to non-Gaussian nature of the compared distributions and can be susceptible to under-sampling.

The simplest way to measure the width of a distribution is to use its RMS. The RMS of each distribution found in Figures 6.44 through 6.46 are compared. It is clear that the widths of the data, in general, are in agreement with the proton measurements and are consistently much wider than the iron distributions. However, RMS can be a susceptible to under-sampling and is difficult to measure with poor statistics. Because of this, care should be taken when looking at the distributions greater than $10^{18.8}$ eV, where the according to Figure 6.47, the shape of the distributions found in the data is compatible with both proton and iron MC.

1. The comparison plots of the reduced $\chi^2$ distributions from the event reconstruction do not agree perfectly. These are shown in Figures 6.10 and 6.11. This lack of agreement has potential for the quality cut on these distributions to affect the data differently than the MC. To ensure that cuts are effect the data and the MC in the same way, the MC is scaled so that the comparison plots are in better agreement. The reduced $\chi^2$ from the geometry fitting is scaled by 1.25 and the profile fit's reduced $\chi^2$ is scaled by 1.52. In each case, the same scaling is used in the proton and iron MC.

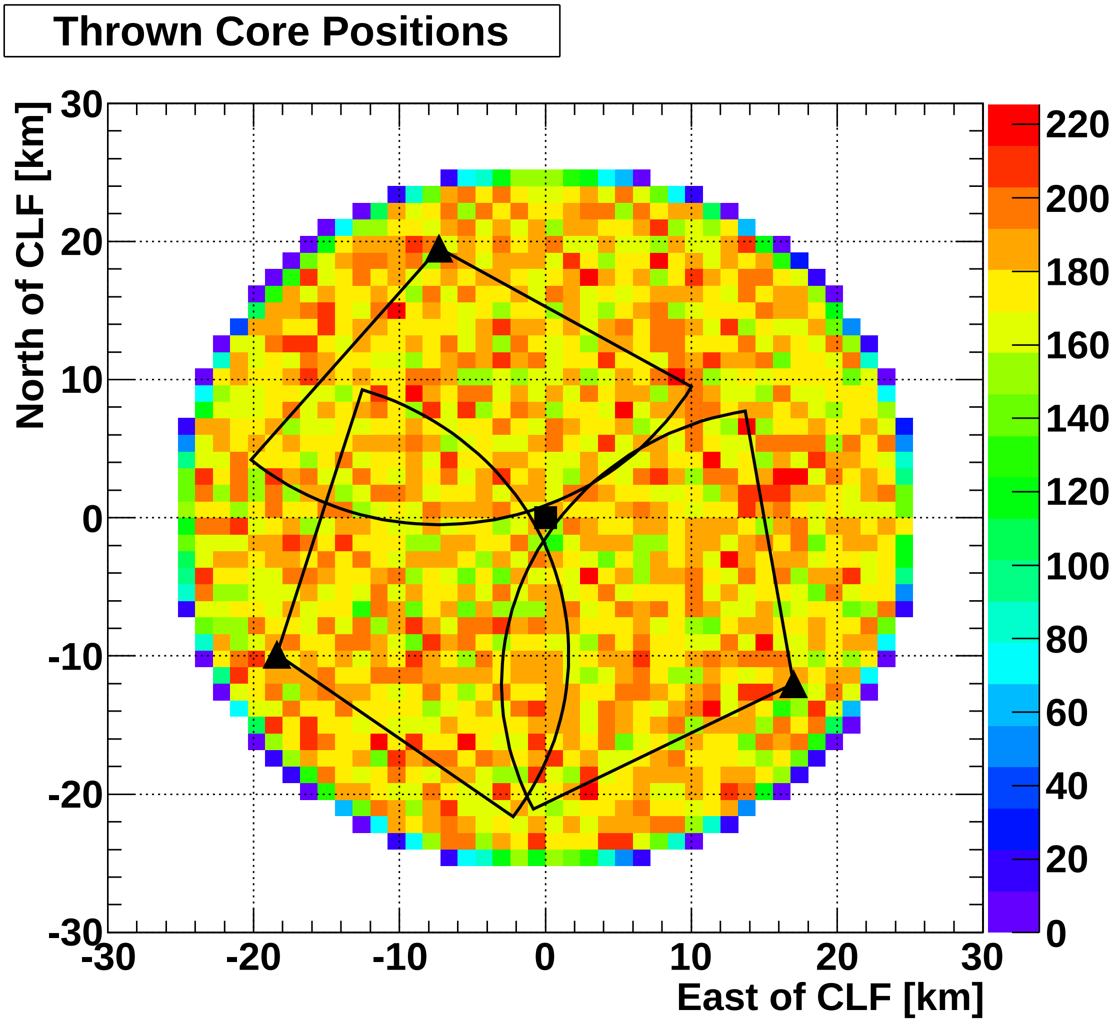

**Figure 6.1**: Thrown Core locations relative to FD detectors (triangles) and the CLF (square). The field of view for each FD is also shown.

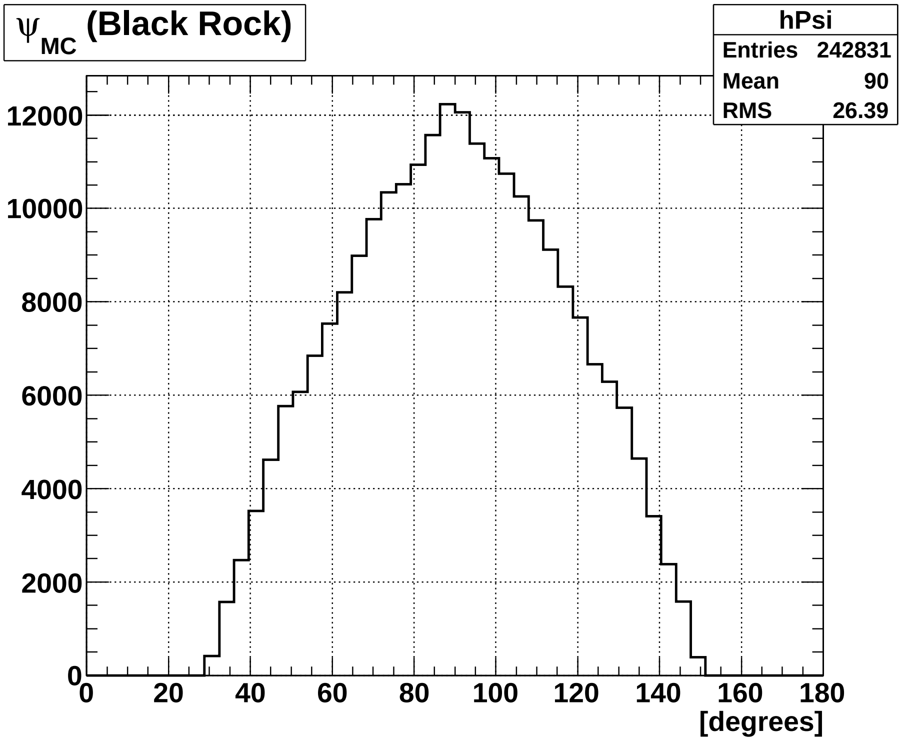

**Figure 6.2**: Thrown $\psi$ distribution relative to the Black Rock Mesa FD station.

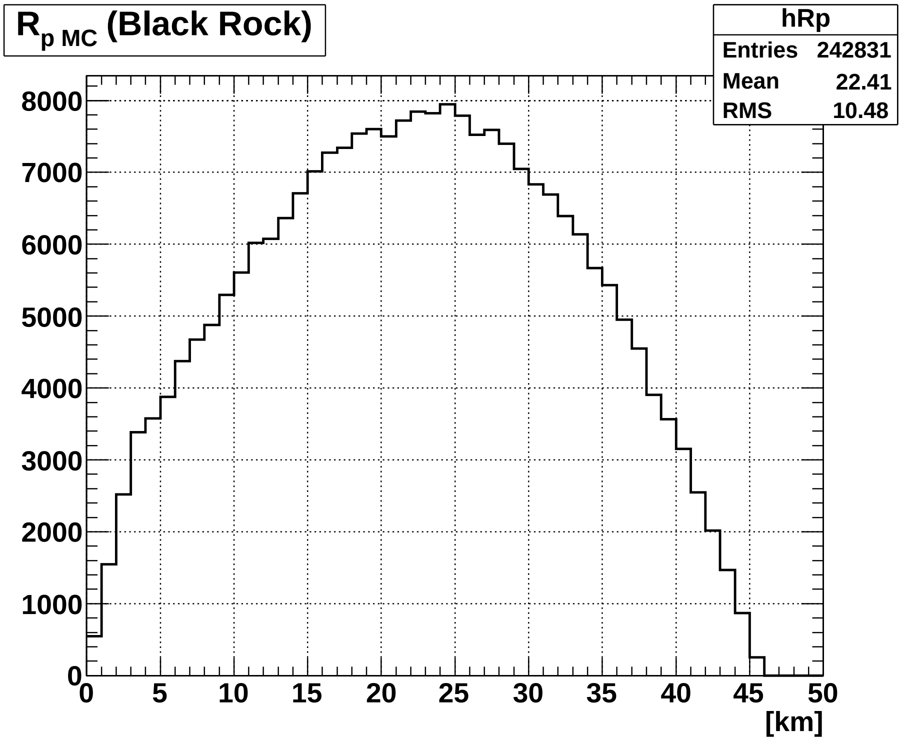

**Figure 6.3**: Thrown $R_p$ distribution relative to the Long Ridge FD station.

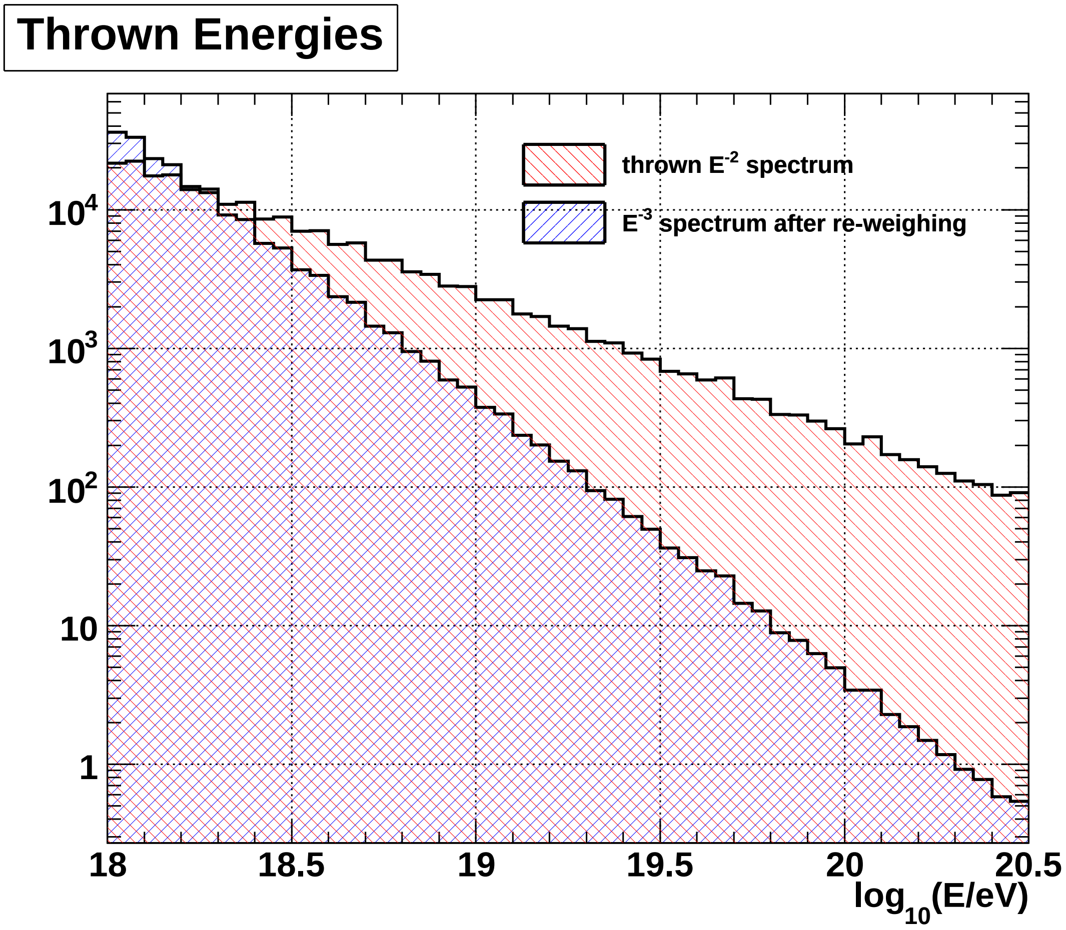

**Figure 6.4**: Thrown MC energies. For comparisons to the data, events are weighted by $E^{-3}$ while maintaining the same area as the $E^{-2}$ distribution.

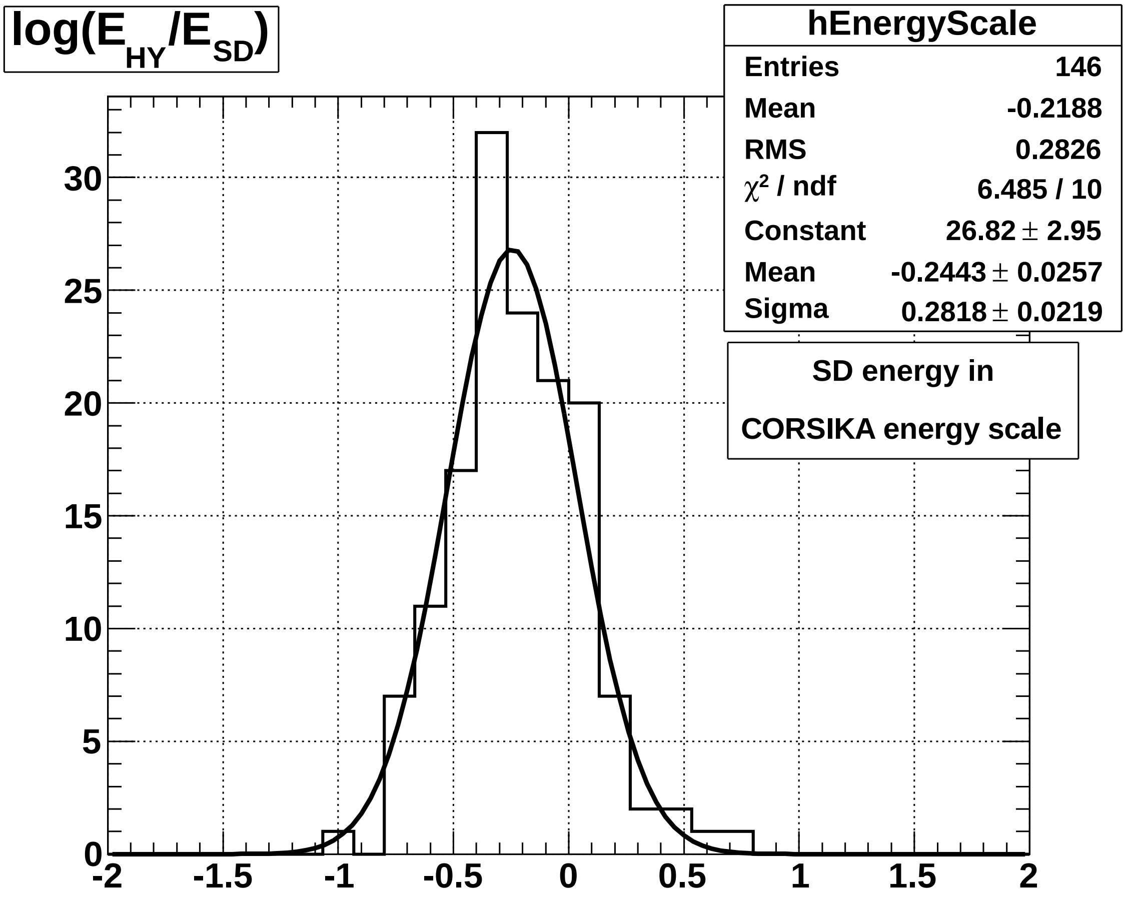

**Figure 6.5**: Comparison of FD and SD based reconstructed energies.

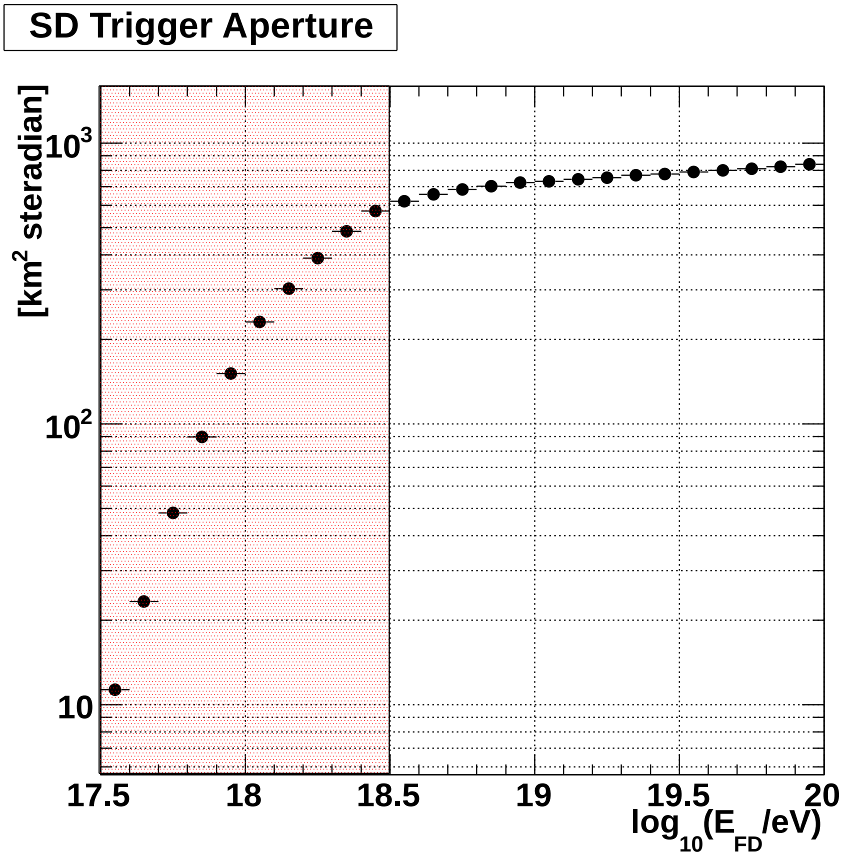

**Figure 6.6**: The SD trigger aperture using the SD detector MC. The x-axis shows the MC energy, but scaled by 0.787 to reflect the 27% energy scale difference. Above the cut at $10^{18.5}$ eV the SD aperture is flat and the energy scale difference does not effect the hybrid aperture significantly.

2. Close inspection of the comparison plots of the energy distribution, shown in Figure 6.19, reveal features in the data that are not found in the MC. These are the result of physical features found in the flux of ultra high energy cosmic ray that are represented in the steady, $E^{-3}$ energy distribution used in this study. The lack of the these small features has no effect the distribution of $X_{max}$ that is presented in this work.

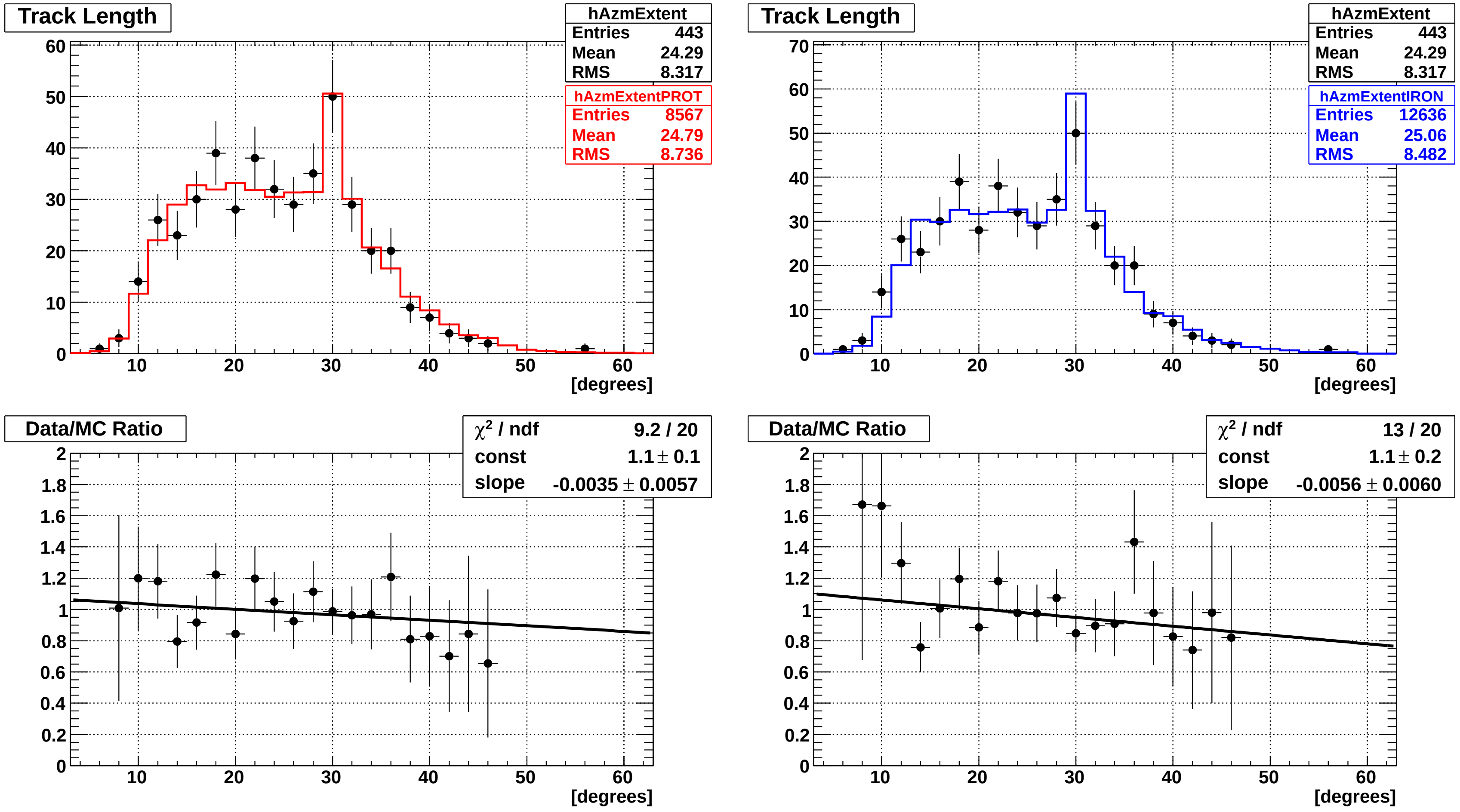

(a) Proton (b) Iron

**Figure 6.7**: Data-MC comparison for the length of tracks seen by FDs for proton MC (left) and iron MC (right). The abrupt peak at 30° corresponds to two mirror events.

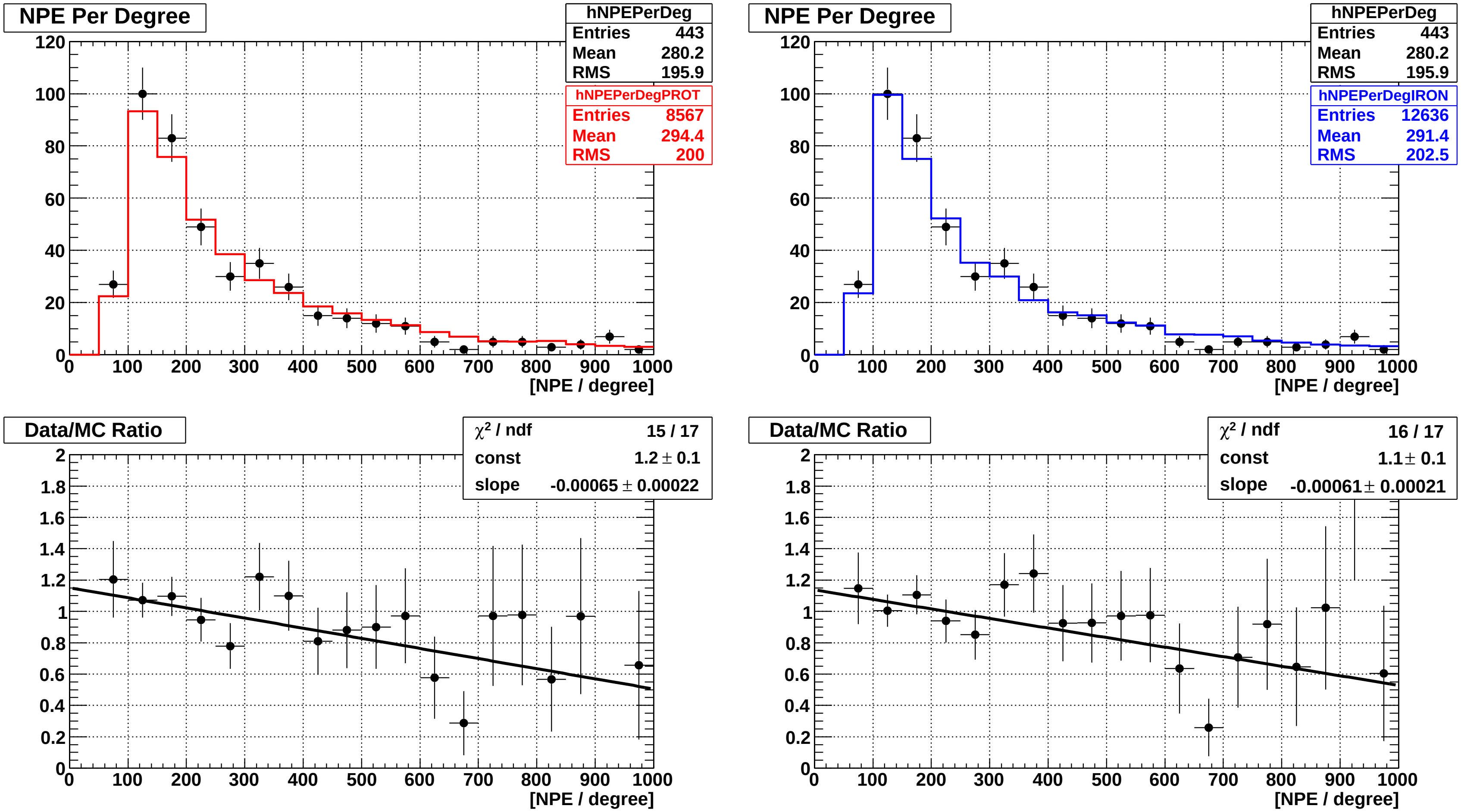

(a) Proton

(b) Iron

**Figure 6.8**: Data-MC comparison for the number of photo-electrons per degree seen in the FDs for proton MC (left) and iron MC (right).

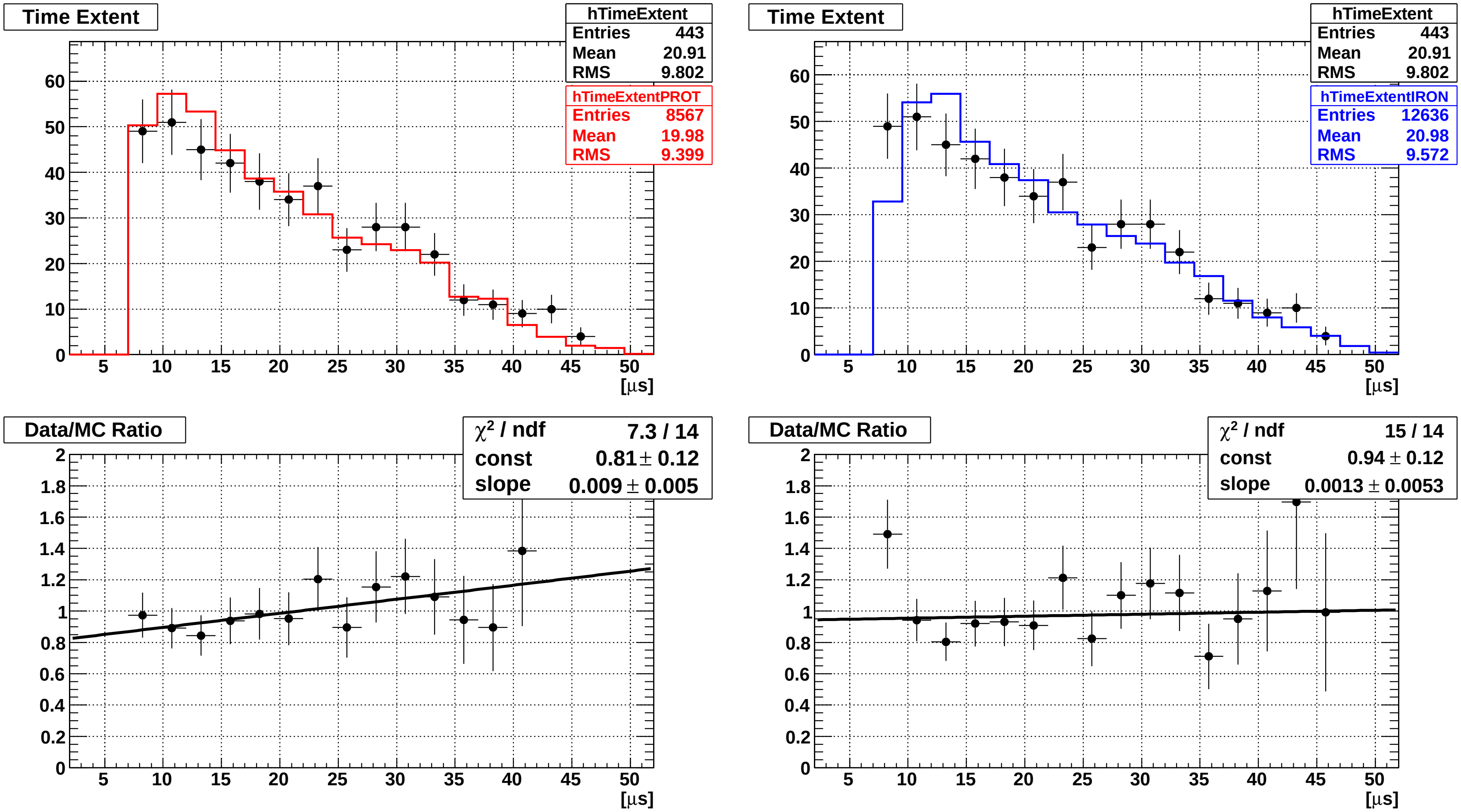

(a) Proton (b) Iron

**Figure 6.9**: Data-MC comparison for the number of photo-electrons per degree seen in the FDs for proton MC (left) and iron MC (right).

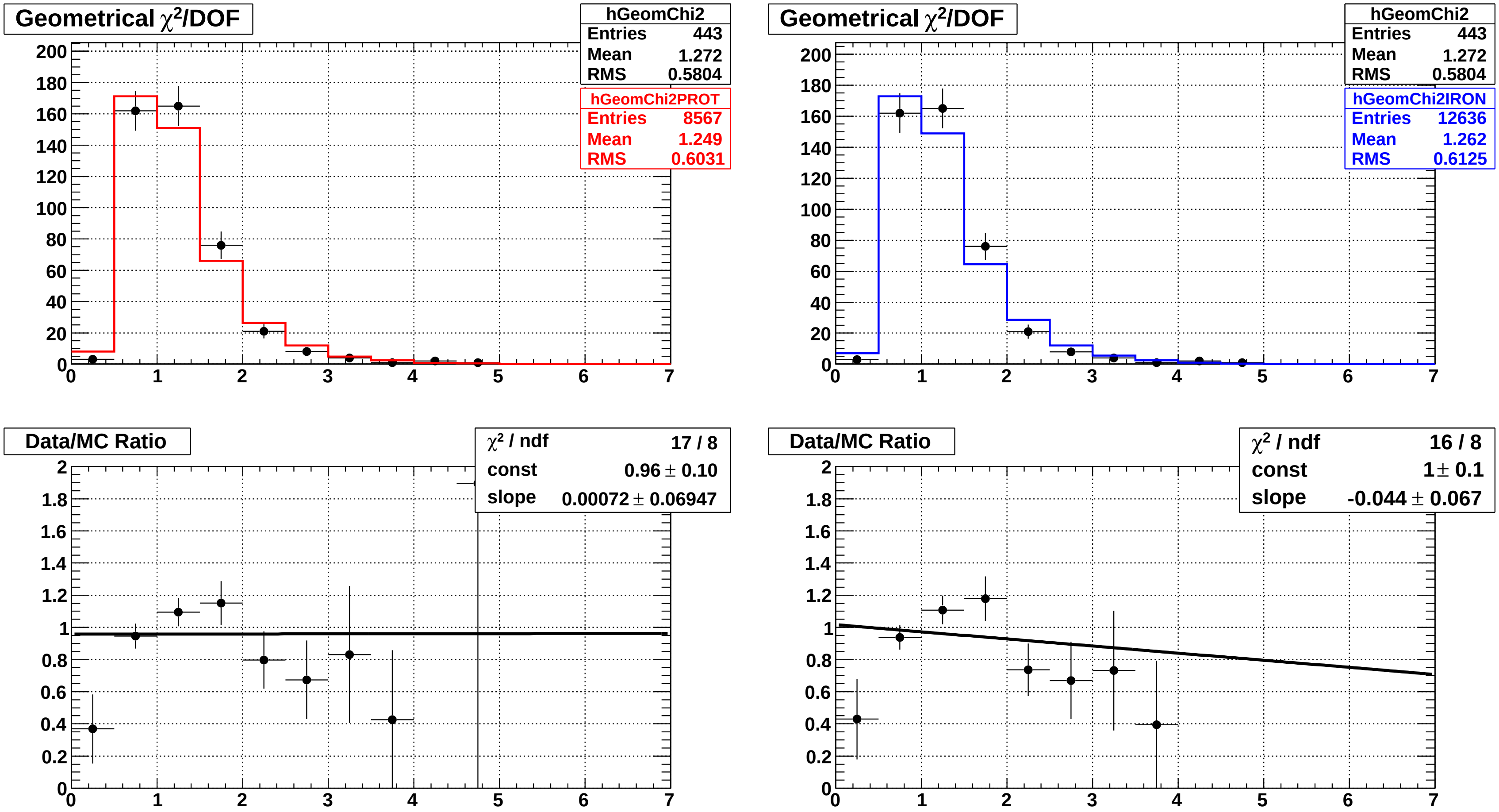

(a) Proton

(b) Iron

**Figure 6.10**: Data-MC comparison for the reduced $\chi^2$ for the hybrid geometry fit for proton MC (left) and iron MC (right). These distributions are not in agreement, but because this is a cut quantity the MC is scaled by 1.25.

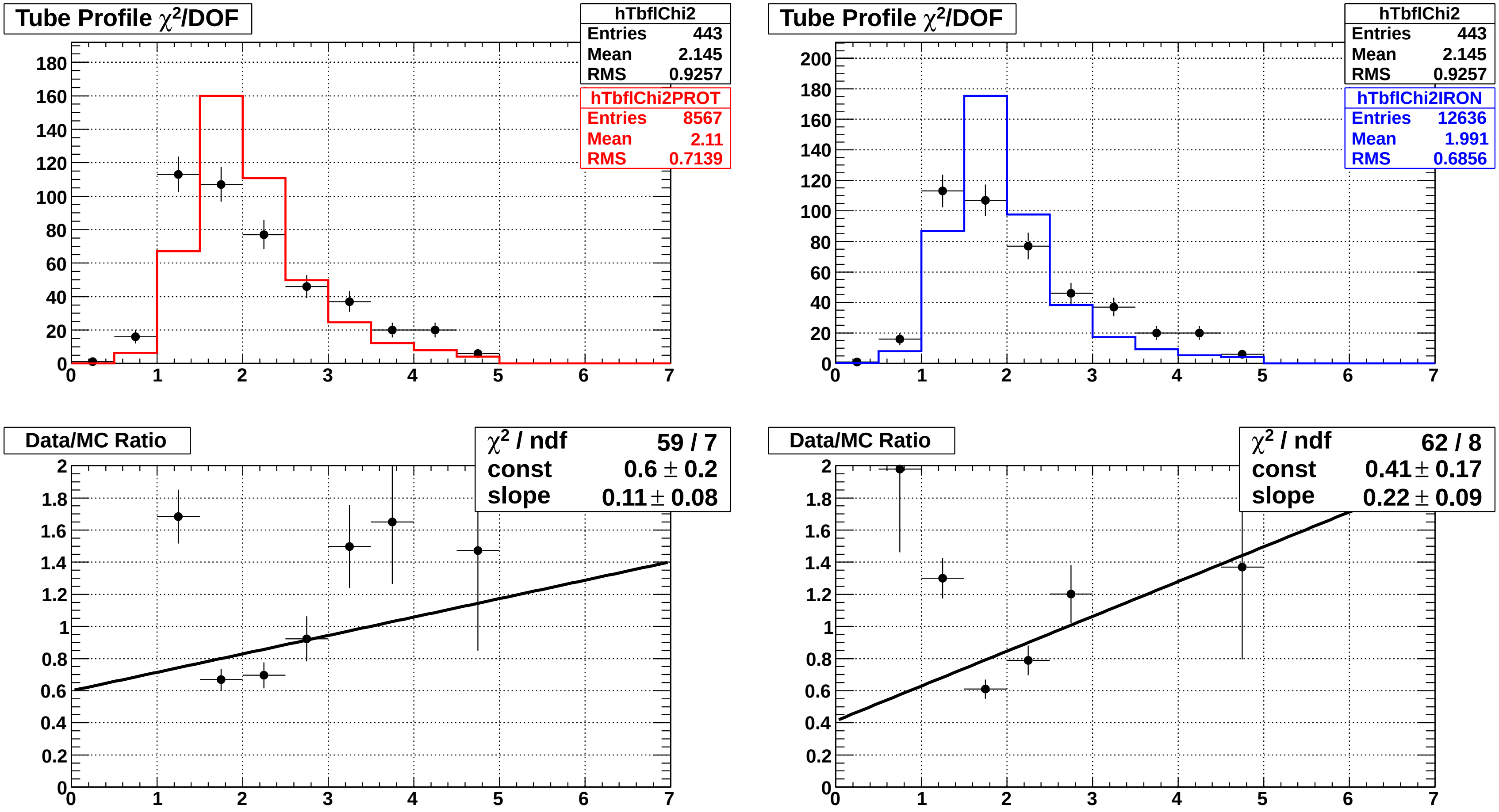

(a) Proton

(b) Iron

**Figure 6.11**: Data-MC comparison for the reduced $\chi^2$ for the profile fit for proton MC (left) and iron MC (right).

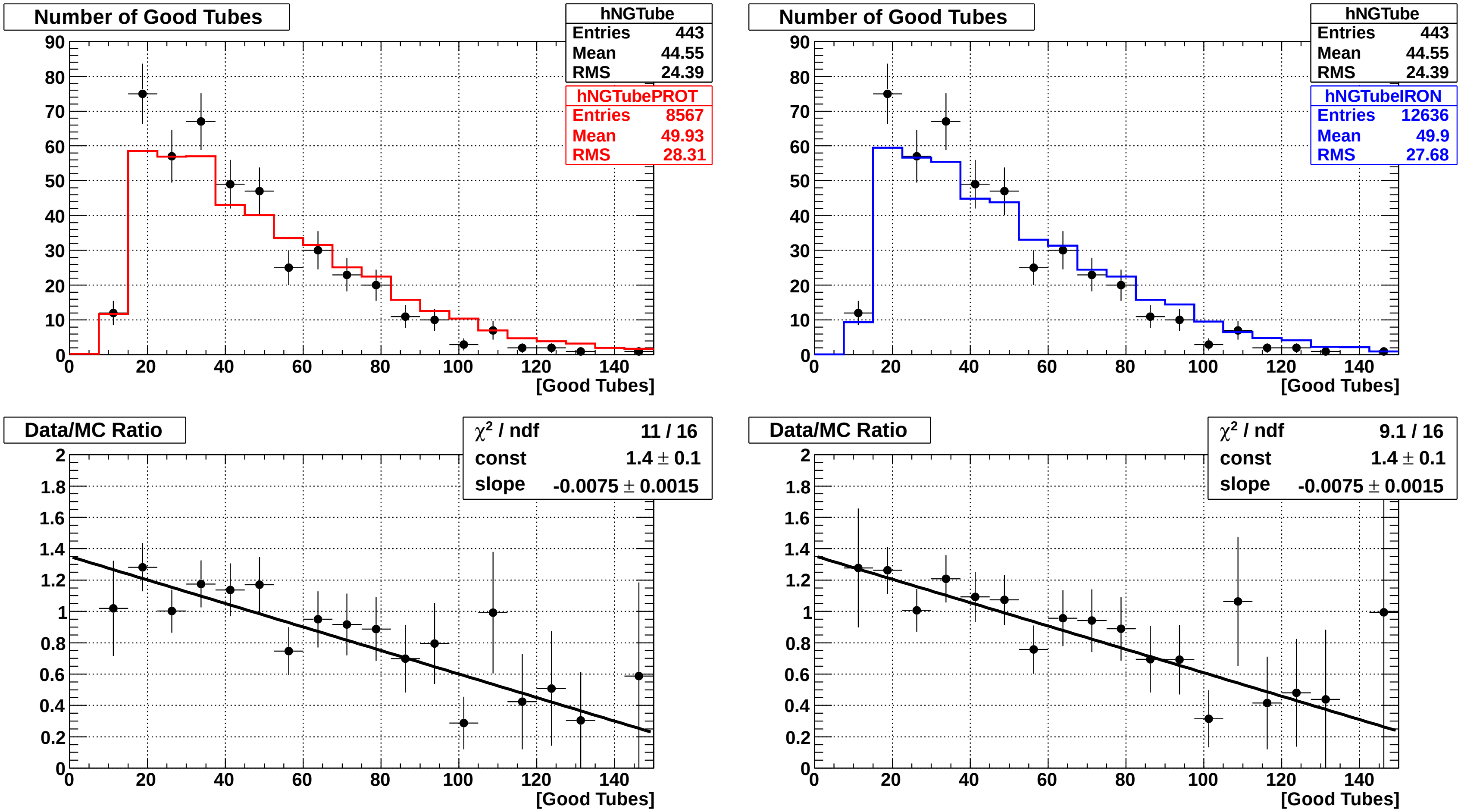

(a) Proton (b) Iron

**Figure 6.12**: Data-MC comparison for the number of photo-electrons per degree seen in the FDs for proton MC (left) and iron MC (right).

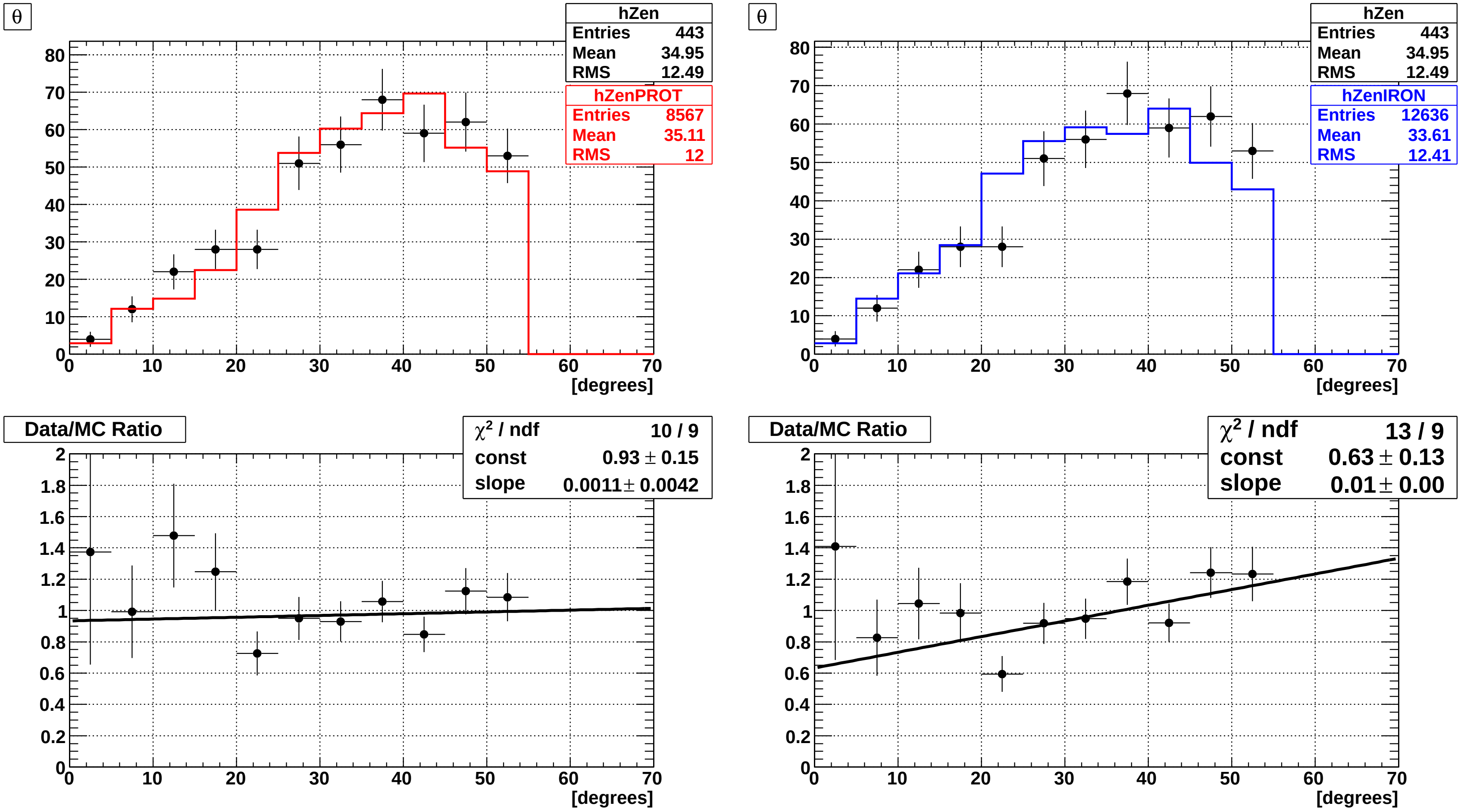

(a) Proton (b) Iron

**Figure 6.13**: Data-MC comparison for reconstructed zenith angles for proton MC (left) and iron MC (right).

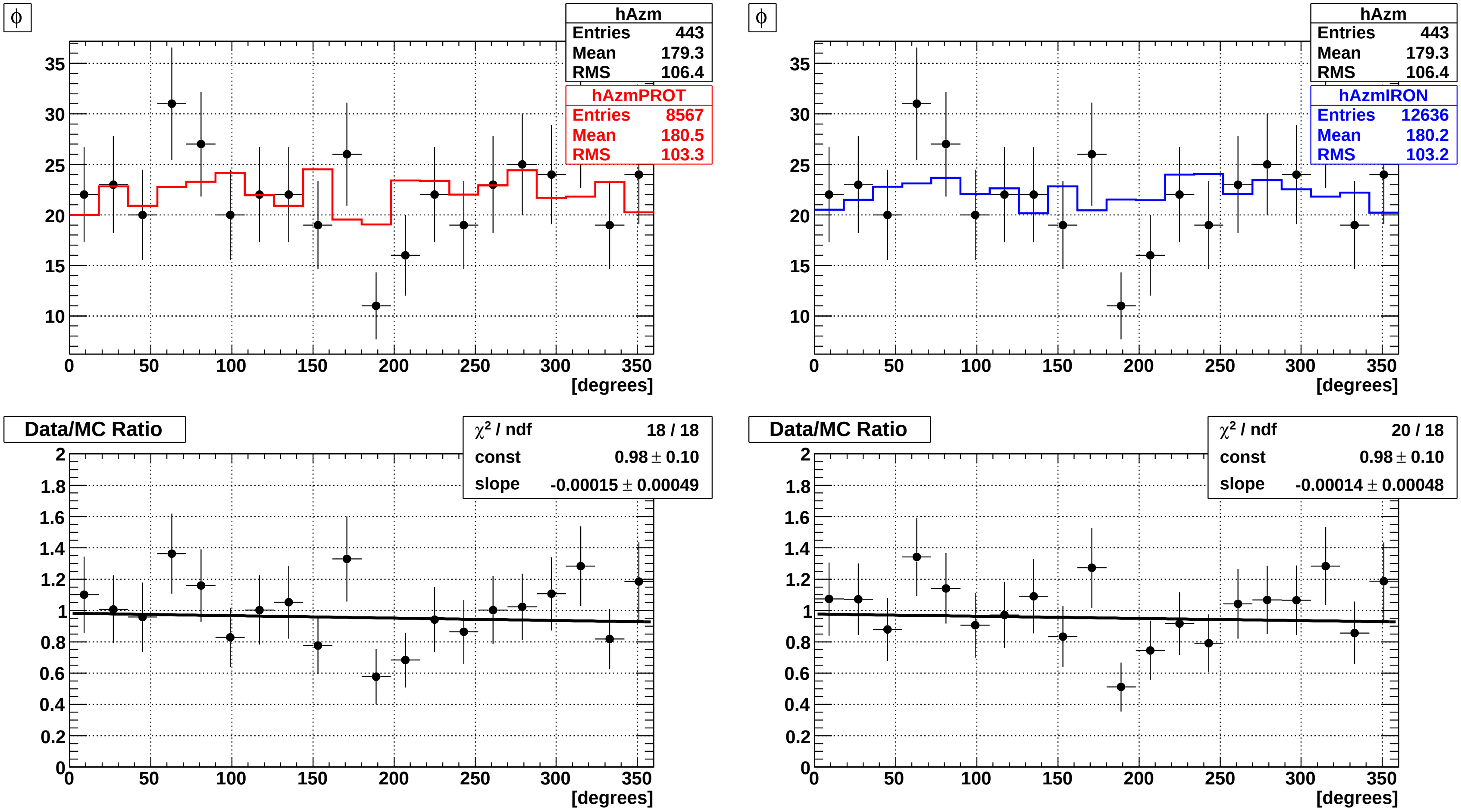

(a) Proton

(b) Iron

**Figure 6.14**: Data-MC comparison for reconstructed azimuthal angles for proton MC (left) and iron MC (right).

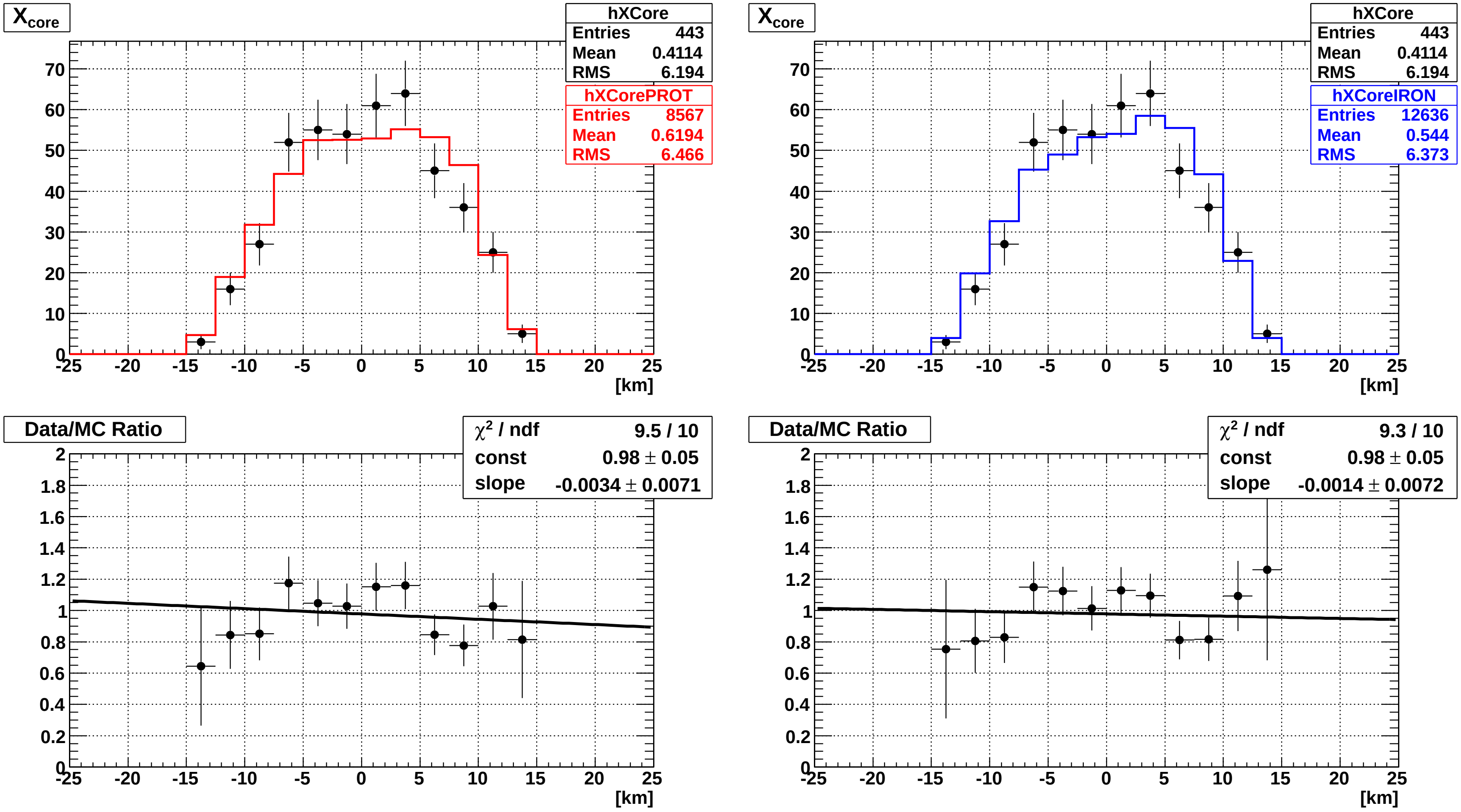

(a) Proton

(b) Iron

**Figure 6.15**: Data-MC comparison for reconstructed $X_{core}$ for proton MC (left) and iron MC (right).

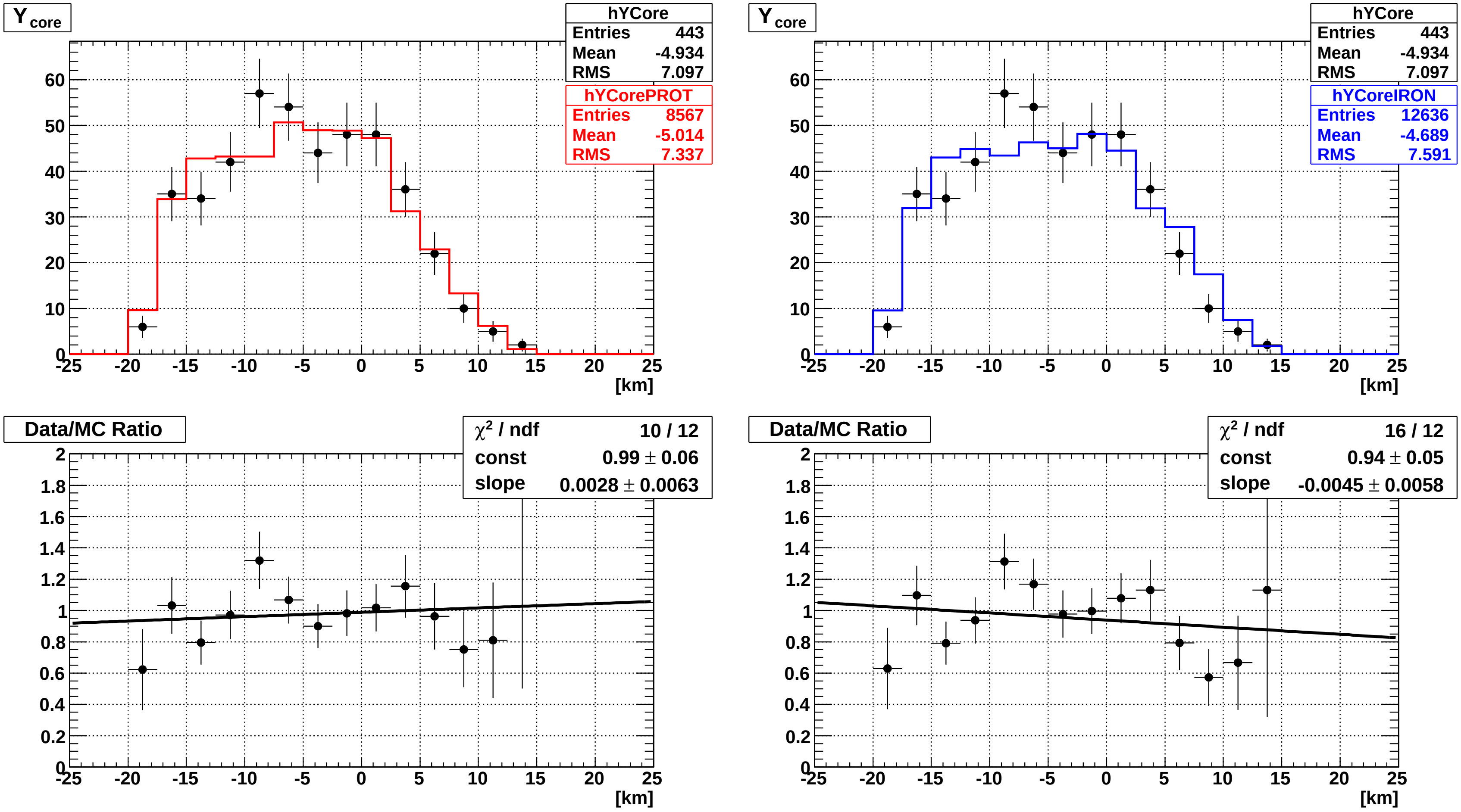

(a) Proton

(b) Iron

**Figure 6.16**: Data-MC comparison for reconstructed $Y_{core}$ for proton MC (left) and iron MC (right).

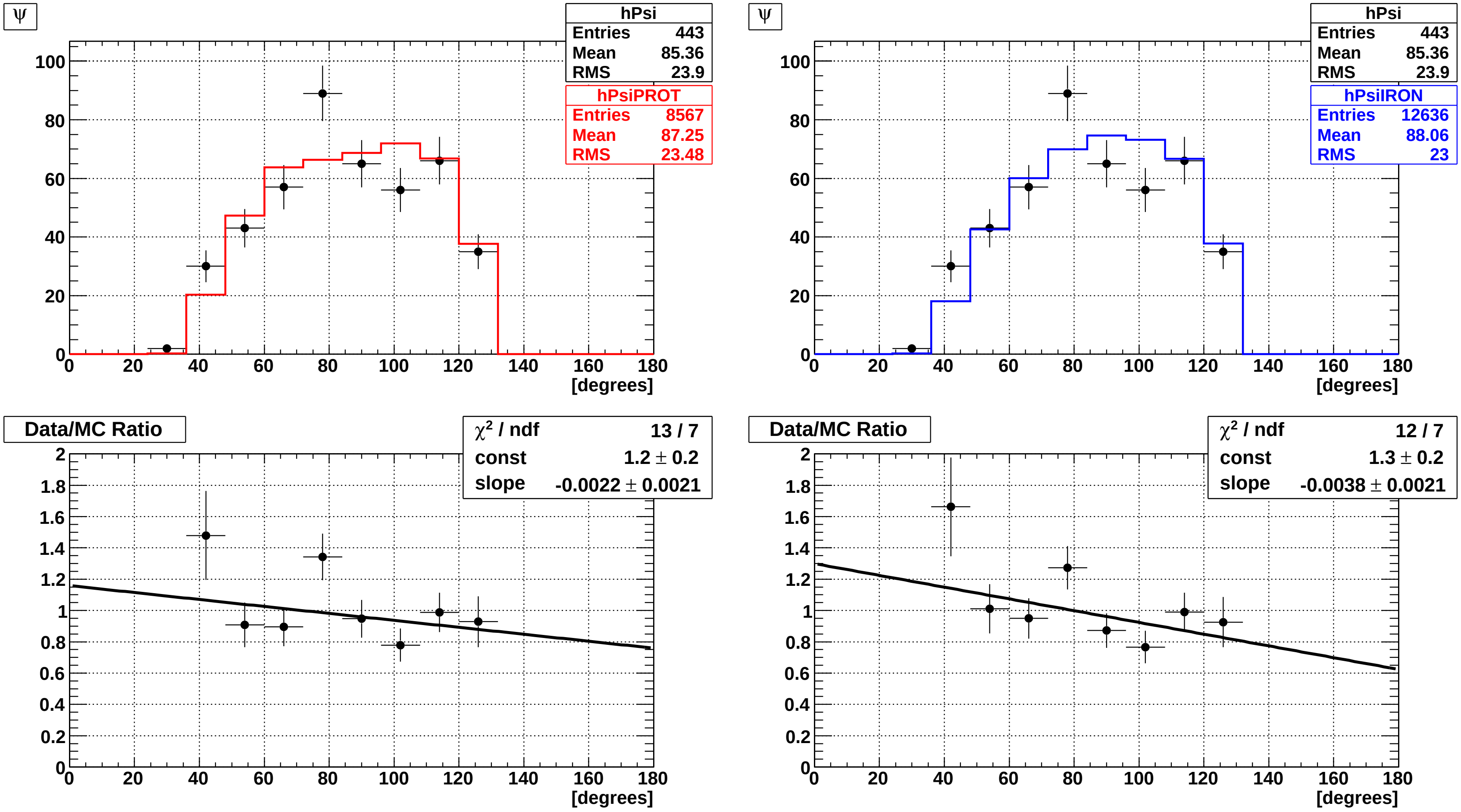

(a) Proton

(b) Iron

**Figure 6.17**: Data-MC comparison for reconstructed $\psi$ angles for proton MC (left) and iron MC (right).

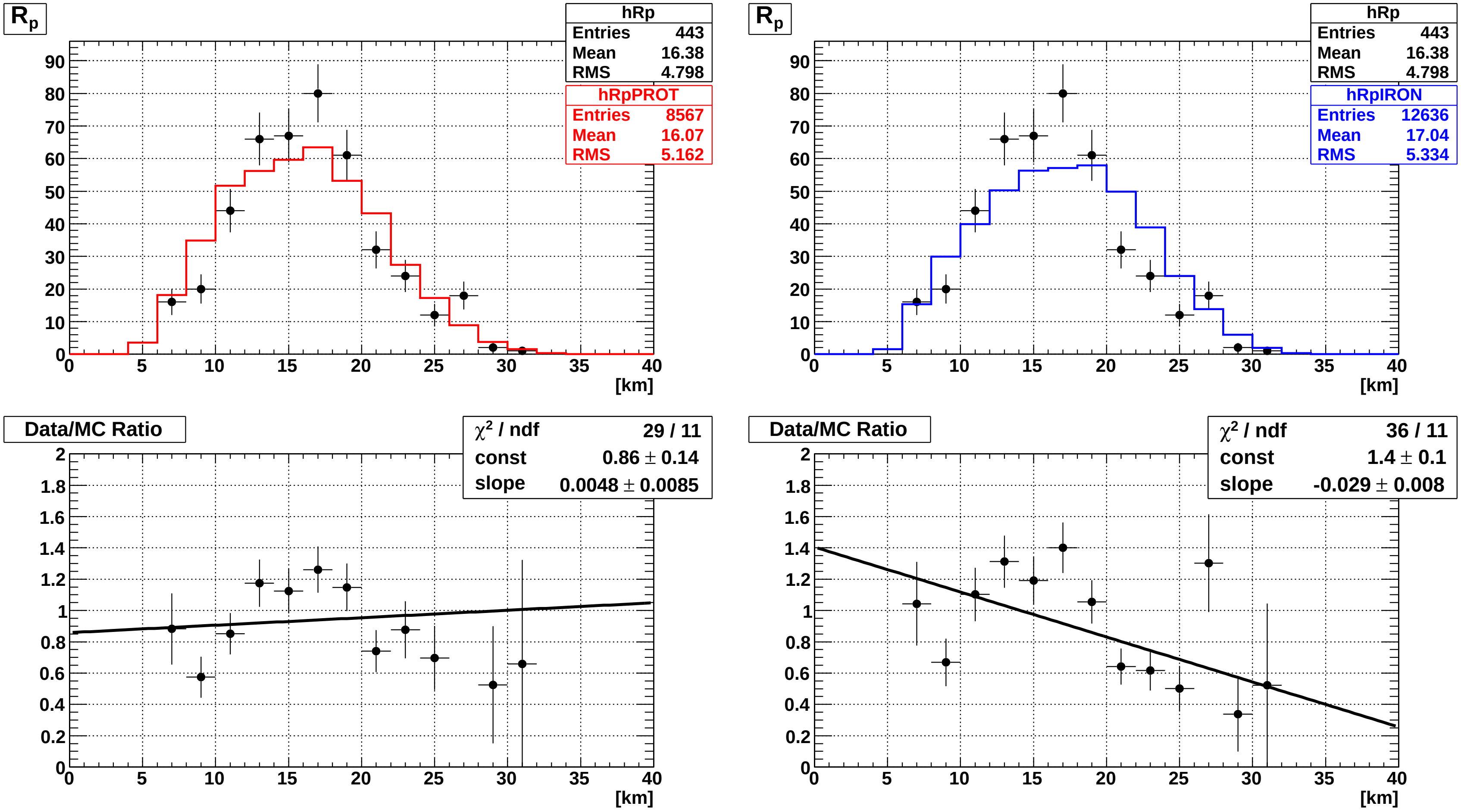

(a) Proton (b) Iron

**Figure 6.18**: Data-MC comparison for reconstructed $R_p$ for proton MC (left) and iron MC (right).

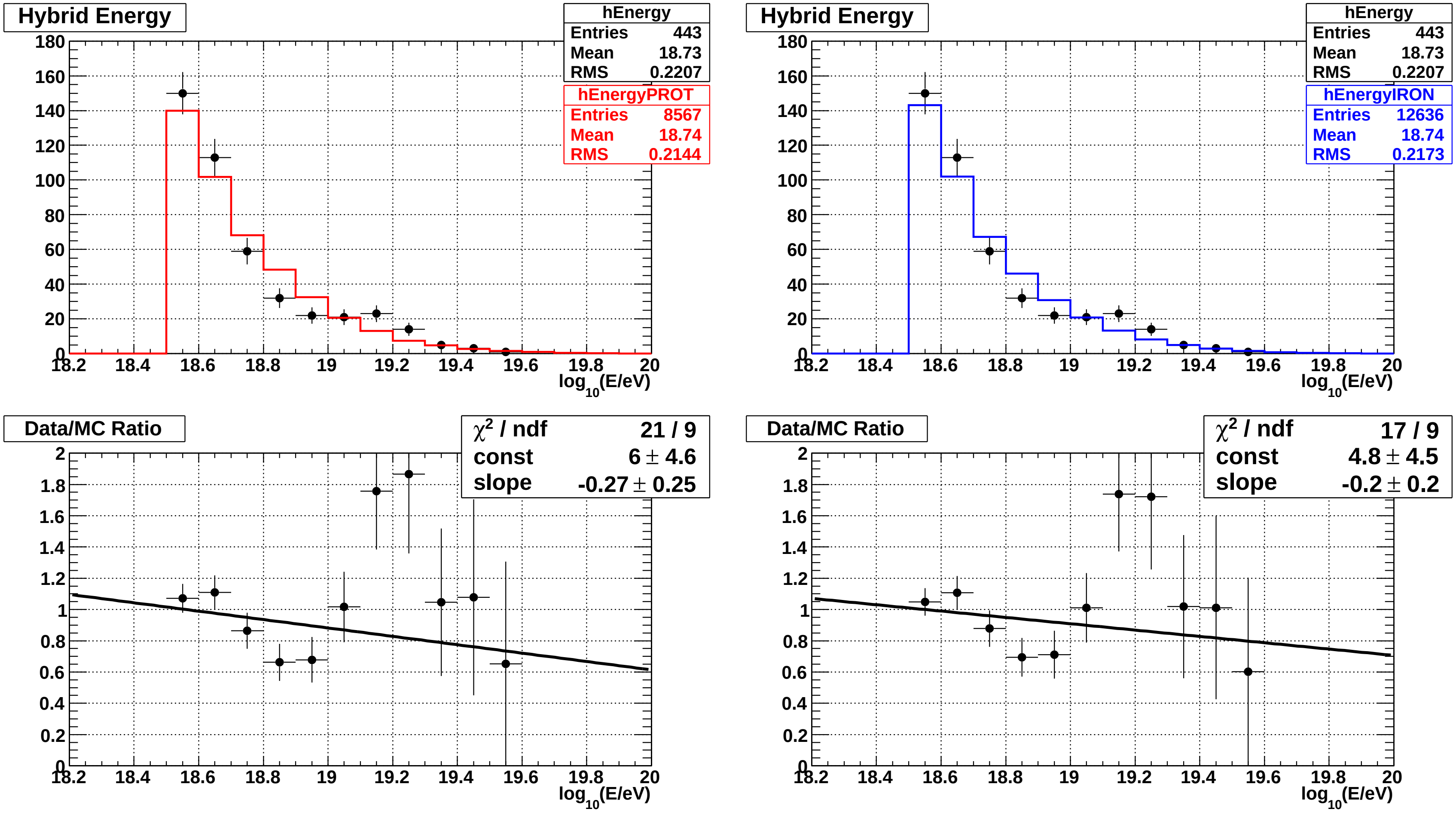

(a) Proton

(b) Iron

**Figure 6.19**: Reconstructed energy data-MC comparison for proton (left) and iron (right).

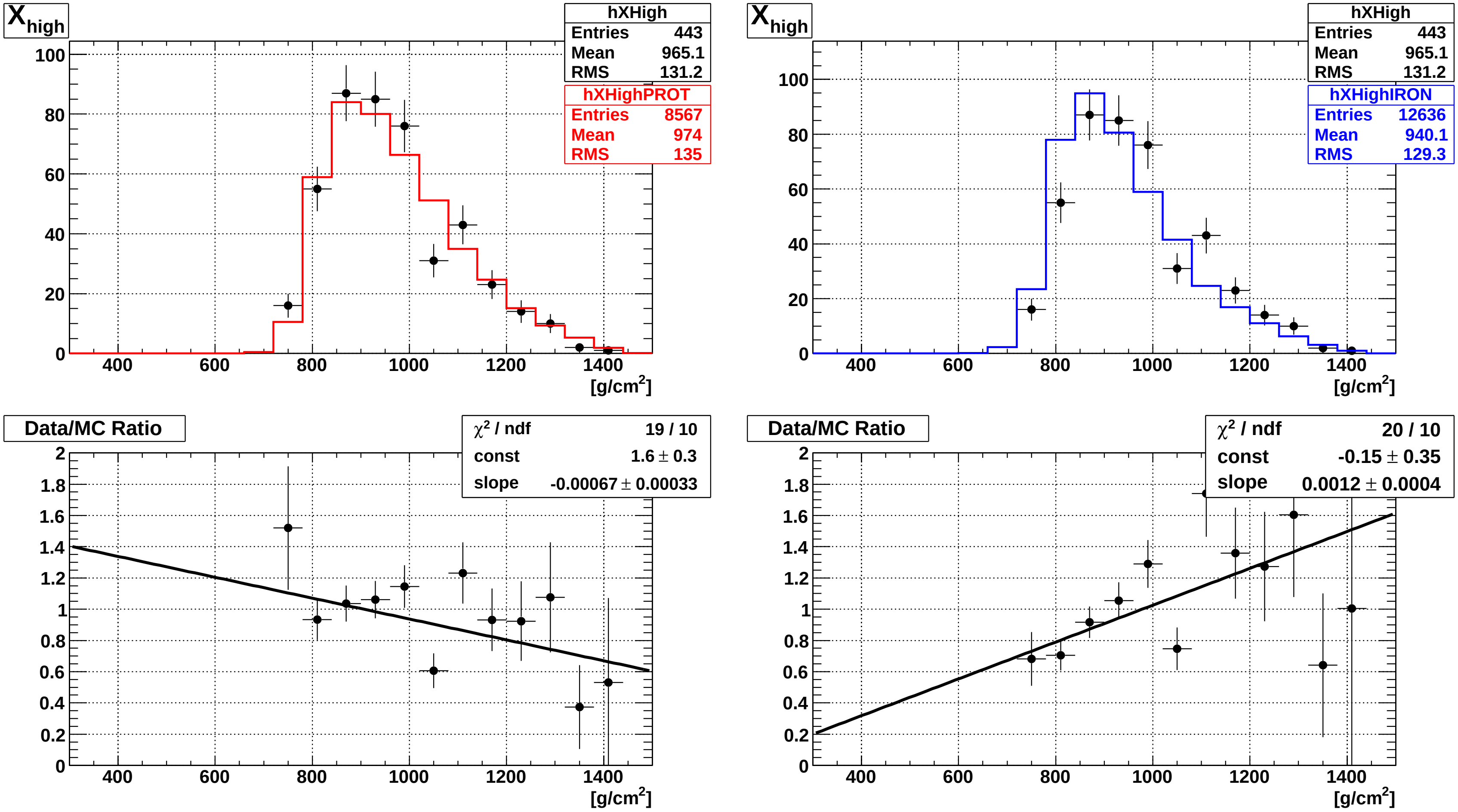

(a) Proton

(b) Iron

**Figure 6.20**: $X_{high}$ data-MC comparison for proton MC (left) and iron MC (right).

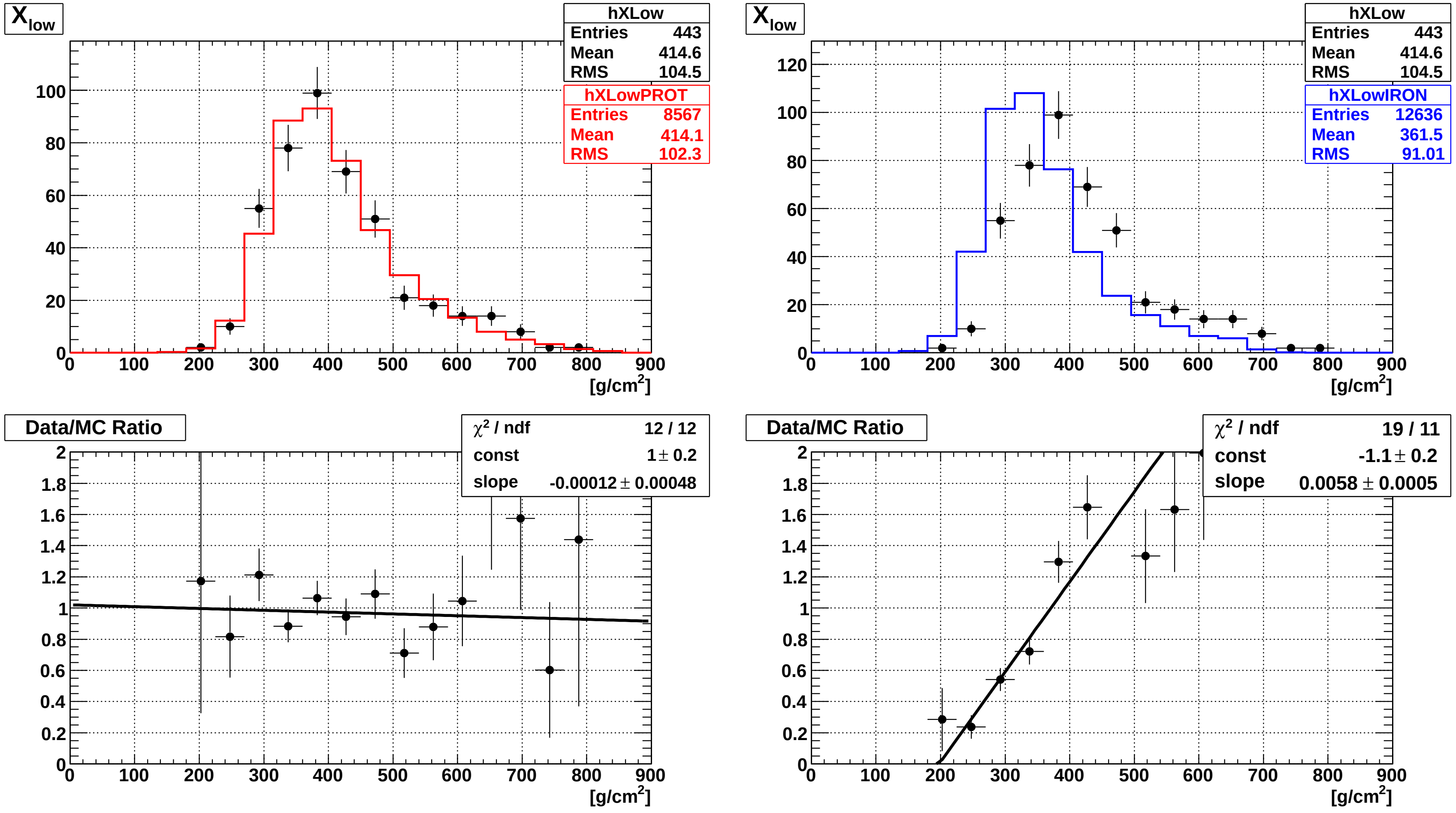

(a) Proton

(b) Iron

**Figure 6.21**: $X_{low}$ data-MC comparison for proton MC (left) and iron MC (right).

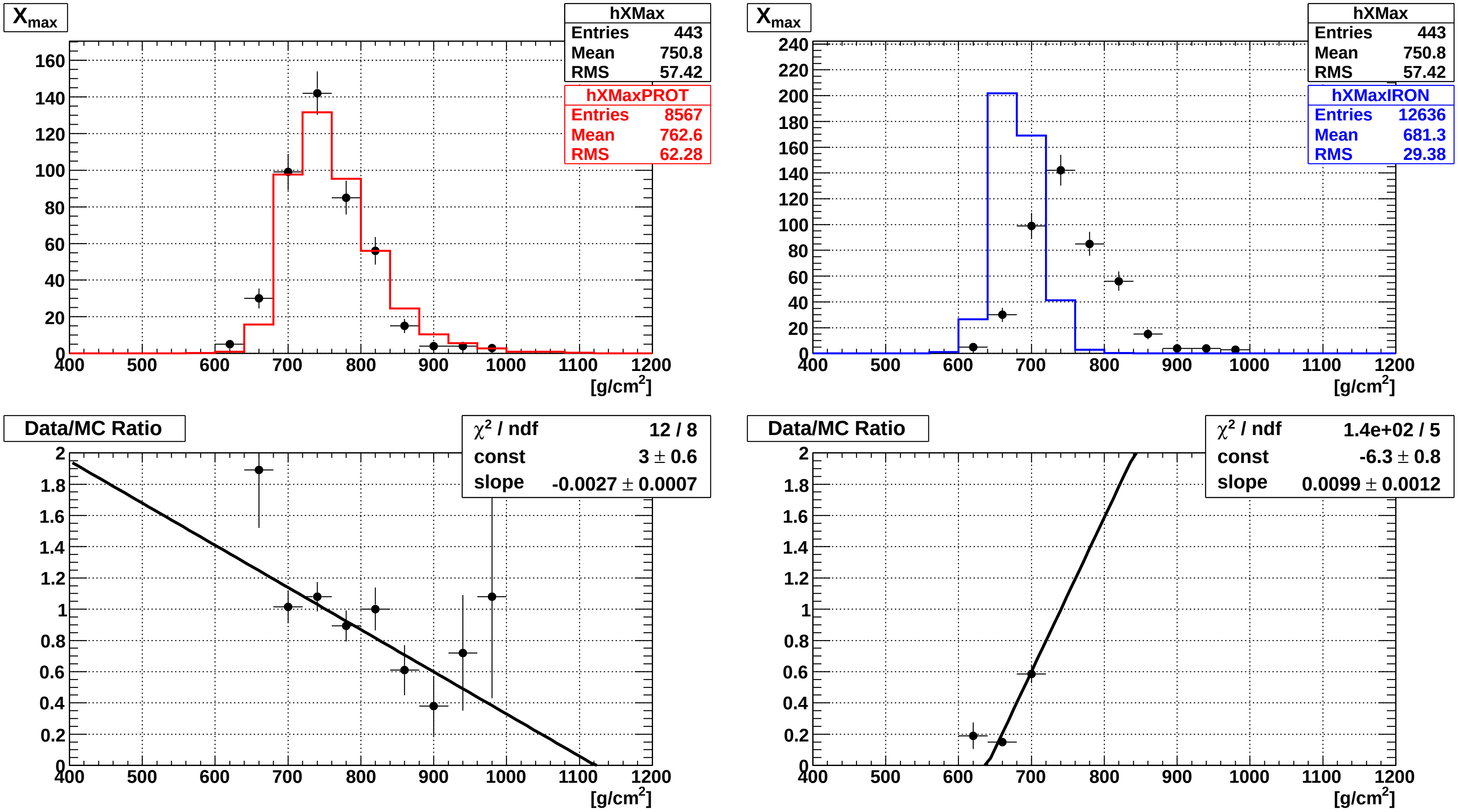

(a) Proton

(b) Iron

**Figure 6.22**: $X_{max}$ data-MC comparison for proton MC (left) and iron MC (right).

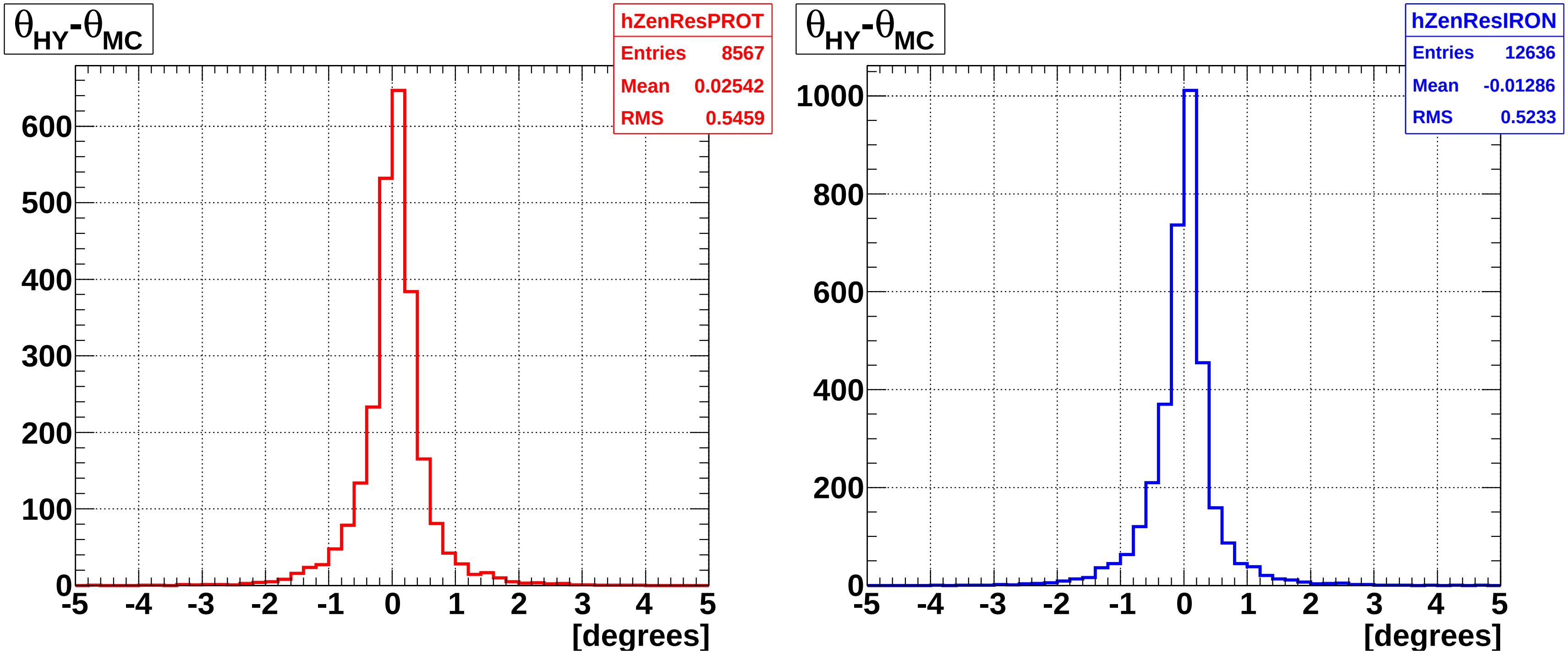

(a) Proton (b) Iron

**Figure 6.23**: Resolution of reconstructed zenith angles for proton MC (left) and iron MC (right) The resolution in reconstructed zenith angles is 0.5° for both proton and iron MC.

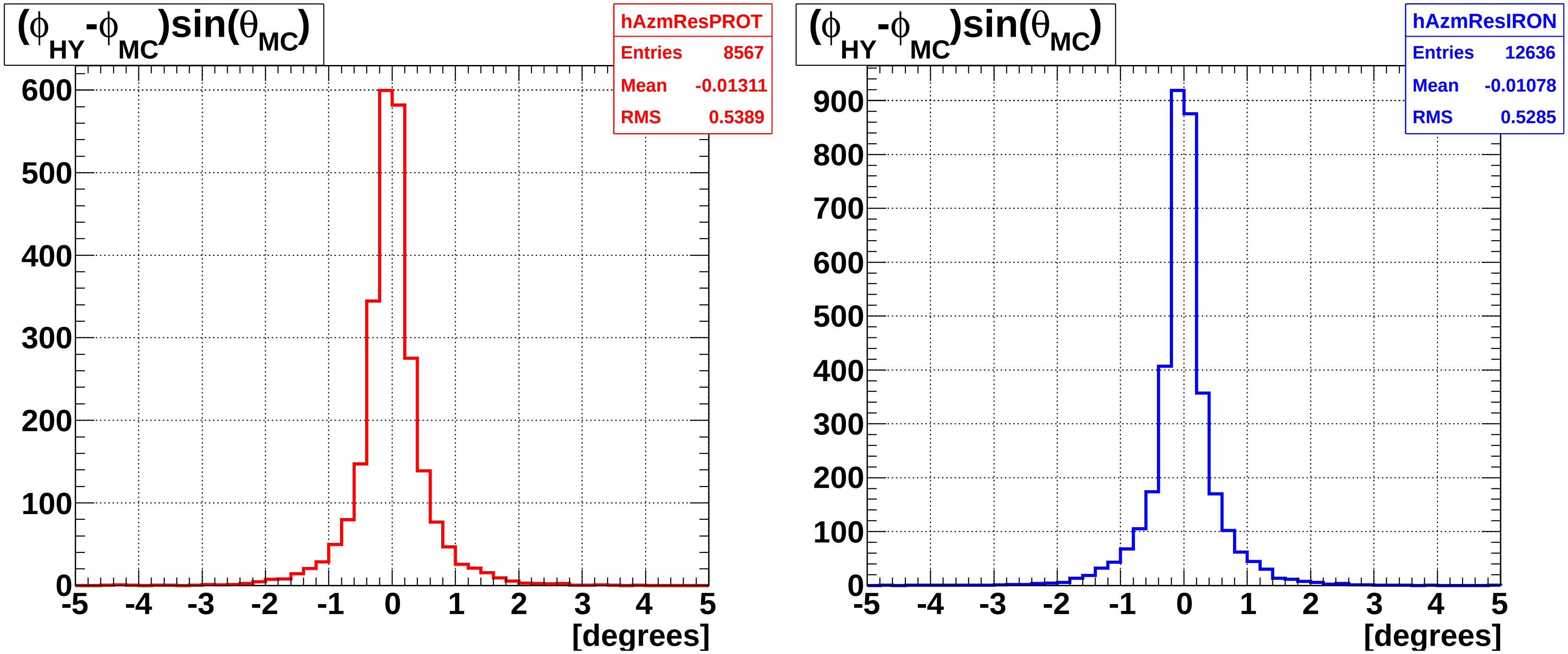

(a) Proton

(b) Iron

**Figure 6.24**: Resolution of reconstructed azimuthal angles for proton MC (left) and iron MC (right). The resolution in reconstructed azimuthal angle is 0.5° for both proton and iron MC.

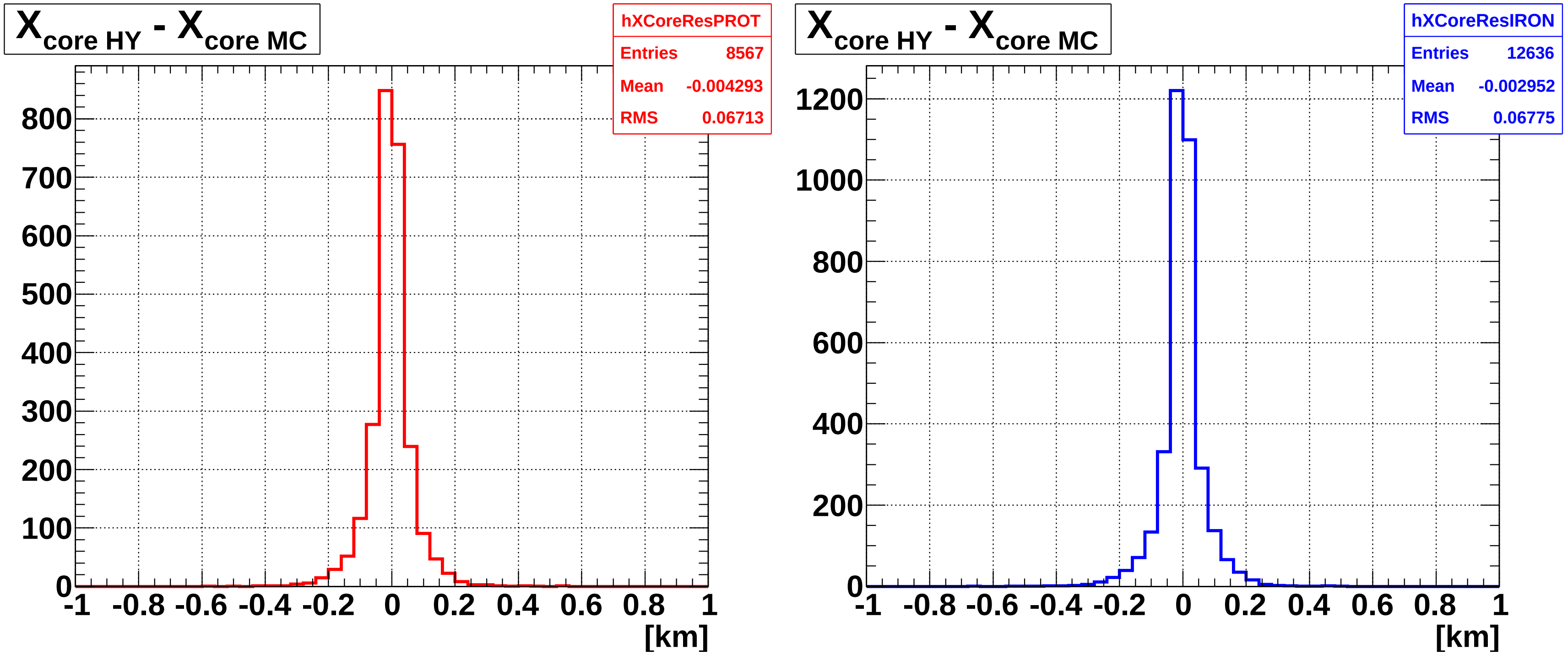

(a) Proton

(b) Iron

**Figure 6.25**: Reconstructed x position of where the air shower reaches the CLF plane for proton MC (left) and iron MC (right). The resolution in $X_{core}$ is 60 meters.

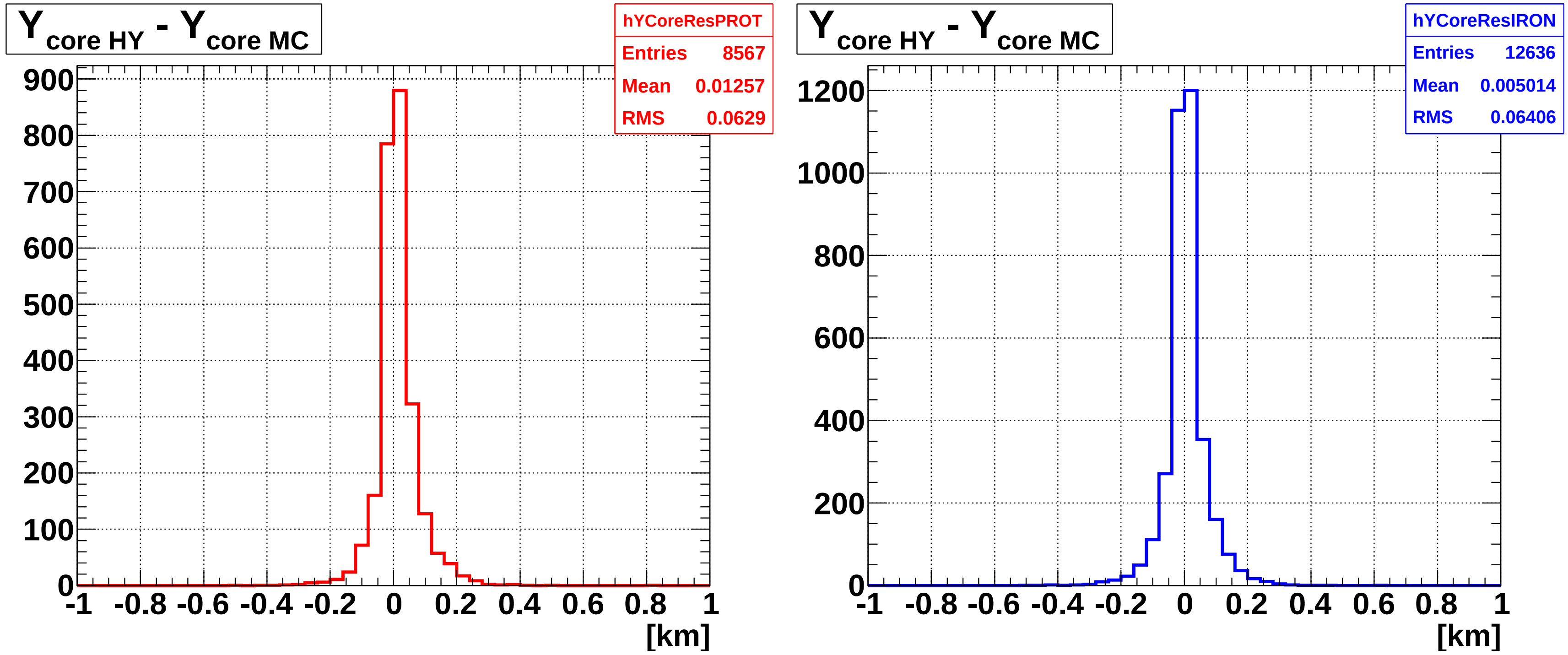

(a) Proton

(b) Iron

**Figure 6.26**: Reconstructed y position of where the air shower reaches the CLF plane for proton MC (left) and iron MC (right). The resolution in $Y_{core}$ is 60 meters.

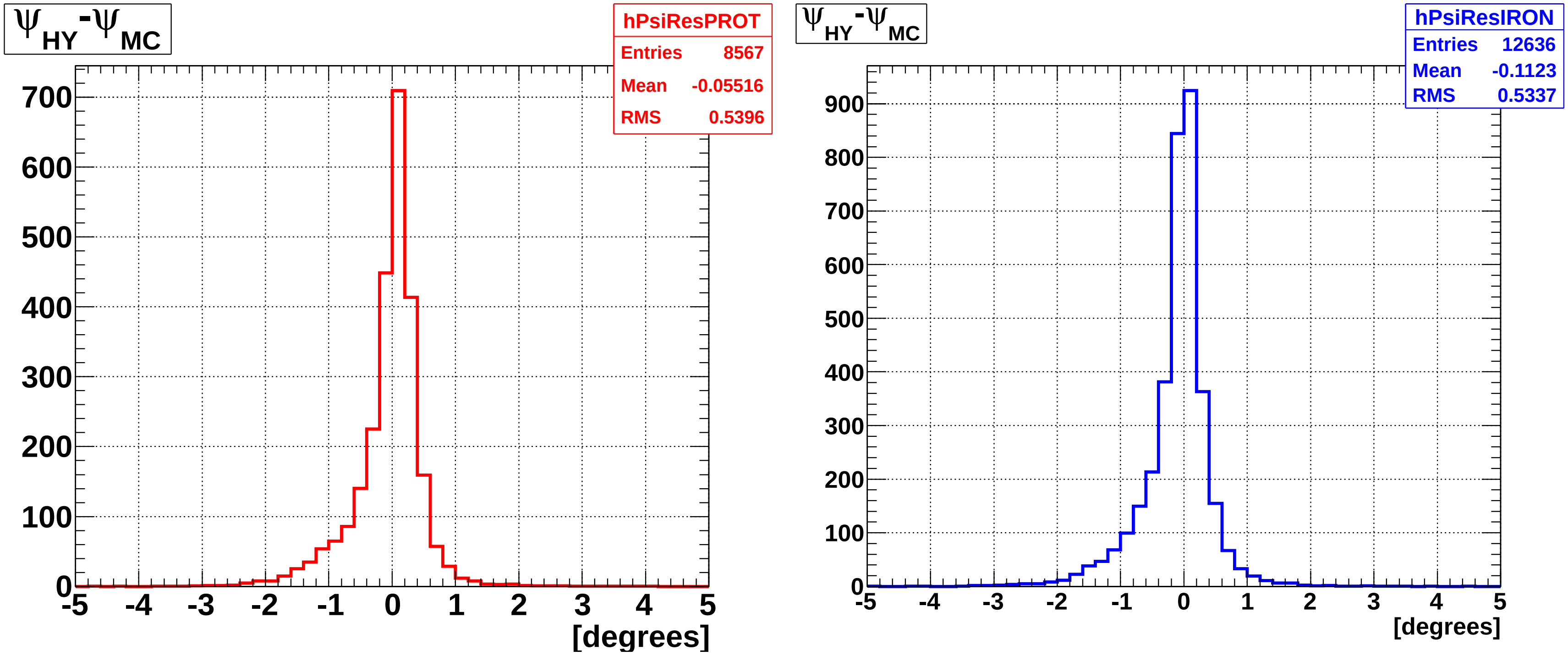

(a) Proton

(b) Iron

**Figure 6.27**: Resolution of reconstructed $\psi$ angles for proton MC (left) and iron MC (right). The resolution in reconstructed azimuthal angle is 0.5° for both proton and iron MC.

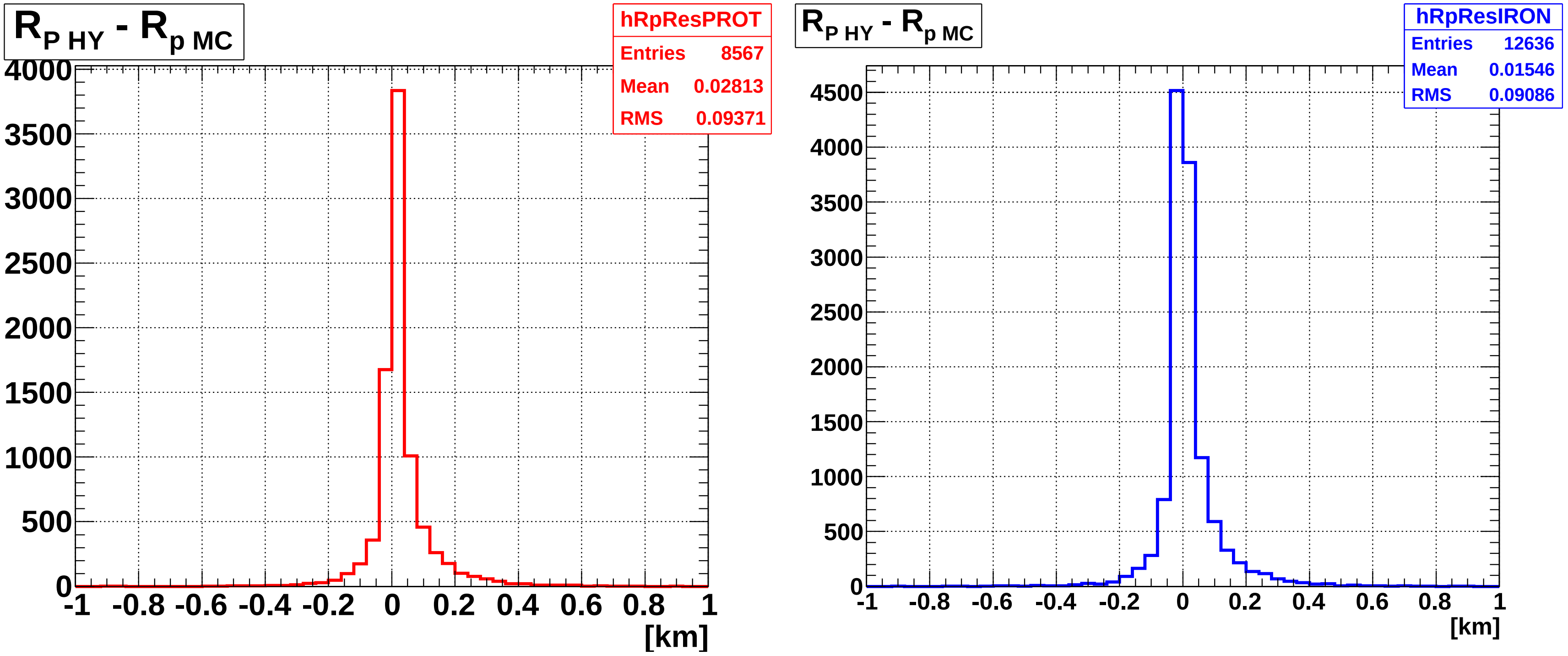

(a) Proton

(b) Iron

**Figure 6.28**: Resolution in reconstructed $R_p$ for proton MC (left) and iron MC (right). The resolution in $R_p$ is 90 meters for both proton and iron MC.

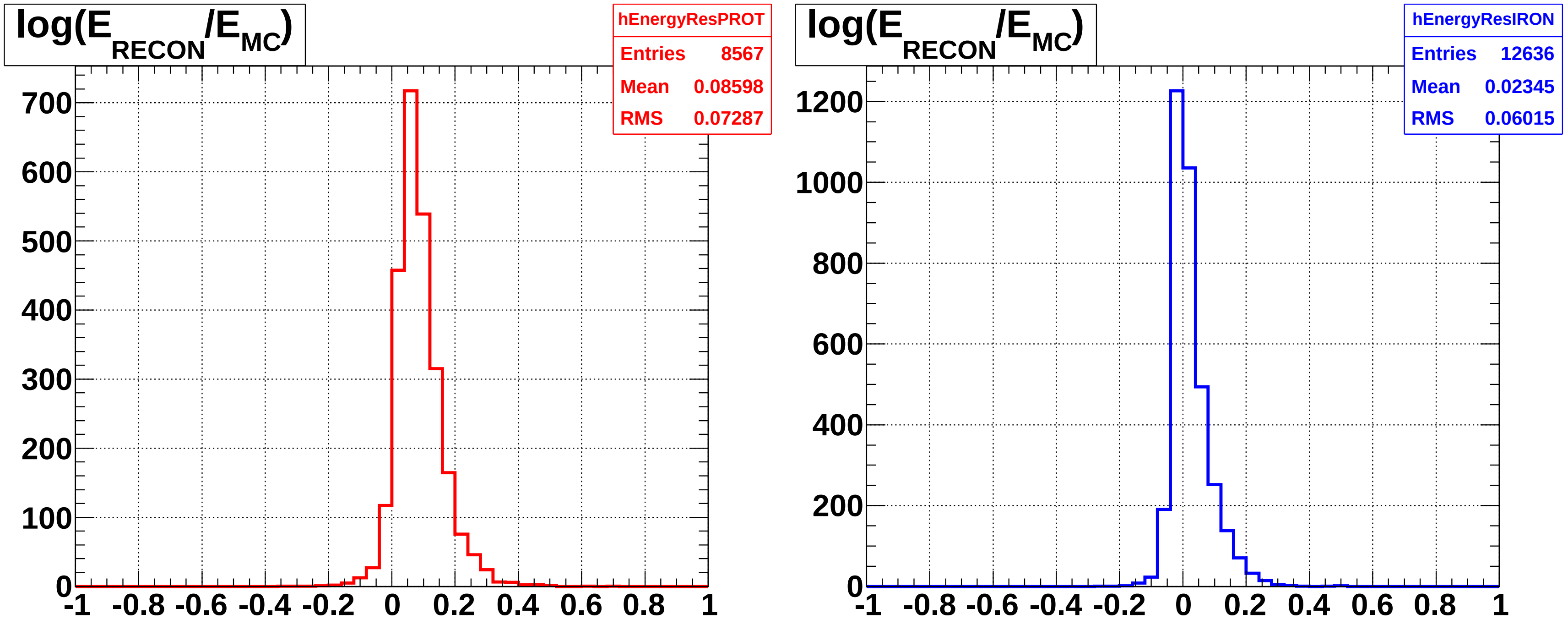

(a) Proton

(b) Iron

**Figure 6.29**: Resolution of reconstructed energy for proton MC (left) and iron MC (right). The resolution of proton MC is 7% and 6% for iron MC. The proton MC has a reconstruction bias of 8.5%, however, the iron MC has a reconstruction bias of only 2.5%.

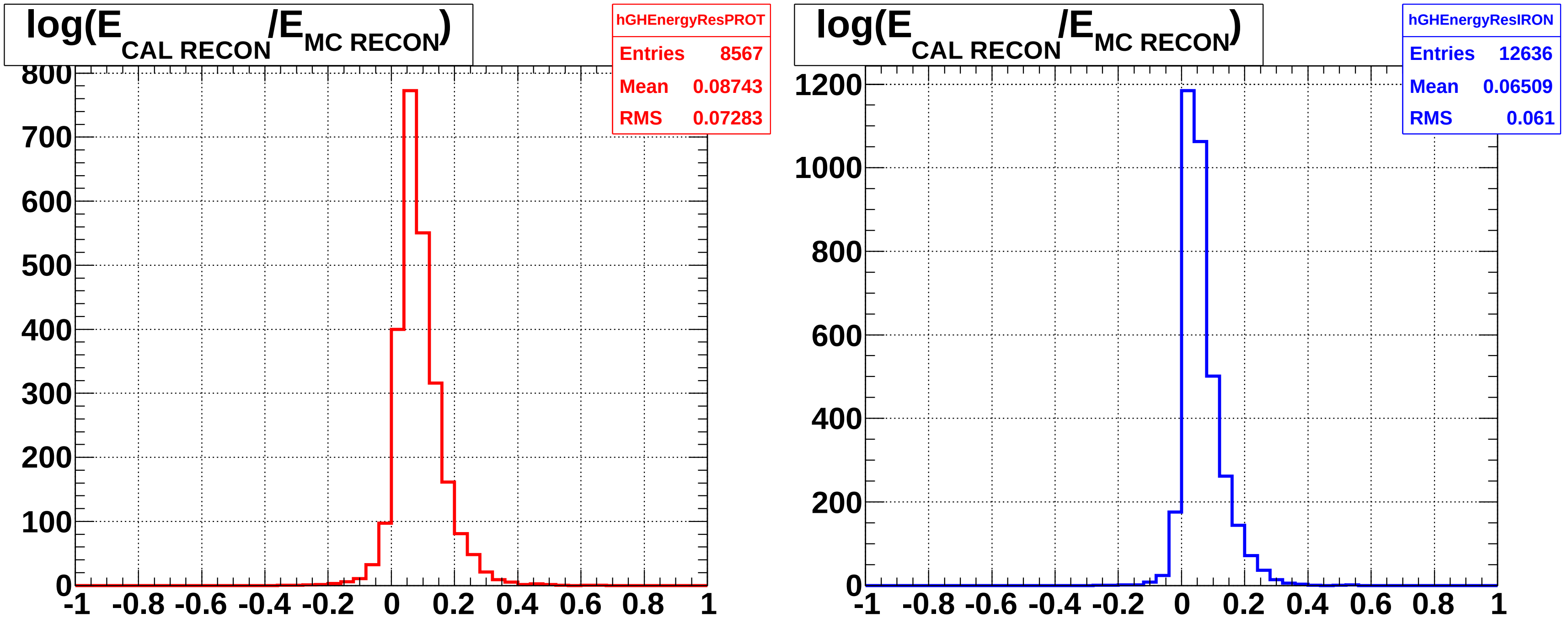

(a) Proton

(b) Iron

**Figure 6.30**: Resolution of reconstructed calorimetric energy for proton MC (left) and iron MC (right). The resolution for proton MC is 7% and 6% for iron MC. The proton MC has a reconstruction bias of 8.7%. The iron MC has a smaller reconstruction bias of 6.7%.

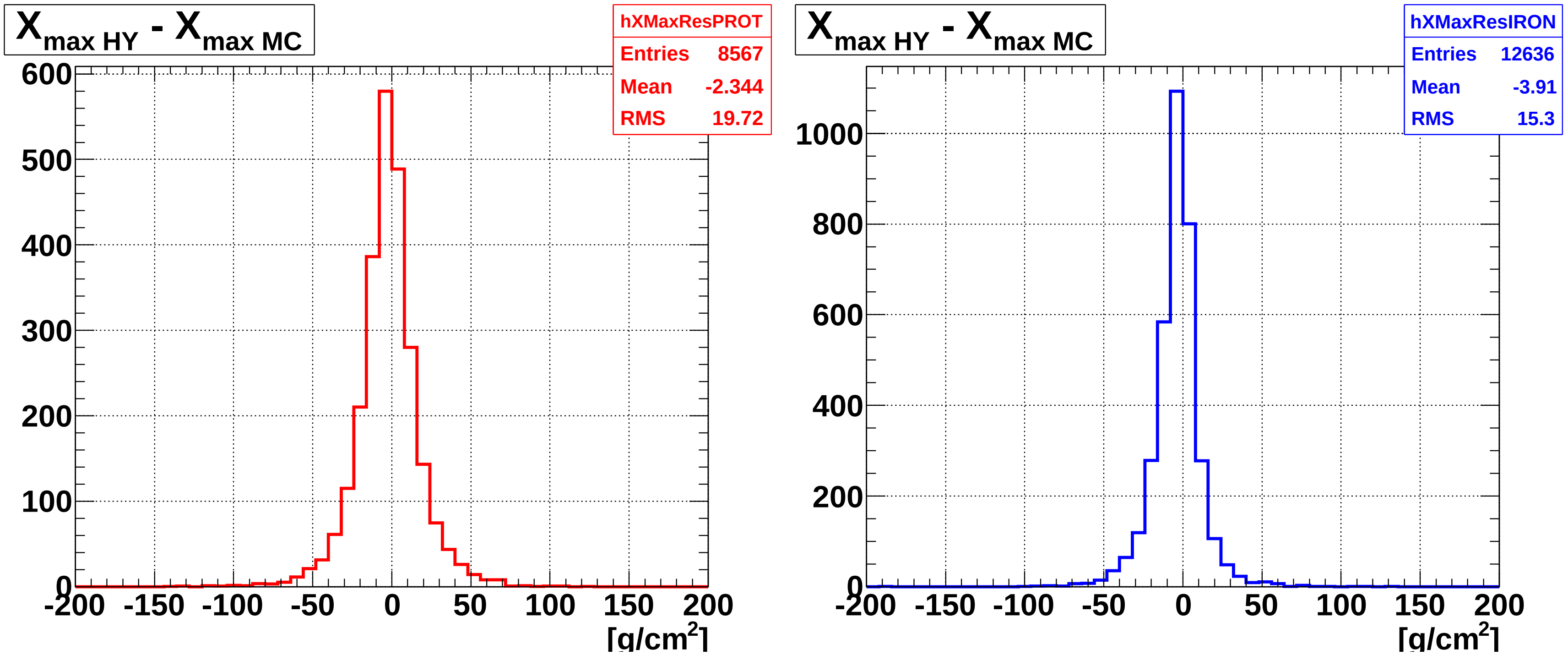

(a) Proton

(b) Iron

**Figure 6.31**: Resolution of reconstructed $X_{max}$ for proton MC (left) and iron MC (right). The resolution of proton MC is 20 g/cm$^2$ and 15 g/cm$^2$ for iron MC. The proton MC has a reconstruction bias of -2 g/cm$^2$. The iron MC has a reconstruction bias of -4 g/cm$^2$.

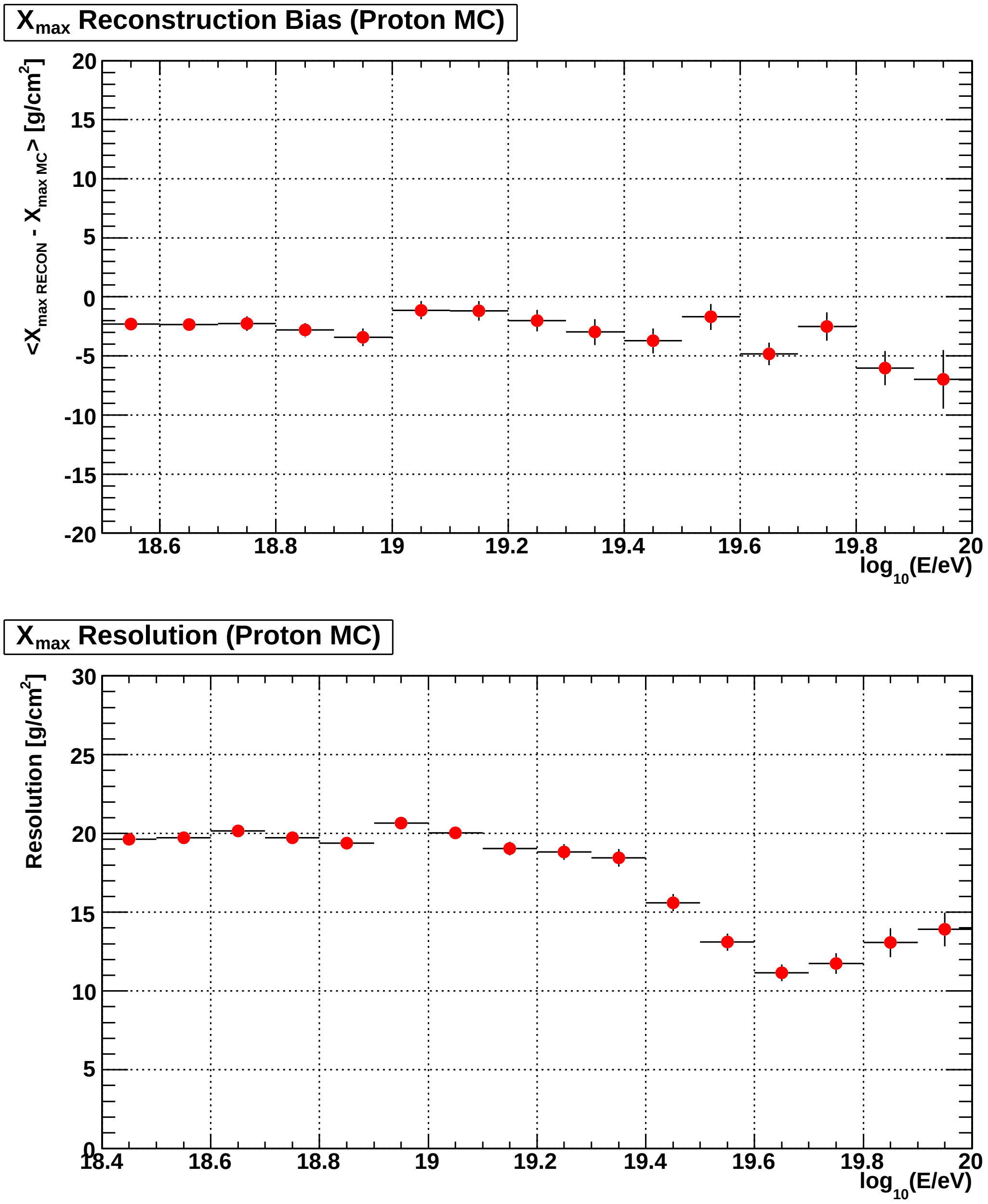

**Figure 6.32**: $X_{max}$ Reconstruction bias (upper plot) and resolution for proton MC. The resolution is 20 g/cm$^2$ for all energies.

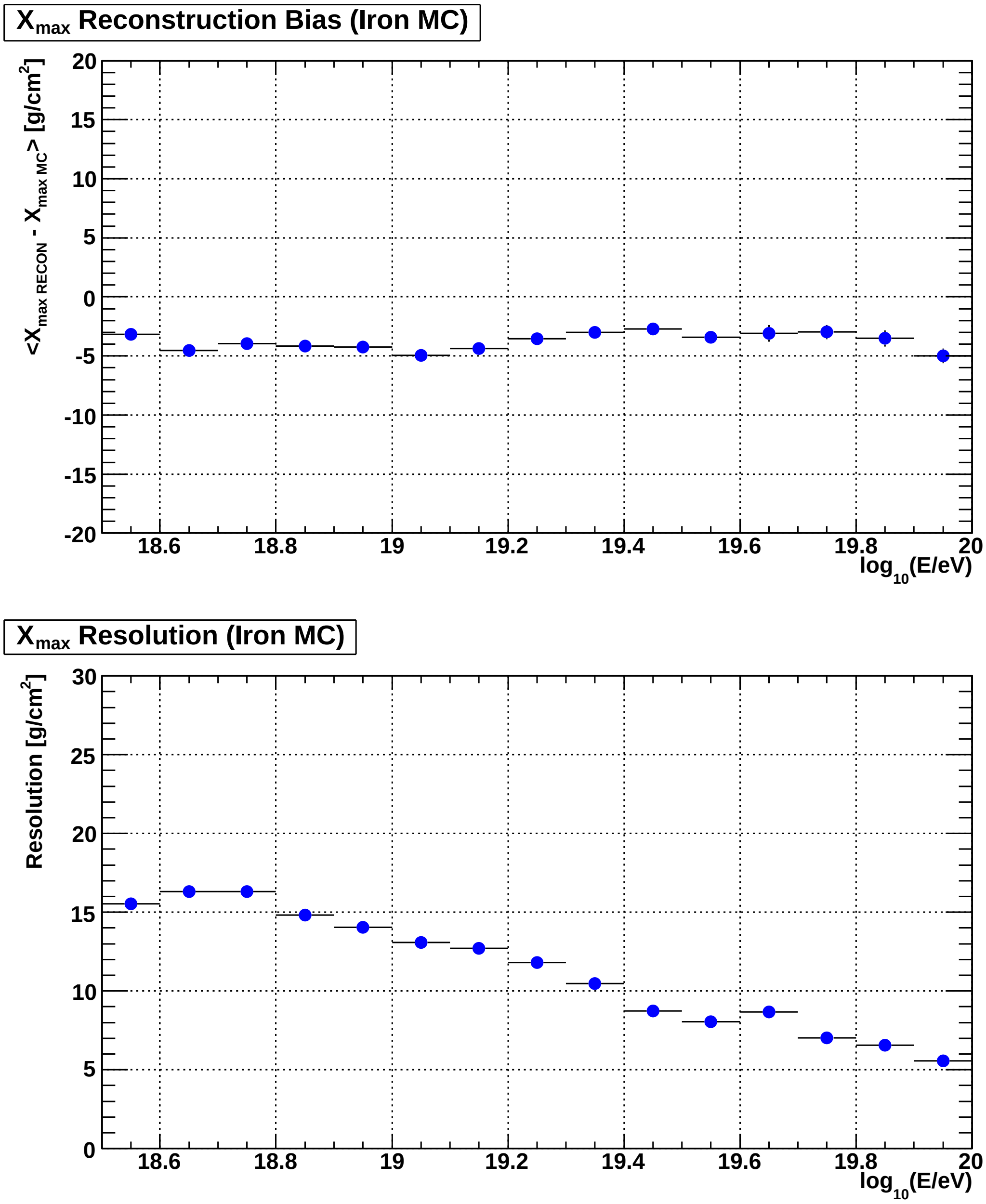

**Figure 6.33**: $X_{max}$ Reconstruction bias (upper plot) and resolution for iron MC. The resolution is 15 g/cm$^2$ for all energies.

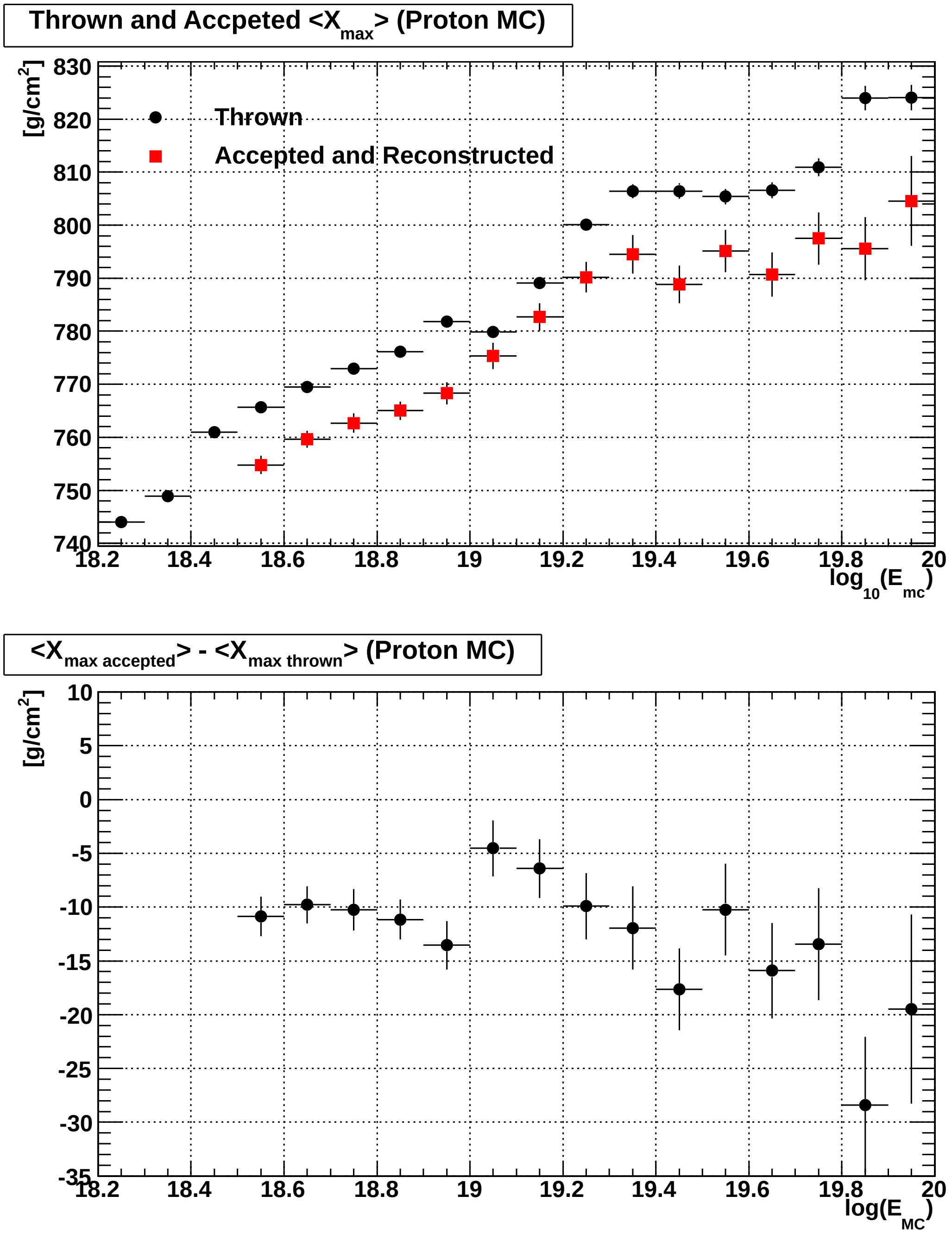

**Figure 6.34**: Thrown and accepted $X_{max}$ for proton MC.

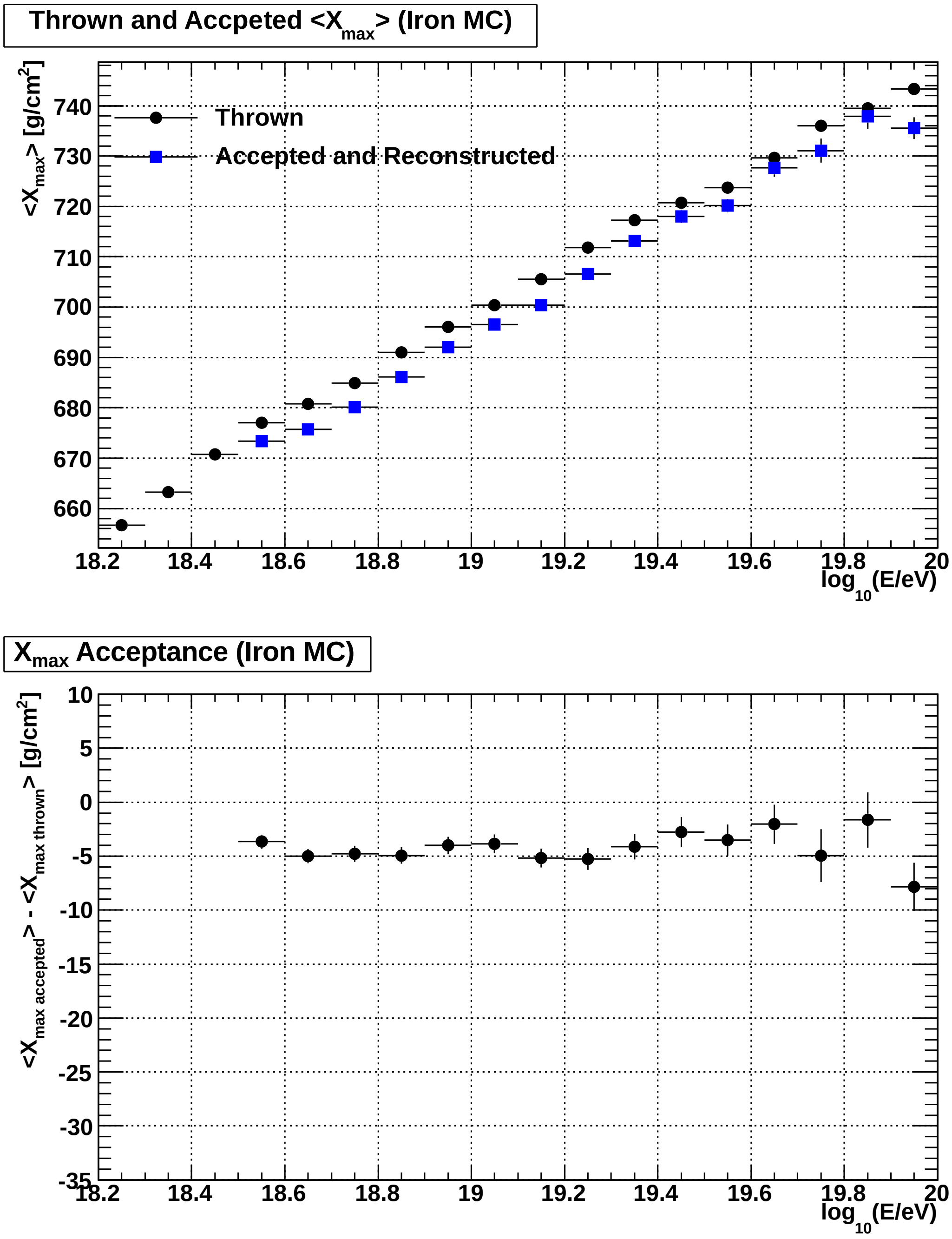

**Figure 6.35**: Thrown and accepted $X_{max}$ for proton MC.

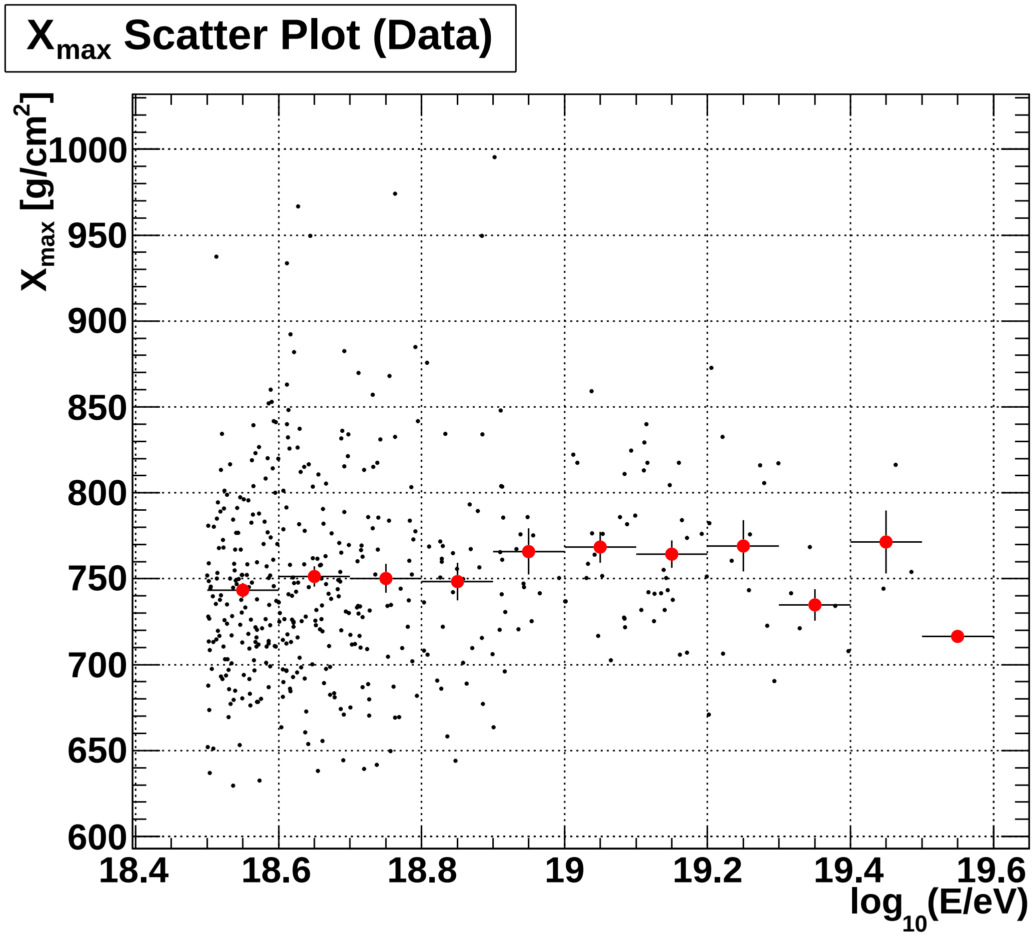

**Figure 6.36**: Scatter plot of $X_{max}$ and $\log_{10}(E/\,\mathrm{eV})$ for all data events that pass the quality s discussed in Section 6.1. The red points is the mean $X_{max}$ in each bin. Above $10^{19.3}$ eV the statistics are low to resolve iron or proton distributions.

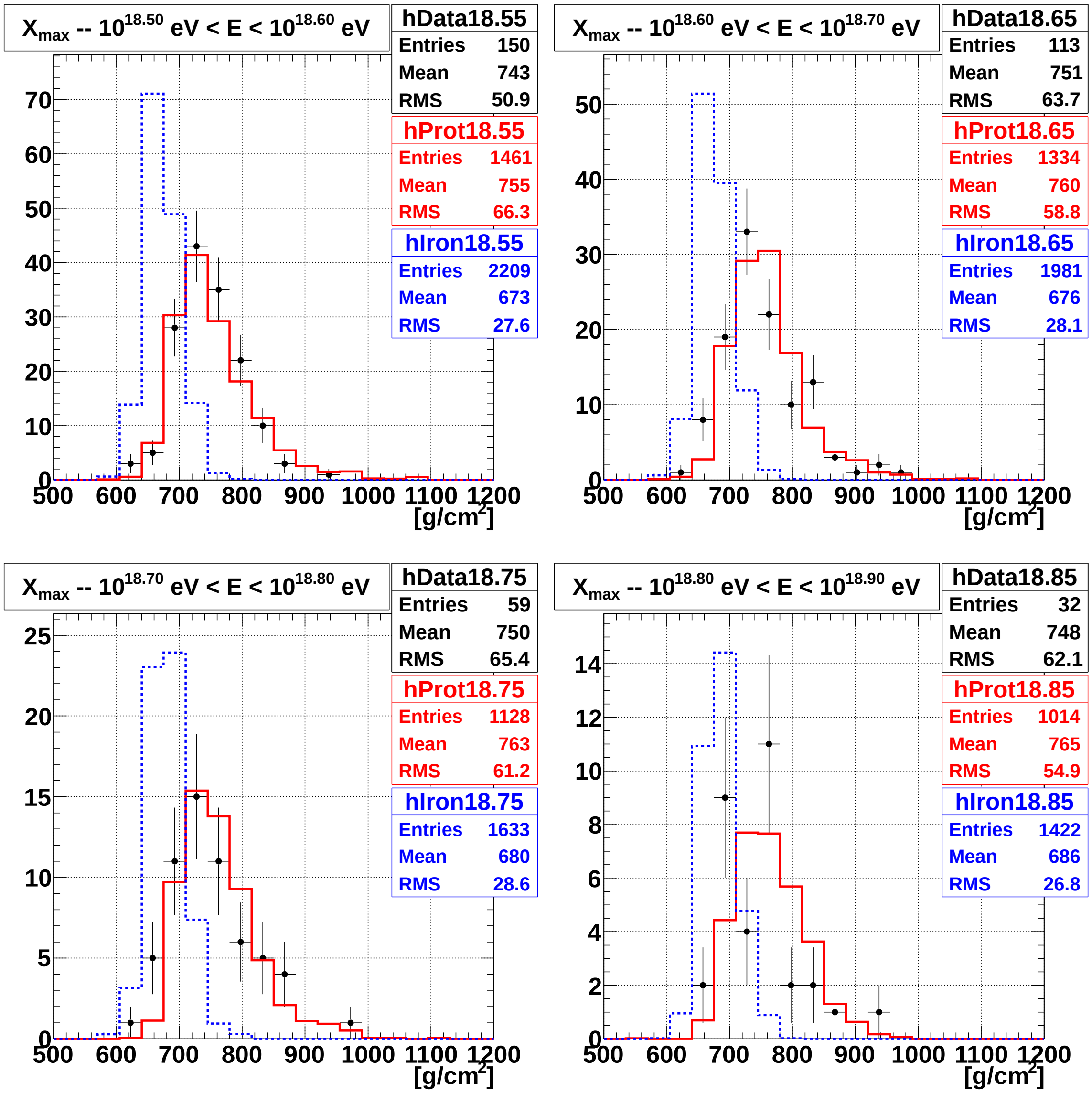

**Figure 6.37**: $X_{max}$ distribution for data and proton MC and iron MC for energy greater than $10^{18.5}$ eV and less than $10^{18.9}$ eV. In each figure, the data is shown with points, proton MC is with a solid histogram, and iron MC with a dashed histogram.

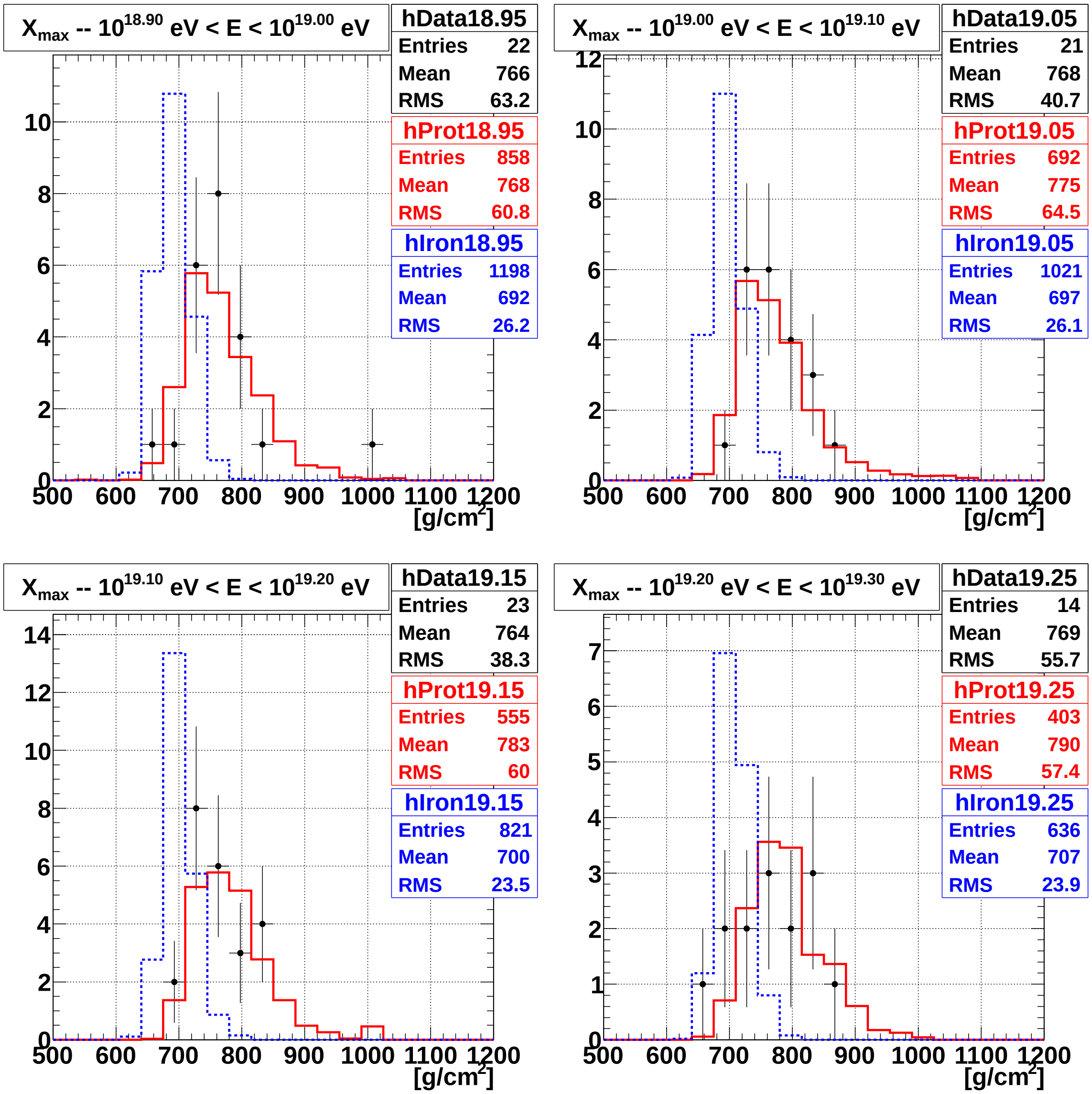

**Figure 6.38**: $X_{max}$ distribution for data and proton MC and iron MC for energy greater than $10^{18.9}$ eV and less than $10^{19.3}$ eV. In each figure, the data is shown with points, proton MC is with a solid histogram, and iron MC with a dashed histogram.

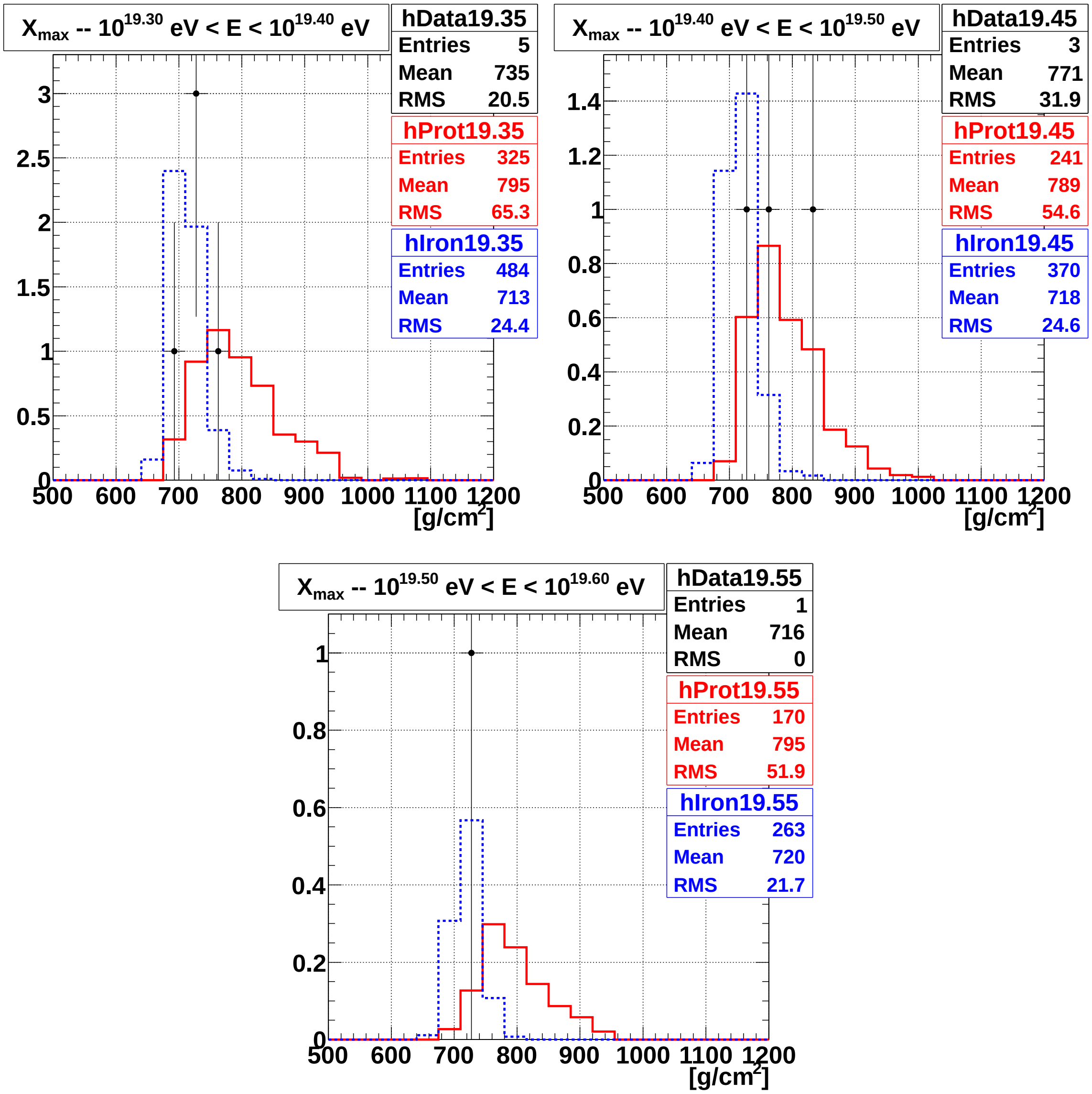

**Figure 6.39**: $X_{max}$ distribution for data and proton MC and iron MC for energy greater than $10^{19.3}$ eV. In each figure, the data is shown with points, proton MC is with a solid histogram, and iron MC with a dashed histogram. Due to poor statistics, the data is compatible with both proton and iron MC.

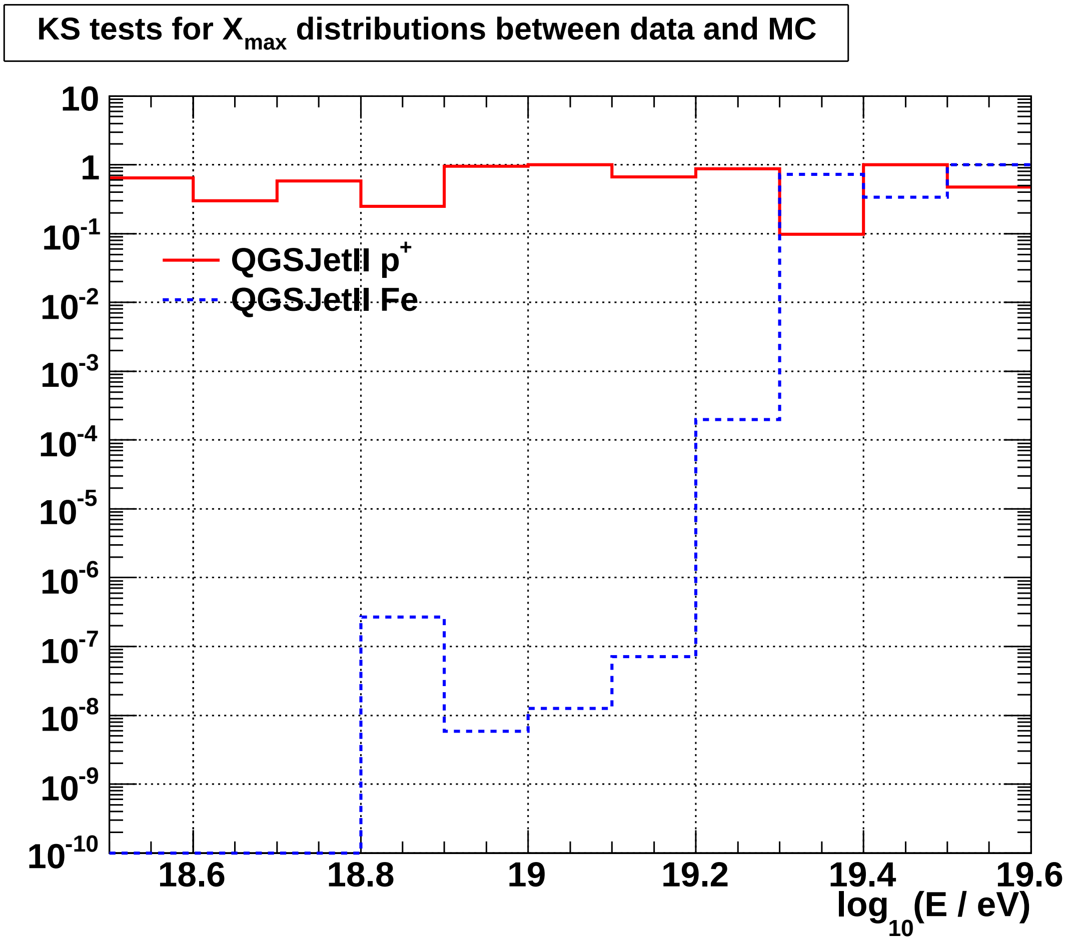

**Figure 6.40**: Results from KS tests of $X_{max}$ distributions from the data and proton and iron MC.

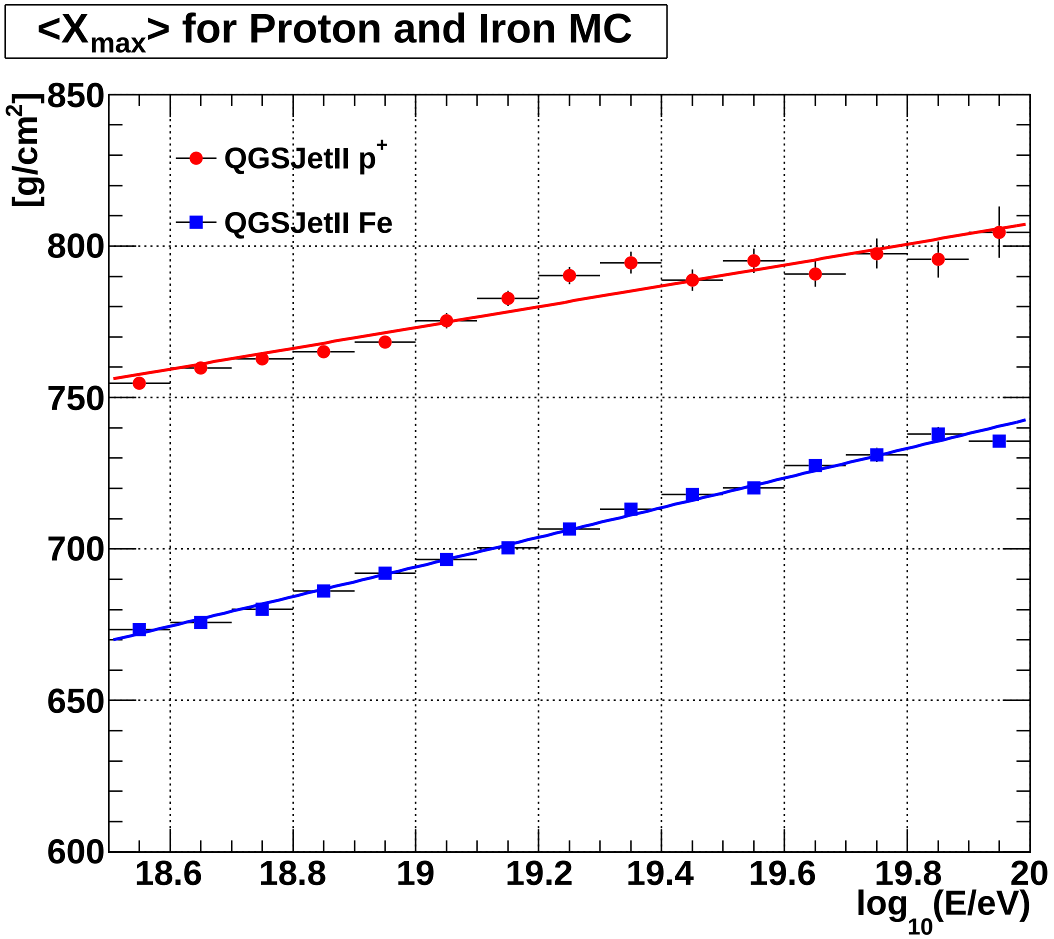

**Figure 6.41**: Elongation rate for proton and iron MC include hybrid detector simulations.

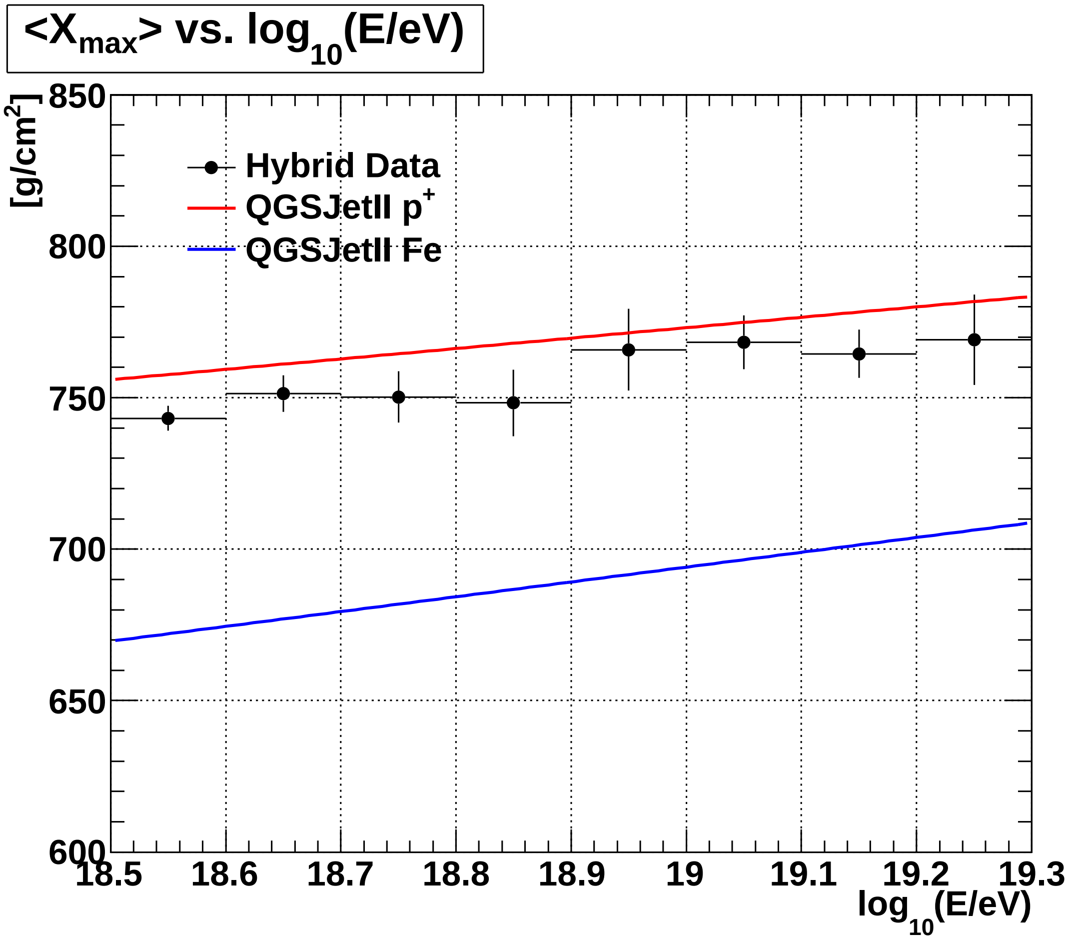

**Figure 6.42**: Experimental $< X_{max} >$ with proton and iron rails

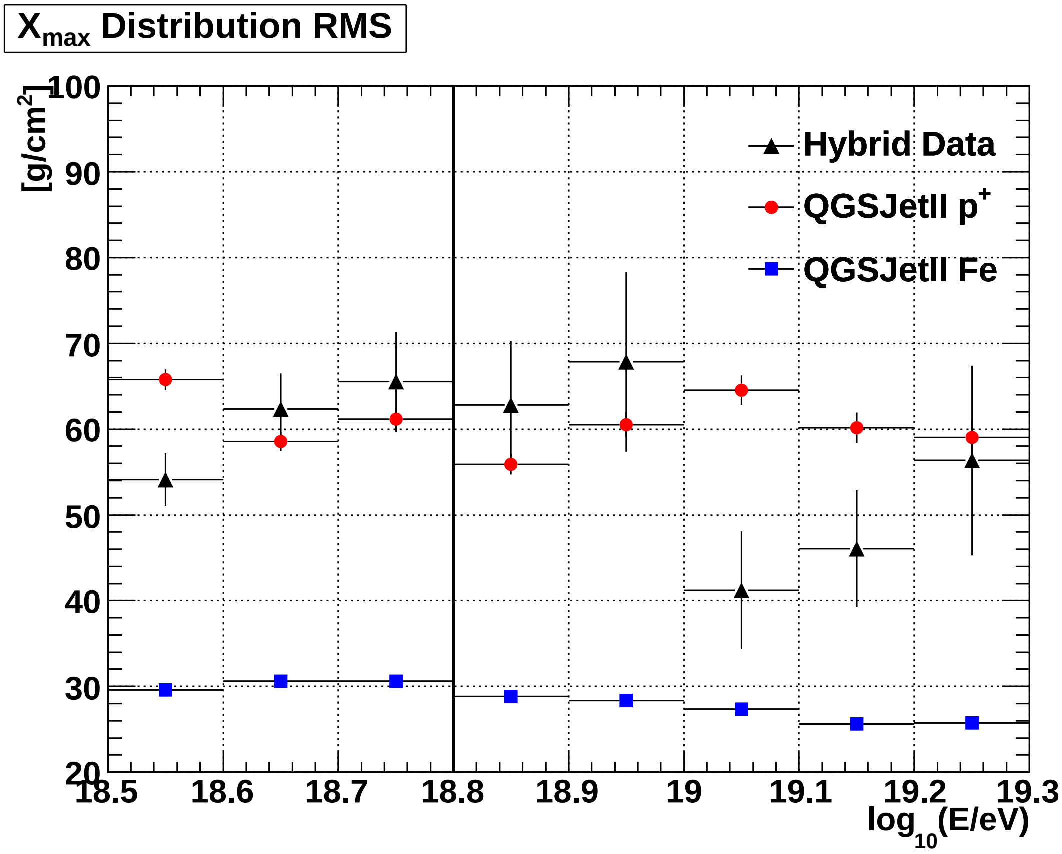

**Figure 6.43**: RMS of $X_{max}$ distributions for data and simulated proton and iron MC. Poor statistics above the solid black line make measurements of the RMS difficult.

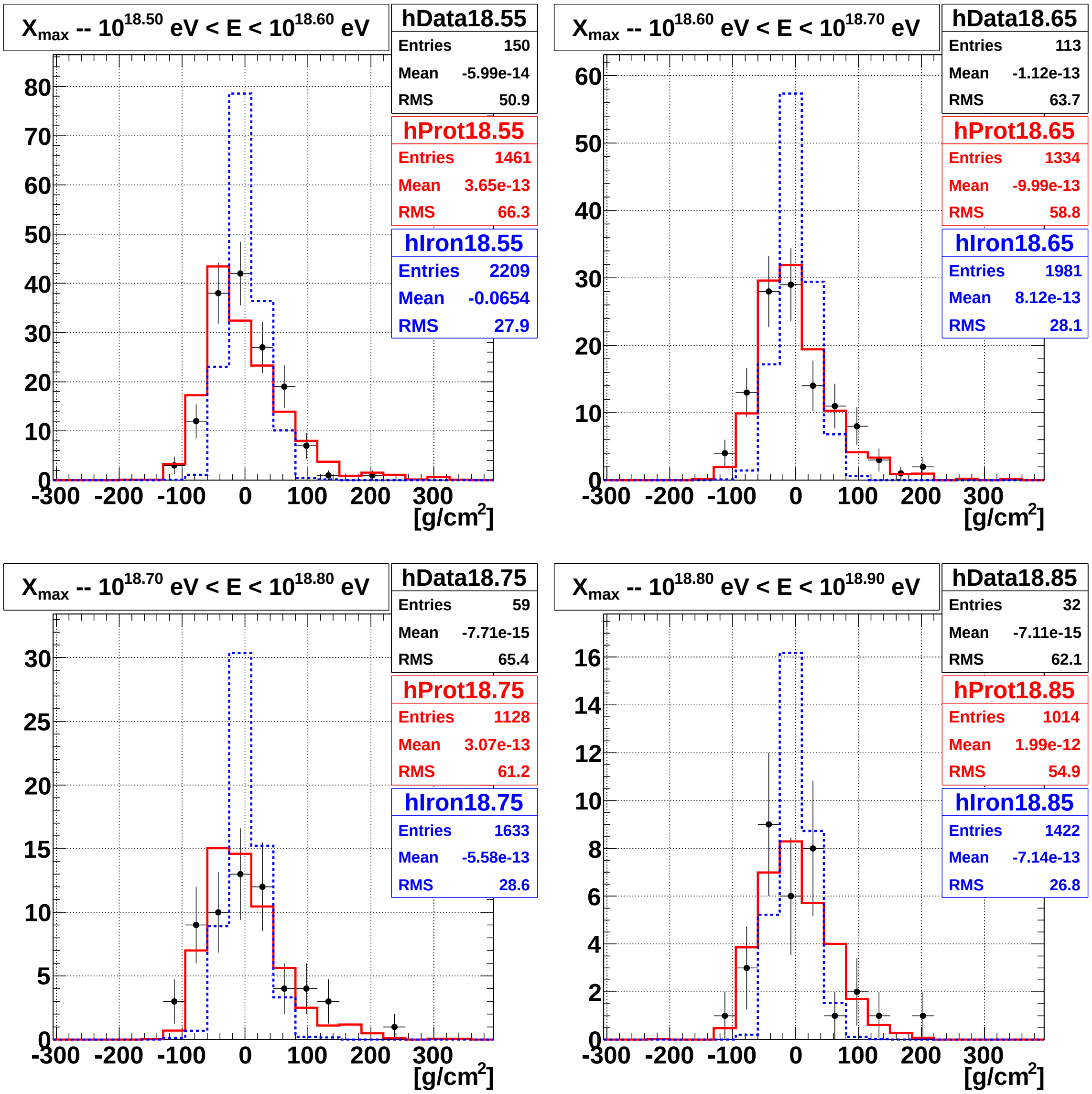

**Figure 6.44**: Mean subtracted $X_{max}$ distributions for data and proton MC and iron MC for energy greater than $10^{18.5}$ eV and less than $10^{18.9}$ eV. In each figure, the data is shown with points, proton MC is with a solid histogram,hData19.55.shift.eps and iron MC with a dashed histogram.

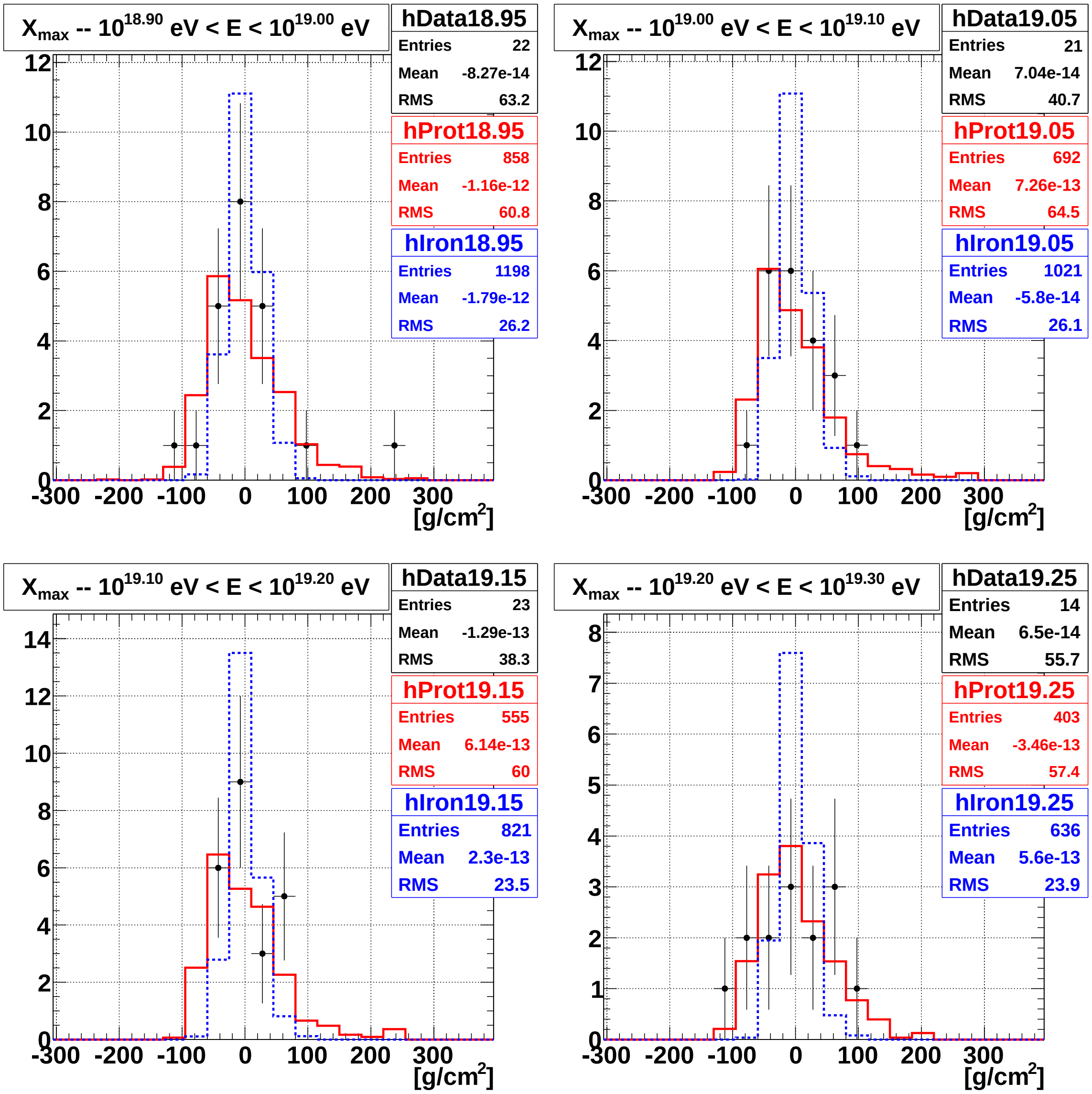

**Figure 6.45**: Mean subtracted $X_{max}$ distributions for data and proton MC and iron MC for energy greater than $10^{18.5}$ eV and less than $10^{18.9}$ eV. In each figure, the data is shown with points, proton MC is with a solid histogram, and iron MC with a dashed histogram.

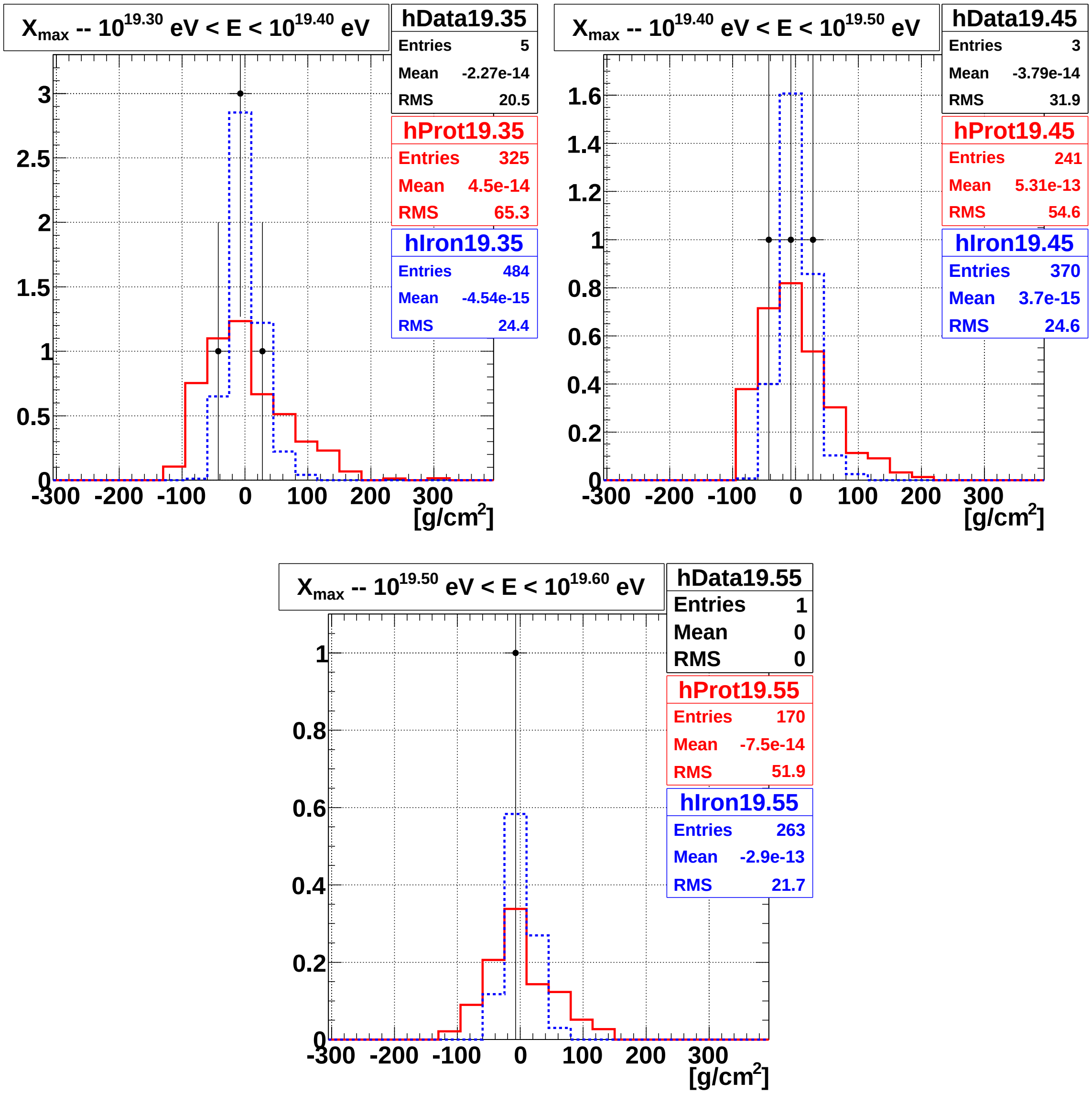

**Figure 6.46**: Mean subtracted $X_{max}$ distribution for data and proton MC and iron MC for energy greater than $10^{19.3}$ eV. In each figure, the data is shown with points, proton MC is with a solid histogram, and iron MC with a dashed histogram. Due to poor statistics, the data is compatible with both proton and iron MC.

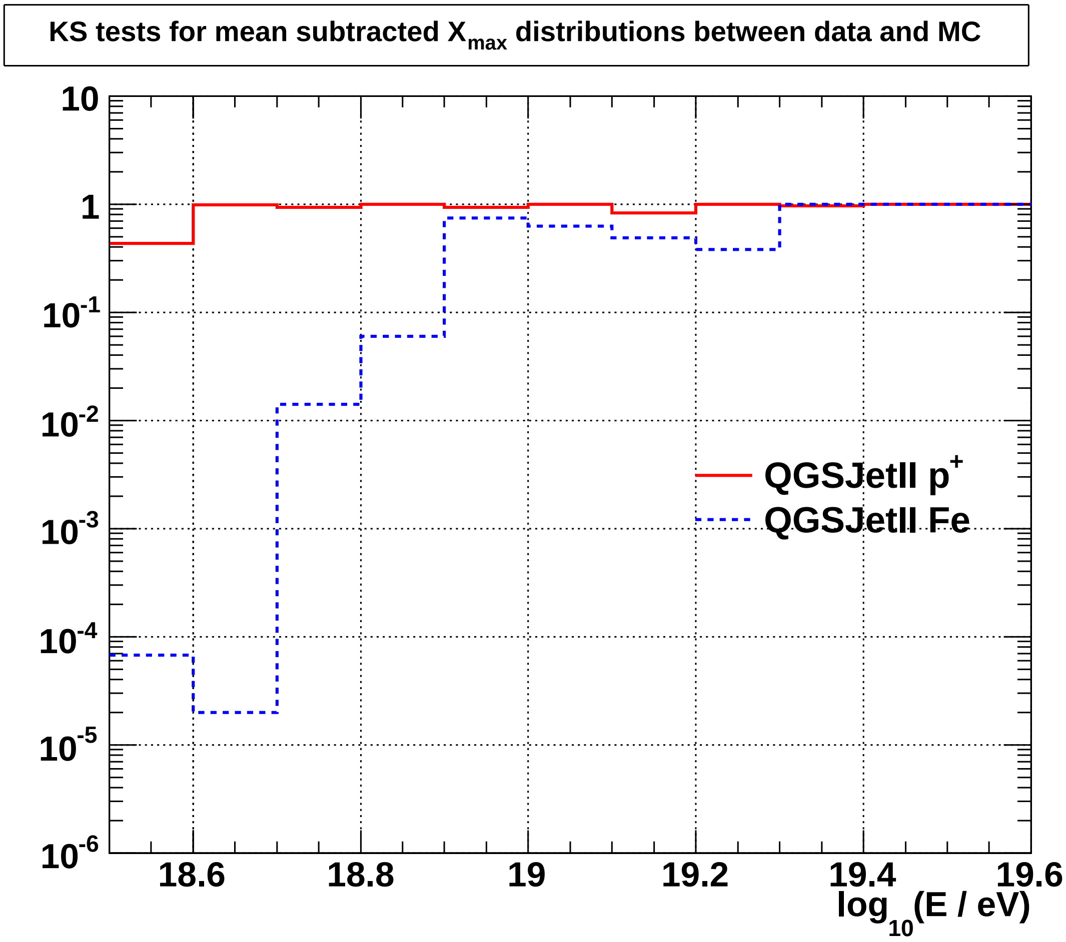

**Figure 6.47**: Results from KS tests of $X_{max}$ distributions from the data and proton and iron MC.

# CHAPTER 7

# CONCLUSIONS

This thesis has presented a complete composition analysis using the $X_{max}$ observable and hybrid reconstruction. Resolving proton and iron $X_{max}$ distributions requires good resolution in reconstructed $X_{max}$, and the hybrid geometry reconstruction was developed for this purpose. This reconstruction achieved resolutions of $\approx 0.5^\circ$ in $\theta$ and $\phi$ and $\approx 20$ g/cm$^2$ in $X_{max}$. In addition, a hybrid MC was developed, making use of existing SD and FD MCs. The validity of these simulations has been verified using data-MC comparisons, ensuring that the MC produces simulations that are representative of the hybrid data above $10^{18.5}$ eV.

This work used hybrid data from the Telescope Array experiment from May $27^{th}$, 2008 to September $7^{th}$, 2010 or approximately 2.5 years of operation. The end point for this data analysis is due to an updated trigger algorithm that was installed in early October, 2010. This new trigger allows the BR and LR FD detectors to directly trigger the SD array and requires an updated detector simulation that is beyond the scope of this work. The 2.5 years of data result in 5332 hybrid events from time matching and 454 events above $10^{18.5}$ eV after quality cuts. This event set has good statistics for $X_{max}$ analysis below $10^{19.3}$ eV in energy, though statistical power to resolve the width of $X_{max}$ distributions was present only below $10^{18.8}$ eV.

Comparisons to $X_{max}$ distributions from the data were made to simulated protons and iron MC in a variety of ways. First the overall $X_{max}$ distributions from the data were compared to corresponding proton and iron $X_{max}$ distributions in bins of 0.1 in $\log_{10}(E/\,\mathrm{eV})$. By eye, it is clear that up to $10^{19.3}$ eV, the data is compatible with the proton MC and rules out iron MC. Further, a statistical test was done, quantifying the same result and showing compatibility with the proton MC.

After looking at the full distributions, a comparison of the mean $X_{max}$ was made in 0.1 size bins in $\log_{10}(E/\,\mathrm{eV})$. This comparison shows that the data is 10 g/cm$^2$

shallower than the QGSJetII proton simulations overall, but was still 80 g/cm$^2$ deeper than the iron MC. Again, the mean $X_{max}$ shows agreement with proton MC. However, the 10 g/cm$^2$ shift could allow for better compatibility with another hadronic model, possibly QGSJet01, which tends to result in a slightly shallower $X_{max}$.

Comparisons were also made between the shape of $X_{max}$ distributions independently from the mean of the distributions. In general, these distributions show that the data is $\approx$ 60 g/cm$^2$ wide and tend to have a long right side tail, similar to the proton MC and incompatible with the shape of $X_{max}$ distributions from iron simulations. A statistical test is again applied showing that below $10^{18.8}$ eV the data is incompatible with the iron MC. However, above $10^{18.8}$ eV, due to low statistics in the data, both models are compatible with the shape of the $X_{max}$ distributions.

Lastly, the width was measured independently using the RMS of the $X_{max}$ distribution in each energy bin. These results corroborate the KS tests using the mean subtracted $X_{max}$ distributions. However, their usefulness is limited as the statistical power drops off after $10^{18.8}$ eV.

Overall, this analysis presents a concise picture. Above $10^{18.5}$ eV the Telescope Array experiment observes cosmic rays that look very much like protons simulated with the CORSIKA software package. This analysis is incompatible with iron MC in any region that the statistics allow for a comparison.

The dominance of protons above $10^{18.5}$ eV found in this work has important implications on the measured cosmic ray spectrum. As was discussed in Chapter 1, the ankle and the cutoff features in the cosmic ray spectrum are found above $10^{18.5}$ eV. Theory to explain these features are sensitive to the chemical composition of the observed cosmic rays. This work strongly supports the GZK mechanism as the cause of the cutoff of cosmic rays above $10^{19.6}$ eV and refutes the notion that the cutoff is caused by an acceleration limit at the cosmic ray sources. Furthermore, the measurement of protons in this work support the pair production theory to explain the ankle region of the spectrum.

Composition plays an important role in anisotropy searches. Cosmic rays of consisting of iron nuclei will experience significantly more deflection due to Galactic and extra-Galactic magnetic fields. This analysis, showing compatibility with protons, bolster the possibility of a positive anisotropy search. However, a strongly significant anisotropy result has yet to be measured.

# REFERENCES

[1] R. Abbasi and the FLASH collaboration. Air fluorescence measurements in the spectral range 300 420 nm using a 28.5 GeV electron beam. *Astroparticle Physics*, 29:77–86, February 2008.

[2] R. U. Abbasi and the HiRes Collaboration. A search for arrival direction clustering in the HiRes-I monocular data above $10^{19.5}$ eV. *Astroparticle Physics*, 22:139–149, November 2004.

[3] R. U. Abbasi and the HiRes Collaboration. First observation of the greisen-zatsepin-kuzmin suppression. *Phys. Rev. Lett.*, 100:101, 2008.

[4] R. U. Abbasi and the HiRes Collaboration. Indications of proton-dominated cosmic-ray composition above 1.6 eev. *Physical Review Letters*, 104(19):199902–+, May 2010.

[5] J. Abraham and the Pierre Auger Observatory. Observation of the suppression of the flux of cosmic rays above $4{\times}10^{19}$ *ev. PhysicalReviewLetters*, 101(6) : 061101 − −+, *August*2008.

[6] R. Aloisio, V. Berezinsky, and A. Gazizov. Ultra high energy cosmic rays: The disappointing model. *Astroparticle Physics*, 34:620–626, March 2011.

[7] T. Antoni and the KASCADE Collaboration. Kascade measurements of energy spectra for elemental groups of cosmic rays: Results and open problems. *Astropart. Phys.*, 24:1–25, 2005.

[8] P. V. Auger. Extensive cosmic-ray showers. *Rev. Mod. Phys.*, 11:3–4, 1938.

[9] J. Belz. Telescope array surface detector fact sheet. 2006. Internal TA document.

[10] V. S. Berezinskii and S. I. Grigor’eva. A bump in the ultra-high energy cosmic ray spectrum. , 199:1–12, June 1988.

[11] V. Berezinsky. Ultra high energy cosmic rays from cosmological relics. *Nuclear Physics B Proceedings Supplements*, 75:119–127, March 1999.

[12] V. Berezinsky, A. Gazizov, and S. Grigorieva. On astrophysical solution to ultrahigh energy cosmic rays. , 74(4):043005–+, August 2006.

[13] V. S. Berezinsky, A. Z. Gazizov, and B. I. Hnatyk. On astrophysics solution to ultra high energy cosmic rays. *Astropart. Phys.*, 21:617–625, 2004.

[14] D. R. Bergman. Fitting the HiRes Spectra. In *International Cosmic Ray Conference*, volume 7 of *International Cosmic Ray Conference*, pages 315–+, 2005.

[15] P. L. Biermann. Topical review: The origin of the highest energy cosmic rays. *Journal of Physics G Nuclear Physics*, 23:1–27, January 1997.

[16] J. Blümer, R. Engel, and J. R. Hörandel. Cosmic rays from the knee to the highest energies. *Progress in Particle and Nuclear Physics*, 63:293–338, October 2009.

[17] C. Amsler et al. Review of particle physics. *Phys. Rev. B*, 667:1, 2008.

[18] T. K. Gaisser. Reliability of the method of constant intensity cuts for reconstructing the average development of verticle showers. In *ICRC*, 1977.

[19] T. K. Gaisser. *Cosmic Rays and Particle Physics*. Cambridge University Press, 1992.

[20] G. Greisen. End of the cosmic-ray spectrum? *Phys. Rev. Lett.*, 16:748–750, 1966.

[21] W. F. Hanlon. *The Energy Spectrum of Ultra High Energy Cosmic Rays Measured By The High Resolution Fly's Eye Observatory in Steroscopic Mode*. PhD thesis, University of Utah, December 2008.

[22] D. Harari, S. Mollerach, and E. Roulet. On the ultrahigh energy cosmic ray horizon. , 11:12–+, November 2006.

[23] D. Heck, J. Knapp, J. N. Capdevielle, G. Schatz, and T. Thouw. CORSIKA: a Monte Carlo code to simulate extensive air showers. February 1998.

[24] W. Heilter. *Quantum Theory of Radiation*. Oxford University Press, 2 edition, 1944.

[25] A. M. Hillas. The origin of ultra-high energy cosmic rays. *Ann. Rev. Astron. AstroPhys*, 22:425–444, 1985.

[26] J. R. Horande and the KASCADE Collaboration. Galactic cosmic rays and the knee - results from the kascade experiment. In *Astrophysical Sources of High Energy Particles and Radiation*, June 20-24 2005. Invited Talk.

[27] D. Ikeda. TA FD Calibration, ver 1.00. March 2009. Internal TA document.

[28] D. Ivanov. *Energy Spectrum Measured by the Telescope Surface Detector*. PhD thesis, Rutgers University, 2012.

[29] F. Kakimoto, E. C. Loh, M. Nagano, H. Okuno, M. Teshima, and S. Ueno. A measurement of the air fluorescence yield. *Nuclear Instruments and Methods in Physics Reseach A*, 372:527–533, 1996.

[30] K. Kamata and J. Nishimura. *Prog. Theoretical Phys. Suppl.*, 6:74, 1958.

[31] M. Kobal and the Pierre Auger Collaboration. A thinning method using weight limitation for air-shower simulations. *Astroparticle Physics*, 15:259–273, June 2001.

[32] J. Linsley. In *Proc. 18th ICRC*, volume 12, page 159, 1985.

[33] M. S. Longair. *High Energy Astrophysics*. Cambridge University Press, 1981.

[34] G. Medina Tanco. Astrophysics motivation behind the pierre auger southern observatory enhancements. In *International Cosmic Ray Conference*, volume 5 of *International Cosmic Ray Conference*, pages 1101–1104, 2007.

[35] F. Nerling, J. Blumer, R. Engel, and M. Risse. Universality of electron distributions in high-energy air showers - description of cherenkov light production. *Astropart. Phys.*, 24:421–437, 2006.

[36] S. Ogio, H. Miyauchi, T. Matsuyama, D. Ikeda, H. Tokuno, and the Telescope Arrray Collaboration. Temperature characteristics of pmts and calibration light sources for the Telescope Array fluorescence detectors. In *31th International Cosmic Ray Conference*, International Cosmic Ray Conference, 2009.

[37] A. V. Olinto, D. Allard, E. Armengaud, and et al. Horizons and anisotropies of ultra-high energy cosmic rays. In *International Cosmic Ray Conference*, volume 4 of *International Cosmic Ray Conference*, pages 527–530, 2008.

[38] S. Ozawa, H. Ohoka, M. Takeda, N. Sakurai, S. Yoshida, S. Kawakami, and H. Tanaka. The system of daq for ta surface array. In *29th International Cosmic Ray Conference*, volume 8 of *International Cosmic Ray Conference*, pages 177–+, 2005.

[39] A. A. Penzias and R. W. Wilson. A measurement of excess antenna temperature at 4080 mc/s. *ApJ*, 142:419–421, 1965.

[40] J. A. Simpson. Elemental and isotopic composition of the galactic cosmic rays. *Annual Review of Nuclear and Particle Science*, 33:323–382, 1983.

[41] P. Sokolsky. *Introduction to Ultrahigh Energy Cosmic Ray Physics*, volume 75 of *Frontiers in Physics*. Westview Press, 2004.

[42] C. Song. *Study of Ultra High Energy Cosmic Rays with the High Resolution Fly's Eye Prototype Detector*. PhD thesis, Columbia University, 2001.

[43] F. W. Stecker. Effect of photomeson production by the universal radiation field on high-energy cosmic rays. *Physical Review Letters*, 21:1016–1018, 1968.

[44] B. T. Stokes, R. Cady, D. Ivanov, J. N. Matthews, and G. B. Thomson. A Simple Parallelization Scheme for Extensive Air Shower Simulations. *ArXiv e-prints*, March 2011. Submitted to Astroparticle Physics.

[45] B. T. Stokes, R. Cady, D. Ivanov, J. N. Matthews, and G. B. Thomson. Dethinning extensive air shower simulations in CORSIKA. *ArXiv e-prints*, April 2011. Submitted to Astroparticle Physics.

[46] B. T. Stokes, R. Cady, D. Ivanov, G. B. Thomson, G. I. Rubtsov, and Telescope Array Collaboration. Using CORSIKA to quantify telescope array surface detector response. In *The 31st ICRC*, 2009.

[47] Y. Tameda and The Telescope Array Collaboration. Trigger electronics of the new fluorescence detectors of the Telescope Array. *Nuclear Instruments of Methods in Physics Research A*, 609:227–234, 2009.

[48] G. B. Thomson, Sokolsky, P. and Jui, C. C. H. and Matthews and J. N. and Ogio, S, and H Sagawa. The Telescope Array low energy extension (TALE). In *International Cosmic Ray Conference*, 2011.

[49] H. Tokuno and The Telescope Array Collaboration. Calibration and monitoring of the air fluorescence detector for the Telescope Array experiment. In *30th International Cosmic Ray Conference*, volume 5 of *International Cosmic Ray Conference*, pages 1013–1016, 2007.

[50] H. Tokuno and The Telescope Array Collaboration. On site calibration for new fluorescence detectors of the telescope array experiment. *Nuclear Instruments of Methods in Physics Research A*, 601:364–371, 2009.

[51] S. Yoshida, N. Hayashida, K. Honda, M. Honda, S. Imaizumi, N. Inoue, K. Kadota, F. Kakimota, K. Kamata, S. Kawaguchi, N. Kawasumi, Y. Matsubara, K. Murakami, M. Nagano, H. Ohoka, Y. Suzuki, M. Teshima, I. Tsushima, and H. Yoshii. Lateral distribution of charged particles in giant air showers above 1 EeV observed by AGASA. *Journal of Physics G Nuclear Physics*, 20:651–664, April 1994.

[52] G. T. Zatsepin and V. A. Kuz'min. Upper limit of the spectrum of cosmic rays. *ZhETF Pis'ma Redaktsiiu*, 4:114–117, 1966.